THÈSE DE DOCTORAT
UNIVERSITÉ PARIS 7 – DENIS DIDEROT
École Doctorale d'Astronomie et d'Astrophysique d'Île-de-France

Présentée pour obtenir le grade de
Docteur ès Sciences de l'Université Paris 7

Spécialité :

Astrophysique

par :

Bob Petrus Franciscus DIRKS

Study and modelling of the new generation Cd(Zn)Te X- and gamma-ray detectors for space applications

Directeurs de thèse: Francois LEBRUN/ Bob VAN EIJK
Responsable de thèse: Olivier LIMOUSIN

Soutenue le 23 novembre 2006
devant la commission d'examen composée de :

T. Patzak	Président du Jury
F. Lebrun	Directeur de thèse
B. van Eijk	Directeur de thèse
E.H.M. Heijne	Rapporteur
G. Duchêne	Rapporteur
H. ten Kate	Examinateur

STUDY AND MODELLING OF THE NEW GENERATION CD(ZN)TE X- AND GAMMA-RAY DETECTORS FOR SPACE APPLICATIONS

PROEFSCHRIFT

ter verkrijging van
de graad van doctor aan de Universiteit Twente,
op gezag van de rector magnificus,
prof. dr. W.H.M. Zijm,
volgens besluit van het College voor Promoties
in het openbaar te verdedigen
op 23 november 2006 om 14.00u

door

Bob Petrus Franciscus Dirks

geboren op 18 maart 1977

te Gennep

Promotores:	Dr. F. Lebrun (Director of Research)
	Prof. Dr. Ing. B. van Eijk

Faculteit der Technische Natuurwetenschappen

Le seul relief aux Pays Bas, c'est la courbure de la Terre.
B.P.F. Dirks

Acknowledgements

The decision to leave the Netherlands to start a PhD thesis in Paris was not evident. It was a personal challenge in an intellectual and social way. Intellectual, because I consider this thesis as the crown on my academic career, and social, because starting a new life in a yet unknown, foreign city, is not evident at all. But I believe I have succeeded, thanks to all the people with whom I worked and those with whom I spent precious moments outside working hours.

One person in particular allowed me to finish this work with satisfaction: Olivier Limousin. I never met a person as motivated, devoted and fanatic as he is, always giving me plenty of new ideas and propositions. Thanks Olivier, also for your warm welcome three years ago and the patience until I finally understood and spoke the French language. (By the way, for a perfect imitation of the Dutch language, please contact him.)

Francis Lugiez and Olivier Gevin, two outstanding electronics scientists, thank you for your precious time to explain and to show me the hidden secrets of micro-electronics of, in particular, the IDeF-X ASIC. And of course I will never forget the great time we had in Japan! (For another Kung-Fu fight, do not hesitate to ask me, Francis!)

Claire Blondel, thanks for your support in the lab and the numerous measurements you took which were necessary for the characterisation of electronics and detectors.

François Dali, thank you for your help in designing and constructing the printed circuits for the leakage current measurements.

Two people that helped and supported me enormously in the understanding and adaptation of the MGS simulation program are Cayetano Santos and Camille Parisel, both from the IReS in Strasbourg. Muchas gracias to both of you.

Also I would like to thank the members of the jury for their precious time they spent to read my thesis and for being present at my defence, and especially Erik Heijne and Gilbert Duchêne for accepting the task as rapporteur. My apologises for the short delay I gave you to read it.

My promotores Francois Lebrun and Bob van Eijk, thank you for giving me the opportunity to perform this thesis.

And then of course the people with whom I spent a lot of time outside working hours. I have had the greatest time in Paris, thanks to you.

Severin, hopefully we get a chance to do some theatre improvisation again or some climbing in Fontainebleau!

Mickey, Matthieu, Guillaume and Patrick, thanks for the numerous hard-core-physics and philosophy discussions, push-up sessions in your bureau, the guitar playing, and the (non)-alcoholic abuse in several bars in Paris.

Marion, again my apologies for calling you ”la secrétaire” the first day I arrived at CEA. I definitely will come back to Madrid very soon again, either to take a bath or dance la salsa! In the latter case I will take Coralie with me. Coco, have fun in Germany!

Benoit, thanks for the great time in Rome and hopefully we will play some jazz together soon again. Nico, if you look for a travelling partner to check out the West of the US, let me know! Christophe and Amelie, thanks for letting me discover the marriage in French

style. It was great.

Greg, I appreciate enormously all the advice and help you gave me before and during my stay in France. It was an honour to be one of your best-men during the marriage.

Lieve Lot, ook jou ben ik ongelooflijk veel dank verschuldigd. De steun die je me gaf in het eerste jaar dat ik hier zat, heeft er toe bijgedragen dat ik door ben gegaan om dit alles met goed gevolg af te ronden.

En dan tenslotte mijn ouders, die een jaar lang zelfs twee zonen moesten missen die naar het buitenland vertrokken waren. Pap en mam, bedankt voor jullie steun de afgelopen drie jaar.

Contents

Abstract

The scientific astrophysics community needs a new instrument to gain more insight in the origin of the cosmic X-ray background, the physics of black holes and particle acceleration mechanisms in the energy range between 0.5 to 80 keV. Existing instruments like Chandra and XMM-Newton show very good results up to ~10 keV but lack sufficient sensitivity above this value. In order to keep or improve the same performances up to ~80 keV, grazing incidence mirrors with a large focal length of at least 20 m should be used. Since satellites this big cannot be launched with existing launchers, the mirror and detector must be placed on two different satellites flying in formation. The Simbol-X space mission will be the first project of this type.

A high sensitivity at 80 keV requires not only a long focal length but also a detection unit with high spatial resolution, using detectors that are still efficient at these relatively high energies.

CEA/Saclay/DAPNIA is developing this crucial element for the Simbol-X space mission. The imager consists of several modules, each built from individual X-ray mini-cameras. A single camera is a hybridisation of custom read-out electronics connected to a Cd(Zn)Te semiconductor crystal. The ensemble must be able to efficiently detect photons of up to 80 keV with an energy resolution of ~1.3 keV (FWHM) at 68 keV. Furthermore it must be equipped with small pixels ($\sim 500 \times 500\ \mu\text{m}^2$) to attain the desired spatial resolution of 15 arcsec. In order to reach a good sensitivity and energy resolution, ultra-low noise read-out electronics in combination with high-quality semiconductor crystals are mandatory.

The read-out electronics, baptised IDeF-X (Imaging Detector Front-end for X-rays), is also developed by CEA/Saclay. A thorough understanding of its functioning as well as its testing forms a part of this work.

The spectroscopic performance of the detector is directly related to the electronics noise. The noise characteristics of the ASIC are therefore examined in detail as a function of the input capacitance and current, two important sources of noise. Since the chip is designed to be DC coupled to the crystals, knowledge of the leakage current (per pixel) inside multi-pixel Cd(Zn)Te detectors is very important.

I developed an electronic circuit which allows an accurate measurement of the very low leakage currents per pixel ($\sim 10^{-12}$ A) in 64 pixels Cd(Zn)Te detectors. Current maps are presented of different detectors at various operating conditions. Moreover, the relation between the current and temperature also allows obtaining activation energy maps of the impurities inside the crystal. In addition, the circuit is a tool to study the mechanical properties of the pixel-substrate contacts.

With four fully operational 16-channels IDeF-X V1.0 ASICs connected to different 64 pixels CdTe and CdZnTe crystals, energy spectra are taken. From the results, optimal operation conditions (bias voltage, peaking time, temperature) are obtained to get the best energy resolution of the 60 keV energy peak of ^{241}Am. For a single pixel CdTe detector (360 V bias, 22^{o}C) an excellent energy resolution of 1 keV (FWHM) is obtained. This value has also been achieved by several individual pixels of a 64 pixels indium diced CdTe detector (400 V bias, -18^{o}C).

In order to better understand the detector behaviour and to predict detector performances, I constructed a full simulation chain. It starts with the particle interactions inside the crystal and continues the simulation up to the output of the read-out electronics. I combine GEANT4, to simulate individual interactions inside Cd(Zn)Te, and MGS-CdTe V1.0 to simulate charge carrier creation, transport, trapping effects and signal induction on the electrodes. By convolving these signals with the (numerical) impulse response function of IDeF-X V1.0, a complete detector response is generated. Simulated spectra are compared with measurements and show excellent agreement.

GEANT4 and MGS-CdTe are also used separately to study different parameters of the detector. These include the size of the charge cloud after an interaction, event multiplicity and detection efficiency.

The simulation chain serves as a powerful tool to predict signal shape, cross-talk between pixels and read-out strategy for the Simbol-X mission.

Résumé

La communauté scientifique d'astrophysique a besoin d'un nouvel instrument pour approfondir sa connaissance sur l'origine du fond cosmique X, de la physique des trous noirs et des mécanismes d'accélération de particules dont l'énergie s'étend entre 0.5 et 80 keV. Les instruments existants comme Chandra et XMM-Newton montrent des résultats excellents jusqu'à ∼10 keV, mais la sensibilité n'est plus suffisante au-dessus de cette valeur. Afin de conserver les mêmes performances jusqu'à ∼80 keV, ou de les améliorer, des miroirs en incidence rasante avec une grande longueur focale (>20 m) devraient être employés. Etant donné que des satellites de cette taille ne peuvent pas être mis en orbite avec les lanceurs existants, le miroir et le détecteur doivent être placés sur deux satellites différents volant en formation. La mission spatiale Simbol–X sera le premier projet de ce type.

Une sensibilité élevée à 80 keV exige non seulement une grande longueur focale, mais également une unité de détection avec une résolution spatiale élevée, ainsi que des détecteurs encore efficaces à ces énergies relativement élevées. Le CEA/Saclay/DAPNIA développe cet élément crucial pour Simbol–X.

L'imageur se compose de plusieurs modules. Ceux-ci sont composés de différentes mini-caméras X, qui sont une hybridation de l'électronique de lecture dédiée et des cristaux Cd(Zn)Te semi-conducteurs. L'ensemble doit pouvoir détecter efficacement des photons jusqu'à 80 keV avec une résolution d'énergie de ∼1.3 keV (FWHM) à 68 keV. En outre, le cristal doit être équipé de petits pixels ($\sim 500 \times 500\ \mu\mathrm{m}^2$) pour atteindre la résolution spatiale désirée de 15 arcsec. Afin d'atteindre une sensibilité et une résolution en énergie satisfaisantes, il est obligatoire de combiner une électronique de lecture en bruit ultra-bas avec des cristaux semi-conducteurs de haute qualité.

L'électronique de lecture, baptisée IDeF-X (Imaging Detector Front-end for X-rays), est également développée par le CEA/Saclay. Une connaissance complète de son fonctionnement ainsi que sa caractérisation font parties de ce travail.

Les performances spectroscopiques du détecteur sont directement liées au bruit de l'électronique. Les caractéristiques du bruit de l'ASIC sont donc examinées en détail en fonction de la capacité d'entrée et du courant, deux sources importantes de bruit. Puisque l'ASIC est fait pour être couplé de façon DC aux cristaux, la connaissance des courants de fuite des détecteurs Cd(Zn)Te multi-pixels est très importante.

J'ai développé un circuit électronique qui permet une mesure précise des courants de fuite très faibles, par pixel ($\sim 10^{-12}$ A) dans les détecteurs Cd(Zn)Te 64 pixels. Des cartes de courants sont présentées pour différents détecteurs dans des conditions diverses de fonctionnement. D'ailleurs, la relation entre le courant et la température permet également d'obtenir des cartes d'énergie d'activation des impuretés à l'intérieur du cristal. En outre, le circuit est un outil pour étudier les propriétés mécaniques des contacts entre pixel et substrat.

Des spectres d'énergie sont acquis avec quatre puces IDeF-X V1.0 (16 canaux) complètement opérationnelles, connectées à différents cristaux CdTe et CdZnTe (64 pixels). Les résultats donnent les conditions opérationnelles optimales pour obtenir la meilleure résolution d'énergie à 60 keV (source ^{241}Am). Pour un détecteur CdTe avec un pixel (360 V

bias, 22^{o}C) une excellente résolution d'énergie de 1 keV (FWHM) est obtenue. Cette valeur a également été réalisée par plusieurs pixels d'un détecteur CdTe avec 64 pixels en indium découpé (400 V bias, -18^{o}C).

Afin de mieux comprendre le comportement et de prévoir la performance des détecteurs, j'ai construit une chaîne de simulation complète. Elle commence par les interactions de particules à l'intérieur du cristal et la simulation continue jusqu'à la sortie de l'électronique de lecture. Je combine GEANT4 pour simuler différentes interactions à l'intérieur du Cd(Zn)Te et MGS–CdTe V1.0 pour simuler la création des porteurs de charge, le transport, les effets de piégeage et l'induction des signaux sur les électrodes. Par convolution de ces signaux avec la fonction de réponse d'impulsion numérique d'IDeF-X V1.0, une réponse complète du détecteur est produite. La comparaison entre les spectres simulés et les mesures montre un excellent accord.

GEANT4 et MGS–CdTe sont également employés individuellement pour étudier les différents paramètres du détecteur. Ceux-ci incluent la taille du nuage de charge après une interaction, la multiplicité des interactions et l'efficacité de la détection.

La chaîne de simulation est un outil puissant pour prévoir la forme du signal, les interférences entre les pixels et la stratégie de lecture pour la mission Simbol–X.

Chapter 1

Introduction

1.1 Scorpius X-1, the first extra-solar X-ray source

X-ray astrophysics was in its infancy in 1962. Instruments as we have nowadays were still science fiction and little was known about the physics of astronomical objects such as stars, galaxies and the interstellar medium and the interactions involved.

One thing that was clear to astrophysicists, was that X-rays could be produced inside the Sun. But the amount of X-ray radiation emitted would be overwhelmed by the flux in visible wavelengths. In order to be seen in X-rays, stars, hundreds of light years away, would have to glow millions of times brighter in this energy range than the Sun. It was unimaginable that these kinds of objects could exist.

Using the X-rays from the Sun one wanted to study the Moon. The Sun shines on the Moon and a fraction of the X-rays is reflected to Earth. If the reflected radiation could be measured, information could be obtained about the surface of the Moon.

X-rays are absorbed by the Earth's atmosphere and can only be detected at high altitudes and in space. On the 18th of June, 1962, a Aerobee rocket was launched with on board an X-ray detector developed by the team of Riccardo Giacconi of the American Science and Engineering Institute in Cambridge (USA). Instead of detecting the faint X-rays coming from the Moon, the detector discovered an extremely bright X-ray source in the constellation of Scorpius. They called it Scorpius X1 (SCO X-1) and it became the first X-ray object discovered outside the solar system. SCO X-1 is situated about 9000 light years from Earth and is the most powerful source in the X-ray sky.

Many years later it was discovered that SCO X-1 is a binary system formed of a compact object and a companion star orbiting it and thereby regularly eclipsing it. The compact object is a neutron star whose gravity pulls the material of its companion into an accretion disk. The matter forming this disk heats up to extreme temperatures and starts to radiate the X-rays we see.

(Space-)technology has drastically advanced in the last decades. Sophisticated satellites have been built that allow us to observe the X-ray sky for longer than the five minutes that were available for the discovery of Scorpius X-1. With their high sensitivity, spectral and spatial resolution, large field-of-views (FOV) etc, paths were and still are paved to

unexplored domains to study new and often exotic processes.
The detection of SCO X-1 but especially the discovery that the Universe is radiating X-rays from all directions, a discovery that led to a Nobel price for Giacconi (see Giacconi and Gursky (1962)), triggered the hunt for finding more of these objects. Thousands of comparable objects have been resolved since.

1.2 Cosmic X-ray background

Fig. 1.1 shows the total cosmic energy density spectrum as measured by different instruments over the years. It comprises the cosmic microwave background (CMB), the cosmic infrared background (CIB), the cosmic optical background (COB) and the cosmic X- (and gamma-)ray background (CXB). This spectrum is seen from all directions in space and its origins are still only partially understood.

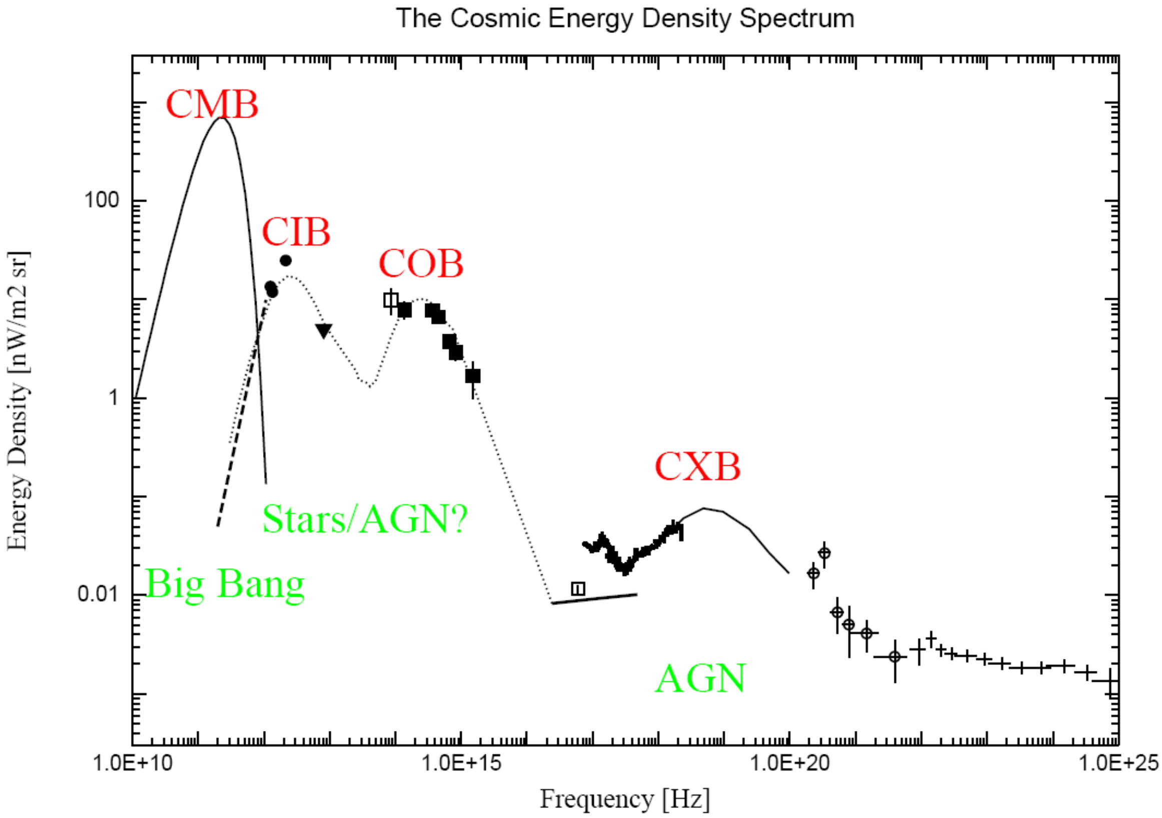

Figure 1.1: The cosmic diffuse background spectrum. Credits: Hasinger (2000)

The CMB was first discovered in 1965 and has been well studied. It fills the entire Universe with an electro-magnetic radiation, characterised by a 2.725 Kelvin black-body spectrum. It peaks in the microwave range at a frequency of 160.4 GHz. It is a fingerprint of the early Universe and one of the strongest evidence for the Big Bang model.

While the CMB is truly diffuse, the other parts of the spectrum are believed to be mainly due to the sum of discrete sources. The cosmic infrared and optic background are created by stars and active galactic nuclei (AGN), but the spectrum is still partly unresolved. In the UV-range even less data are known.

The CXB spectrum has been measured for decades. Below energies of 5-6 keV about 80% of it has been resolved, primarily due to studies carried out with the Chandra (Weisskopf et al. 2003) and XMM-Newton (Jansen et al. 2001) observatories, both operating in the $0.2-10$ keV range. At higher energies, the situation is completely different. The most sensitive observations have been carried out by INTEGRAL (Winkler et al. 2003) and at the moment also the Swift gamma-ray burst explorer (Gehrels et al. 2004). INTEGRAL recently measured the CXB in the 15–70 keV range (Churazov et al. 2006).

INTEGRAL and Swift's sensitivity and angular resolution are two orders of magnitude smaller than Chandra or XMM-Newton, therefore bright sources can be studied with obvious limitations in crowded regions. Nevertheless, several sources have been discovered but their contribution to the CXB amounts to only ∼5%.

This CXB, that peaks at $\sim 0.7 \times 10^{19}$ Hz and corresponds to a photon energy of ∼30 keV, therefore remains mostly unresolved. Strong indices exist that AGNs are the most probable candidates but there could be a possibility for the existence of a true, hot and diffuse, intergalactic plasma. Though, there is no proof, yet.

1.3 Instrument requirements

In order to resolve the CXB and to study in detail the (known and unknown) sources which make up this spectrum, an instrument is needed which must comply with several important requirements. First of all, it must have a high sensitivity in order to *see* them. It is currently held that 40 to 70% of the total energy in the 10-40 keV band, should come from highly obscured sources. If we want to make a significant step forward with respect to Chandra and XMM-Newton at least 50% of the sources in the 20-40 keV and 80% in the 10-30 keV bands must be resolved. This implies that a minimum flux of $\sim 7 \times 10^{-15}$ erg·cm^{-2}·s^{-1} ($< 1\ \mu$Crab) for the 20-40 keV and $\sim 2 \times 10^{-15}$ erg·cm^{-2}·s^{-1} ($< 0.15\ \mu$Crab) for the 10-30 keV range must be detected.

In an even broader energy range, this allows the direct study of black hole physics and census, as well as the study of particle acceleration mechanisms. Also, binary systems of our Galaxy can be studied in their "normal" quiescent state or binaries of outer galaxies.

High sensitivity entails high angular resolution since it will only useful if a maximum of sources can be resolved. A small point spread function (PSF) sampled by small pixels is thus necessary.

It is also desirable to have a large field-of-view (FOV) to detect a statistically meaningful number of X-ray sources, as well as to study acceleration sites in extended sources like clusters of galaxies or supernova remnants (SNRs).

Supernovae are the blacksmiths of the elements, most of them being radioactive. Among them, ^{44}Ti, which has a relatively short lifetime (85 yrs), is the best indicator of very

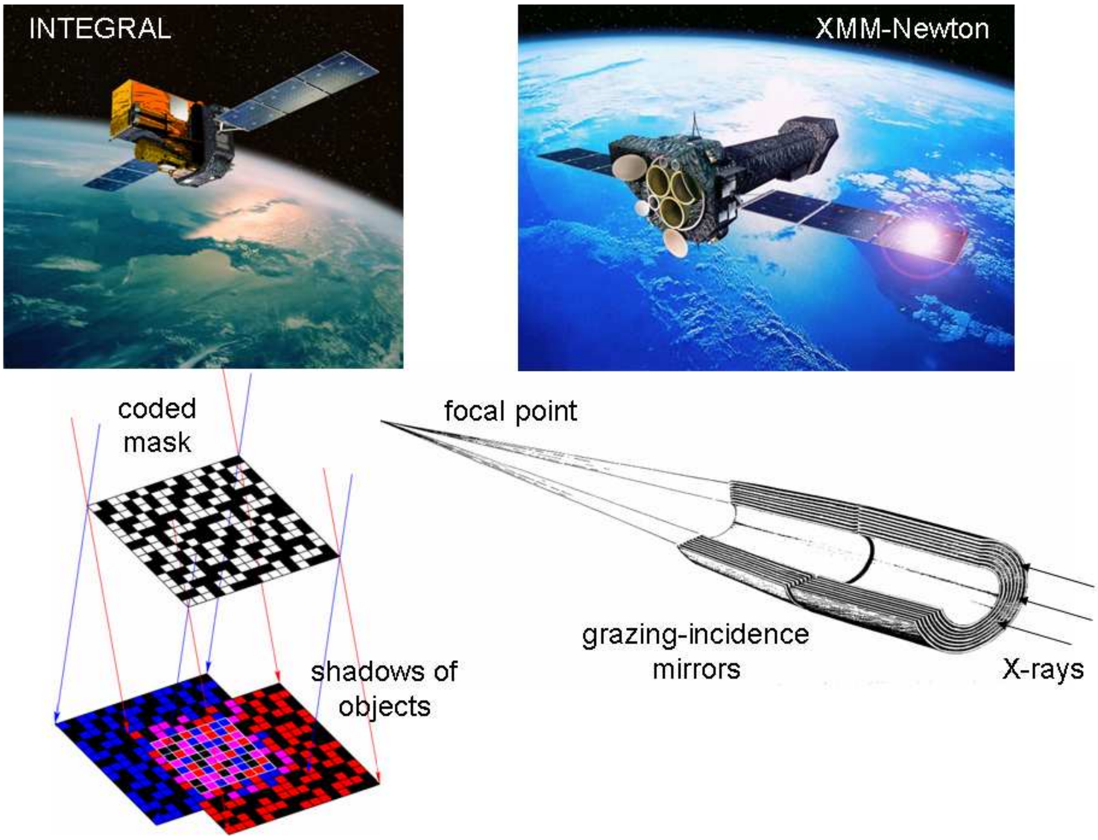

Figure 1.2: On the left: an artist's impression of the INTEGRAL Observatory with a schematic view of its coded mask system. On the right the XMM-Newton satellite with its grazing incidence focusing technique using Wolter I mirrors.

young SNRs. It decays to ^{44}Sc whose de-excitation produces lines at 68 and 78 keV. Their detection requires not only a good sensitivity but also a good spectral resolution. Finally, a good time resolution is needed to measure the absolute phase of pulsars.

1.4 Implications

In order to arrive at the desired sensitivity, a sufficient number of photons must be collected per unit detector area. As it is not easy to focus highly energetic photons, special techniques are used to image X- and gamma sources. Presently, a non-focusing technique is used at photon energies higher than 10 keV. INTEGRAL and Swift use a coded mask that, when irradiated, creates a shadow onto a large detector surface (see Fig. 1.2). Deconvolving the detected mask pattern allows for a reconstructed sky image. However, without focusing, the sensitivity, but also the angular resolution, are rather moderate.

Chandra and XMM-Newton both use mirrors having grazing incidence reflection properties to focus the X-rays onto a small detector surface (see Fig. 1.2). In comparison with the coded mask, good signal-to-noise and angular resolution (down to 0.5 arcsec for Chandra) can be obtained. Unfortunately, the technique is limited to a maximum energy which depends on the focal length of the mirror. And this is directly related to the maximum size of a satellite that can fit into a single spacecraft.

In order to use the focusing technique at higher energies, the focal length of the mirror must be increased. Then the angle of reflection is reduced, allowing higher energetic photons to be reflected. This can only be achieved by two satellites flying in formation. This is the aim of the Simbol–X space mission which I describe in detail in the following chapter. The instrument will operate in the 0.5–80 keV range. It will have the appropriate equipment to reveal the mysteries of the CXB, the physics of black holes, particle acceleration mechanisms and will be especially well suited to map the ^{44}Ti in young SNRs.

1.5 Detector specifications

The above instrument needs and the use of a focusing technique puts constraints on the design of the detectors of Simbol–X that measure the hard X-rays.

Concerning the sensitivity, up to 80 keV, detectors built from materials with a high atomic number (Z) and a high photo-peak efficiency are required.

To avoid excessive background, from outside the field of view, which lowers the signal-to-noise ratio (S/N), the surrounding mass should be limited and an active and passive shielding must be used.

To obtain a high angular resolution, small pixels must be used that sufficiently sample the PSF whose size depends on the mirror characteristics (in the next chapter I will show that a pixel size of $\sim 500 \times 500\ \mu\text{m}^2$ is necessary for Simbol–X).

Also, the detector must be able to effectively transform the detected photon into a number of charge carriers, giving a measure of the initial photon energy. For this reason, charge losses inside the material must be minimised.

The detector must operate in combination with proper read-out electronics. To obtain sufficient spectral resolution the electronics must show extremely low-noise performances. It is generally custom made in order to be compatible with the detector geometry, material and desired performances. Especially for space applications it needs to satisfy strict rules related to radiation hardness, robustness, and low power consumption.

1.6 Detection material choice

As particle detection and tracking materials, germanium (Ge) and silicon (Si) are considered as excellent candidates, having extremely good energy resolution and charge-transport properties. However, the small band gap in Ge demands an operation at cryogenic temperatures which limits its applications and the stopping power of Si is limited for high energy photons. This is partly why semiconductors with high atomic numbers and wide band gaps at room-temperature have been studied extensively during the last decades. Since the early 1970's cadmium telluride (CdTe) has become a very promising material for the detection of X- and gamma-rays. Its high atomic number (Z_{Cd}=48, Z_{Te}=52) leads to good quantum efficiency, and its relatively large band-gap of 1.5 eV makes it suitable for room-temperature operation. Unfortunately, its production process is rather difficult. Crystal inhomogeneities and high production costs have limited its use for spectroscopic applications.

Major progress has been made in the production technology over the last 20 years to produce high quality and large size monolithic CdTe crystals. Also the emergence of cadmium zinc telluride (CdZnTe) drastically changed the situation of high energy room temperature detectors. In the latter, extra zinc (Zn) atoms are added to increase the band-gap energy from 1.5 eV for CdTe up to 2.2 eV for ZnTe. The most common composition is $Cd_{0.9}Zn_{0.1}Te$ with a band-gap of 1.6 eV which is widely used.

The proof of the excellent performances of the new generation CdTe detectors is provided by the INTEGRAL satellite, now in its fourth year of operation. It has two main detectors on board: IBIS (Imager on Board the Integral Satellite) and SPI (Spectrometer on INTEGRAL). The IBIS detection unit has two parallel detector planes on top of each other. Below is the PICsIT detector with 4096 caesium iodide (CsI) pixels of $9 \times 9 \times 30$ mm^3 sensitive in the range $\sim 0.5 - 8$ MeV. On top is the ISGRI camera operating at energies between 15 keV and 1 MeV. ISGRI has eight modules of 2048 CdTe crystals each. These 4×4 mm^2 macro-pixels are grouped in "poly-cells" as shown in Fig. 1.3. After four years in space, the CdTe detectors have delivered an enormous amount of data leading to important astrophysical discoveries (Lebrun et al. (2004), Bélanger et al. (2004), Renaud et al. (2006), etc.)[1] The material shows only slight degradation which proves their radiation hardness (Lebrun 2005).

CdZnTe shows impressive results too. The group of the HEFT balloon-born experiment[2] reports a resolution of 760 eV (FWHM) at 59.54 keV, +18^{o}C, obtained with a 8×8 pixel prototype CdZnTe detector. It is therefore a logical choice to continue working with CdTe or CdZnTe detectors as detection material for Simbol–X.

1.7 Outline

In this thesis I will present in detail the results obtained during three years of research and development of the X-ray mini-camera for the Simbol–X space mission. My work articulates around two principal axes: 1) the characterisation of the detectors Cd(Zn)Te with small pixels for X-ray spectro-imagery in combination with the custom made IDeF-X read-out electronics, and 2) a complete 3D detector modelling and simulation of the above system.

This is preceded by a semiconductor theoretical overview that I present in Chapt. 3. It includes the description of semiconductor functioning and doping, material choice, metal-semiconductor contact, radiation detection with semiconductor devices, charge carrier

---

[1] For an overview of INTEGRAL highlights, see:
http://integral.esac.esa.int/Publications/SRTWinkler2005.pdf

[2] http://www.srl.caltech.edu/HEFT/results.html

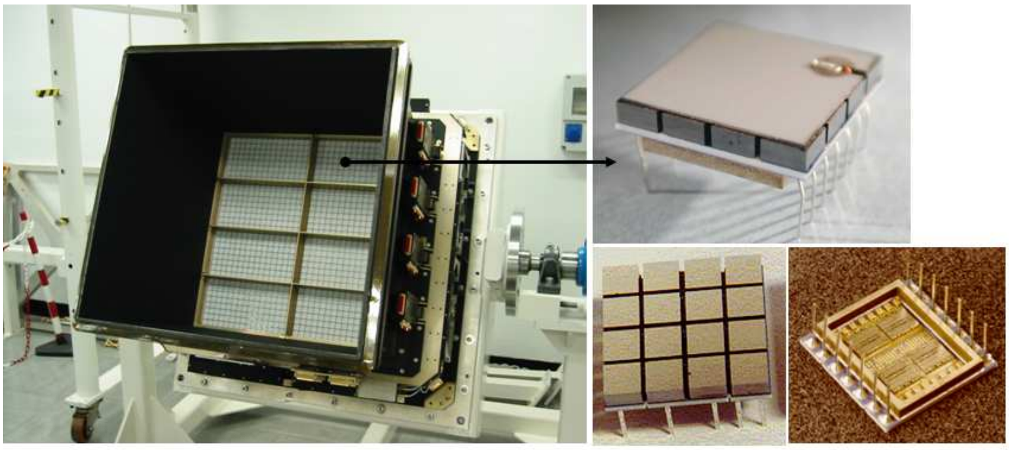

Figure 1.3: The ISGRI camera on the INTEGRAL satellite. It consists of eight modules of 2048 CdTe crystals of $4 \times 4 \times 2$ mm^3. The latter are grouped in so-called poly-cells as shown on the right, consisting of 4-by-4 crystals.

transport, etc.

In Chapt. 4, I give a thorough description of the custom designed read-out electronics, IDeF-X. The behaviour of the detection system largely depends on how well the sensor and signal processing system can be matched to provide an optimal signal-to-noise ratio, threshold detection etc. Key parameters are the detector capacitance and leakage current and their influence on the electronics performances is therefore carefully studied.

Prediction of detector performances as well as impurity concentration diagnostics can be obtained with the knowledge of the detector leakage current. These measurements are very difficult because the currents are very small (∼pA). I measured the leakage current on single pixel CdTe Schottky detectors. At this stage, these are not matrices yet. The measurement serves as a preparation to study the current per pixel in the CdZnTe matrices, since these are expected to be comparable with those in Schottky detectors.

The first prototype of the X-ray mini-camera will have 64 pixels. To measure every pixel current individually I designed and constructed an automatic test bench. It comprises powerful and highly isolating printed circuits, equipped with relays. Several tests on prototypes prove the feasibility to measure pixel currents with an excellent accuracy. Current maps of different detectors as a function of voltage and temperature are obtained, as well as impurity activation energy maps (Dirks et al. 2006). The data serves to evaluate the homogeneity of the detectors and the overall performance of the system.

In Sect. 4.6, I present the spectroscopic measurements carried out with several prototypes to find optimal operating conditions.

In Chapt. 5 the most important work of this thesis is described, namely the development of, and results obtained with the simulation and modelling program I wrote. The program includes the complete chain from particle interaction inside the semiconductor to the spectra obtained. The first element is GEANT4, which allows me to model the physics of photon interactions inside the crystal.

The second element is a Matlab based program, baptised MGS-CdTe v1.0, which allows me to calculate the electrical properties, the shape of the electro-magnetic field, the transport of the charge carriers and the signal induction on the electrodes of different detectors. The program is an adaptation of the Multi Geometry Simulation (MGS) initially developed at IReS, Strasbourg (France) (see Medina et al. (2004)) to characterise the performances of large segmented germanium detectors using numerical methods with no restriction to geometry. Keeping only the core elements I completely adapted it for small, single or multi-pixel Cd(Zn)Te detectors.

The simulated detector signals are convolved with the electronics transfer function and simulated spectra are created which are compared with measurements. Also, the simulated resolution of a single pixel CdTe detector as a function of energy and equivalent noise charge (ENC) is shown. Simulated detection efficiencies of Cd(Zn)Te detectors are compared with measurements. The program serves as a powerful tool to study the architecture of the camera, its geometry and data acquisition strategy.

1.8 Finally...

After putting the work in its proper context, I conclude this chapter with an image of the Moon in soft X-rays shown in Fig. 1.4. This image was eventually taken using the Röntgen Observatory Satellite ROSAT. The sunlit crescent clearly shows that the Moon's X-ray luminosity arises from backscattering of solar X-rays. This is exactly what Giacconi was seeking during the 1962 observation that led to the discovery of SCO X-1 and the CXB.

The dark site also emits X-rays, although very few. These are very probably the result of energetic solar-wind electrons striking the Moon's surface.

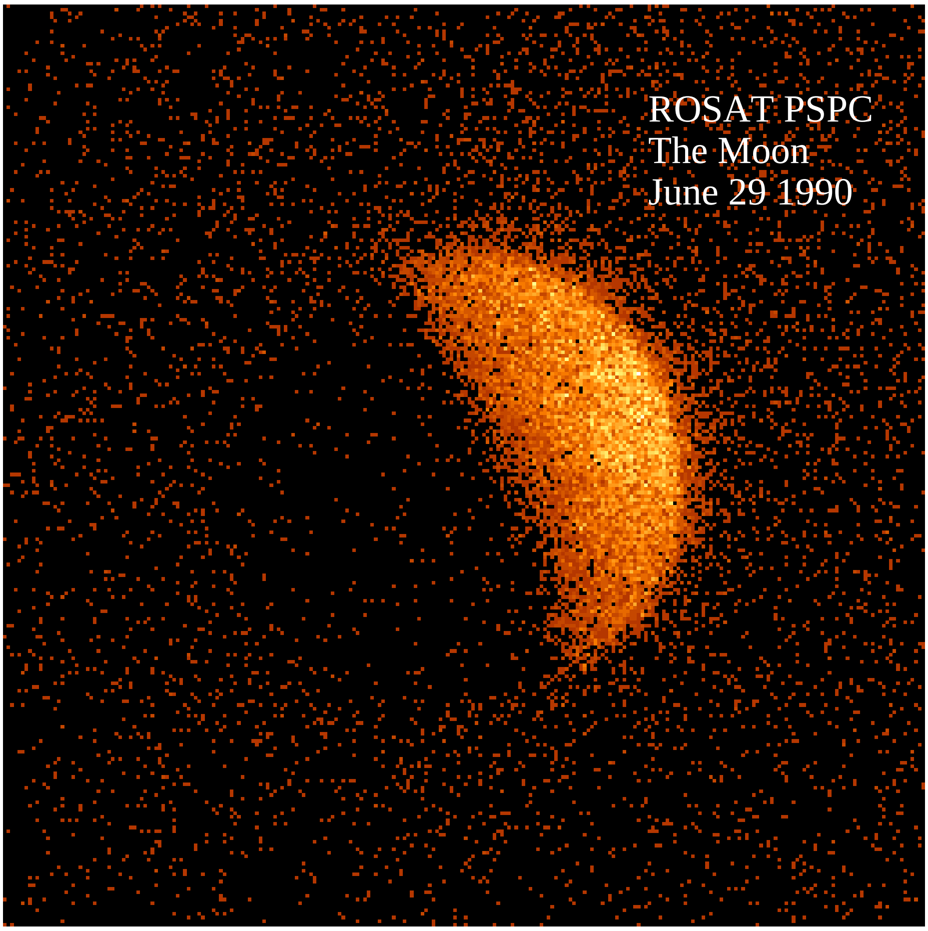

Figure 1.4: Rosat image of the Moon in X-rays. (Credit: Schmitt et al. (1991))

Chapter 2

The Simbol–X space mission

The X-ray mini-camera is a crucial element of the Simbol–X space telescope and is indispensable for success of the mission. In order to get a complete picture of the two satellites that will fly in formation, I will describe Simbol–X in more detail in this chapter. For a complete overview, see Dirks et al. (2006).

2.1 General description

Simbol–X (see Fig. 2.1) is a next generation hard X-ray mission proposed by an international consortium of European institutes.[1] This in response to a call-for-ideas issued by the CNES for a scientific payload to be put onboard a formation flight demonstrator. After a thorough assessment study, called phase 0, Simbol–X has been selected in autumn 2005 for a phase A study. This is now jointly performed by the CNES and ASI. The launch date resulting from the phase 0 study is set to mid 2013.

Operating in the $\sim 0.5 - 80$ keV energy domain, Simbol–X will fully cover the cosmic X-ray background peaking at 30 keV. This includes the transition from thermal to non-thermal emissions, as well as the iron (6 keV) and ^{44}Ti (68 keV) line regions. These are important characteristics for the study of the highly variable accreting sources which are the prime scientific targets of the mission. A thorough description of the scientific mission objectives is given by Ferrando et al. (2004).

Simbol–X is essentially a classical X-ray telescope having an exceptionally large focal length ($\sim$ 20 m in the present configuration) obtained by formation flying techniques. One satellite houses the Wolter I optics to focus, for the first time in space, X-rays above $\sim$ 10 keV onto the focal plane located in the second satellite. This leads to angular resolution and sensitivity which are two orders of magnitude better than those obtained so far with non-focusing techniques. A general paper of grazing incidence mirror technology is given by Pareschi et al. (2005).

The detector spacecraft, accommodating a low and high energy detector, maintains its position relative to the mirror by means of an active control loop on the telescope axis

---

[1] CNES, ASI, CEA/Saclay, APC, CESR, MPE, INAF, AIT, Osservatorio Astronomico di Brera

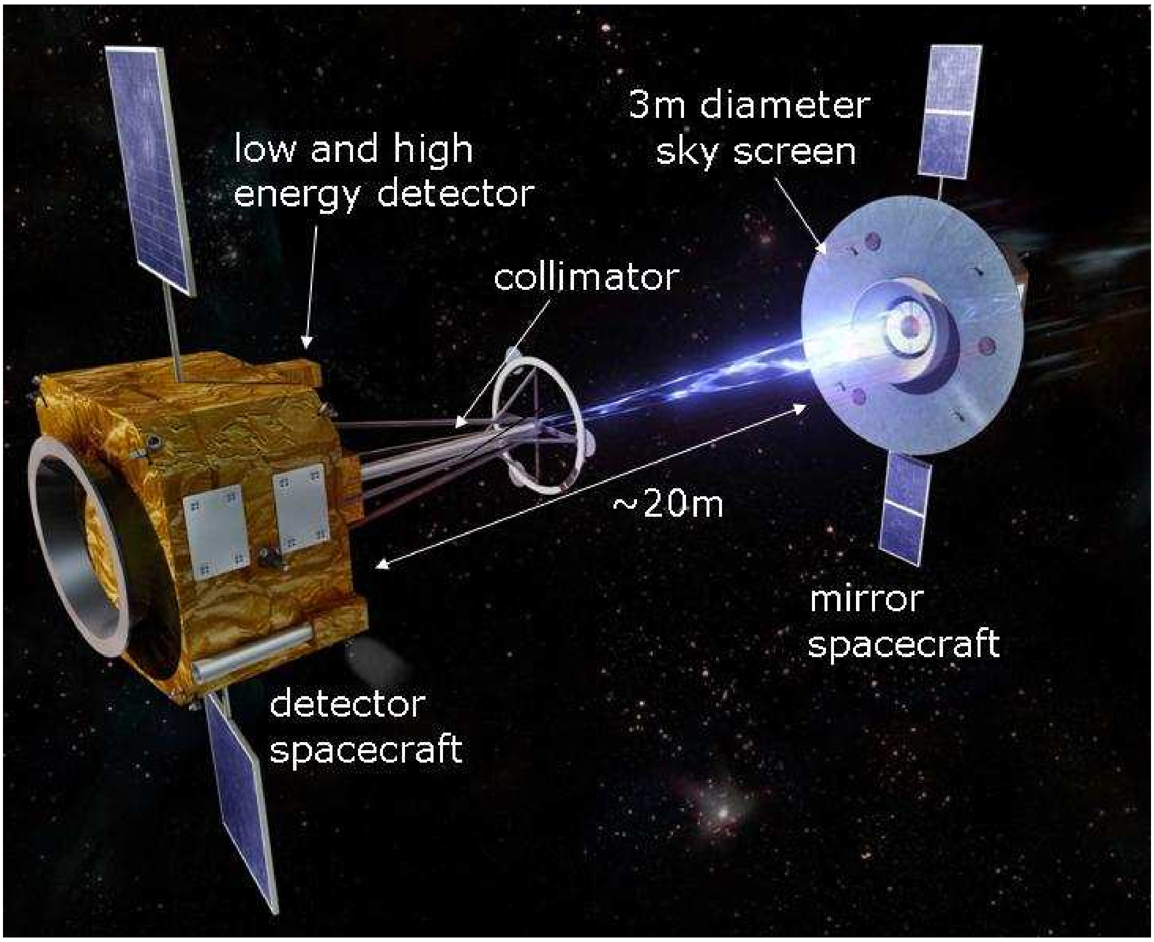

Figure 2.1: Artist's impression of the Simbol–X space mission consisting of two satellites flying in formation. One spacecraft houses the Wolter I mirror that focuses the X-rays onto a second satellite detector, at a distance of ∼20 metres. The latter accommodates a low and high energy detector. (Courtesy of CNES)

using formation flight technology. The design of the detector assembly will be tightly tailored to the final mission parameters that are worked out and optimised during the phase A study. The present (preliminary) design takes into account the most important scientific mission requirements. These are listed in Table 2.1 and will not be discussed any further. (See Ferrando et al. (2006) for more details.)
These parameters led to the design of a two-stage focal plane system detailed in the following sections.

2.2 Configuration

The two satellites forming Simbol–X will be launched together by a Soyuz rocket. Both vehicles will be injected into a high elliptical orbit to minimise the background level in the instruments and to facilitate formation flying. The presently planned orbit (from the

Parameter	Requirement
Energy range	$<$0.5–80 keV
Field of view (at 30 keV)	9–13 arcmin (diameter)
On-axis effective area	$>$100 cm^2 at 0.8 keV $>$1000 cm^2 at $<$2 keV $>$ 600 cm^2 at 8 keV $\sim$450 cm^2 at 20-40 keV $>$100 cm^2 at 70 keV
On-axis sensitivity	$<$1 μCrab (3 σ, 1 Ms) at 20-40 keV
Line sensitivity at 68 keV	$1 - 2 \times 10^{-7}$ ph/cm^2/s (1 Ms)
Angular resolution	$\sim$15 arcsec
Spectral resolution	E/ΔE = 40-50 at 6-10 keV E/ΔE = 50 at 68 keV (goal)
Absolute timing accuracy and time resolution	100 μs (50 μs goal)
Mission duration	3 yrs including commissioning and calibrations (2 yrs of scientific program)
Total number of pointings during the mission	$>$1000 (tbc)

Table 2.1: Simbol–X top-level scientific requirements.

phase 0 study) has a perigee of 44,000 km and an apogee of 253,000 km at launch. In observation mode, the relatively heavy mirror satellite (master) maintains its orbit while the detector satellite (slave) is stabilised along the mirror axis, keeping the distance between the mirror and the focal assembly at the focal length value.

Fig. 2.2 is an overview of the different elements of the mission. Fig. 2.2a shows the space vessels in nominal observation mode. The baffle around the mirror and the collimator mounted on the detector satellite are a part of the radiation shielding. Fig. 2.2b to f are a succession of figures that show in detail the detection area.

The focal plane detection area is mounted inside a protective aluminium enclosure. Located on the top are a turnable disk, which offers the possibility to operate in calibration, protection and measurement mode, and the collimator to stop photons outside the field of view. The thermal lines to the detectors are linked to an external radiator by means of a heat-pipe to allow passive temperature control. The operating temperature will be between -30 and -40^{o}C.

Surrounded by an active and passive shielding is the low energy silicon detector (see Sect. 2.3) on top of the Cd(Zn)Te[2] high energy detector (see Sect. 2.4). The former is built from a single silicon wafer which is divided into four regions which can be read out independently while the Cd(Zn)Te detector is constructed from 8 identical modules of 2×4 individual X-ray cameras (Fig. 2.2.e-f). An individual camera is a hybridisation of a 2 mm thick Cd(Zn)Te crystal covered with (probably) 256 pixels of 500×500 μm^2

---

[2] The final material choice will be made at the end of phase A.

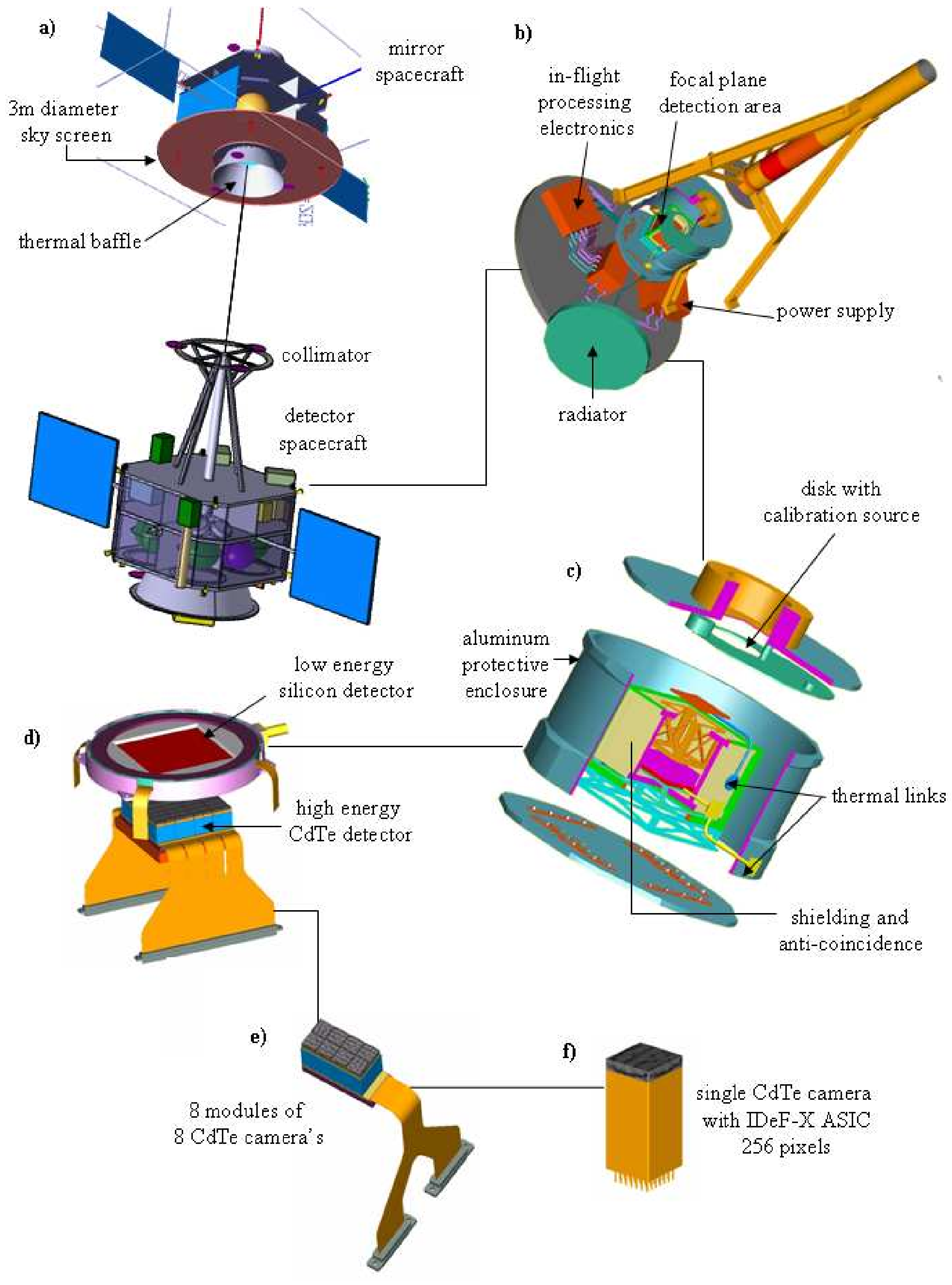

Figure 2.2: The Simbol–X mission configuration: a) In observation mode the detector satellite will follow the mirror satellite in a high elliptical orbit. The sky screen and collimator prevent diffuse background photons outside the field of view to enter the detector satellite. b) The focal plane, with the detection area, electronics, power supply, radiator etc. c) The detection area is protected by an aluminium enclosure which contains an active and passive shielding surrounding the low and high energy detectors. d) The thermal links and large radiator allow passive temperature control. e) The Cd(Zn)Te high energy detector is built from 8 identical modules of 2×4 individual X-ray cameras. f) A camera is a hybridisation of a 256 pixels Cd(Zn)Te crystal connected to the IDeF-X electronics.

surrounded by a guard ring and an IDeF-X ASIC. The modular design has the advantage that the different modules can be tested and replaced separately.

2.3 The low energy detector

The low energy detector (LED) of Simbol–X is a silicon drift detector (SDD) with DEPFET (DEPleted Field Effect Transistor) readout (see Fig. 2.3), also called "Macro Pixel Detector" or "Active Pixel Sensor" (APS). Prototypes of macro pixel detectors have already been developed, built and tested by the MPI semiconductor laboratory (HLL) (Strüder et al. 2006).

The LED consists of 128×128 pixels with a baseline size of $500 \times 500\ \mu m^2$ with ~450 μm depletion depth. This thick depleted bulk in combination with a thin entrance window results in a high quantum efficiency for the bare detector: >85% at 0.1 keV, 95% at 10 keV and still 45% at 20 keV. The thermal blanket in front of the mirrors and the optical filter of the detector will limit the lower energy of the LED to 0.5 keV, resulting in a nominal energy range for the LED of $\sim 0.5 - 20$ keV.

The detector is logically and functionally divided into four quadrants of 64×64 pixels each. All four quadrants are read out in parallel at a frame time of 256 μs. This short integration time allows the operation of the detector even at room temperatures with an expected energy resolution of about 500 eV (FWHM). In order to further reduce the noise contribution by leakage currents and to achieve an energy resolution of <145 eV (FWHM) at 5.9 keV, the wafer must be cooled down to only -30^{o}C (assuming a leakage current of 0.26 nA/cm^2 at room temperature). The energy resolution strongly depends on the pixel size (and the frame time). Increasing the pixel size requires a lower operation temperature.

2.3.1 Mechanical concept of the low energy detector

The left part of Fig. 2.3 (see also Fig. 2.2) shows the present mechanical concept of the low energy detector inside the detector spacecraft. The central square represents the area of the active pixel sensor (APS) with its 128×128 pixels, which are integrated onto one single silicon wafer. The wafer is mounted between two ceramic boards which themselves are clamped by the round support structure. The support structure has an interface to a heat pipe which is connected to the radiator. The passive cooling, together with active heaters, act to stabilise the operating temperature of the silicon wafer. Since the APS is backside illuminated, the lower ceramic board (not visible) is designed as a multi-layer board and contains the front-end electronics of the APS such as the CAMEX readout ASICs and the SWITCHER control ASICs. The latter are connected to the rows and channels of the APS via wire bonds. Indicated in the corner are flex-leads which connect the front-end electronics with the sequencer electronics, ADCs and digital electronics, and with the power supplies. The entrance window of the detector will be coated by a thin aluminium layer, which will suppress optical light. The APS support structure is

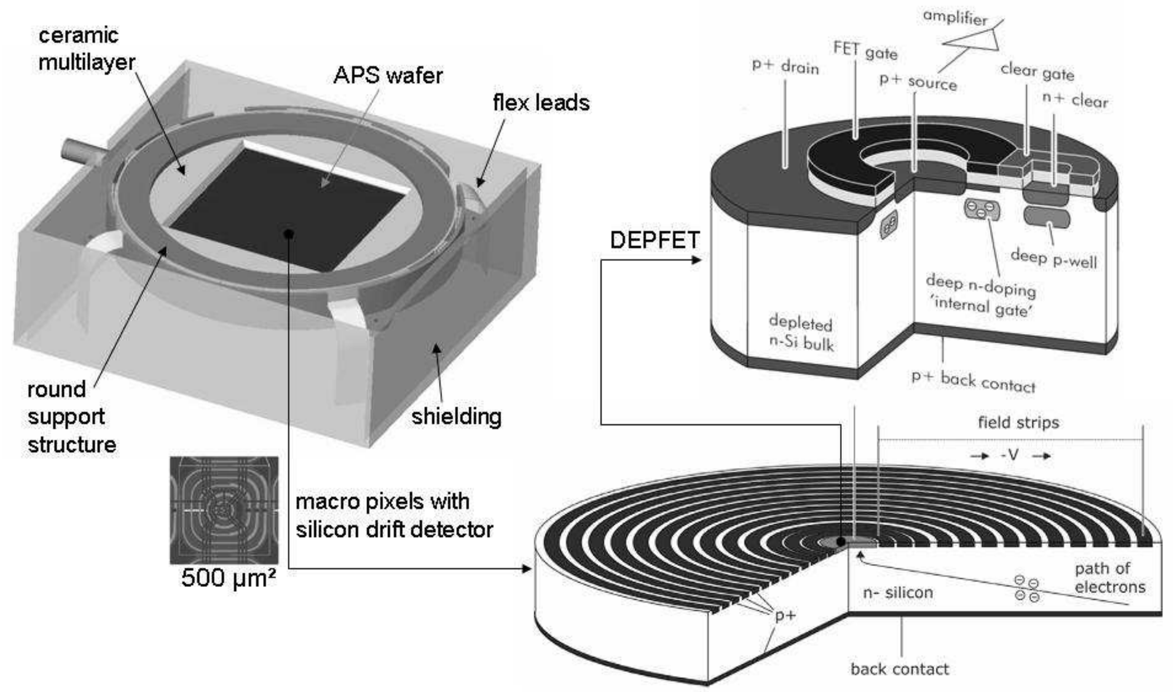

Figure 2.3: Present concept of the Simbol–X low energy detector formed by a single silicon wafer with 128 by 128 pixels, logically divided into four quadrants of 64×64 active pixel sensors consisting of a silicon drift detector with DEPFET read-out. The wafer is mounted between two ceramic boards which themselves are clamped by the round support structure. The baseline pixel size is envisaged to be a square of 500×500 μm^2.

surrounded by the anti-coincidence and shielding system (see Sect. 2.5).

2.3.2 Electrical concept

Fig. 2.4 shows the silicon wafer divided into four quadrants of 64×64 macro-pixels of 500 μm^2 (pointed out). On the right is the electrical block diagram of the assembly. Each quadrant of the LED has its own power supply unit and readout electronics. In full frame mode the 4096 pixels of a quadrant are read row by row, the active row being selected by the gate SWITCHER and reset by the clear SWITCHER. All other pixels are turned off and are in integration mode until they are activated for read out. The 64 pixels of an active row are processed in parallel by a preamplifier filter and multiplexer chip, called CAMEX64, which is an improved version of the CAMEX successfully operating in the EPIC pn-CCD camera on board XMM-Newton for more than 6 years. After signal sampling, the internal gates of the 64 active DEPFETs are cleared by a short ($\sim$200 ns) clear pulse from the clear switch chip. After the clear process, the pixel output returns to its reference level. This level is probed by baseline samplings. The difference between signal and baseline is then stored in an analogue shift register for serial readout while the 64 pixels from the next row are processed. The aim is to read out one row within 4 μs, resulting in a total read-out time for the full frame mode of only 256 μs. The output of the CAMEX is then converted by a fast 12 bit ADC and the pixel information from one frame is further processed by the digital event pre-processor.

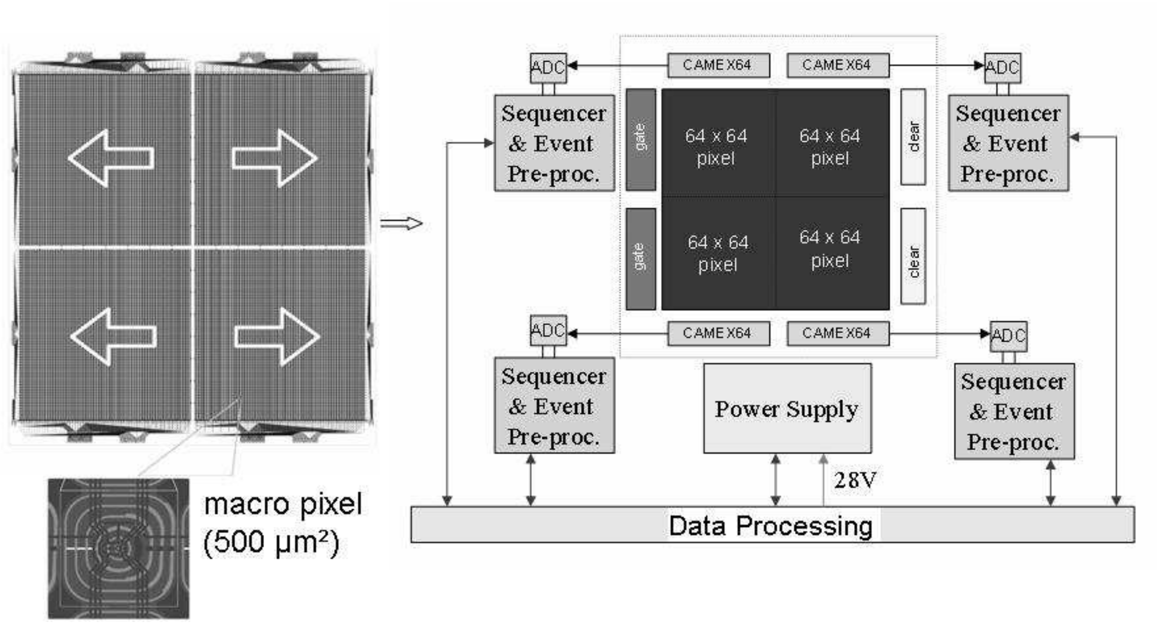

Figure 2.4: The silicon wafer is logically divided into four blocks of 64 × 64 macro pixels. On the right, we show the electrical block diagram of the low energy detector assembly.

2.4 The high energy spectro-imager

The high energy detector (HED) of Simbol–X is positioned below the LED and is constructed from 4-side juxtaposable pixelated CdTe or CdZnTe crystals ($10 \times 10 \times 2$ mm^3) covered with probably 256 pixels of about 500×500 μm^2 in size. Both material types are studied at the moment. Each crystal is connected to its own read-out electronics, the IDeF-X (Imaging Detector Front-end for X-rays) ASIC developed at the CEA/Saclay, forming a complete individual X-ray camera operating in the 5–80 keV range partly overlapping the low-energy range of the silicon detector. In the current design, eight individual X-ray camera's will be merged to form a 2-by-4 module having its own flex for in- and output signals. The detection plane is composed of eight such modules. A high energy resolution of $\sim$1.3 keV at 68 keV is required with a pixel size of $\sim 500 \times 500$ μm^2 (see table 2.1). Reliable, radiation tolerant, low power consuming and low-noise read-out electronics in combination with high quality Cd(Zn)Te crystals covered with small pixels are therefore mandatory.

The development of the HED is an important part of this thesis, and details about its components, configuration, functioning, etc, are described in the rest of this document.

2.5 Shielding

Since the mission consists of two satellites without any telescope tube connecting them, diffuse background photons, not coming from the mirror, can directly enter the detector spacecraft through its aperture, decreasing the sensitivity. The problem is resolved by putting a baffle around the mirror spacecraft that screens a large part of the sky without interfering with the mirror's field of view. In addition a collimator is placed on the opening of the detector spacecraft (see Fig. 2.5). Both elements are composed of a layer of tantalum (with a transmission coefficient of $\sim 10^{-4}$) followed by a series of layers of different materials, each able to stop the fluorescence photons of the previous layer although emitting a lower energy X-ray. In the present configuration this multi-layer is fabricated from Ta (tantalum), Sn (tin), Cu (copper), Al (aluminium) and C (carbon). The latter will emit photons of ∼0.4 keV which are below the low energy threshold level of Simbol–X.

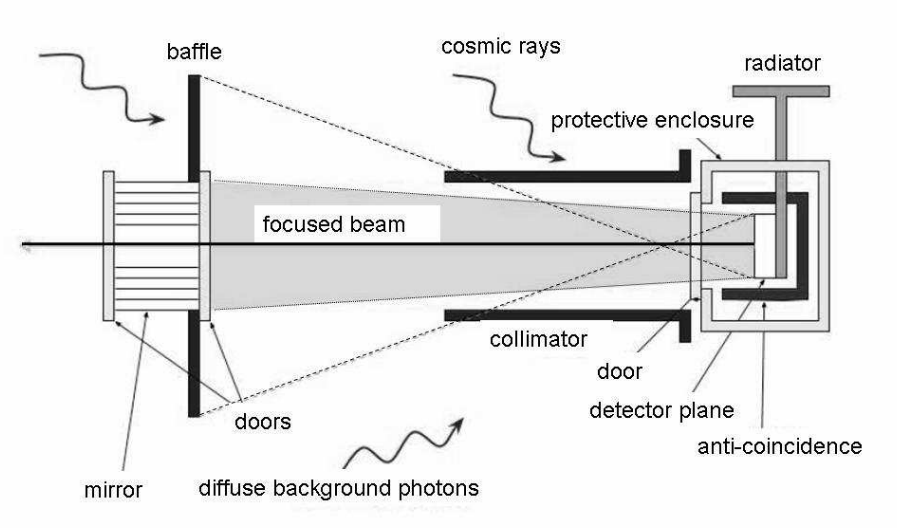

Figure 2.5: Schematic view of the shielding system of Simbol–X.

Beside the X-rays entering the detector housing directly, one also needs to account for cosmic rays (essentially protons) hitting the detector spacecraft isotropically, inducing a high detection count rate. To avoid degradation of performances, the detectors will be protected by an active anti-coincidence (AC) system in combination with a passive shielding. When a proton crosses the payload, it triggers simultaneously the detectors and the active shielding. The recorded event is tagged and can be easily removed from the science data. Prompt secondary particles generated by incoming cosmic-rays can also be removed by this means.

Presently two possible shielding configurations are studied: the first consists of plastic scintillators in combination with a passive shielding of the same material as the collimator, while the second uses NaI crystals only. The former has the advantage that it is mechanically and electronically easy to construct (small photodiodes are used for the scintillator read-out) and uses no high voltage (HV). Photons with energies <100 keV are stopped and protons can be detected. However, photons having an energy superior to 100 keV can easily traverse the shield. In the case of NaI, γ <100 keV are stopped. In addition, protons and γ >100 keV are detected. Analysis and simulation work is currently being performed to optimize the choice between these two options.

Fig. 2.6 shows a detailed view of the detection area with the different anti-coincidence layers and shielding as foreseen in the configuration using scintillators. The two detectors are protected by a first, exterior shielding surrounding the whole system except for the X-ray entrance aperture and the opening for the different flexes and thermal links. To avoid particles entering via this opening, a second, inner shielding is added. In this setup, a veto count rate of about 5000 cts/s is expected. A veto window of 1μs is foreseen to guarantee that the dead time generated by the veto signal stays well below 1 %. This requires a measurement of the signal time with an accuracy of about 10 % of the coincidence window size, i.e. 100 ns.

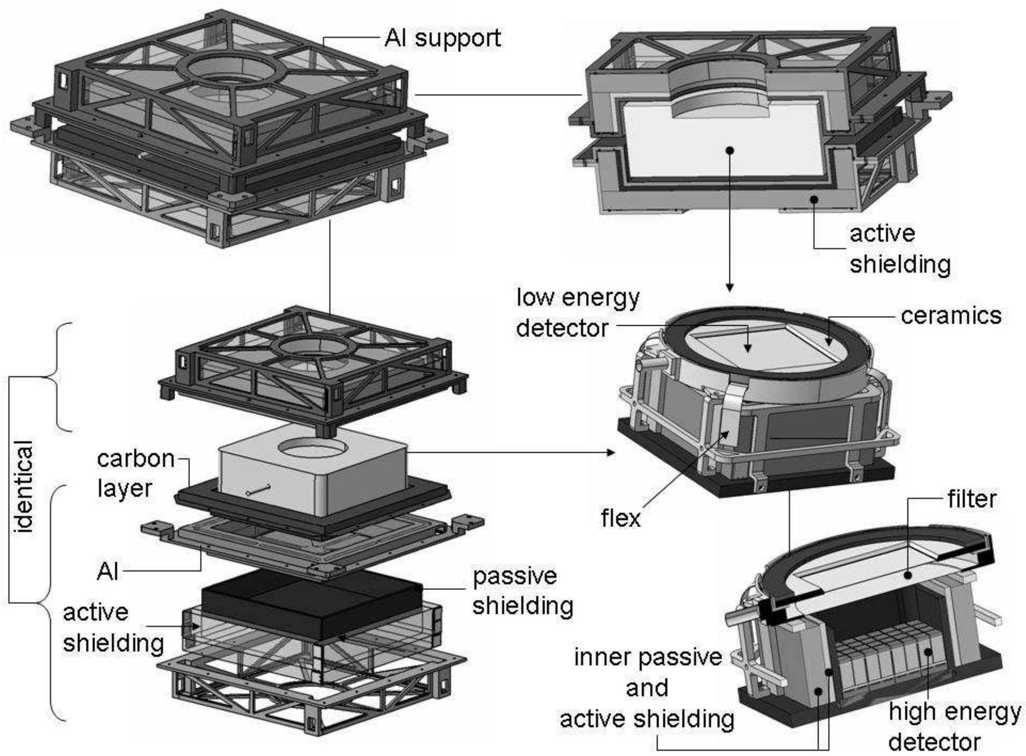

Figure 2.6: Exploded view of the Simbol–X focal plane, showing the arrangement of the different layers of the AC/shielding system.

Chapter 3

Semiconductor detector fundamentals

In Fig. 3.1 the logical layout of this chapter is depicted. After a brief general description of the properties of semiconductors (1), I focus on the Cd(Zn)Te semiconductor sensors. I explain their production process and show the main crystal properties. To obtain a signal from the crystals, they have to be equipped with metal contacts. In (2) I explain the consequences of such a metal-semiconductor contact. Then, the physics of photon interactions inside a semiconductor are described (3). Charge carrier transport and signal induction on the electrodes are investigated in the next sections (4,5). Finally, I give a detailed explanation of the polarisation effect in Schottky detectors.

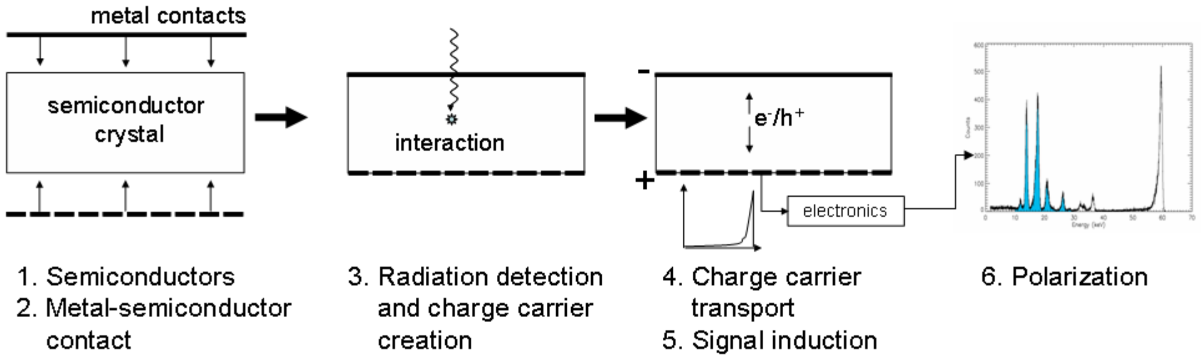

Figure 3.1: The different elements described in the theory chapter.

3.1 Semiconductors

3.1.1 Crystalline materials

The periodic structure of any crystalline material causes electrons to move in strictly defined energy bands separated by band gaps. The positions of these bands are a function of the inter-atomic spacing of the crystal and therefore of the temperature. With increasing temperature the spacing becomes larger. The potential seen by an electron becomes smaller and will diminish the size of the band gap.

Two bands that are of main interest are the valence band (E_V), consisting of the outer shell electrons that form the covalent bond in the crystal, and the conduction band (E_C), where electrons are able to migrate freely through the material. The latter contributes to the conductivity of the material. The size of the band gap is used to distinguish between three different types of materials: metals, insulators, and semiconductors, as shown in Fig. 3.2.

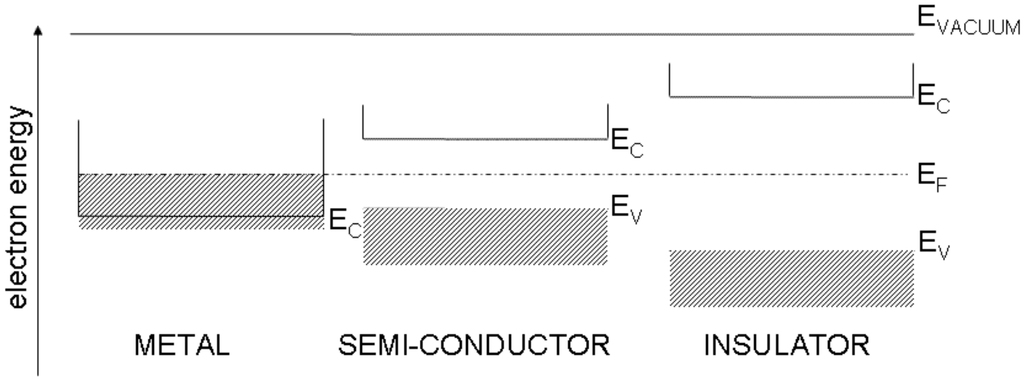

Figure 3.2: Energy level diagrams for a metal, semiconductor and insulator. The size of the band-gap ($E_{gap} = E_C - E_V$) defines the material type. In the case of a metal the Fermi level, E_F, lies inside the conduction band, even at $T = 0$ K.

Metals have a Fermi level (the energy at which the occupation probability is one half) that lies inside the conduction band. This means that there are always electrons available for conduction, even at 0 K.

Semiconductors have a Fermi level that lies in between the conduction and valence band. At very low temperatures at which there is nearly no thermal excitation, the valence band is completely filled and no charge carriers are present in the conduction band. In this situation the material does not show any conductivity. If the temperature rises, some electrons are able to gain enough energy to be excited into the conduction band, causing the material to become slightly conductive. The number of free charge carriers (electrons in the conduction band or holes in the valence band) determines the electrical behaviour of the semiconductor.

Insulators have a band gap that is relatively large ($E_{gap} > 5$ eV) compared to semiconductors. Even at high temperatures these materials show no or almost no conductivity.

Well-known insulators are glass and porcelain.

In order to serve as a radiation detector, a material must first of all be able to stop radiation, by means of electro-magnetic interactions, preferably by the photo-electric effect as I will explain later on. The deposited energy must lead to an amount of electric charge inside the detector volume, proportional to the energy of the photon. The charge must be collected in order to create a detectable electric signal.

These requirements are linked to multiple parameters such as the resistance of the detection material, the capacitance, the band-gap energy, the pair creation energy, the carrier mobilities and lifetimes, the carrier concentration and type (p or n) and the activation energy.

Metals and insulators are no good candidates. The former because it is a conductor. Particles may interact but are indistinguishable from free charge carriers already present. Insulators neither, because of their large band gap they will not create enough charge carriers to form a detectable signal. In addition, the mobility of these carriers will be extremely low.

Semiconductors do not or nearly not have these problems and have shown to be able to act as excellent radiation detectors. I will therefore go into more detail in explaining their functioning.

3.1.2 Free charge carriers in semiconductors

The electronic properties of a semiconductor are related to the occupation of its energy bands. The occupation probability of a certain electronic energy state is given by the Fermi-Dirac distribution, $f(E)$:

$$f(E) = \frac{1}{1 + exp(\frac{E - E_F}{k.T})} \tag{3.1}$$

With E, the energy level (eV) considered, E_F the Fermi level (eV), k the Boltzmann constant (eV/Kelvin) and T the temperature (K). The above formula is illustrated in Fig. 3.3. Electrons are fermions and cannot occupy the same state. At $T = 0$ K, they will occupy the states from $E = 0$ up to $E = E_{Fermi}$. The occupation probability, $f(E)$, is 1 for $E < E_{Fermi}$ while 0 for $E > E_{Fermi}$. As the temperature rises, certain electrons are able to gain enough energy to be promoted to an energy level above E_{Fermi}. However, since these lay in the forbidden gap no occupation takes place. Only at higher temperatures ($T >> 0$) electrons will be able to reach the conduction band and contribute to the electrical conduction.

Besides the electrons, holes (h^+) can also contribute to the electronic properties of a semiconductor, by being promoted to the valence band. If E_F is located in the middle of the forbidden gap at a distance of more than $3kT$ from either edge, Eq. 3.1 can be approximated by Boltzmann statistics, by ignoring the 1 in the denominator. This results in:

$$f_n(E) \simeq e^{-\frac{E-E_F}{k.T}} \tag{3.2}$$

$$f_p(E) \simeq e^{-\frac{E_F-E}{k.T}} \tag{3.3}$$

With $f_n(E)$ the electron and $f_p(E)$ the hole occupation probability.

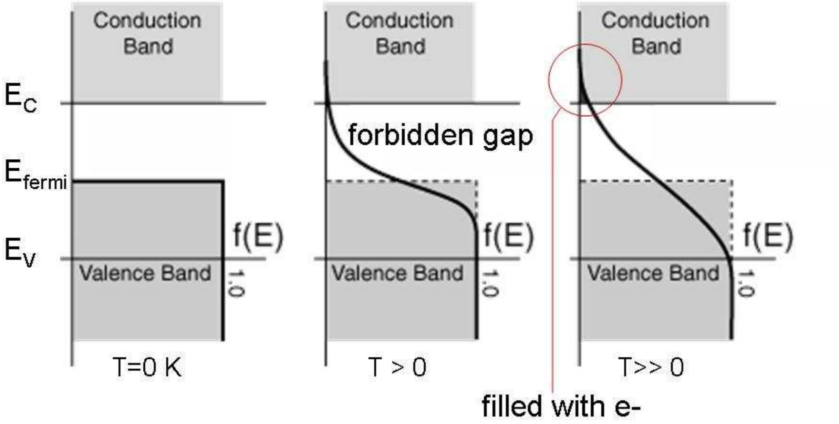

Figure 3.3: Occupation probability inside a semiconductor. At T=0 K, the electrons occupy the states up to E_{Fermi}. If the temperature rises, certain electrons may gain enough energy to be raised to higher energy states but they will not populate them because they lay in the forbidden gap. Only at higher temperatures electrons can reach the allowed conduction band.

The number of e$^-$ in the conduction and h$^+$ in the valence band can be calculated by multiplying the above probability functions with the total number of states available in the energy range considered. Doing this for electrons and holes separately the following densities for free electrons in the conduction band and free holes in the valence band are obtained (Lutz 1999):

$$\text{electrons:} \quad n = 2.(\frac{2\pi m_n kT}{h^2})^{\frac{3}{2}}.e^{-\frac{E_C-E_F}{k.T}} = N_C.e^{-\frac{E_C-E_F}{k.T}} \tag{3.4}$$

$$\text{holes:} \quad p = 2.(\frac{2\pi m_p kT}{h^2})^{\frac{3}{2}}.e^{-\frac{E_F-E_V}{k.T}} = N_V.e^{-\frac{E_F-E_V}{k.T}} \tag{3.5}$$

With

$$N_C = 2.(\frac{2\pi m_n kT}{h^2})^{\frac{3}{2}} \tag{3.6}$$

$$N_V = 2.(\frac{2\pi m_p kT}{h^2})^{\frac{3}{2}} \tag{3.7}$$

N_C and N_V are the effective densities of states in conduction and valence band, respectively. With m_n and m_p the electron and hole effective masses and h Planck's constant. The product np is known as the law of mass action and is independent of the Fermi level:

$$n.p = N_C.N_V e^{-\frac{E_C-E_V}{k.T}} \tag{3.8}$$

In a purely intrinsic semiconductor n and p are equal. By setting $np = n_i^2$, with n_i the intrinsic carrier concentration (see 3.1), we get:

$$n_i = \sqrt{N_C.N_V} e^{-\frac{E_C - E_V}{2k.T}} = \sqrt{N_C.N_V} e^{-\frac{E_G}{2k.T}} \tag{3.9}$$

$$E_i = \frac{E_C + E_V}{2} + \frac{kT}{2} ln(N_V/N_C) \tag{3.10}$$

With E_i the Fermi level of the intrinsic semiconductor. The above formulae implies that the Fermi level is dependent on the number of available states in valence and conduction band.

Eq. 3.4 and 3.5 are also valid for extrinsic semiconductors and can be used to determine the conductivity:

$$\sigma = |e|(n\mu_n + p\mu_p) \tag{3.11}$$

With e the unit charge, n and p the electron and hole densities (cm^{-3}) and μ_n and μ_p the electron and hole mobility (cm^2/V.s). If an electric field is applied, we get the following current density:

$$\vec{J} = \sigma\vec{E} = |e|(n\mu_n + p\mu_p)\vec{E} = |e|(n\vec{v_n} + p\vec{v_p}) \tag{3.12}$$

with

$$\vec{v_n} = \mu_n\vec{E} \tag{3.13}$$

$$\vec{v_p} = \mu_p\vec{E} \tag{3.14}$$

With $\vec{E}$ the applied electric field (V/cm) and $\vec{v_n}$ and $\vec{v_p}$ the charge carrier velocities (cm/s). As the above formulas indicate, the electric properties of semiconductors depend on the amount of free charge carriers n and p. Changing their concentration by doping is a tool to influence the semiconductor behaviour.

3.1.3 Doping and impurities

It is practically impossible to produce intrinsic semiconductors. Even the purest materials commercially available contain unintentional electrically active impurities, crystal defects or imperfections. The electrical properties of a semiconductor can also be influenced by artificially adding them. These can be donor or acceptor atoms which have relatively low activation energies. This means that only a small amount of energy is required to promote an electron (or hole) from its proper atom to the conduction (or valence band). In a band diagram this can be depicted as an extra energy level close to the conduction band in the case of a donor. An acceptor will cause a level close to the valence band. A donor present in a semiconductor lattice will add "free" electrons in the conduction band, resulting in an n-type material. An acceptor adds "free" holes to the valence band and makes the material p-type.

P- or n-type doping causes the Fermi level to shift away from the intrinsic level which normally lies in the middle of conduction and valence band. In a doped semiconductor the free charge carriers mainly come from the doping. We can therefore safely assume that $n = N_D$ and $p = N_A$. The change of Fermi level can be calculated by re-writing Eq. 3.4 and 3.5. For a n-type material:

$$E_F = E_C - kT.ln(\frac{N_C}{N_D}) = E_C - kT.ln(N_C) + kT.ln(N_D) \tag{3.15}$$

And for a p-type:

$$E_F = E_V + kT.ln(\frac{N_V}{N_A}) = E_V + kT.ln(N_V) - kT.ln(N_A) \tag{3.16}$$

This implies that when donors are added (n-type), the Fermi level shifts towards the conduction band while the addition of acceptors (p-type) results in a downward shift to the valence band.

Doping can also be used to compensate for the unwanted impurities: one defect cancels out the doping effect of another. The simplest version of compensation involves an electron from a shallow donor state filling a shallow acceptor state. This effect temporarily removes both the donor and the acceptor from acting on the device.

In the now following section I will introduce the Cd(Zn)Te semiconductors that are used in my research.

3.1.4 CdTe and CdZnTe semiconductors

Cadmium Telluride (CdTe) is a compound semiconductor material of type II-VI (with Cd in group II and Te in VI in Mendeleev's Periodic Table), having a mixed covalent-ionic bonding between Cd and Te. It has a zinc blend (cubic) crystal structure. In the bulk crystalline form it is a direct band-gap semiconductor with a gap of 1.51 eV[1] and an electron- hole pair creation energy of 4.42 eV. The transition occurs directly between valence and conduction band without change of momentum of the two states involved.

The CdTe crystals used in this research are produced by ACRORAD in Japan, which provided also the detectors for the ISGRI camera on the INTEGRAL satellite. The company employs the travelling heater method (THM) to produce single crystal ingots as shown in Fig. 3.4. By applying newly developed technologies within the THM, ACRORAD has achieved to grow the world's largest 3-inch CdTe crystals with high uniformity. The production is based on the following process: pure cadmium and telluride are mixed together to form a rough pre-synthesised ingot. This serves as starting material for the THM. The ingot is vertically injected into a heating zone where additional chlorine in the form of $CdCl_2$ is added to compensate for the Cd vacancies acting as acceptors sides and created during the process. These are however not completely compensated, keeping the material slightly p-type. After the heater the mix re-crystalises to form a highly resistive monolithic CdTe crystal with excellent purity.

---

[1] I assume that the temperature dependence of the band gap energy of CdTe or CdZnTe, expressed as $\frac{dE_{gap}}{dT}$, is comparable with that of Si, Ge or GaAs (see Lutz (1999), p.13). This means a variation in the order of 10^{-4} eV/K. In the temperature range from -50^{o}C to +30^{o}C, I may safely adapt the same band gap energy at all temperatures.

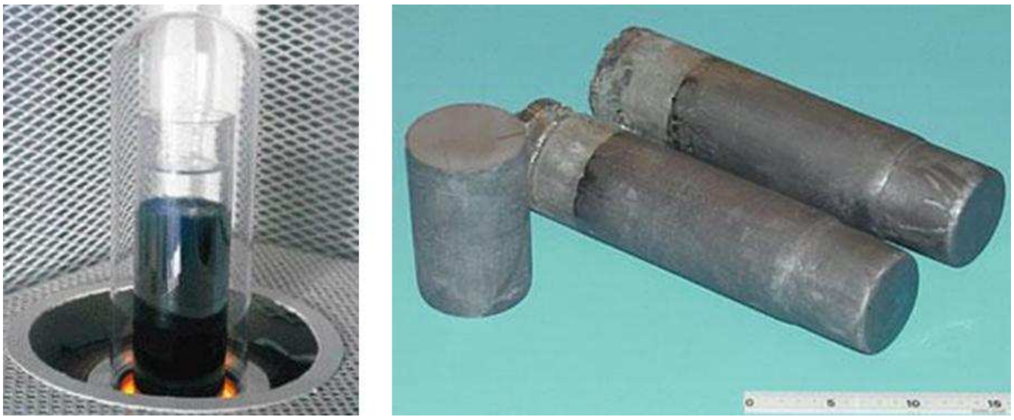

Figure 3.4: a) The traveling heater method (THM) is employed by ACRORAD to produce its CdTe crystals. b) 3-inch CdTe ingots.

The main characteristics of CdTe, CdZnTe and two other important semiconductor detectors, Si and Ge, are given in Table 3.1. Silicon and germanium are the most famous semiconductor materials for radiation detection. They are favourable in many aspects: good energy resolution because of the small band-gap (leading to many e^- /h^+ pairs per interacting photon), high charge carrier mobilities (nearly all carriers created are collected), and a high-purity crystal production. Though, the atomic numbers ($Z_{Si} = 14$ and $Z_{Ge} = 32$) are relatively low resulting in a moderate photo-electric absorption. Furthermore, detector operation requires cryogenic temperatures (in the case of Si).

CdTe and CdZnTe combine the relatively high atomic numbers of Cd ($Z_{Cd} = 48$) and Te ($Z_{Te} = 52$), to form a material with a high photo-electric absorption efficiency. Also, because of its relatively large band-gap, the material is highly resistive ($\sim 10^9$ Ω.cm) and makes room temperature operation possible.

Unfortunately, the compound is limited in its (spectroscopic) performances mainly due to the low mobility of holes. Progress is made to use Schottky CdTe diode detectors for spectrometry. The CdTe diodes allow applying a higher bias voltage than is possible with previous CdTe detectors because of the presence of a blocking contact (see next section). For a relatively thin detector of 0.5-1 mm thick, the high bias voltage results in a high electric field in the device. This leads to better charge collection efficiency in combination with a low-leakage current and therefore less noise and improved energy resolution.

In the 90's an alternative for CdTe was introduced, namely CdZnTe (CZT). The production process of CZT is based on the high pressure Bridgeman (HPB) technique. The crystals are grown from a melt of nearly equal quantities of cadmium and tellurium and a variable amount of zinc, with small cadmium excess, making it an n-type material. The crystal grows at high temperature, above 1100^{o}C , at a high growth rate of few millimetres per hour. The HPB technique yields high quality detectors and detector arrays, however, the crystal uniformity is limited, and the yield is low.

CZT is nearly identical to CdTe except that the presence of zinc results in a band gap from 1.44 eV for CdTe up to 2.2 eV for ZnTe. In this research $Cd_{0.9}Zn_{0.1}Te$ detectors are

Semiconductor	$Cd_{0.9}Zn_{0.1}Te$ [1]	CdTe (THM) [3]	Si [2]	Ge [2]
Atomic numbers	48,30,52	48,52	14	32
Density (300K) ρ (g/cm^3)	5.78	5.85	2.33	5.32
Band gap (300K) E_g (eV)	1.57	1.51	1.12	0.67
Relative permittivity	10.9	10.3	11.7	16
Pair creation energy (eV/pair) (300K)	5	4.42	3.62	2.96 (77K)
Resistivity $(\Omega.cm)$ (300K)	3×10^{10}	10^9	2.3×10^5	47
Electron mobility μ_e (cm^2/V.s)	1350 [3]	950	1350	3900
Hole mobility μ_h (cm^2/V.s)	120 [3]	73	480	1900
Electron lifetime τ_e (s) (293K)	3×10^{-6}	1.2×10^{-6}	10^{-3} [1]	10^{-3} [1]
Hole lifetime τ_h (s) (293K)	1×10^{-6}	4.6×10^{-6}	2×10^{-3} [1]	10^{-3} [1]
Fano factor	0.14 [3]	0.2 [3]	0.084-0.16 (77K)	0.057-0.129 (77K)
Charge carrier concentration [4] n$_i$ (cm^{-3}) (300K)		6.9×10^5	1.45×10^{10}	2.4×10^{13}

Table 3.1: Intrinsic properties of Si and Ge and the properties of compound semiconductors CdTe and CdZnTe. (Sources: [1] eV-Products, [2] Knoll (2000), [3] Limousin (2001), [4] Manach (2005), [5] Lutz (1999).)

used from eV-Products in the USA. They have a band gap of ∼ 1.6 eV. The electrical resistivity (3×10^{10} Ω.cm) is about 10 times higher than that of CdTe. This results in a low dark current and therefore good spectroscopic performances, even at room temperature. Fig. 3.5 shows several Cd(Zn)Te prototype detectors present at CEA/Saclay. This includes single pixel CdTe crystals with blocking contacts, 64 and 256 pixelated CdTe detectors with or without blocking contacts, all from ACRORAD, Japan. The American company eV-products provides us with different CdZnTe detectors, 64 and 256 pixels. The dimensions of both detectors are clarified in Fig. 3.6.

Fig. 3.5b is a special kind of detector. It is a CdTe 64 pixels detector with a Pt planar electrode on one side. To exploit the advantages of the blocking contact, which I will explain in detail in the next section, indium instead of platinum pixels are used. This is realised by dicing the indium electrode. As far as we know the technique has not been

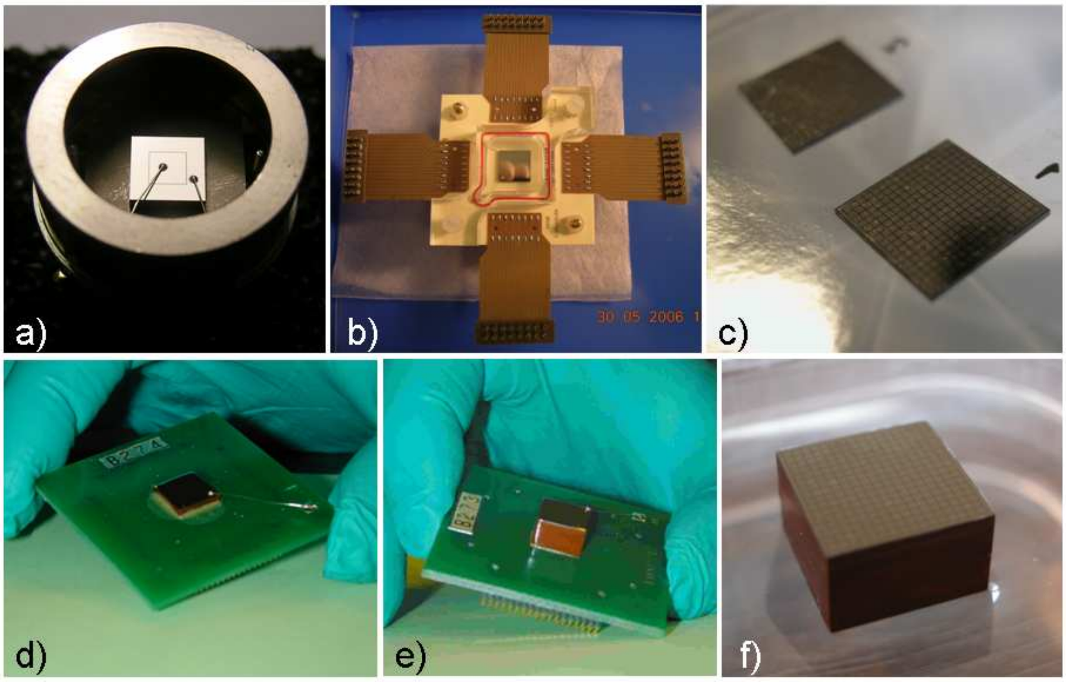

a), b) and c) from ACRORAD, Japan d), e) and f) from eV-Products, USA

Figure 3.5: The different Cd(Zn)Te detectors present at CEA/Saclay. a) Single pixel CdTe detector with indium blocking contact and guard ring. b) 64 pixels CdTe detector with blocking contact on pixel side. c) 256 pixels CdTe detector with blocking on the planar side. d) and e) 64 pixels CdZnTe detectors of 2 and 6 mm thick. f) 6 mm thick 256 pixels CdZnTe detector.

used before and promising results are obtained as I will show.
In this thesis I concentrate on prototype single and 64 pixels detectors. The study of 256 pixels is planned for the next phase.

3.1.5 Radiation hardness

The application of Cd(Zn)Te in the Simbol–X space mission means that the detectors have to operate in a hostile space environment. To guarantee a stable operation during the complete flight duration, the detectors and electronics (see Sect. 4.3) must be radiation hard.
CdTe is radiation hard to gamma-rays, but its hardness against protons is not well defined. Cosmic ray protons, with a typical energy of ∼1 GeV, will not be stopped by the shielding, and deposit about 2 MeV in the crystals. This can lead to slight degradation of the spectral resolution but also to complete damage of detector and electronics.
In preparation for the INTEGRAL space mission, irradiation tests with protons have been performed to test the CdTe crystals. Slight degradation has been observed in gain and resolution. The results are described in Lebrun et al. (1996). The proton fluxes that were applied (10^3 cm$^{-2}\cdot$s^{-1}), were much higher than those expected in orbit (1-2 cm$^{-2}\cdot$s^{-1}).

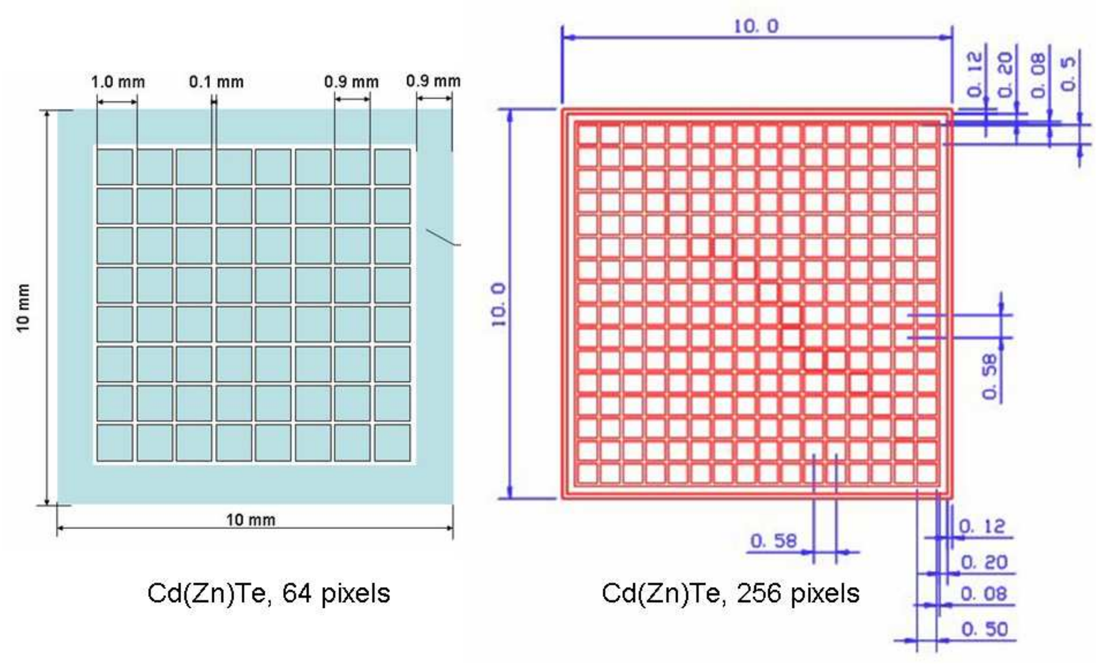

Figure 3.6: Dimensions of the 64 and 256 pixels Cd(Zn)Te detector.

Since the detector degradation strongly depended on the dose rate, Lebrun et al. concluded that CdTe should not significantly degrade by proton irradiation. This conclusion was later confirmed by in-flight data (Lebrun 2005).
Irradiation tests, using protons and neutrons, have also been performed on CdZnTe and CdTe detectors by Fraboni (2005) and (2006). The exposure of their detectors to increasing doses/fluences of ionizing radiation showed a seriously affected spectroscopic performance due to high leakage currents and limited charge collection, caused by damage.
Knowledge of the comportment of the Cd(Zn)Te detectors for Simbol–X, under radiation, is important. Presently, the prototype detectors used in our research have not been tested yet. Plans are made to use low energy protons (∼20 MeV) at low flux to irradiate them when connected to the electronics. This in order to study the behaviour of the electronics when it is saturated. Also, irradiation tests using neutrons are foreseen.

3.2 Metal-semiconductor contact

The type and quality of the contacts on semiconductors are of great importance. They are partly responsible for the functioning of the detector. The detectors used in this research are covered with either platinum (Pt) or indium (In) contacts. Different methods are available to deposit these metals on the semiconductor surface. The CdTe detectors from ACRORAD have either a Pt//CdTe//Pt or In//CdTe//Pt configuration while the CdZnTe from eV-Products have a Pt//CdZnTe//Pt configuration. ACRORAD uses lithographic techniques and chemical electroless deposition to create the Pt planar or pixelated electrodes. The indium contacts are deposited by a sputtering process. The technique used by eV-Products is not known by us.

For a better understanding of what happens at the interface between metal and semiconductor, a schematic representation of the different energy bands at the contact is shown in Fig. 3.7 and 3.8. In the first figure the band diagrams are shown of a metal and a p- and n-type semiconductor. The energy difference between the vacuum and Fermi-level is defined as the work function: Φ_M for a metal and Φ_S for a semiconductor. Since the Fermi level in the latter is dependent of the doping concentration and therefore not a constant value, it is more convenient to use the electron affinity χ. It is defined as the difference in energy between vacuum (E_{vac}) and conduction band (E_C).
As soon as the metal and semiconductor are brought together the different energy levels rearrange. Fig. 3.8a shows the situation directly after the connection and 3.8b a few moments later. In thermodynamic equilibrium the Fermi levels of both materials have to coincide. This is achieved by the transport of charge carriers from one material to the other. In an n-type semiconductor the majority charge carriers are electrons. They will diffuse into the metal leaving behind a positive space charge near junction and creating a negative surface charge on the metal. In p-type materials, such as our CdTe, holes diffuse into the metal, leave behind a negative space charge and create a positive surface charge on the metal electrode. The space charge region is called the depletion zone. It does not contain any charge carriers anymore, making it highly resistive. Another consequence of the charge carrier diffusion is the appearance of an intrinsic voltage working against the diffusion and compensating it. The result is an equilibrium between diffusion to the metal and the drift from the metal to the semiconductor. In a band diagram this can be represented by a bending of valence and conduction band. I show this effect for a p-type material.
The potential barrier which appears between metal and semiconductor has a height Φ_B expressed as:

$$\Phi_B = \frac{E_g}{q} + \chi - \Phi_M \tag{3.17}$$

With E_g the band gap energy. The barrier is also know as a Schottky barrier. Charge carriers that would like to enter the semiconductor from the contact side see this barrier and first need to gain enough energy to pass it. This is possible by diffusion, thermal emission or quantum mechanical tunnelling through the barrier. Charge carriers which exit the semiconductor toward the metal see another potential wall, namely the built-in voltage Φ_{bi} with a height of:

$$\Phi_{bi} = \chi + \frac{E_c - E_{F,p}}{q} - \Phi_M \tag{3.18}$$

By a applying an external voltage, the equilibrium is disturbed. A negative voltage increases the Fermi level in the metal, as shown in Fig. 3.8c. The Schottky barrier, Φ_B, remains unchanged while the built-in voltage Φ_{bi} becomes smaller. More holes diffuse to the metal and the depletion region gets smaller. The junction is said to be forward biased.

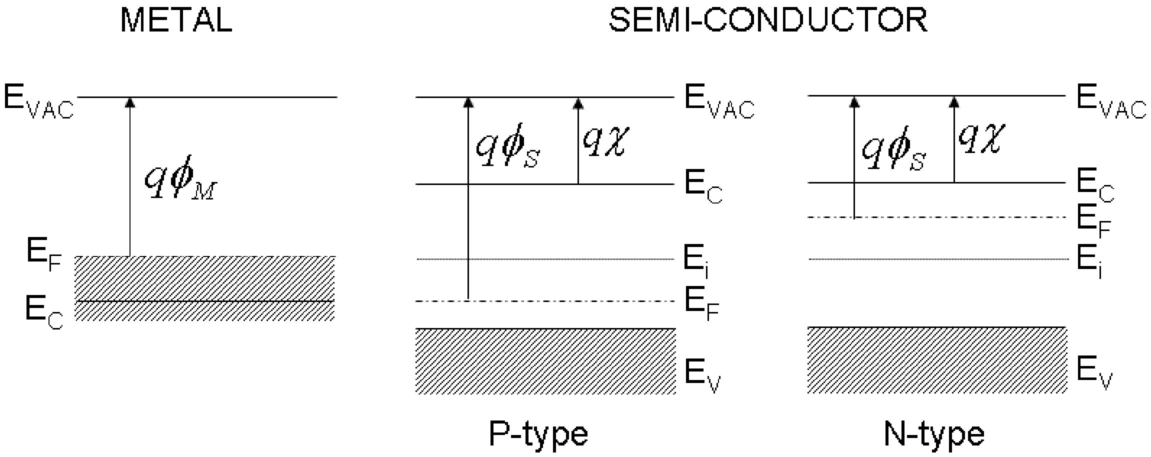

Figure 3.7: Band diagram of a metal and a p- and n-type semiconductor.

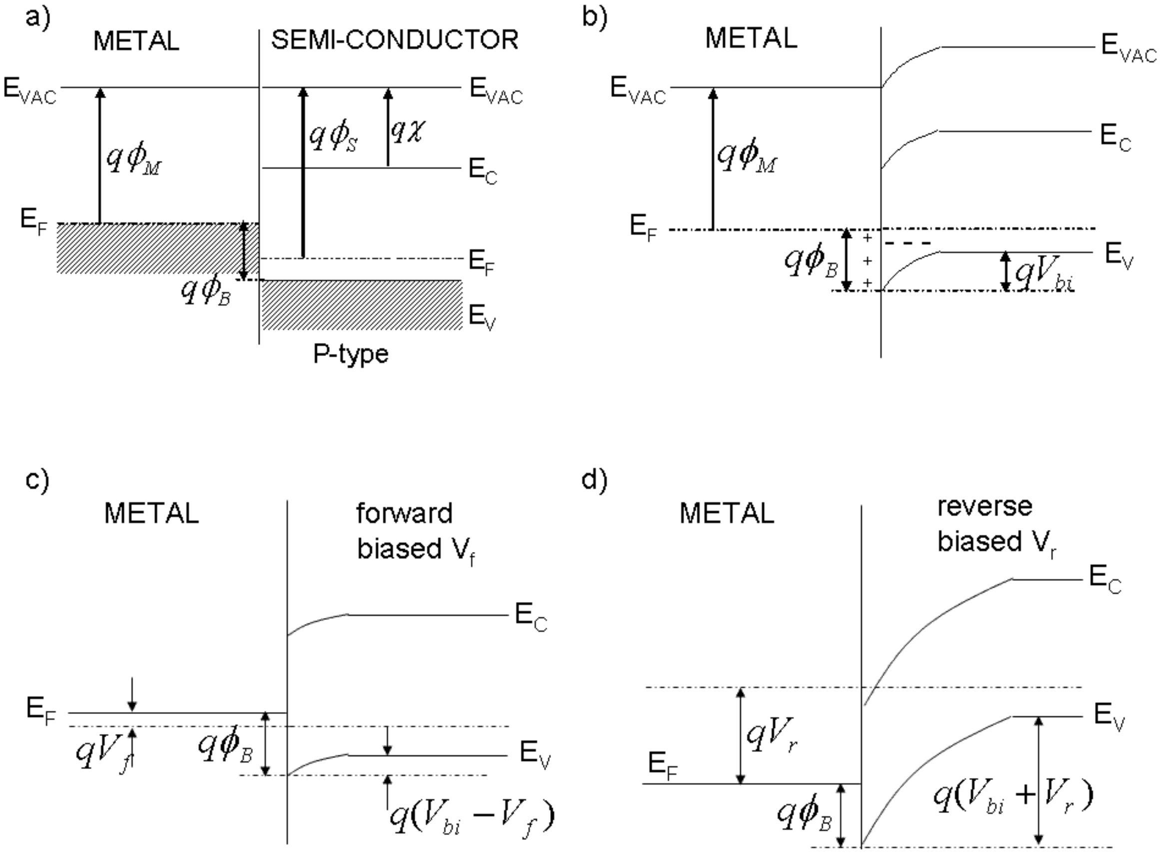

Figure 3.8: Band diagrams for a p-type semiconductor in contact with a metal. a) The metal and semiconductor are brought together. b) Thermal equilibrium. c) Forward biased. d) Reverse biased.

A positive voltage lowers the Fermi level of the metal and increases the built-in voltage. The size of the depletion layer increases and makes the junction more electrically isolating. The junction is said to be reverse biased.

A detector with a Schottky contact has several advantages. Operating the detector in reverse bias mode and applying a sufficiently high external voltage leads to a completely depleted detector region with high effective resistivity. Even at high voltages the leakage current stays low. Charge carriers created by radiation are quickly collected with only little charge loss, even for holes.

Low current means less noise, and a strong electric field means quick charge collection and little ballistic deficit or charge loss. Therefore very good energy resolution can be obtained.

Unfortunately there is one major drawback to the use of Schottky contacts: the polarisation effect. Since the description of this effect demands knowledge of several other important parameters, that I have not introduced yet, I will explain it in detail in Sect. 3.6.

Beside Schottky contacts, showing characteristic diode V-I behaviour, ohmic contacts between metal and semiconductor exist too. The CdZnTe as well as some CdTe detectors I used are covered with platinum electrodes leading to a quasi-ohmic contact. The conduction through the junction is the same for both polarities and obeys Ohm's Law. An ohmic contact can be obtained in two different ways:

1) by lowering the barrier height between metal and semiconductor by taking a metal with the same work function as the semiconductor or,

2) by making the barrier size very small so that quantum mechanical tunnelling becomes possible.

The advantage of an ohmic contact is that charge carriers can freely enter or exit the semiconductor. After an interaction inside a biased semiconductor, the created electrons and holes tend to drift to the electrodes. This so-called photo-current is accompanied by an opposite current passing through the electrodes. Since holes are slower, the electrons, which are generated to compensate for this hole current, will arrive faster at the hole position than holes at the electrode. The induced signal is therefore quicker and less sensitive to hole charge loss.

Evidently, the disadvantage of an ohmic contact is the absence of a blocking contact. In order to sufficiently accelerate the charge carriers a high bias voltage is necessary (especially in thick detectors). Due to the ohmic relation between bias voltage and leakage current, the latter can become very high, resulting in bad spectroscopic performances. In CdZnTe this is compensated by a high intrinsic resistance due to the large band-gap.

In the following section I will explain the different processes involved in the creation of a detectable signal on the pixels after a photon interaction inside a semiconductor.

3.3 Radiation detection by charge carrier creation

Semiconductors are well-suited to detect radiation: they have a small band-gap, a high density, good charge carrier mobility, a vast rigidity and its electrical properties can be manipulated by means of doping. In this section I will briefly explain the different aspects that are involved in the detection of interacting photons.

3.3.1 Interactions

An interacting photon in a semiconductor transforms its energy directly into a measurable electric signal instead of passing by the creation of light which is the case in scintillator materials like NaI, CsI and BGO.

The photon can interact by means of the following main electro-magnetic processes: the photo-electric effect, incoherent Compton scattering, coherent Rayleigh scattering or pair creation (in the electric field of the nucleus or of an orbiting electron). The probability of each of these interactions, represented by their individual cross-sections, is depicted in Fig. 3.9 for CdTe and Si. For Si, the photo-electric absorption is favorable up to ∼60 keV and up to ∼175 keV for CdTe. At higher energies the Compton effect becomes more probable.

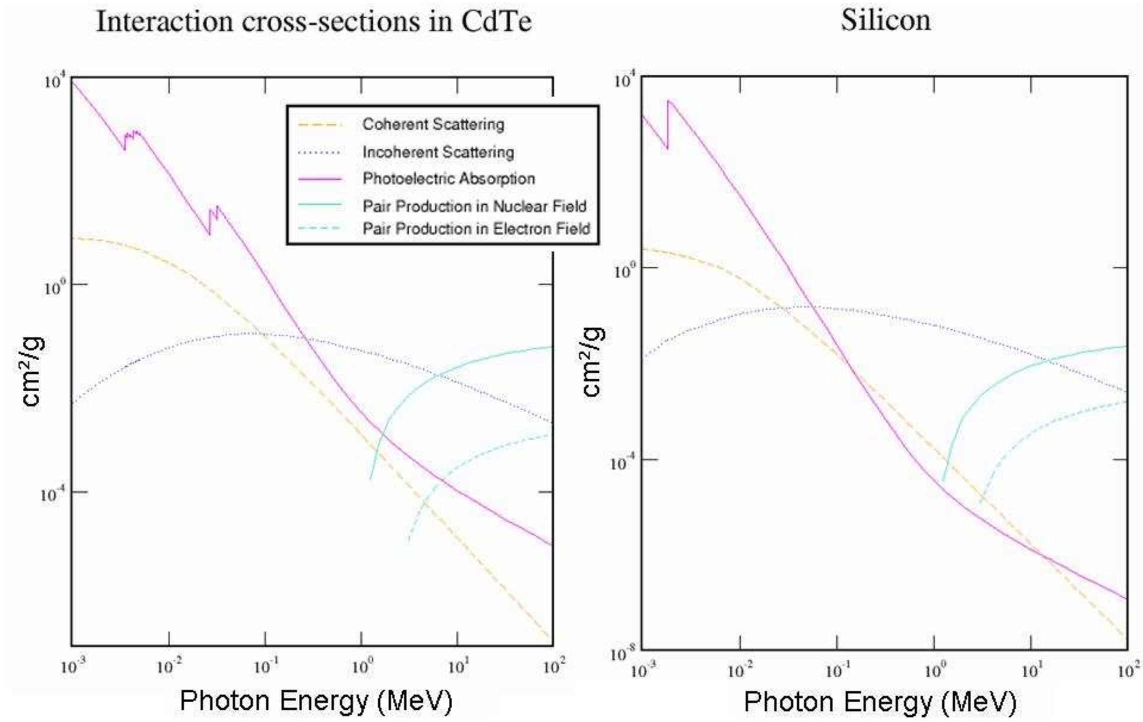

Figure 3.9: Cross-sections of the different interactions in CdTe and Si. This includes photo-electric absorption, (coherent) Rayleigh and (incoherent) Compton scattering and pair production. (Source: NIST-XCOM.)

An effective radiation detector should have a good photo-electric absorption efficiency. In this case all of the energy of the interacting photon will be transferred to a photo-electron which creates the electron-hole pairs that induce the signal on the electrodes. The kinetic energy, E_e, of a photo-electron is equal to incident photon energy, $h\nu$, minus the binding energy, E_b, of the orbit from which the electron originated $E_e = h\nu - E_b$. Since there is an electron missing in the inner bands of the atom, electrons from the outer bands or a free electron in the material can fill the vacancy by emitting a characteristic X-ray or by the creation of an Auger electron. If escaping the detector material, the missing X-rays cause characteristic lines in the spectrum, called escape lines. Each element has its own unique set of X-rays that it emits by fluorescence. Characteristic X-rays are labeled K, L, M, N and denote the shells from which they originate, while α, β, γ, mark the shells from which the electron originated that filled the vacancy. For example, if an X-ray interacts in a CdTe detector by means of the photo-electric effect, it may eject the electron in the innermost shell, indicated as K. An electron from the above lying shell L_3 can fill the vacancy by emitting an X-ray with an energy equal to the difference of binding energies between K and L shell. This X-ray is denoted as a $K_{\alpha1}$. In the same shell there are other orbits of higher and lower binding energy so a further designation is made with $\alpha1$, $\alpha2$, $\beta1$ and $\beta2$. If the electron falls back from L_2, the transition energy is denoted as $K_{\alpha2}$, while a transition from the M to K shell is written as K_β etc.

Table 3.2 gives the most significant transition energies for Cd, Te and Zn.

	Cd	Te	Zn
Z	48	52	30
$K_{\alpha1}$ (K-L_3)	23.17374	27.47210	8.63910
$K_{\alpha2}$ (K-L_2)	22.98449	27.20174	8.61623

Table 3.2: Transition energies in keV of $K_{\alpha1}$ and $K_{\alpha2}$ for Cd, Te and Zn. The $K_{\alpha1}$ transition is the most probable. Source: NIST, USA.

3.3.2 Electron-hole pairs

The ejected photo-electron will lose all of its energy by creating a number of electron-hole pairs that is proportional to the photon energy. The average energy necessary to create a pair inside a semiconductor is about three times the band gap energy. This difference can be explained by the fact that both energy and momentum must be conserved. The energy required to promote an electron from the valence to conduction band (and a hole from the conduction to valence band) requires extra momentum which goes into the creation of lattice vibrations, called phonons. In CdTe the energy gap, E_{gap}, is equal to 1.51 eV while the pair creation energy ω is 4.42 eV/pair (for CdZnTe $E_{gap} = 1.57$ eV and $\omega = 5$ eV/pair).

The number of electron/hole pairs, N_0, created in CdTe by a photon of energy E_γ is then:

$$N_0 = E_\gamma/\omega \tag{3.19}$$

A photon of 59.54 keV coming from ^{241}Am radio-active decay will therefore create about $59.54/4.42 \times 1000 \approx 13470$ e^-/h^+ pairs.

3.3.3 Fano factor

The number of electron/hole pairs will not always be equal to Eq. 3.19. It will fluctuate around N_0 because of the discrete character of the charge carriers. This process can by approximated by Poisson statistics. Poisson can be applied if the chance of success of an event is small but constant and if the individual events are independent. In our case the chance to have exactly the same number of charge carriers per photon is very small compared to the number of interacting photons. The standard deviation of the number of e^- /h^+ pairs can therefore be written as:

$$\sigma = \sqrt{\bar{x}} = \sqrt{N_0} \tag{3.20}$$

A histogram of N will show a Gaussian shape with standard deviation σ and a Full Width at Half Maximum (FWHM) defined as:

$$\mathrm{FWHM} = 2.35\sigma \tag{3.21}$$

The spectral resolution of a detector can be expressed as follows:

$$R = \frac{2.35\sqrt{N_0}}{N_0} = \frac{2.35}{\sqrt{N_0}} \tag{3.22}$$

It turned out that in semiconductor detectors the individual charge carrier creation is not independent. This was first described by Fano (Fano 1947) for gas detectors. He shows that the possibility to create an electron-hole pair is dependent on the amount of energy already lost. Fano introduced an additional factor, F, which defines the relation between the observed and Poisson predicted variance. The adjusted resolution which includes the Fano factor is then:

$$R = 2.35\sqrt{\frac{F}{N_0}} \tag{3.23}$$

If the above expression is translated to energy units the statistically limited energy resolution becomes:

$$\mathrm{FWHM}_{stat} = 2.35 \times \omega \times \sqrt{F \times E_{gamma}/\omega} \tag{3.24}$$

3.4 Carrier transport

3.4.1 Mobility

By applying an electric field charge carriers can be transported to their proper electrode in order to induce a signal. The electron-hole pairs created as described in the previous subsection are not static and will either drift (after application of an electric field) or diffuse (concentration gradient) inside the detector material. If no field present, the net displacement of charge carriers will be zero. However, if an electric field is applied, the electrons and holes will be accelerated in between random collisions in the direction of anode and cathode respectively. The average drift velocities are given by:

$$\begin{aligned} \vec{v_n} &= -\frac{q \cdot \tau_c}{m_n} \cdot \vec{E} = -\mu_n \vec{E} \\ \vec{v_p} &= -\frac{q \cdot \tau_c}{m_p} \cdot \vec{E} = -\mu_p \vec{E} \end{aligned} \tag{3.25}$$

With q the unit charge, τ_c the mean free time in between two scattering events on the crystal lattice imperfection, m_n and m_p the effective electron and hole masses, μ_n and μ_n the electron and hole mobility and $\vec{E}$ the applied electric field.

Suppose a photon interacts near the (negative) cathode of a 2 mm thick CdZnTe detector, biased at 100 V. The holes arrive almost instantly at the cathode while the electrons have to traverse the full detector thickness. With an electron mobility of $\sim$ 1350 cm^2·V^{-1}·s^{-1}, the mean velocity is $-\mu_n \cdot \vec{E} = 1350 \cdot 100/0.2 = 6.75 \times 10^5$ cm·s^{-1}. The time to arrive at the anode is then $0.2/6.75 \times 10^5 = 3.0 \times 10^{-7}$ s. Evidently, this is equal to duration of the induced signal. An interaction near the anode will have a (hole) signal duration of 3.3×10^{-6} s assuming a hole mobility of 120 cm^2·V^{-1}·s^{-1}.

3.4.2 Charge cloud

Directly after a photon interaction in a semiconductor, the ensemble of created electron/hole pairs is generally considered as a point charge (see for example Hecht's hypotheses in Sect. 3.5.2). There are however two mechanisms which make that this assumption is not true.

First of all, due to fluorescence and Compton scattering, interactions can take place at different positions inside the material. (In Chapt. 5 I will show the importance of these events on the pixel read-out.) Although these interactions are treated individually in the simulation, I cannot consider them to be point sources. The creation of e$^-$ /h$^+$ pairs at each of these specific positions is due to ionisation of the primary photo-electron (and energetic higher order electrons) along its trajectory. The different tracks that are created, are situated at random positions and have a mean distance from the origin. This makes that the charge is concentrated in a certain minimum volume.

A detailed description of the size of the volume, or charge cloud, is given in Sect. 5.1.4 where I use the GEANT4 toolbox to simulate the different interactions.

The second mechanism which makes that charge carriers may spread out inside the detector, is diffusion. Although the net displacement of the charge cloud is zero if no electric field is present, it does expand (I assume an equal expansion in all directions). In the detector modelling and simulation I do not take into account this effect because it is negligible for the pixel sizes used (0.5^2 and 1.0^2 mm^2).

To justify this, I will give an example of the width of an expanding charge cloud inside a CdZnTe detector of 2 mm thick at T=273 K and 100 V bias. The expansion time is taken equal to the signal rise-time which is a function of the interaction depth. An interaction near the cathode will create a nearly pure electron induced signal while an interaction near the anode leads to a slow hole signal. The pure electron signal has a time duration equal to:

$$t_h = \frac{0.2}{v_h} = \frac{0.2}{\mu_h.\vec{E}} = \frac{0.2}{1350 \times \frac{100}{0.2}} \approx 0.3\ \mu\text{s} \tag{3.26}$$

If the charge cloud spherically expands, the continuity equation reads:

$$\frac{\partial n(x,t)}{\partial t} = D\frac{\partial^2 n(x,t)}{\partial x^2} \tag{3.27}$$

With $n(x,t)$ the number of charge carriers at position x and time t, and D the diffusion constant. Assuming a Gaussian distribution, $n(x,t)$ will be of the form:

$$n(x,t) = a(t)\exp^{-b(t)x^2} \tag{3.28}$$

Using this in Eq. 3.27 leads to the following solution for $n(x,t)$:

$$n(x,t) = \frac{C}{\sigma}\exp^{-\frac{x^2}{2\sigma^2}} \text{ with } \sigma = \sqrt{2D(t+t_0)} \tag{3.29}$$

The Einstein equation connects the diffusion constant with the mobility:

$$D = \frac{kT}{q}\mu \tag{3.30}$$

After 0.3 μs, the width of the charge cloud will then be:

$$\sigma = \sqrt{2\frac{kT}{q}\mu_n t} = \sqrt{2 \cdot \frac{1.38 \cdot 10^{-23} \cdot 273}{1.602 \cdot 10^{-19}} \cdot 1350 \cdot 3 \cdot 10^{-7}} \approx 4.3 \cdot 10^{-2}\ \text{mm} \tag{3.31}$$

Here, I used the mobility (μ_n) of the fast electrons. They can travel the largest distance in a given time and thus determine the maximum size of the cloud. Taking the hole mobility and life-time, leads to the same value of σ.

The above values show that within the maximal signal duration of 0.3 μs the width of the charge cloud stays relatively small compared to a pixel size of 1 mm^2 and even to 0.5^2 mm^2. Smaller pixel sizes will suffer more from diffusion.

To conclude: in the case of relatively large pixels ($> 0.5 \times 0.5$ mm^2) and by treating Compton scattering and fluorescence as separate events, it is justified to consider the charge carrier pairs as moving point sources as they drift to the electrodes.

3.5 Signal induction

3.5.1 Shockley-Ramo

From the moment the electron-hole pairs are created inside the detection medium, a mirror (surface) charge is formed on the electrodes (see Fig. 3.10). The surface charge gets more and more concentrated on the pixel as the (point) charge approaches. Directly after the interaction, the contribution of holes and electrons to the induced charge is equal and will cancel out each other. As soon as both charge carrier types separate, under the influence of the applied electric field, the mirror charge is formed and output signal is created. It should be emphasised that the charge induction does not only take place when the electrodes are reached (what is often thought), but as soon as the charge carriers start to move.

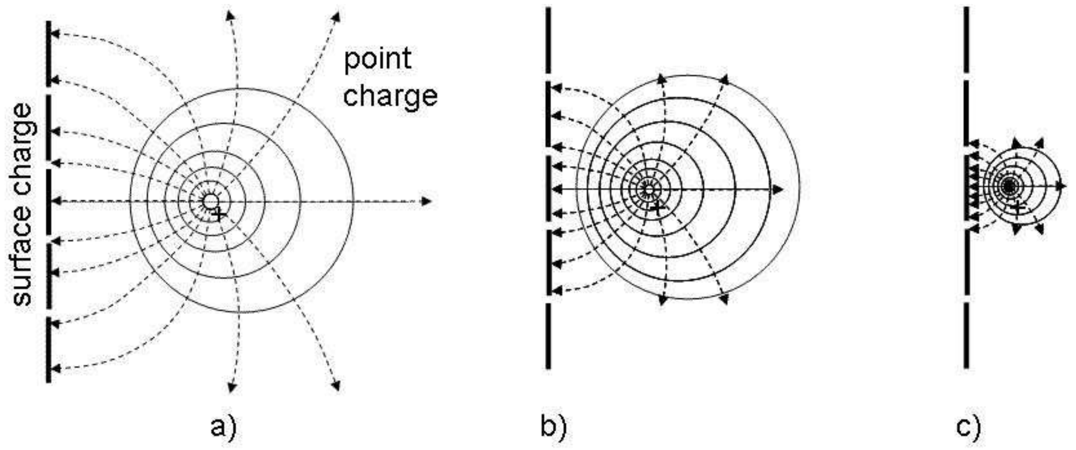

Figure 3.10: A point charge approaching the segmented electrode will create a surface charge on all pixels. As it reaches the electrode, the surface charge will be concentrated on the pixel which eventually “absorbs” the charge.

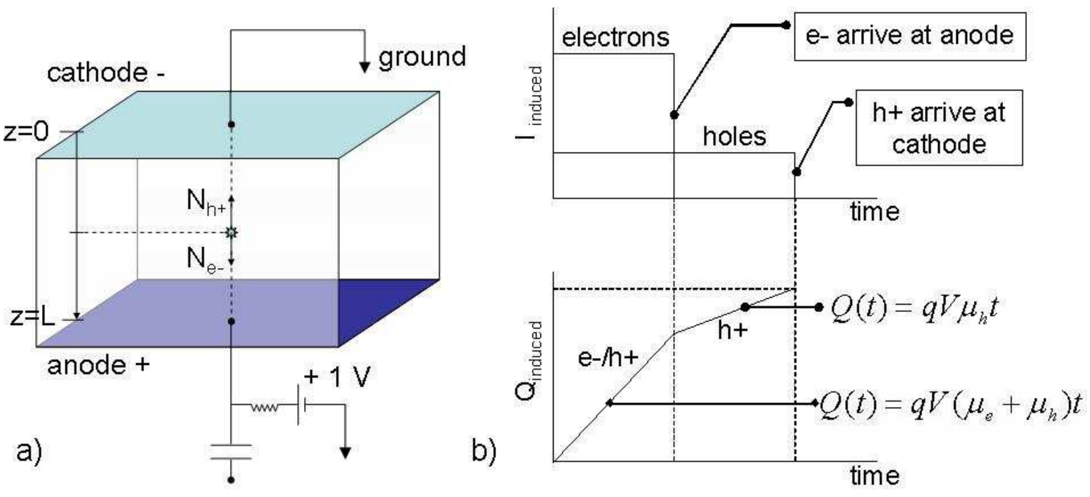

Figure 3.11: a) A planar detector with thickness L. An interaction takes place at position z and N electron-hole pairs are created. b) The corresponding induced current and charge.

To create the surface charge a current towards the pixel is necessary. This is the induced current. The shape and size of the current strongly depends on the detector geometry. To illustrate this I will start with a simple example of a detector having two planar electrodes (see Fig. 3.11a). An incoming photon has an interaction inside the detector creating a number (N) of electron-hole pairs. The applied electric field makes them drift to their proper electrode. Shockley and Ramo state that the total induced charge Q_{ind} and current I_{ind}, created by these moving charge carriers, are equal to:

$$Q_{ind} = \int_{x_i}^{x_f} q\vec{E}_w.d\vec{x} = -q[\varphi_w(x_f) - \varphi_w(x_i)] = -q.\Delta\varphi_w(\vec{x}) \tag{3.32}$$

$$I_{ind} = \frac{dQ}{dt} = q\vec{E}_w(\vec{x}) \cdot \frac{d\vec{x}}{dt} = q\vec{E}_w(\vec{x}) \cdot \vec{v} \tag{3.33}$$

With $\vec{E}_w$ the electric field and φ_w the potential in the following circumstances:

- the selected electrode at unit potential (1 V) and all others at 0 V
- all space charge removed

$\vec{E_w}(\vec{x})$ and $\varphi_w(\vec{x})$ are called the weighting field and weighting potential, respectively. x_i and x_f are the initial and final position of the charge q, and $\vec{v}$ is the instantaneous velocity of the charge at a certain position x.

To obtain the induced signals, Poisson equation must first be solved for the detector geometry considered:

$$\bigtriangledown^2\Phi = -\rho/\epsilon \tag{3.34}$$

With ρ the space charge density and ϵ the permittivity of the material. This leads to the electric potential and field from which the velocity of charge carriers can be calculated. For a detector with infinitesimally large electrodes and no space charge this reduces to a one-dimensional problem with the simple solution

$$\Phi(z) = \frac{z}{L} \cdot V \tag{3.35}$$

With z the vertical position, L the detector thickness and V the applied voltage. A photon interacting at position z and creating $N = E_\gamma/\omega$ electron-hole pairs, will induce the following total charge:

$$Q_{ind} = -(N.e_0)(0 - z) + (N.e_0)(1 - z) = N.e_0 \tag{3.36}$$

With the first part corresponding to the holes and the second part to the electrons. The voltage is set to 1 V and the other electrode to zero. The induced charge is independent of the interaction depth. The energy spectrum of this ideal detector is a single peak, with a width (or resolution) which only depends on the statistical fluctuations of N and the noise of detector and read-out electronics.

To view the induced signals as a function of time, the positions of e^- and h^+ need to be calculated using their proper velocity. Eq. 3.25 showed already that the latter is directly related to the applied electric field and charge carrier mobilities by $\vec{v} = \mu.\vec{E}$. Using Shockley-Ramo and setting $V = 1$ and $\rho = 0$, the induced current is expressed as:

$$\begin{aligned} I_{ind} &= \frac{dQ}{dt} = q.\frac{d\vec{x}}{dt}.\vec{E}_w = q(\vec{v}_e + \vec{v}_h).\vec{E}_w \qquad (3.37) \\ &= q(\mu_e.\vec{E} + \mu_h.\vec{E}).\vec{E}_w \\ &= qV/L(\mu_e + \mu_h).1/L = qV/L^2(\mu_e + \mu_h) \end{aligned}$$

With $\vec{E}_w$ the weighting field and $\vec{E}$ the normal electric field. In this example, the current is constant along the trajectory because the weighting field is constant too. For more complicated detector geometries this is not the case as I will show in Sect. 3.5.4.

3.5.2 Hecht's relation

In reality electrons and holes also have a limited lifetime. A fraction of the charge is lost during their trajectory toward the electrodes. They are trapped by potential wells caused by impurities inside the material or by recombination processes. Hecht was able to describe the charge loss using a simple exponential relation by making the following hypotheses:

Hecht:

- the applied electric field is uniform
- distribution of created charge is a Dirac function
- e- and h+ are trapped with time constants τ_e and τ_h [s]
- no un-trapping during charge collection
- no diffusion of the charge cloud

Then the number of electrons, n(t), and holes, p(t), can be described as follows:

$$n(t) = N_0 \exp(\frac{-t}{\tau_e}) \tag{3.38}$$

$$p(t) = N_0 \exp(\frac{-t}{\tau_h}) \tag{3.39}$$

With $N_0 = E_\gamma/\omega$ the initial number of e-/h+ pairs and τ_e and τ_h the electron and hole lifetimes. Combining this with Eq. 3.37 leads to:

$$\begin{aligned} I_{ind}(t) &= e_0 V/L^2[n(t)\mu_e + p(t)\mu_h] \qquad (3.40) \\ &= e_0 V/L^2 N_0[\mu_e e^{\frac{-t}{\tau_e}} + \mu_h e^{\frac{-t}{\tau_h}}] \end{aligned}$$

And the induced charge:

$$Q_{ind}(t) = e_0 V N_0/L^2[\mu_e\tau_e(1 - e^{\frac{-t}{\tau_e}}) + \mu_h\tau_h(1 - e^{\frac{-t}{\tau_h}})] \tag{3.41}$$

These two expressions have important consequences for the detector comportment. They show that a part of the induced signal is lost by charge trapping. Also the fact that electrons and holes have different mobilities and lifetimes cause that the signals become dependent of the interaction position.

A consequence of the difference and limitation of the mobility and lifetime of both charge carriers is the effect of ballistic deficit, which I will explain now.

3.5.3 Ballistic deficit

The rise-time of the pulse in a pre-amplifier (pre-amp) connected to a detector is nearly equal to the charge collection time in the detector itself. If the full amplitude of the pre-amp pulse is to be preserved during the filtering process, the shaping time (of the filters) should be very large. Unfortunately, the existence of different types of noise (see Chapt. 4.2) limits the choice of the duration of the shaping. Thermal noise (series) is large when taking a short shaping time, while the influence of the leakage current increases as the time becomes longer. The optimal shaping time must thus be limited and is generally too short in order to see the final amplitude of the signal.

The difference of the real and measured amplitude is called "ballistic deficit". Its effect is revealed in an energy spectrum by long tails on the left of the peaks. Interactions near the cathode result in a quick electron signal (1) having little charge loss, while deeper interactions (2) have a large hole contribution. The signal is therefore slower and exposed to more charge loss resulting in a smaller amplitude.

The use of small pixels may avoid this problem as I will show in the next section.

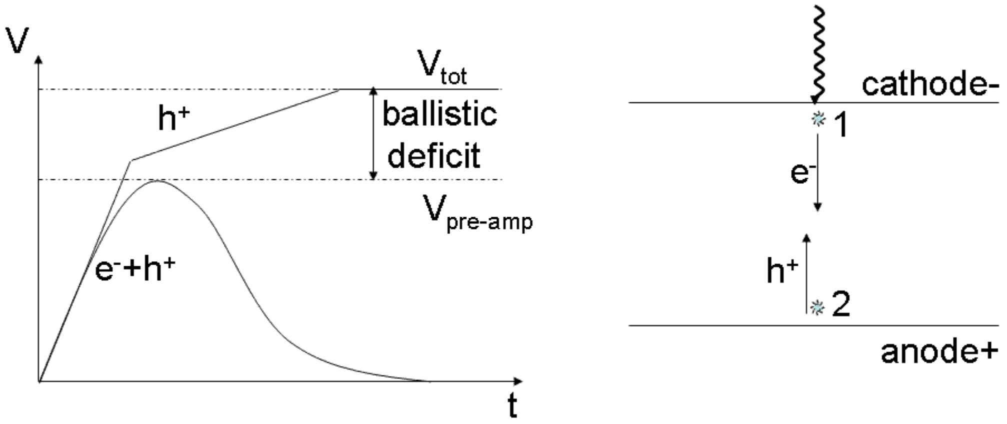

Figure 3.12: Ballistic deficit inside a planar detector.

3.5.4 Small-pixel-effect

Holes and electrons have different mobilities and lifetimes. The signal created due to charge carrier motion inside a semiconductor will therefore consist of two components: a quick electron plus hole signal and a slow hole signal only. This is illustrated in Fig. 3.13 and 3.14. Both show a measurement of the total induced charge as function of time at the output of the charge sensitive amplifier (CSA) connected to a single pixel CdTe Schottky detector ($4.1 \times 4.1 \times 0.5$ mm^3), biased at 21.5($\pm$0.1) V. This low voltage is taken in order to obtain slow signals that can easily be analysed. The signals are not exposed to the filtering system. However, a small distortion exist due to the non-ideal behaviour of the CSA.

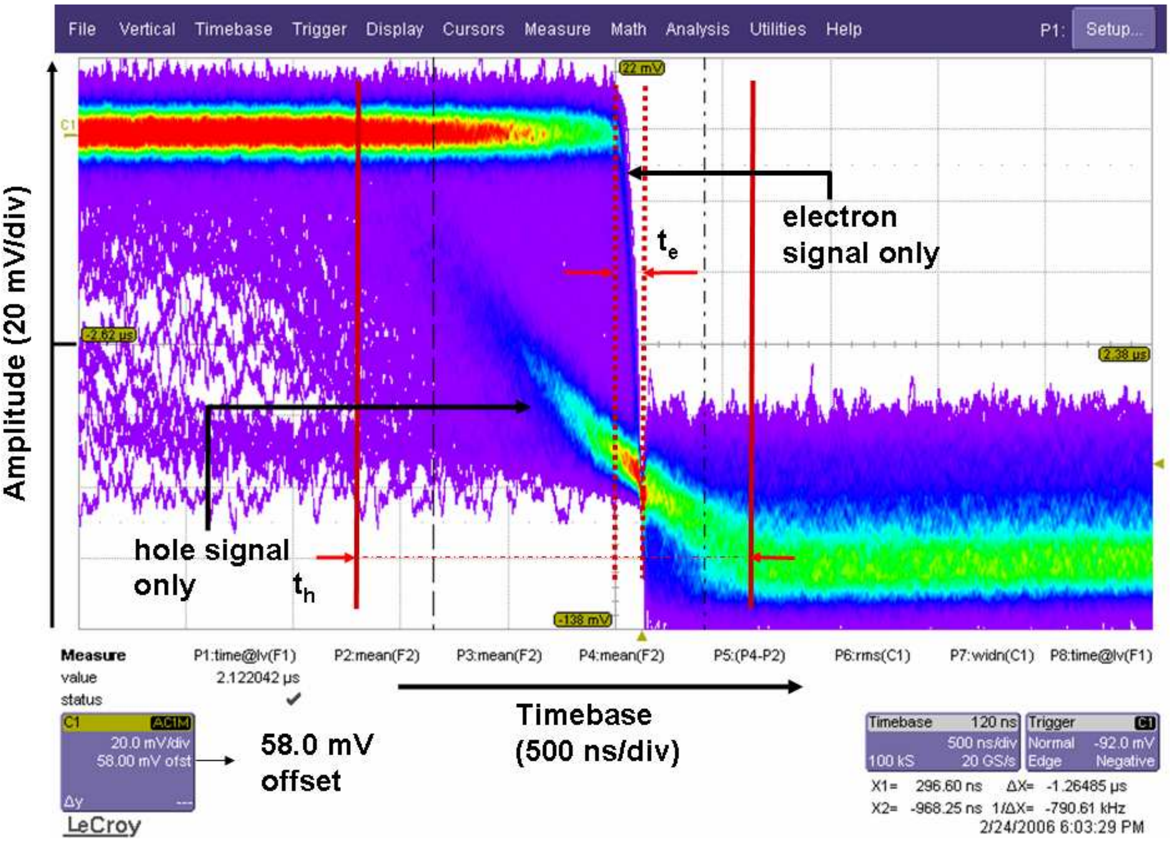

Figure 3.13: Total induced charge as a function of time measured directly at the output of the CSA connected to a single pixel CdTe Schottky detector ($4.1 \times 4.1 \times 0.5$ mm^3) biased at 21.5 V. The electron and hole signal are clearly visible.

The first figure, 3.13, shows a collection of several hundreds of signals as measured by a LeCroy digital oscilloscope (in persistence mode). The horizontal axis corresponds with a time base of 500 ns per division. The vertical axis gives the amplitude as 20 mV/div and a small offset of 58 mV.

Two groups of signals can clearly be distinguished. One created by electrons only: these are interactions close to the cathode(-). And a second, created by holes only, after interactions near the anode(+).

The signals begin at the moment the amplitudes start to decrease, and stop as the amplitude reaches a constant value again (which is not really constant, but slowly returns to its initial amplitude (due to clearing of the feedback capacitor)). By measuring the signal duration and using Eq. 3.25, I can calculate the electron and hole mobility. The short electron signal lasts $t_e = 0.12(\pm 0.01) \cdot 10^{-6}$ s and the hole signal $t_h = 1.8(\pm 0.1) \cdot 10^{-6}$ s. Then:

$$\mu_e = \frac{L/t_e}{V/L} = \frac{0.05/0.12 \cdot 10^{-6}}{21.5/0.05} = 969 \pm 85 \text{ cm}^2\cdot\text{V}^{-1}\cdot\text{s}^{-1} \tag{3.42}$$

$$\mu_h = \frac{L/t_h}{V/L} = \frac{0.05/1.8 \cdot 10^{-6}}{21.5/0.05} = 65 \pm 4 \text{ cm}^2\cdot\text{V}^{-1}\cdot\text{s}^{-1} \tag{3.43}$$

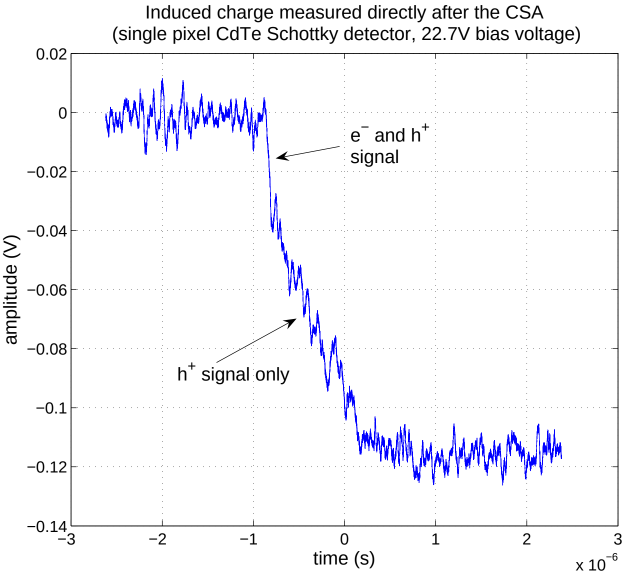

Figure 3.14: Single measurement of the induced charge on the single pixel Schottky detector.

Comparing these values with those of Table 3.1 shows a good agreement ($\mu_e = 950$ and $\mu_h = 73$). The non-ideal behaviour of the CSA is not taken into account in the above simulation.

Fig. 3.14 shows a single signal of the same detector. In this case the interactions took place not far from the middle of the crystal leading to a quick electron (and hole) and a slow hole component.

As a comparison, Fig. 3.15 shows the result of a simulation of the induced charge obtained with MGS-CdTe V1.0 which I will explain in detail in Chapt. 5. It concerns the signal created on one of the planar electrodes (10×10 mm^2) of a 2.1 mm thick[2] CdZnTe detector biased at 100 V. The interaction takes place exactly in the middle. It is clear that when charge loss is included, a large part of the amplitude is lost mainly due to hole loss while the electron component does not show any significant variation. The signal is positive because the induction takes place at the opposite electrode, compared with the above measurements.

The results (measurement and simulation) show two important effects, namely the ballistic deficit due to slow holes, and charge loss, due to a short hole life time. Both can be avoided, if the hole contribution to the total induced charge is limited.

A very appropriate technique can be used, namely the *small-pixel-effect*. Beside the fact that small pixels allow imaging, they create a special kind of weighting field. The weighting field is strong near the pixel but weak in the rest of the detector. Especially when the relation pixel-size to detector thickness gets smaller, the effect becomes stronger. This is

---

[2] The real detector is 2 mm thick, but for practical purposes related to the grid-size, I take 2.1 mm in this example.

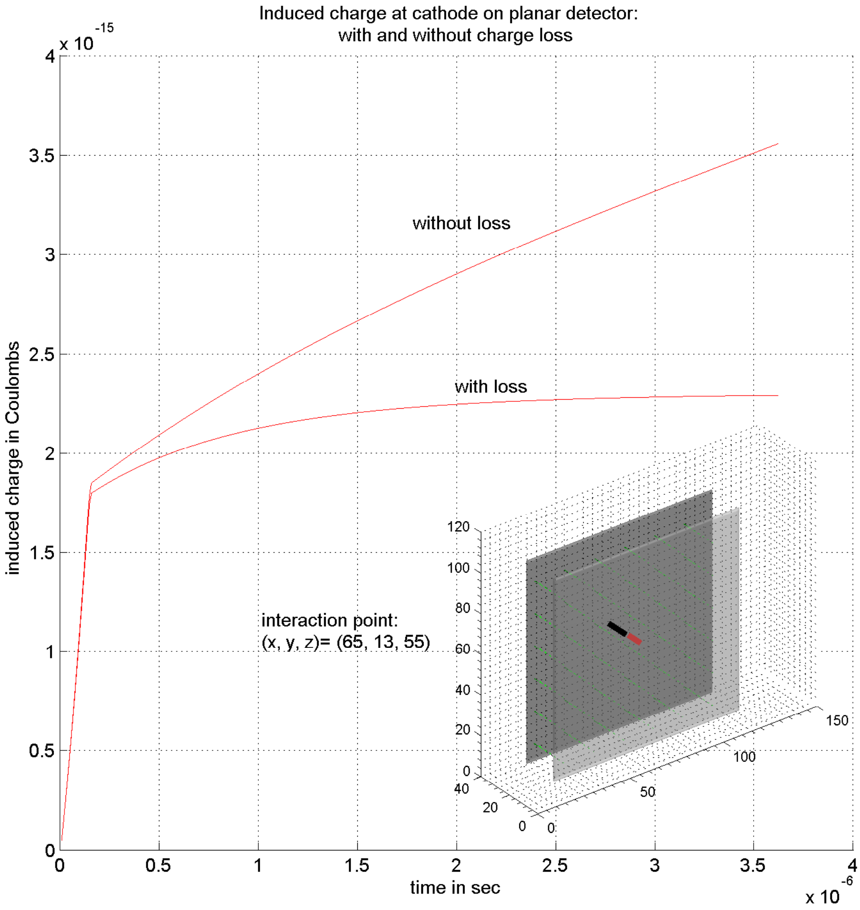

Figure 3.15: Simulation of the total induced charge as a function of time in the case of an interaction in the middle of a 2.1 mm thick CdZnTe detector having 10 × 10 mm^2 electrodes at both sides.

clearly shown in Fig. 3.16 in which the weighting potential (V_{weigth}) is plotted against the relative position (x/L) inside a detector of varying thickness L. The pixel size is kept at 500×500 μm^2. The right side shows the geometry of the weighting potential of one pixel for L equal to 1, 2, 3 and 4 mm.

The small-pixel-effect limits the contribution of the hole signal. After an interaction in the middle of the detector ($x/L = 0.5$) with the pixel side positively biased, holes drift towards the cathode (at $x = 0$), away from the pixels (at $x/L = 1$). They experience only a weak weighting field and induce nearly no charge. On the contrary, the electrons drift towards the pixels and initially feel a weak field, but just before arriving at the anode the field suddenly increases. Nearly all of the induced signal is therefore created in the last part of the trajectory. Especially for interactions near the cathode, the induced signal has an electron component only. The charge loss effect due to holes on spectroscopic performances is thus limited.

I would like to emphasise that the loss still exists. It is however screened by the special shape of the weighing field. The small-pixel-effect is only useful if the pixels are located at the positive anode (if not, holes will induce most of the signal).

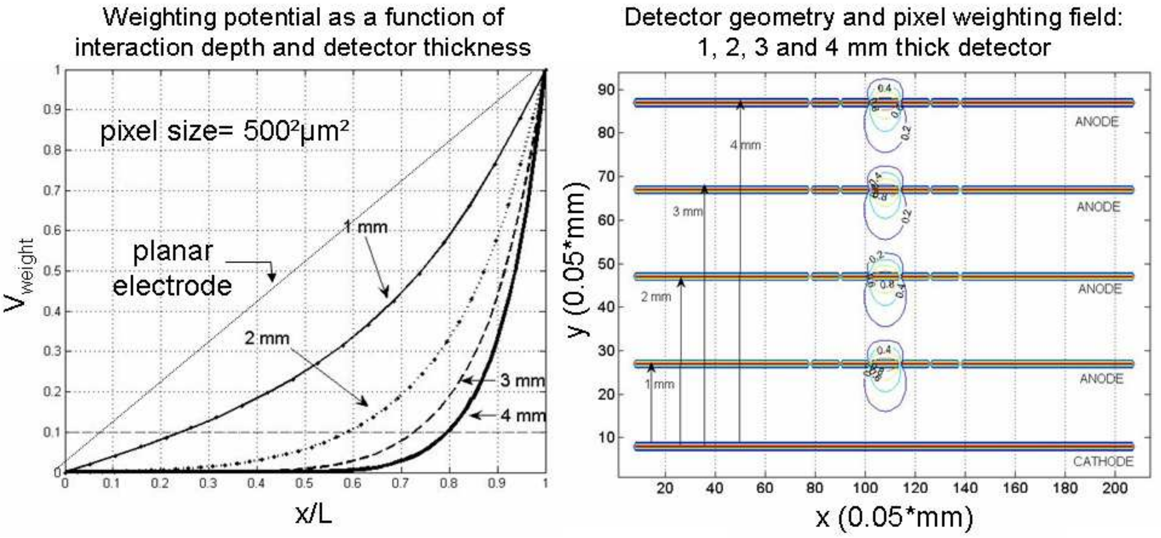

Figure 3.16: Left: the weighting potential as a function of the position for different detector thicknesses. As the thickness, L, increases, the small-pixel-effect becomes stronger. Right: the numerically obtained weighting potentials. The pixels have a size of 500 μm with a large guard ring surrounding them. (Plots obtained with the modelling and simulation program described in Chapt. 5)

The small-pixel-effect has some other consequences. First of all, if no charge loss is present, the pixel which is touched must collect all of the charge ($N_0 e_0$). The other pixels must end at zero induced charge. Also, the sum of induced charges of all pixels must be equal to the induced charge at the opposite electrode (cathode) and of opposite sign.

If charge loss is included, it is possible to have a non-zero charge at neighboring pixels. Since the charge loss of electrons and holes is not the same, neither their mobility, the induced charges of holes and electrons will not exactly cancel out each other at neighbouring pixels. Also, since the charge induction on the pixels and cathode is induced from different weighting fields (that of the pixel and that of the planar electrode), the influence of (hole) charge loss is larger at the cathode than at the anode. The latter will have a larger signal.

Furthermore, the shape of the (pixel) weighting field allows having negative currents. I will explain this in detail with the help of Fig. 3.17. It shows a zoom of two pixels of a detector having a pixelated and planar electrode. Suppose an interaction took place near the cathode. Hole contribution can be ignored. The electrons will follow the electric field lines [3] (not shown) leading them in a nearly straight line to the pixel which is "touched". To calculate the induced signal on the neighbouring pixels I use Shockley-Ramo again by

---

[3] The charge carriers follow the normal electric field lines and not those of the weighing field.

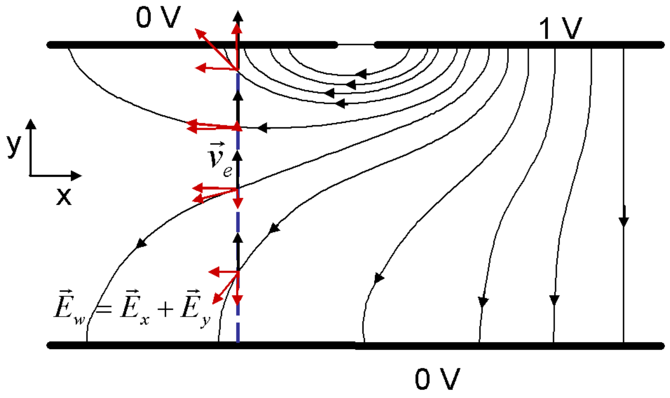

Figure 3.17: Schematic view of the weighing field of a pixel next to the pixel which is touched. Its shape results in bipolar induced signals.

putting all other electrodes at zero potential except for the one on which I would like to calculate the signal. Remember Eq. 3.33:

$$\begin{aligned} I_{ind}(t) &= q\vec{E}_w(\vec{x}) \cdot \vec{v} \\ &= q|E_W||v|cos(\theta) \end{aligned} \tag{3.44}$$

With θ the angle between $\vec{E}_w$ and $\vec{v}$. At positions close to the point of first interaction the scalar product of both vectors is negative (taken the direction towards the anode as positive) but at a certain moment it switches sign. The current will therefore also switch sign from positive to negative. For an interaction near the anode a comparable effect is observed except that holes are the most important charge carriers. They drift towards the cathode. The scalar product with the weighting field is negative at the beginning (and the current as well) and becomes positive. Induced signals on neighbouring pixels can therefore be bipolar. More details and examples are given in Chapt. 5.

After having introduced the most important parameters useful to understand the presented work, I conclude this theory chapter with an explanation of the unwanted polarisation effect in Schottky type detectors, as mentioned before.

3.6 Polarisation

An unwanted effect using CdTe detectors equipped with blocking contacts, is the appearance of polarisation that drastically influences the detector behaviour. When applying a bias voltage, a decrease of the counting rate and charge collection efficiency as a function of time can be observed. This is illustrated in Fig. 3.18. It shows the evolution of the ~60 keV energy peak of an ^{241}Am spectrum, measured with a CdTe detector of $4.1 \times 4.1 \times 0.5$ mm^3, having an indium electrode at the anode, and a platinum pixel (2.0×2.0 mm^2) and guard ring at the cathode side. The time between two adjacent spectra is one minute.

The temperature is ∼20^{o}C. Note the slow movement of the peak maximum to the left while the tail at the left side increases.

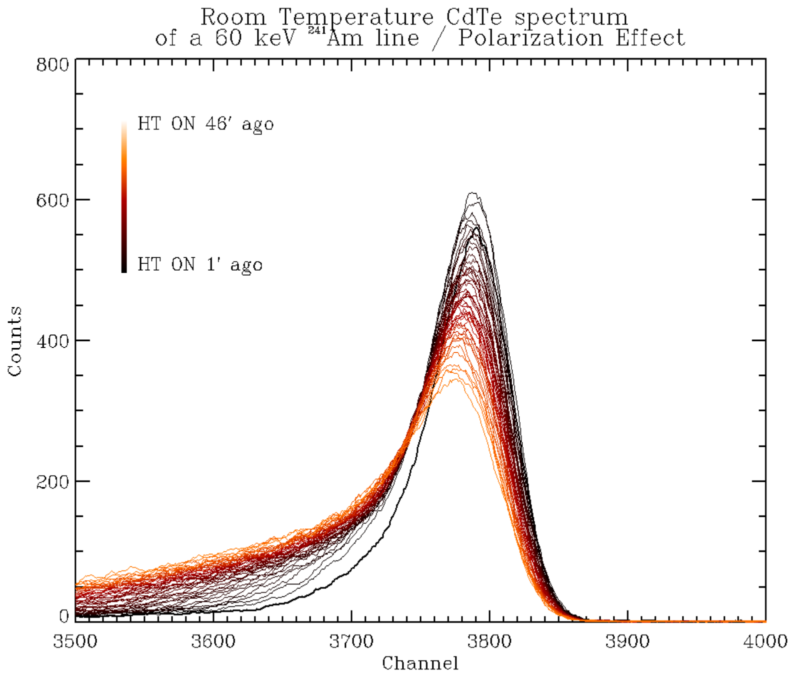

Figure 3.18: Measurement of the 59.54 keV of ^{241}Am peak with a CdTe Schottky detector for successive time intervals at room temperature.

The polarisation of high resistive, p-type CdTe detectors with blocking contacts is a rather difficult process which is still not completely understood. Bell et al. (1974) give an explanation that it is due to the ionisation of deep acceptor [4] levels inside the material. If one side of the CdTe detector is covered with a metal having a low work function, such as indium, a Schottky contact is created (see subsection 3.2). The bending of the energy levels makes it possible for the deep acceptor levels to cross the Fermi level, allowing them to gain enough energy to be activated. This is shown in Fig. 3.19. The deep traps can get easily ionised by promoting holes into the valence band. A space charge is created, consisting of the ionised traps and the normal depletion layer. The corresponding electric field consists of a strong component in the first layer near the (anode) contact (A) and a weak component in the depletion layer (B) (and a zero component if the detector is not completely depleted (C)).

This has the following consequences for the spectrum: since the detector acts as a diode,

---

[4] "Deep level" meaning, an energy level away from the edges of the conduction and valance bands and close to the intrinsic Fermi level.

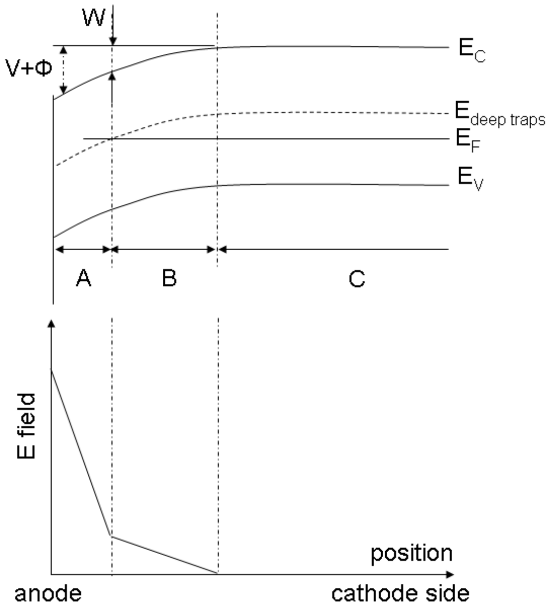

Figure 3.19: The polarisation effect seen at the 59.54 keV energy peak of ^{241}Am , as measured by a CdTe Schottky detector.

the Schottky contact needs to be biased positively. Electrons will therefore drift to this contact while holes move to the other side. If a photon interacts near the Schottky contact, electrons and holes first see a strong electric field. Electrons are easily collected and because of their short path, they are (nearly) not subjected to any charge loss. Holes however will have to traverse almost the entire detector and will pass the areas of weak electric field. Since their mobility is relatively low, they will spend a non-negligible time in that area, increasing the chance of recombination, and thus charge loss. This is clearly seen in the spectrum as the long tail of higher energy peaks and a movement of the peak maximum.

An interaction near the negative electrode leads to a quick collection of the holes. Now the electrons need to traverse the entire detector. However, their large mobility makes them less sensitive to charge loss. Low energy peaks show therefore less degradation.

The ionisation rate of the deep acceptors has a characteristic time, τ_I, of:

$$\tau_I \propto \frac{1}{N_0 \sigma < \nu >} \exp(E/kT) \tag{3.45}$$

With N_0 the number of deep acceptors, σ the acceptor captor cross section, ν the thermal velocity and E the energy depth of the trap. Since $kT \sim 10^{-2}$, which is almost two orders smaller than typical values of E, the ionisation time can be very long. Operating the detector at low temperatures is therefore favorable.

The reverse situation, de-ionisation, is much quicker since no activation energy is involved.

Its characteristic time, τ_D, is described as follows:

$$\tau_D \propto \frac{1}{N_V \sigma < \nu >} \tag{3.46}$$

With N_V the density of states at the top of the valence band.
This is exactly what I see in CdTe Schottky detectors: when applying a bias voltage at high temperatures, a quick degradation of the spectrum takes place. Cutting the bias voltage and re-applying it, de-ironizes the acceptor sites and leads to a correct detector functioning (although for a limited time).
The value of the applied voltage also plays a significant role in the polarisation effect. To explain this, I assume that directly after applying the bias, the detector is completely depleted. A constant space charge is present, creating a straight descending electric field, shown below and described as:

$$E(x) = V_0 + \frac{\rho}{\epsilon}(x - L/2) \tag{3.47}$$

With $E(x)$ the electric field, V_0 the applied bias voltage at the indium side (and with the other side at 0 V), ρ the space charge, x the position and L the thickness of the detector. A higher voltage leads to an increase of the electric field in the entire detector (the "shape" stays the same). As the extra space charge in zone A, due to the activation of deep acceptors, starts to form, the electric field in the "normal" depleted region (B) will weaken but will stay sufficiently high to avoid significant charge loss. However, as time passes, more and more charge is formed in region A, weakening the field in B. This eventually leads again to a visible degradation in the spectrum.
The polarisation effect is a disadvantage of CdTe detectors with Schottky contacts. A stable, long term operation of the detectors (which is absolutely necessary for a space mission like Simbol–X) is in principle possible, but at low temperatures (<0^{o}C) and high bias voltages (∼6 kV/cm).

Chapter 4

Electronics and detector characterisation

The work related to the development of the IDeF-X (Imaging Detector Front-end for X-rays) ASIC (Application-Specific Integrated Circuit) is outlined, as well as the characterisation of different detectors in combination with the electronics.
First, the pre-amplifier of the ASIC is described, followed by a detailed description of the different noise sources and their influence on the performance of the detector and ASIC. The leakage current is an important source of noise. Since a DC coupling exists between electronics and detector, it is a critical parameter in the design of the ASIC and highly determines the (spectroscopic) performance of the complete sensor. Knowledge of its value is therefore mandatory.
I describe in detail the leakage current measurements of single pixel CdTe and 64 pixels CdZnTe detectors in different operating conditions. In addition, the temperature dependence of the current is used to obtain activation energy maps, which are directly related to the impurity distribution inside the crystals. Furthermore, the results of spectroscopic measurements obtained with single pixel and 64 pixels Cd(Zn)Te detectors, either with Schottky or ohmic contacts, are presented and discussed.

4.1 The pre-amplifier

In Chapt. 3 the different physical processes involved in the functioning of a semiconductor detector were explained. The induced signals created by the moving charges now have to be read out. These signals can be extremely small. For example, suppose that all charge created by a photon of 6 keV (corresponding to the Fe-line) is collected at a pixel of a CdZnTe detector. Using Eq. 3.19, I obtain a number of electron/holes pairs,

$$N = \frac{6.0 \times 10^3 \text{ eV}}{5.0 \text{ pairs/eV}} \times 10^3 = 1200 \tag{4.1}$$

representing a total charge of $1200 \times 1.602 \cdot 10^{-19} = 1.92 \cdot 10^{-16}$ C. The purpose of the preamplifier is to convert this small charge pulse into a voltage pulse large enough to be handled by subsequent pulse analysis circuits.

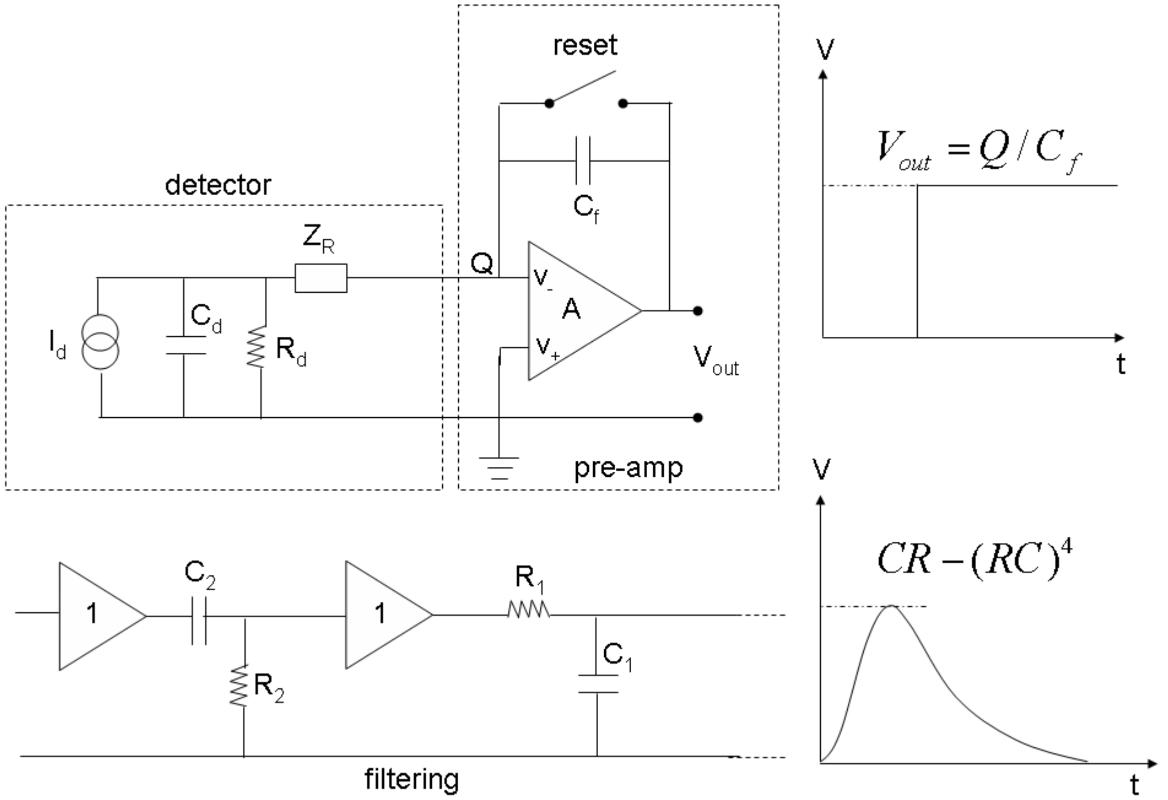

Figure 4.1: Above: equivalent circuit of a charge sensitive amplifier connected to a detector. A charge generated inside the detector creates a step function at the output of the CSA with an amplitude V_{out} equal to Q/C_f. Below: a CR-RC^4-filter shapes V_{out} to a nearly Gaussian signal with improved S/N ratio.

Fig. 4.1 shows the diagram of a semiconductor detector connected to a charge sensitive amplifier (CSA).

The detector is represented by a current source I_d, a capacitor C_d and a resistor R_d in parallel and an impedance Z_R in series with the detector output.

The CSA consists of an inverting op-amp circuit which delivers an output voltage proportional to the input charge Q and a feedback capacitor C_f. The reset in the feedback loop serves to empty the C_f before the next charge pulse from the detector arrives. Assuming an ideal op-amp (with amplification $A >> 1$, an infinite input impedance and both input terminals at the same potential), all of the charge will be collected on C_f. Then, the output voltage (V_{out}), with a charge pulse equal to $Q \cdot \delta(t)$ as input, is equal to a step function with amplitude Q/C_f.

In order to reduce the interference with subsequent signals (pile-up) and to improve the signal to noise ratio (S/N), the output signals of the CSA must be shaped. The lower part of Fig. 4.1 shows two elements of a standard shaping circuit: a CR- and RC-filter, separated by buffers. The transfer function in Laplace space of the CR-filter is:

$$H(s) = \frac{\tau s}{\tau + 1} \tag{4.2}$$

The Laplace transformation of the step function is equal to $\frac{1}{s}$. The CR output in the time domain due to this step function is:

$$V(t) \quad = \quad L^{-1}(\frac{\tau s}{(\tau s + 1)(s)}) = L^{-1}(\frac{\tau}{(\tau s + 1)}) = e^{-t/\tau} \tag{4.3}$$

The CR-filter saves the characteristics of the front of the input signal but shortens the back of it. The RC filter has the following Laplace transfer function:

$$H(s) = \frac{1}{\tau s + 1} \tag{4.4}$$

Its output to a step function is:

$$V(t) = L^{-1}\frac{1}{(\tau s + 1)s} = \frac{\frac{1}{\tau}}{(s + \frac{1}{\tau})s} = 1 - \exp^{-t/\tau} \tag{4.5}$$

Combining both filters leads to the following response (to the step function):

$$V_{out}(t) = Q/C_f \frac{t}{\tau} \exp^{-t/\tau} \tag{4.6}$$

By combining multiple RC circuits with a CR filter, a CR-RC^n filter is formed. In general $n = 4$ is sufficient to transform the step function in a nearly Gaussian pulse with good S/N ratio.

The choice of the time constant τ, or shaping time, is subject to a number of considerations. First of all, to avoid pile-up, a short shaping time is favorable. However, if it becomes too short, it will “see” that the step function of the pre-amp is not really a step function. This results in a ballistic deficit or loss of signal. On the other hand, a longer shaping time leads to an increase of pile-up.

The S/N ratio also depends on the shaping time, which I will explain in the next section. I would like to emphasise that within this topic two rather similar parameters are used: the shaping time (τ) and the peaking time.

The shaping time is the time constant of the filter. The peaking time is defined as the time between the moment at which the signal reaches 5% of its maximum amplitude and the moment at which the maximum is reached (see fig. 4.2).

4.2 Noise

Noise is an important parameter related to the functioning of the detector and read-out electronics. It can be expressed as the amount of Equivalent Noise Charge (ENC).

Like every electronics system, a pre-amp produces noise. Suppose, that the pre-amp is ideal, generating no noise. A repetitively injected charge will give rise to the same

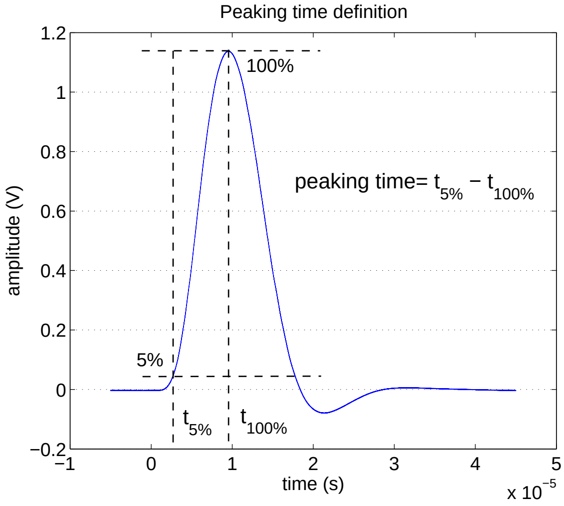

Figure 4.2: Definition of the peaking time.

maximum output amplitude every time it is injected. Representing these maxima in a histogram, leads to a delta-peak at one single value.

The pre-amp adds electronic noise to the output. This leads to output signals with variable maximum amplitude, resulting in an enlargement of the peak, which becomes Gaussian. The ENC is expressed as the number of electrons that have to be injected to the ideal pre-amp (without noise) to create a maximum output voltage equal to the standard deviation (often expressed as the root-mean-square (RMS)) of the above Gaussian peak.

The ENC can therefore be used to express the width (FWHM) of an energy peak in a spectrum. Beside the electronic noise, a varying number of e^- /h^+ -pairs created per photon, broadens the peak too. This can also be expressed in ENC. The relation between the ENC and FHWM is expressed as:

$$FWHM(eV) = 2.35 \times \omega \times ENC \tag{4.7}$$

With ω the pair creation energy of the material concerned. The noise sources present in the detector and read-out system can be divided into series, 1/f and parallel noise. (The noise in the read out electronics is dominated by the input transistor of the CSA. Other noise sources can be neglected.) The individual contribution to the total noise as a function of the peaking time is shown in Fig. 4.3. In the following sections I will give a short explanation of each component.

4.2.1 Series noise

A source of series noise is thermal or Johnson-Nyquist noise. It is generated by the thermal agitation of the charge carriers inside an electrical conductor in equilibrium, independent

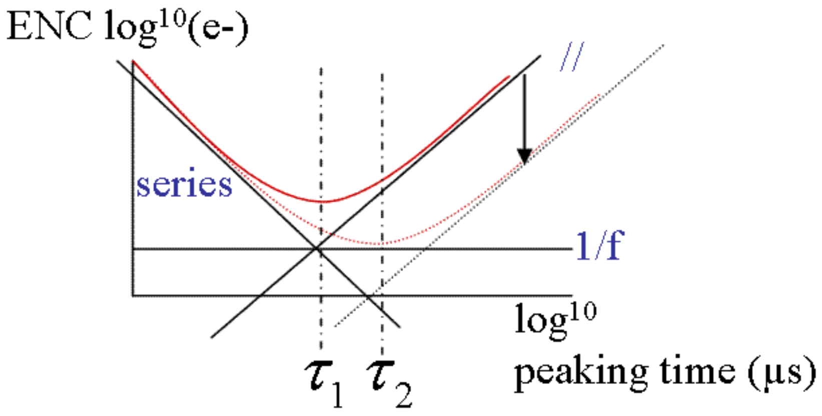

Figure 4.3: The different noise components present in a detector and electronics system. At small peaking times the series noise is dominant while at higher values the parallel noise dominates. The 1/f noise is independent of the chosen peaking time. If the parallel noise is reduced the peaking time at minimum ENC shifts to higher values.

of the applied voltage. Its spectral density is given as:

$$\frac{d\bar{U}_n^2}{df} = 4kTR \tag{4.8}$$

With R the resistance of the component from which the noise originates, k Boltzmann constant, T the temperature and f the frequency. Every resistor inside a circuit creates thermal noise, even if no current is flowing. The noise source can be represented as a voltage source in series with the input impedance (Z_R in Fig. 4.1).
Series noise is also created by the electronics, especially inside the transistor of the input stage of the CSA (see Sect. 4.3.1). For a detailed description of the noise behaviour of transistors and other electronics components I refer to Chang and Sansen (1991) and Lutz (1999). I restrict this explanation by citing the following relations:

$$ENC^2_{series} \propto \frac{C^2_{tot}}{g_m \tau_p} \tag{4.9}$$

Thus, the series noise is proportional to the total input capacitance C_{tot} (which includes the capacitance of the detector C_{det}, of the different connections (parasitic capacitance) C_{par}, the input transistor C_{trans} and of the feedback C_f) and inversely proportional to the square root of the peaking time τ_p. The transconductance, g_m, depends on the transistor depletion regime:

$$g_{strong} \propto \sqrt{\mu C_{ox} \frac{W}{L} I_0} \tag{4.10}$$

$$g_{weak} \propto I_0 \frac{q}{kT} \tag{4.11}$$

With μ the majority carrier type, C_{ox} the capacitance of the oxide layer and W and L the width and length of the transistor and I_0 the current inside the input transistor. For this pre-amplifier, the weak inversion corresponds to low I_0 (~50 μA) and high inversion to $I_0 \geq 1$ mA. (The above current values strongly depend on the chosen size of the pre-amp). The above parameters will return in the characterisation of the IDeF-X ASIC (Sect. 4.3.1).

4.2.2 1/f noise

The 1/f noise component consists of low-frequency voltage noise and has a 1/f dependence:

$$\frac{dU_n^2}{df} \sim \frac{1}{f^{\alpha}} \text{ with } \alpha \approx 1 \tag{4.12}$$

1/f noise is independent of the chosen peaking time. There is no general accepted explanation for 1/f noise. Possible sources are the metal-semiconductor contacts of the detector or the trapping of charge carriers by crystal defects.
Like series noise, 1/f noise also exists in the input transistor. It is proportional to the total input capacitance C_{tot} and inversely proportional to the square root of transistor surface $W \times L$:

$$ENC_{1/f}^2 \propto \frac{C_{tot}^2}{WL} \tag{4.13}$$

4.2.3 Parallel noise

An example of parallel noise is Shot noise. It is due to the discrete nature of charges creating statistical fluctuation on the number of charge carriers forming a current I. In a detector it can be represented as an extra current source parallel to the signal source. Its power frequency spectrum is given by:

$$\frac{d\langle i_n^2 \rangle}{df} = 2Iq \tag{4.14}$$

With q the elementary charge. Parallel noise is related to the detector leakage current. Expressed in ENC the parallel noise can be described as:

$$ENC_{//}^2 \propto (I_{leak}) \times \tau_p \tag{4.15}$$

The parallel noise is proportional to the square root of the leakage current I_{leak} and peaking time. The above noise considerations serve to characterise the electronics connected to the different Cd(Zn)Te detectors which I will introduce now.

4.3 The IDeF-X ASIC

To fulfil the scientific objectives of Simbol–X, high quality Cd(Zn)Te crystals in combination with ultra-low noise electronics are mandatory. Also the application in space environment demands special electronic components. They should be radiation hard and must show stable functioning for at least three years in space. Since commercial available read-out electronics do not fulfil these requirements, we are obliged to design the ASIC ourselves.

The ASIC has been baptised *IDeF-X*, standing for Imaging Detector Front-end for X-rays. The development includes several steps. It starts with a set of stand-alone pre-amplifier prototypes (see Fig. 4.4a) to the final complex multi-channel (32 to probably 256) circuit for high density pixel detectors. The final version is used to read out the 256 pixels Cd(Zn)Te detector for Simbol–X. Another application will be the coded aperture telescope ECLAIRs (Schanne et al. 2004), a space mission for gamma-ray bursts with multi-wavelength observations.

I will start with the description of the first member of the family: the IDeF-X V0 chip.

4.3.1 IDeF-X V0

IDeF-X V0 has been developed to study the performances of different CSAs built with AMS [1] 0.35 μm CMOS technology in terms of noise, power consumption and radiation hardness. The chip has ten CSAs, with a NMOS or PMOS input transistor in different sizes, each having a specific optimal input capacitance range. The CSAs are slightly different from the one explained in Sect. 4.1. Instead of the switch, shown in Fig. 4.1, to empty the capacitor C_f, a feedback transistor is used which is biased by the detector leakage current. This means that the CSA works properly, only if a leakage current exists (in the good direction).

Each CSA has its own signal input and an individual test capacitor to inject an artificial signal. To simulate a detector leakage current or to compensate it, a compensation current source is added. The output of the pre-amps are connected to a 10× voltage gain stage. These stages are multiplexed towards a low output impedance buffer.

The CSAs have shown to be extremely sensitive to external noise. Even the connection to the pads that form the connection between CSA and the chip carrier in which the ASIC is placed, add a significant amount of noise, as I will show now.

Noise behaviour To study the noise created by the CSA and/or its connections, a charge pulse is injected via the integrated test capacitor of 200 fF. The output signals are sent to an external shaper (CR-RC^2) with variable peaking times ranging from 20 ns to 10 μs. A digital oscilloscope allows measuring the signal shape and amplitude. If no noise is present, the output will have constant amplitude. This ideal case does not exist and the amplitude will have a certain variation determined by the noise. The noise is expressed as a number of e$^-$ r.m.s. equivalent noise charge (ENC), as explained before, and can be calculated as follows:

$$ENC(e^-) = \frac{V_{std}}{V_{output}/(V_{inj} \times C_{inj})} \times \frac{1}{1.602 \times 10^{-19}} \tag{4.16}$$

With V_{std} the standard deviation of the measured amplitude, V_{output} the mean maximum output voltage, V_{inj} the amplitude of the injected signal and C_{inj} the test capacitor.

---

[1] AMS standing for Austria Micro-Systems, the global leader in the design and manufacture of high performance analog ICs (integrated circuits)

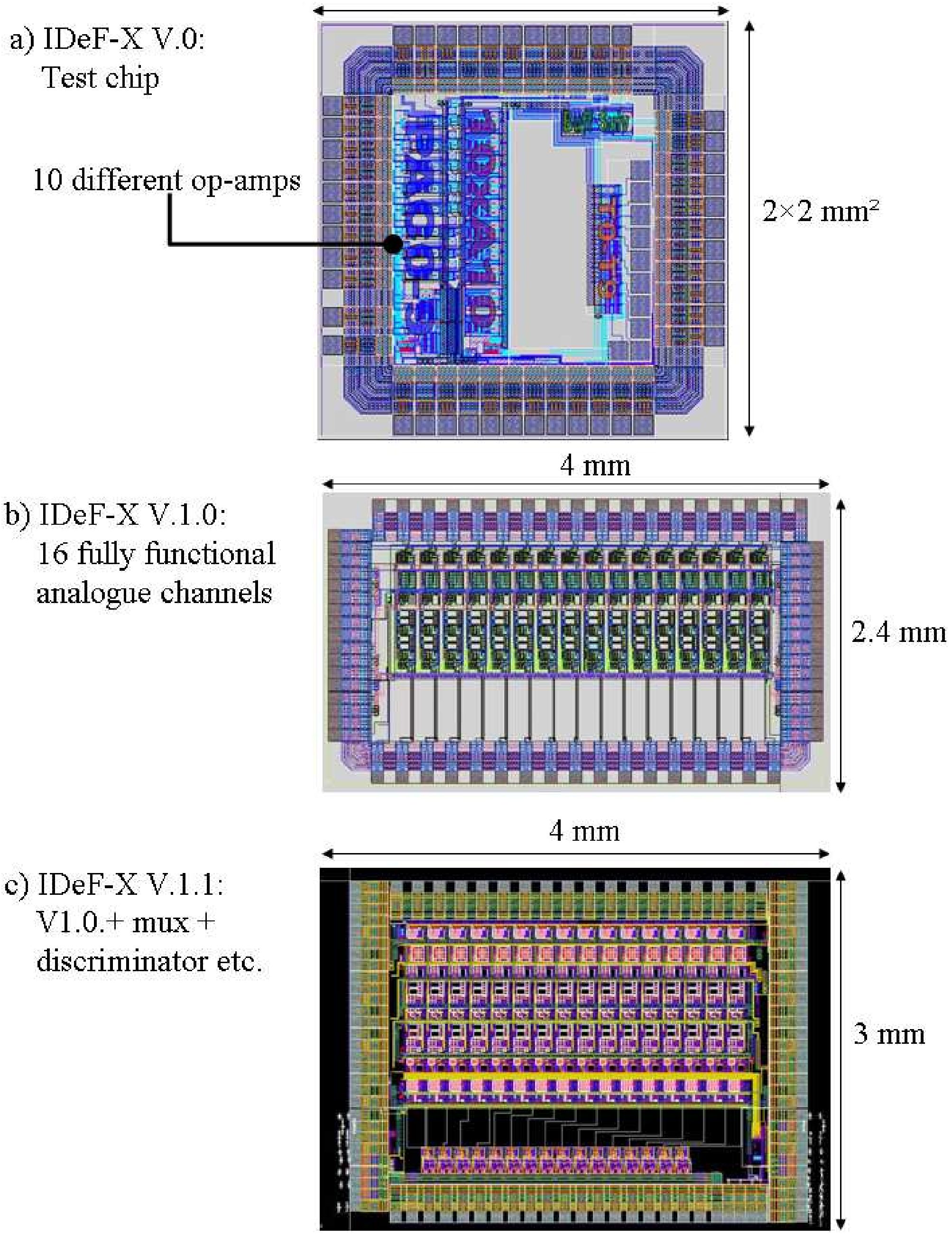

Figure 4.4: a) The development of the IDeF-X ASIC starts with a test chip IDeF-X V0 which consists of 10 different CSAs (PMOS and NMOS transistors). b) The most appropriate CSA is chosen to be implemented in the next version, IDeF-X V1.0. The latter has 16 complete, individual spectroscopic input channels. c) Version 1.1. is an expansion of V1.0 with a multiplexer, discriminator, peak detector and analogue memory.

The ENC value is measured as a function of peaking time for all ten CSAs in the IDeF-X chip. The lowest (floor-)noise (inputs not connected to chip carrier pads) is measured to be between 29.2 and 49.3 electrons.

From the above results three CSAs are chosen for further study. The first, called CSA #0, is used as a reference because it is configured in such a way that it has no pad at all and thus no connection to the external carrier. It will only experience intrinsic noise. The second, CSA #3, is a PMOS CSA which showed the lowest noise: 32.3 e^- . Moreover, it is optimised for input capacitances ranging from ∼ 5 to 10 pF, comparable with the expected sum capacitance of detector and connections. The third, CSA #6, is taken as a comparison since it has the same geometry as CSA #3 but NMOS instead of PMOS input transistor.

The ENC measurement is repeated with CSA #3 and #6 connected to the external carrier via the pads mentioned before. In a later stadium these pads will serve as the connection between the chip and a CdTe detector.

The ENC as a function of peaking time for the three CSAs is shown in Fig. 4.5a. As expected, CSA #0 without pad connection has the lowest noise: 12.4 e^- at 9.1 μs peaking time. PMOS CSA #3 has 69 e^- at 9.1 μs peaking time and NMOS CSA #6 has 76 e^- at 4.5 μs peaking time. The high value of the latter is due to an extra compensation current which is needed for a proper functioning of the CSA. Unfortunately this leads to extra parallel noise. In the PMOS the extra compensation current is not necessary.

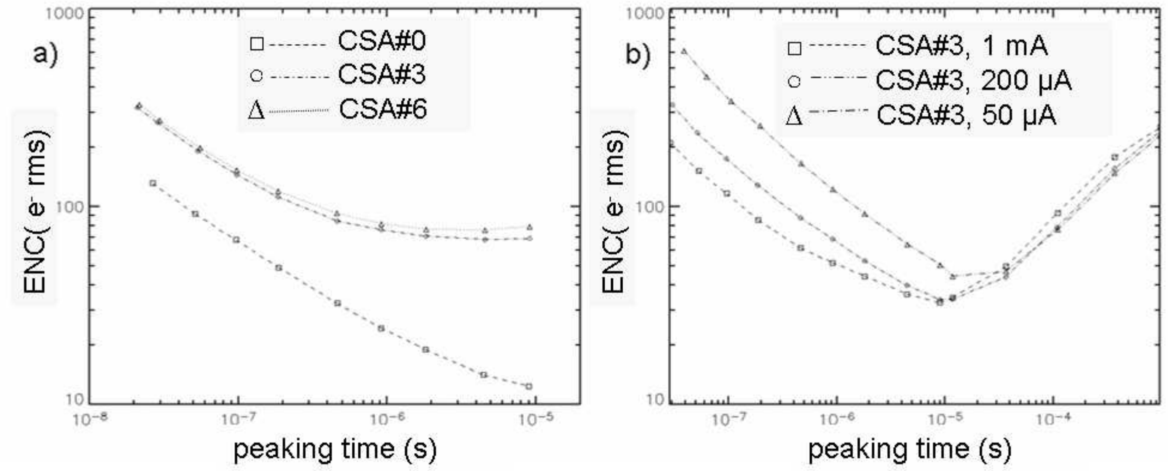

Figure 4.5: a) ENC as a function of peaking time for 3 different CSAs. b) The same measurement but with different input transistor currents corresponding to different power consumption.

Power consumption CSA #3 shows the best results and is used to study the influence of power consumption on the noise. In the above measurements the CSAs were polarised at 1 mA/3.3 V and consumed 3.3 mW. Application in space experiments requires power consumption as low as possible. It is therefore important to study the influence of the applied voltage and/or current on the noise. Since nearly all of the current runs through the input transistor we can use its current as a measure for the power consumption. In future versions of IDeF-X this will not be true since extra filter stages will consume a large part of the power.

An ENC measurement as a function of the peaking time is performed for three different transistor currents I_0: 1 mA (3.3 mW), 200 μA (660 μW) and 50 μA (165 μW). The results are shown in Fig. 4.5b. If I_0 is reduced the series noise increases. Eq. 4.9 predicted this behaviour already.

Low power consumption in combination with low noise is possible at higher peaking times. Since the latter leads to higher parallel noise, low detector leakage currents in the order of pico-amperes are required. Knowledge of these currents in different prototype detectors is therefore very important. In Sect. 4.5 I will show that moderately cooled ($\sim 0^o$C) CdTe single pixel Schottky detectors and individual pixels of pixelated CdZnTe detectors have sufficiently low currents.

AMS 0.35 μm PMOS technology has proven to be well adapted to low noise and low power consumption. Also, irradiation tests with a 589 GBq ^{60}Co source during 224 hours at a 1 krad/h dose rate, show that this technology is tolerant to gamma-rays. The technology will be used for further implementation in the next generation IDeF-X chips which I will introduce now.

(A detailed description of the above measurements and results is given by Limousin et al. (2005).)

4.3.2 IDeF-X V1.0

The IDeF-X V1.0 ASIC is a complete 16 channels analogue front-end. Each channel is fully independent. The design is optimised for X-ray detectors having a low capacitance (2 to 5 pF) and low dark currents (1 pA to 1 nA). Each channel includes a CSA, a pole zero cancellation stage (PZC), two second order Sallen & Key (SK) type filters, and an output buffer (see Fig. 4.6).

Like in version 0, the detector leakage current serves to empty the feedback capacitor. More precisely, the current runs through the feedback transistor and is a continuous reset of the capacitor. If a charge is collected on the latter, the voltage over the transistor changes and more current can run through it. The larger the signal from the detector, the larger the current through the transistor and the quicker it is emptied.

Instead of using a detector, an artificial current can be injected at the current input i_l. The test input is used to inject a calibrated charge through a capacitor C_{inj}. The PZC stage avoids long duration undershoots at the output. Undershoot exists because the output pulse of the CSA is not a pure step function but decays slowly. The shaping times of the S&K filter can be chosen manually. Table 4.1 shows the main characteristic of the chip.

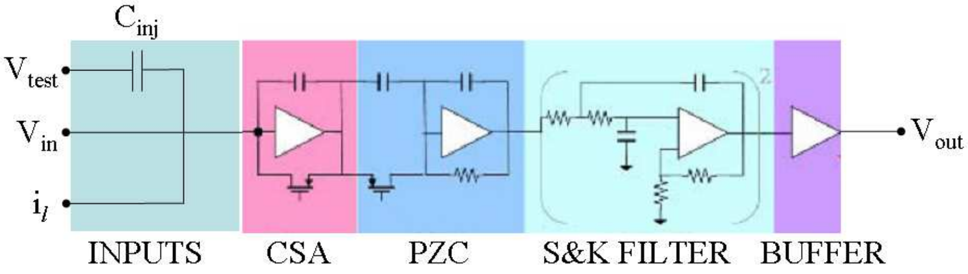

Figure 4.6: The IDeF-X V.1.0 ASIC has 16 independent spectroscopy channels. A single channel as shown above has a signal- and test-input (V_{in} and V_{test}). The current input i_l is used to inject a simulated detector leakage current. The injected charge is converted into voltage by the CSA. The output of the CSA is injected into two Sallen & Key type filters via a pole zero cancellation stage. The final stage is an output buffer.

Parameter	Value
Chip size	$2355 \times 4040\ \mu m^2$
Number of channels	16
Power supply	3.3 V
Power dissipated	2.26 mW/channel
Gain	200 mV/fC at 6 μs
Dynamic range	-40000 to 40000 e^- (0 to 176 keV for CdTe)
Peaking times [μs]	0.5 / 0.9 / 1.5 / 2.4 / 3 / 4 / 4.5 / 6

Table 4.1: IDeF-X V.1.0 main characteristics.

ENC measurements ENC measurements are also performed on the IDeF-X V1.0 ASIC (Gevin et al. 2005). The setup of Fig. 4.7a is used. The ASIC is mounted on a glass-Teflon chip carrier to reduce excessive noise from capacitive load and dielectric losses. One of the sixteen channels (# 8) of the ASIC is studied in this experiment and serves as representative for all other channels which are identical. The output signals are sent to an external ADC and acquisition station.

Fig. 4.7b shows the measured ENC as a function of peaking time (τ_p) in three different configurations: a) the input not connected, b) the input connected to the detector board (Teflon) with the possibility to connect a capacitor and c) the input connected to a single pixel CdTe Schottky detector of $4.1 \times 4.1 \times 0.5$ mm^3, biased at 330 V, 22^{o}C . The latter has one side covered with a platinum pixel of 2.0×2.0 mm^2 surrounded by a guard ring of 1 mm large. The electrode at the other side is an indium planar contact, which forms a Schottky barrier with the CdTe.

The ENC can directly be translated to an energy resolution (FWHM) in electron-volts, using the following relation:

$$FWHM = 2.35 \times \omega_{CdTe} \times ENC \tag{4.17}$$

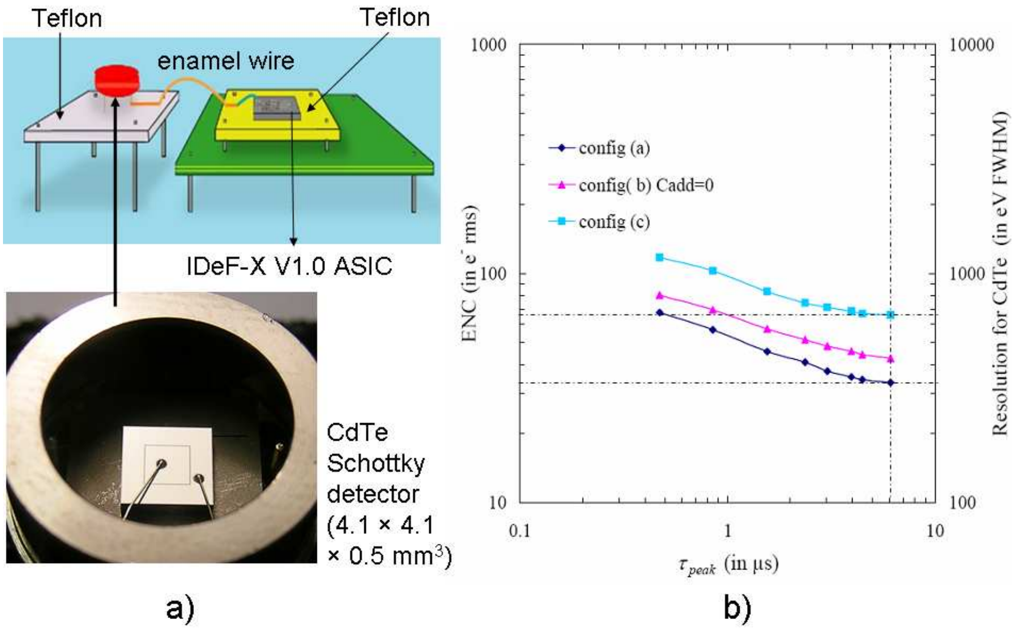

Figure 4.7: a) The IDeF-X V.1.0 ASIC is mounted on a Teflon board and can be connected to a single pixel CdTe Schottky detector. b) ENC and resolution (FWHM) in eV as a function of the peaking time for three different configurations.

With ω_{CdTe} the pair creation energy of CdTe and ENC the equivalent noise charge. This is shown on the right axis of the same figure.
Configuration a) has a minimum ENC of ~35 e$^-$ at 6 μs peaking time, which is consequent with the results obtained with the IDeF-X V.0 ASIC (which was 32.3 e$^-$). This is the floor noise only. Connecting the input to the detector board leads to a total of 42 e$^-$. When the ASIC is connected to the CdTe detector, 66 e$^-$ are measured. This extra noise is generated by the detector (due to its capacitance of ~0.7 pF and leakage current) and its housing (~2 pF) at 22^{o}C .
The ENC has been measured as a function of the input capacitance and current, at optimum peaking time. Fig. 4.8 shows the results in the case of an added input capacitance, C$_{add}$, of 0 and 2.4 pF (i.e. C$_{tot}$ ~ 3.1 and 5.5 pF, resp.). The input current has been calibrated using the signal fall-time of the output signal of the CSA which is inversely proportional to the current through the reset transistor.
The two curves are fitted with the following function:

$$ENC^2 = 2\sqrt{\alpha_d \cdot \alpha_{//} \cdot C_{tot}^2 \cdot i_l} + \alpha_{1/f} \cdot C_{tot}^2 \tag{4.18}$$

With α_d, a parameter which depends on the filter order and the transconductance of the input transistor of the CSA. $\alpha_{//}$ depends only on the filter order. $\alpha_{1/f}$ depends also on the filter order as well as on the area of the input transistor. Details of the above fit can be found in Gevin et al. (2005).
For leakage currents below ~10 pA, the minimal ENC is nearly constant while at higher

values the parallel noise starts to become important. This leads to an increase of the minimal ENC (ENC$_{min}$). For low values of i_l (< 10 pA) the ENC$_{min}$ is reached at the highest peaking times. In this case the 1/f noise is dominant. Higher currents increase the parallel noise and shorter peaking times have to be chosen to reach ENC$_{min}$. The two curves of Fig. 4.8 are very important and extremely useful. I will use them several times in the next chapter.

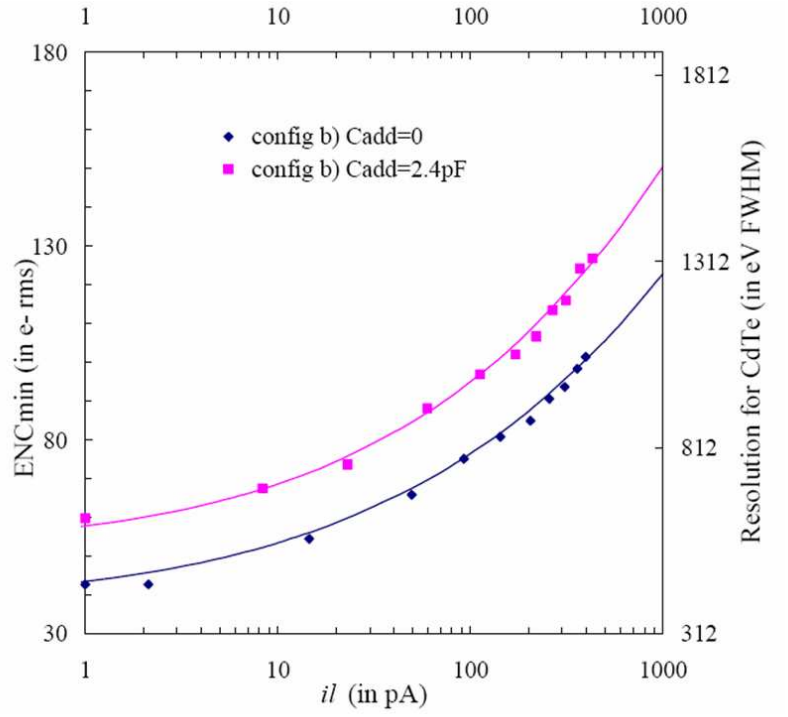

Figure 4.8: The ENC as a function of the input current i_l in the case of a 0 and 2.4 pF additional input capacitance.

4.3.3 IDeF-X V1.1

The third member of the IDeF-X family, version 1.1, has recently been developed and is actually in its test phase. It is identical to version 1.0 except that several extra components are added such as a discriminator per channel, a peak detection system, analogue memory and a multiplexed analogue output. Multiple tests are now in progress. Another important part of development of the electronics is its combination with the Cd(Zn)Te detectors. This hybrid, called Caliste, is presented in the following section.

4.4 Hybridisation

In the description of Simbol–X (Fig. 2.2f) I showed that the high energy detector will be built from 8 identical modules of 2 × 4 individual X-ray cameras. In the final version the

X-ray cameras will be a hybridisation of the IDeF-X ASIC and (probably) a 256 pixels Cd(Zn)Te detector. The design and construction of this module is done in cooperation with an industrial partner, 3D Plus[2]. The company has developed an outstanding technology in 3D electronics packaging which has been space qualified by the ESA and CNES. The application in space demands that the module is compact, light-weight and space proof. The first prototype is a combination of a 64 pixels CdTe detector connected to four IDeF-X ASICs in a compact module of $\sim 10 \times 10 \times 20$ mm^3. Fig. 4.9 shows a schematic view of the hybridisation. The ASICs are juxtaposed in a special resin. Each chip has sixteen channels that are connected to the pixels by means of a highly conducting glue. The pins on the other side serve to control the electronics and to recover the output signals. By multiplexing the signals less output pins are necessary than the number of pixels. The prototype is baptised Caliste and has recently been delivered by the company. Fig. 4.10 shows a picture of the module. Next to it, is a scan which clearly reveals the four ASICs inside the resin that fills the volume of the Caliste module. Sixty-four of these extremely compact and valuable objects will fly on the Simbol–X mission in 2013.

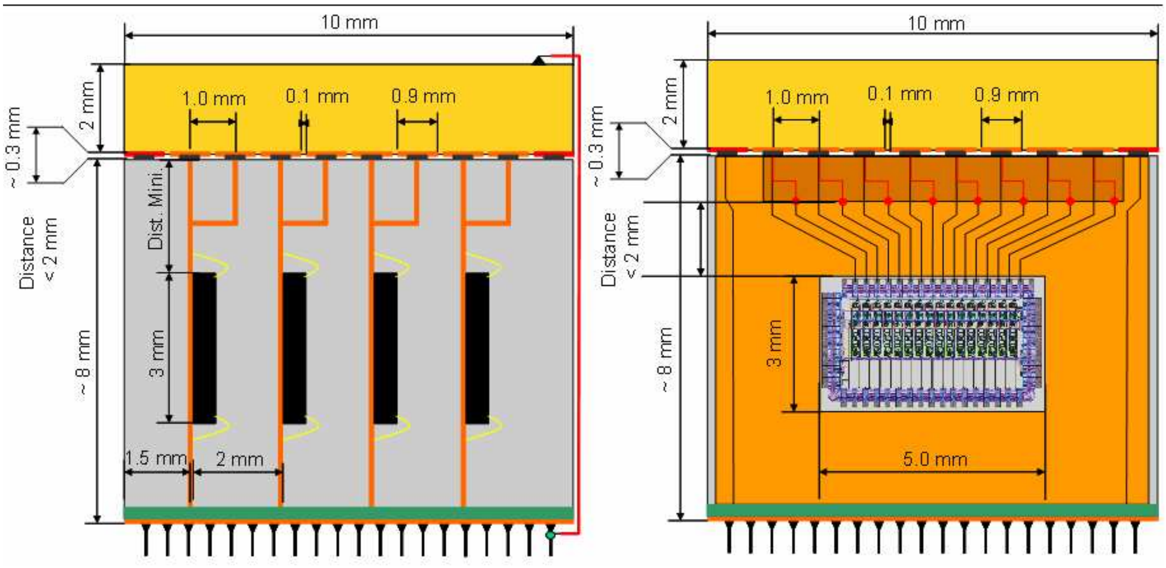

Figure 4.9: Schematic view of the Caliste prototype. Four IDeF-X ASICs each having 16 channels are mounted in a special resin and connected to a 64 pixels Cd(Zn)Te detector.

---

[2] See http://www.3d-plus.com

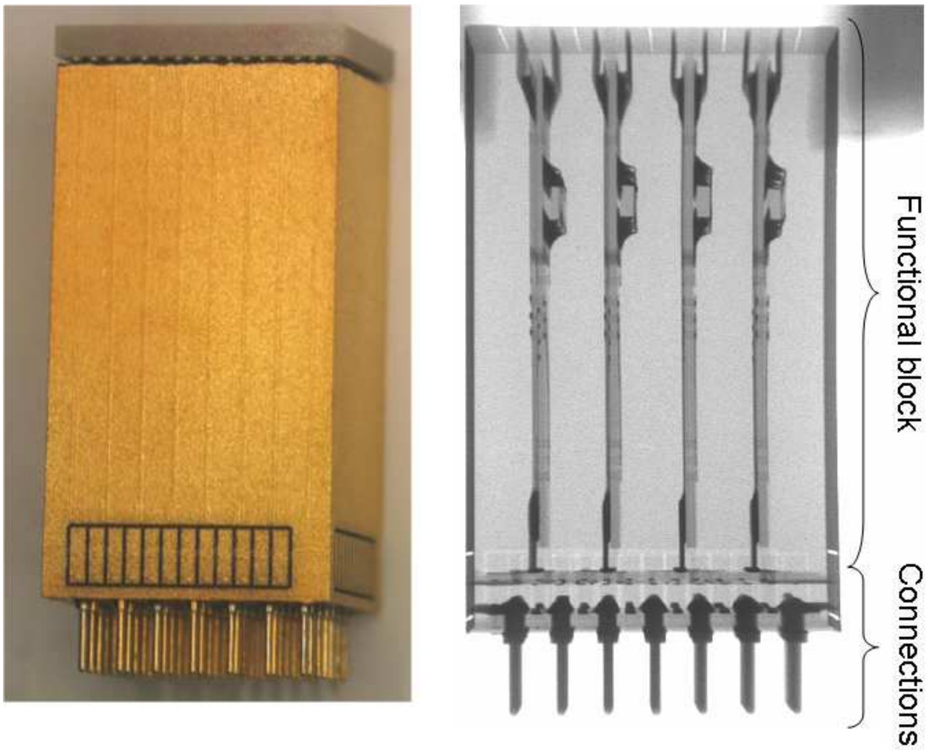

Figure 4.10: The first prototype of the Caliste module. The light-weight module is extremely compact: $10 \times 10 \times 20$ mm^3. Right: a scan of the interior. This prototype only has resistors inside it to test the different connections.

4.5 Leakage current measurements

From the previous sections it has become clear that the leakage current is a crucial parameter of the performance of the electronics and the detector. It is therefore very important to know its value in single pixel CdTe Schottky detectors or in individual pixels of multi-pixel Cd(Zn)Te detectors, that are DC connected to the ASIC.
With the use of Fig. 4.8 a prediction can be made of the spectroscopic performances of the pixel in question. Also, the relation between current and temperature can be used to obtain the impurity concentration inside the crystals, which is important to study crystal homogeneity. The current measurement is also a mechanical tool to study the quality of the pixel-substrate contact.

4.5.1 Initial leakage current measurements

Instead of directly starting to measure the current per pixel in multi-pixel detectors, I first study the current in single pixel CdTe detectors. For these preliminary measurements, I choose samples with a leakage current and capacitance comparable with those of a single pixel of a multi-pixel detector. Because of their simplicity, they are perfectly suited to test individual channels of the IDeF-X ASIC. I use the electronics diagram shown in Fig. 4.11 to measure the current.

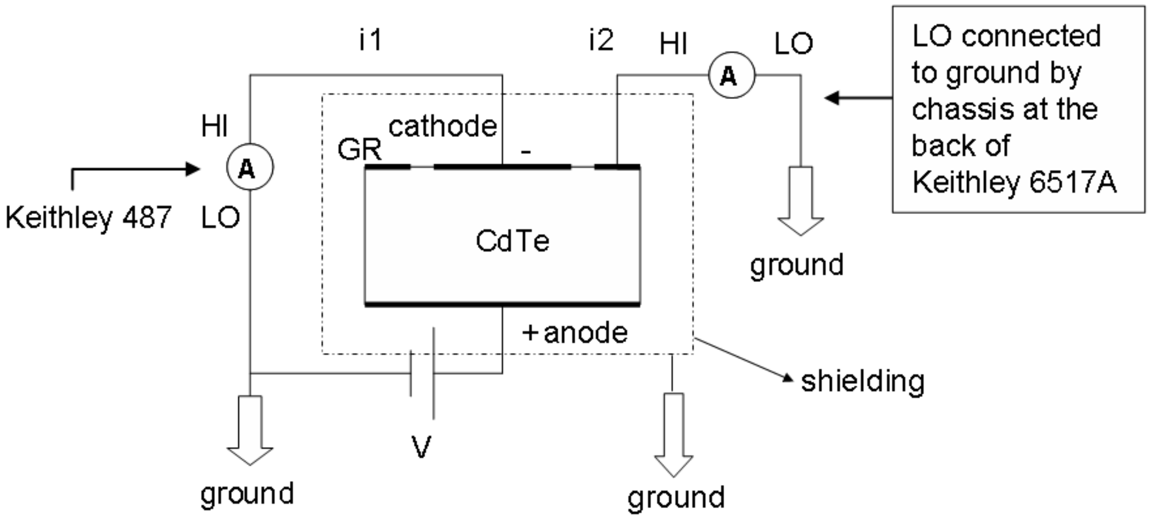

Figure 4.11: Single pixel leakage current measurement setup.

For the measurement two Keithley ampere-meters are used: one for the pixel, and the second for the guard ring (GR) current. Special care is taken to shield the setup, by placing it into a metal box. Fig. 4.12 shows the results which are obtained with three CdTe Schottky detectors, having an indium electrode on the anode side and a platinum pixel and GR on the cathode side (noted as In//CdTe//Pt). The currents vary from a few pico-amperes at 50 V bias for the $4.1\times4.1\times0.5$ mm^3 detectors up to several nano-amperes

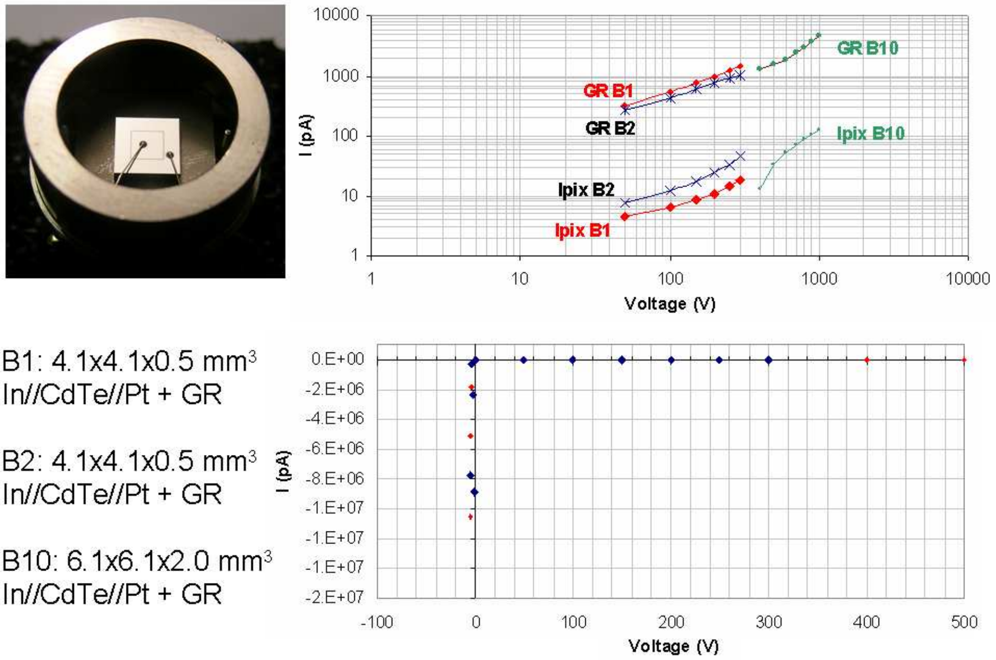

Figure 4.12: Leakage currents in three different single pixel CdTe detectors (ACRORAD) at room temperature (20^{o}C). The crystals are mounted into an aluminium housing. Pixel currents are noted as Ipix and the guard ring current as GR. Applying negative voltages puts the detector in forward bias leading to high leakage currents (see plot below).

at 1000 V for the 2 mm thick detectors. In the latter case the pixel is 4.0×4.0 mm^2 in size.

In order to obtain the resistivity of the CdTe material, I use an ohmic CdTe crystal covered with platinum electrodes at both sides (noted as Pt//CdTe//Pt). The pixel has a surface of $4.0 \times 4.0 = 16$ mm^2 and the guard ring is 1 mm large, with a total surface of 20 mm^2. The current density as a function of the applied electric field is shown in Fig. 4.13. The data points are fitted with a straight line. The quality of the fit is expressed with parameter R. If R is one, the fit is perfect, while for R equal to zero, a fit is not possible. Both lines show a good fit quality, meaning that Ohm's Law ($\vec{J} = \vec{E}/\rho$, with $\vec{J}$ the current density in A/mm^2, $\vec{E}$ the electric field in V/m and ρ the resistivity in Ω.m) is valid.
The pixel resistivity is equal to $1.80(\pm0.02) \times 10^9$ Ω.m and $1.58(\pm0.02) \times 10^9$ Ω.m for the guard ring. The values are in agreement with those given by O. Limousin, as shown in Table 3.1.
Since the pixel and GR are both part of the crystal, their currents must in principle lead to the same resistivity ρ. This is not the case and can be explained by the fact that besides the current passing through the detector, the GR also absorbs the surface currents running on the sides.
To have an idea of the value of the surface resistivity, I make the following calculation: the pixel current at 180 V is ~81 nA per 16 mm^2. Without surface currents, I should

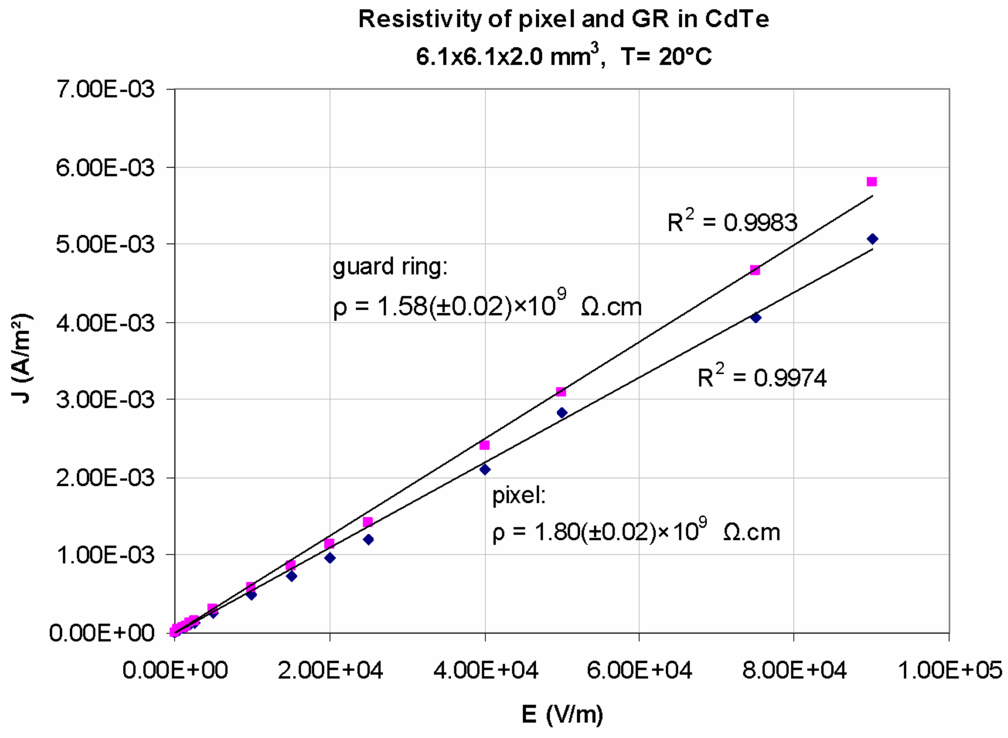

Figure 4.13: The leakage current in an ohmic single pixel CdTe detector ($6.1 \times 6.1 \times 2.0$ mm^3) with a pixel of 4.0×4.0 mm^2 and a guard ring of 1 mm large.

measure a GR-current of $81/16 \times 20 \approx 101$ nA. The measured current is 116 nA. Thus, at 180 V, the surface current is equal to $\sim$15 nA. By plotting the applied voltage as a function of the surface current and fitting it with a straight line, the slope gives the surface resistance. I measure a value of $1.24(\pm0.02) \times 10^{10}$ Ω for a total surface of 48.8 mm^2.

The above results show the importance of the GR. If not present, this current will be absorbed by the pixel or pixels. This leads to an increase of the parallel noise and a degradation of detector spectroscopic performance.

Theoretically, the GR can be very small in order to absorb the surface current. But, Tanaka et al. (2004) report that the leakage current in the single pixel of a $2 \times 2 \times 0.5$ mm^3 CdTe detector starts to increase if the width of the GR becomes smaller than 500 μm . This probably means that the material causing the lower resistivity on the surface, is partly migrated into the bulk. Since the prototypes I use all have the same GR size, I am not able to verify the above statement.

Next, the total current of all pixels of several 64 pixels CdZnTe detectors is measured. Therefore I use nearly the same electronic circuit as before (see Fig. 4.11) except that the single pixel is replaced by 64 pixels that are all connected to one output. The pixels are read-out at the same time and the current is summed. The results of two different CdZnTe detectors are shown in Fig. 4.14. At a typical bias voltage of 250 V and a temperature

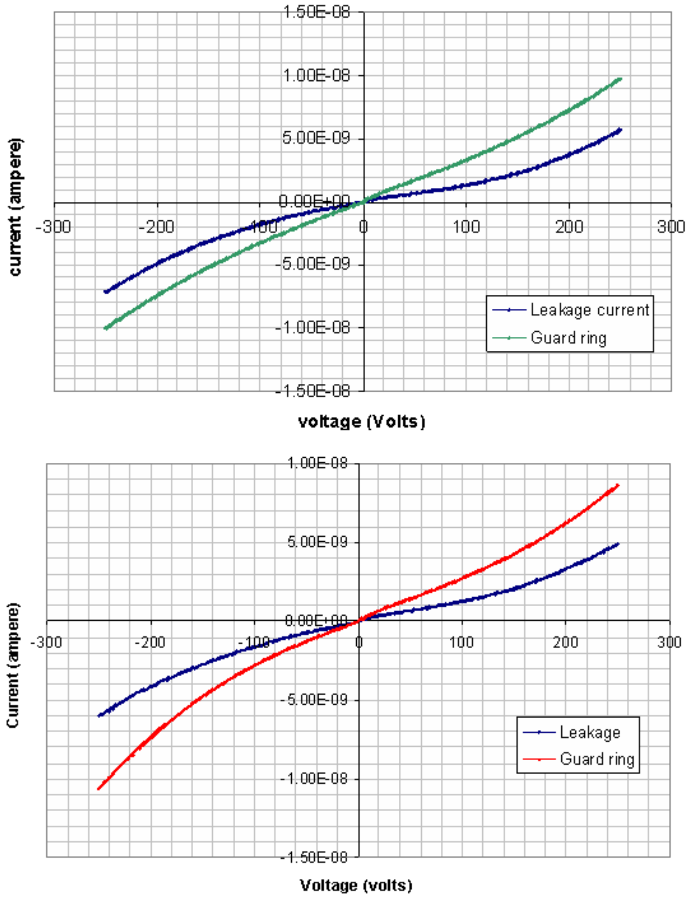

Figure 4.14: The total current of 64 pixels of two different CdZnTe detectors of 2mm thick as a function of voltage.

of ∼23^{o}C , the mean current per pixel is: ∼ 6.0 nA /64 ≈ 94 pA/pixel for the first and 5.0/64 nA / ≈ 80 pA/pixel for the second detector. The GR current is ∼10 nA and ∼9 nA, respectively.

The above results serve as a guide to construct the measurement setup for individual pixel leakage currents which I will explain now.

4.5.2 Pixel leakage current measurement setup

From the above measurements it has become clear that a leakage current of several tens of pico-amperes per pixel can be expected. In order to accurately measure these low values, a special electronic circuit is required, with an extremely low intrinsic noise and internal leakage current. Also, individual pixels need to be read out separately while the others stay correctly biased.

A dedicated circuit is designed and constructed based on the scheme of Fig. 4.15. The currents in the pixel and GR are measured with two Keithley 6517A ampere-meters. In order to make the measurement completely automatic, a PC controlled PC-DIO card is used, connected to several shift registers in series. Each register output is connected to a relay via an inverter/buffer. The latter inverses and reenforces the current which is necessary to activate the relays.

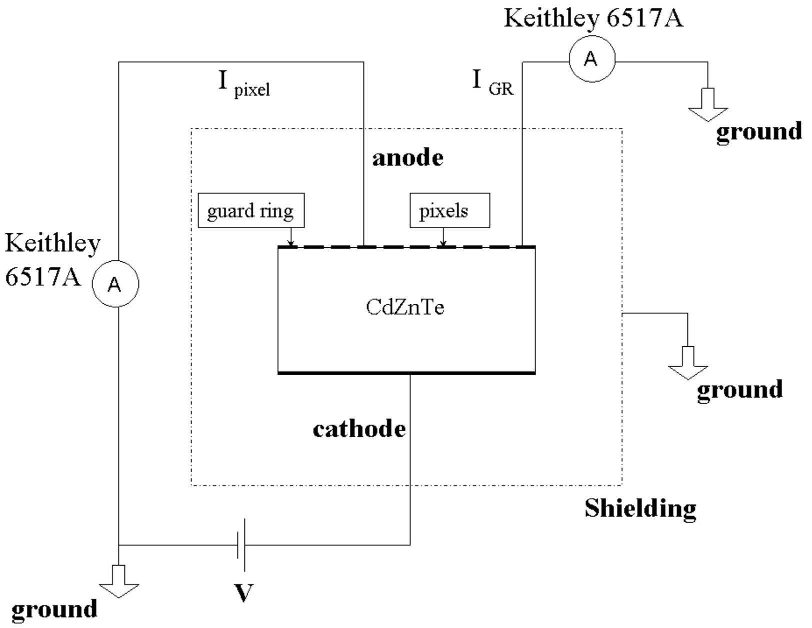

Figure 4.15: The measurement setup for individual pixel leakage current measurements.

If a relay is activated, the pixel is connected to ground *via* the Keithley. If not active, the pixel is *directly* connected to ground. If one relay is activated, only the current in the pixel connected is measured, while the others stay correctly biased. The GR is connected to ground via a second Keithley. The bias voltage is applied at the cathode side. The entire setup is properly shielded by placing it in a heavy, thermally controlled test chamber (see Fig. 4.16).

To measure the temperature, different thermometers are placed in the chamber with one directly put on the substrate on which the crystal is mounted. The exact crystal temperature can only be approximated. However, by taking a sufficiently long relaxation time (several hours), I assume that the crystal eventually reaches the same temperature as that of the substrate.

Depending on external weather conditions (our lab is not 100% isolated) and the refrigerator used, a minimum temperature of -40°C can be reached. Since the crystal performances degrade at high temperatures, the upper limit is set to ~20°C .

I constructed four identical circuits each having 17 (16 pixels + 1 GR) relays mounted on highly isolating print-board material, RO4003. It has a bulk resistivity of $1.7 \cdot 10^{10}$ MΩ·cm, a surface resistivity of $4.2 \cdot 10^9$ MΩ and a dielectric constant of $\epsilon_r = 3.38$.

Test measurements, without any detector connected, show a nearly zero internal leakage current with a standard deviation of ~ 50 fA (at 20°C). This makes it possible to perform accurate measurements of pixelated Cd(Zn)Te detectors, even at low temperatures when

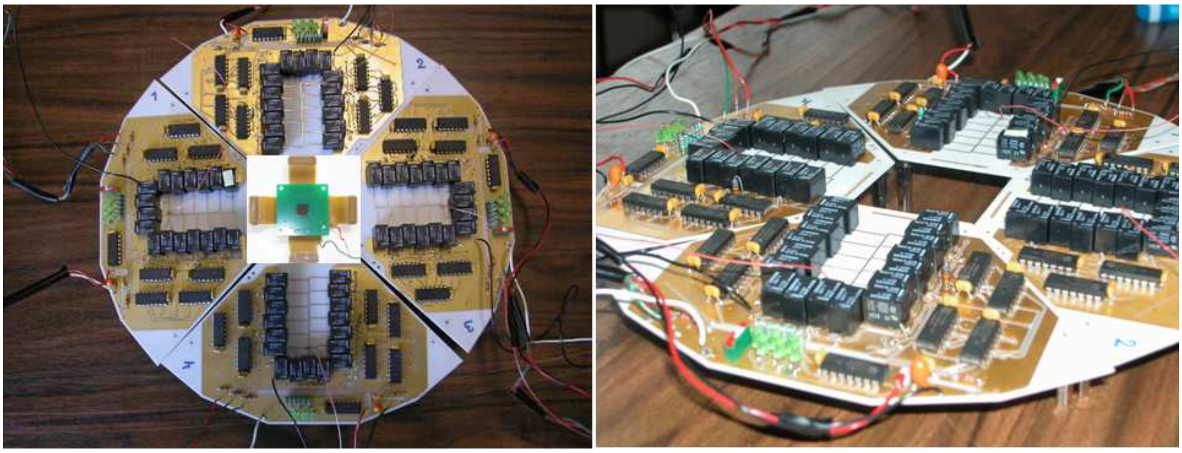

Figure 4.16: Four identical highly isolating circuits each equipped with 17 relays to measure the leakage current in individual pixels of a 64 pixel Cd(Zn)Te detector as shown in the left plot.

the currents are expected to become extremely small (see also Dirks et al. (2006)).

4.5.3 Current maps

After applying the bias voltage, the system is allowed to stabilise. Then, a pixel is connected to the Keithley and up to 200 current measurements are taken within ∼15 seconds. The mean value and its standard deviation are measured. Current maps of several prototype Cd(Zn)Te detectors as function of bias voltage, temperature and time, are obtained. The mean current per pixel ranges from less than 100 fA at -12^{o}C , -250 V, up to 100 pA, 20^{o}C , -500 V with standard deviations varying from less than 10 fA at the lowest temperatures and voltages, up to several pico-amperes.

Fig. 4.17 shows two current maps of a 64 pixels CdZnTe detector ($9.9 \times 9.9 \times 2$ mm^3) at $-1.32(\pm0.06)^o$C and $16.79(\pm0.05)^o$C [3] when biased at -450 V and -250 V, respectively. Every square corresponds to a pixel and the value of the current is expressed in its corresponding color. We observe directly that the current is not uniform and that some pixels show nearly no current (black, < 1 pA), while others have a relative high value (white, 20/ 40 pA at -1.3/ 16.8^{o}C) in comparison with the mean value (12.0(±0.4)/ 18.4(±0.3) pA at -1.3/ 16.8^{o}C). The pixels which have no or nearly no current show a spectrum with a significantly lower gain than the others (see spectra below current maps) which can be explained by a capacitive instead of an ohmic coupling between pixel and substrate.
The temperature also influences the connection. For instance, at -1.3^{o}C pixel (3, 6) shows no problems while at 16.8^{o}C it is not connected anymore. The same effect is also seen as a function of time. Pixels re- or disconnect from the substrate as time passes. The current

---

[3] Errors on the temperature measurement are taken to be equal to the variation within one current measurement cycle of 64 pixels.

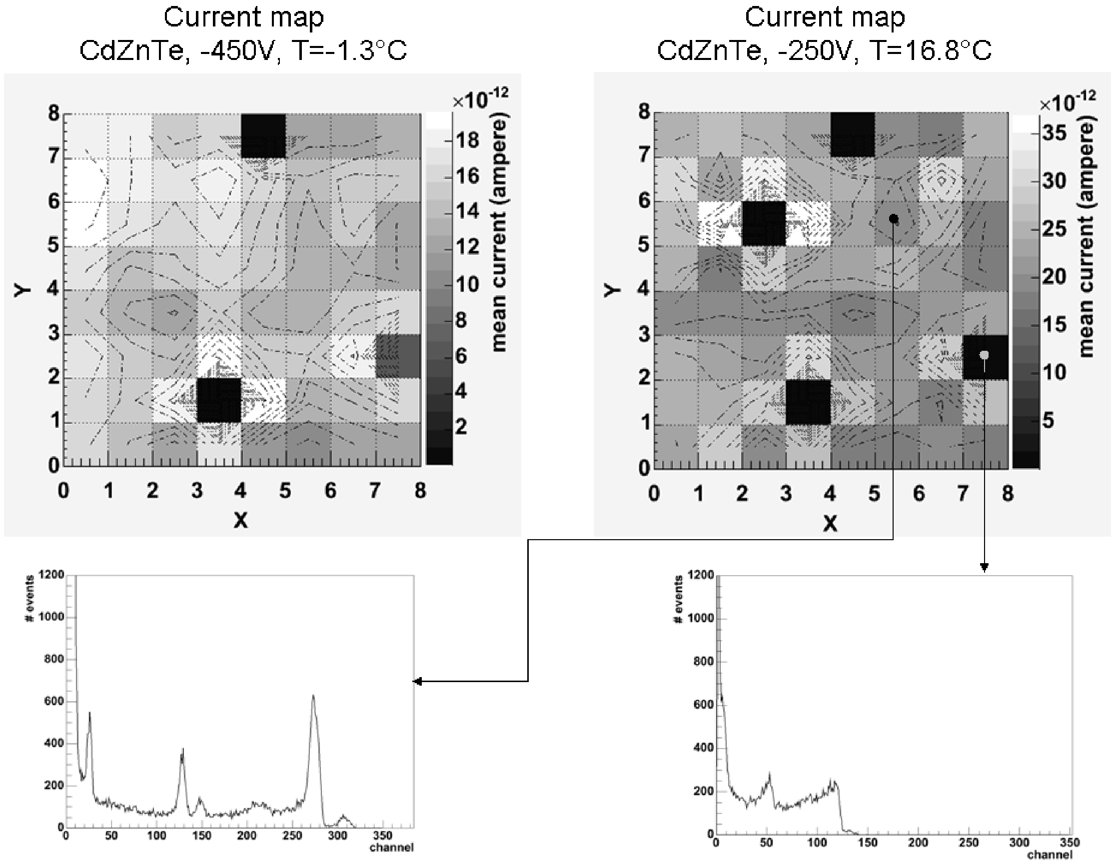

Figure 4.17: Current maps of a 64 pixels CdZnTe detector. Below on the left, the ^{57}Co spectrum of a properly connected pixel having a correct gain. The spectrum on the right is from a pixel which is probably not connected. Though, due to a capacitive coupling it still shows a spectrum but with a lower gain.

which normally would pass via the non-connected pixel is now absorbed by its neighbours which show a significantly higher current.

The current in the GR is 2.08(±0.02) nA at -1.3^{o}C (450 V) and 4.42(±0.01) nA at 16.8^{o}C (250 V). To obtain the surface current I perform the same calculation as with the single pixel Pt//CdTe//Pt detector.

At -1.3^{o}C , the mean current per pixel is 12.0 pA/mm^2. The surface of the GR is $9.9^2 - 64 = 34.01$ mm^2. Without surface currents the GR should measure $12.0 \times 34.01 \approx 408$ pA. The surface current is then $2.08 - 0.41 \approx 1.67$ nA. If the GR would be absent (and the detector would have 10×10 pixels) this current would be absorbed by the 36 pixels at the border, adding 1.67/36=0.05 nA to the 12.0 pA already present. At 16.8^{o}C the surface current is 3.79 nA, adding ~0.11 nA per pixel. This would result in a significant degradation of the pixel's spectroscopic performances.

The above calculation shows again the importance of a guard ring. But besides its capacity to absorb unwanted surface currents, it has a drawback. In combination with the inter-pixel spacing, it increases the insensitive zone of the detector. The charge carriers created by photons interacting above the GR, will not or not completely be collected on a pixel.

In the case of Simbol–X, sensitivity is most important and a compromise must be made between the amount of dead zone and the absorption of surface leakage currents. A solution could be to improve the crystal's surface passivation. This results in a higher surface resistivity and less current, making the GR less important.

The pixel current is also studied as a function of the temperature. Fig. 4.18 shows the current maps at six different temperatures of a 6 mm thick CdZnTe detector. The current increases as the temperature is raised because the material gains energy to promote charge carriers into the conduction band. A detailed description of the relation between temperature and activation energy is given in the next section Sect. 4.5.4. Current maps like those of Fig. 4.18 then become very important.

For the moment I will restrict the analysis of the above figure only to observations. First, pixels that are completely black have currents equal or higher than the maximum value given by the palette on the right. I limit the range in order to see inhomogeneities in pixels having less current.

The white colored pixels have no of nearly no current. It happens regularly (in nearly every detector I tested) that pixels show a mechanically non-stable behaviour. That is, at different temperature, voltage or time, they may de-connected from the substrate.

The explanation may be found in the substances used for the connection between pixels and substrate. eV-Products uses an anisotropic[4], conductive film to connect the pixels to the FR4 epoxy substrate. Thermal differences cause dilatation of the epoxy and CdZnTe and stresses the contact which eventually may break. Also the poor adherence between the different materials may cause a de-connection.

This kind of conductive film is not tolerated in space applications. Special care has to be taken for the interface of crystal and substrate to be space proof.

4.5.4 Impurity distribution diagnostics

The current density inside a semiconductor was introduced in Chapt. 3.1.2 by Eq. 3.12:

$$\vec{J} = \sigma \vec{E} = |e|(n\mu_n + p\mu_p)\vec{E}$$

It shows that the leakage current I_0 is, beside the applied voltage, proportional to the number of free charge carriers, n and p, as defined by Eq. 3.4 and 3.5. Consequently, it is a function of the impurity mean energy (E_a) and the temperature (T):

$$ln(I_0) \propto \frac{-(E_c - E_a)}{k.T} \propto \frac{-\delta E_A}{k.T} \tag{4.19}$$

With δE_A the mean activation energy of an n-type material, defined as the difference between the conduction band (E_c) and the impurity mean energy.

---

[4] This glue does not conduct the same in every direction.

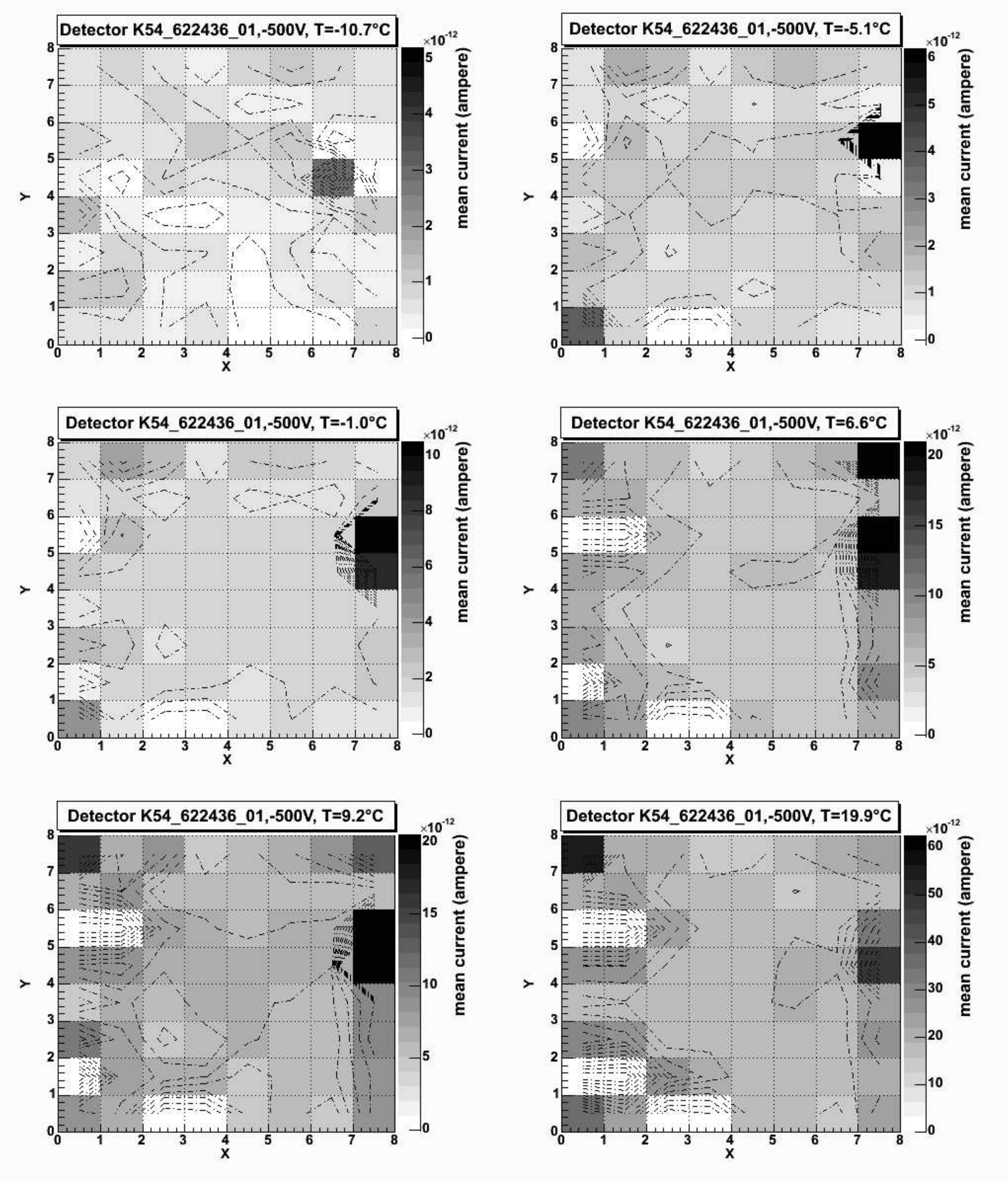

Figure 4.18: Current maps of a CdZnTe detector as a function of temperature. White squares correspond to pixels with no or nearly no current. Black squares represent pixels with high currents, up to 60 pA/pix at 500 V bias and a temperature of 19.9^{o}C .

By measuring the current of pixel and GR as a function of the temperature, the above formula allows calculating the mean activation energy of the defects and impurities present in the CdZnTe bulk material and on its surface. If ln(I) is plotted as a function of 1/T, the slope of a fitted straight line gives the mean activation energy of the material.

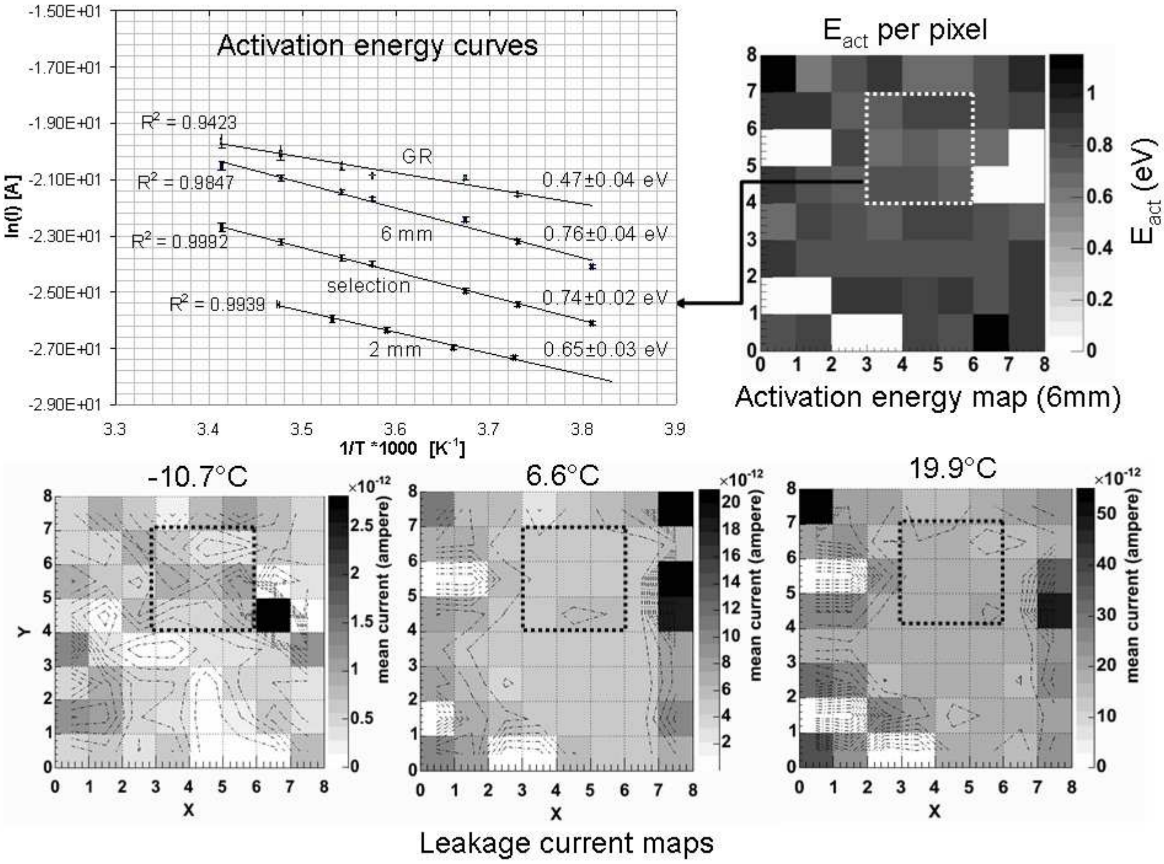

Figure 4.19: Above left shows the natural logarithm of the mean leakage current as a function of the inverse temperature for a 2 and 6 mm thick detector, the GR and a selection of the latter. Below are three current maps at different temperatures. Above on the right is an activation energy map of the 6 mm thick detector.

In Fig. 4.19 I show the activation energy curves for a 2 and 6 mm thick CdZnTe detector. It includes a measurement of the mean activation energy of both detectors by using the mean pixel leakage current, the surface activation energy by using the GR current (of the 6 mm thick detector) and of a selection of nine pixels which were stable at every temperature. These can be recognised by a black square surrounding them. Below, three current maps are plotted of the 6 mm thick detector at different temperatures. The data points are fitted by a straight line. The R^2 value gives the quality of the fit (1.0 is a perfect fit). By measuring the slope of the ln(I)–1/T curve for every pixel separately, an activation energy map is obtained as shown above on the right in the same figure. It is a representation of the impurity concentration inside the material and can be used to study crystal uniformity. The completely white squares in correspond to unsteady pixels and should be ignored.

For the 2 mm thick detector a mean activation energy of 0.65 ± 0.03 eV is obtained. The 6 mm thick detector has a mean value of 0.76 ± 0.04 eV, while the selection of nine pixels leads to an activation energy of 0.74 ± 0.02 eV. These values imply that the material is close to be quasi-intrinsic, in other words, to be almost perfectly compensated. For intrinsic CdZnTe the difference between the conduction band E_c and intrinsic Fermi level E_i is half of the band-gap, 1.57/2=0.79 eV. The activation energy of the impurities, δE_A lies just above this value as illustrated by the figure below (Fig. 4.20). The material is thus slightly n-type, which was expected.

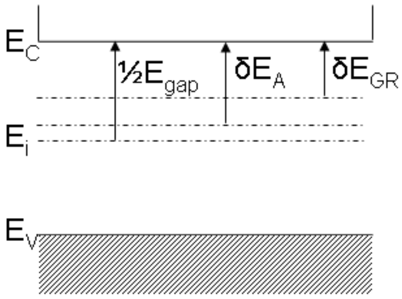

Figure 4.20: The band positions in an n-type material. E_i is the intrinsic Fermi level, lying exactly in the middle of the valence E_v and conduction band E_c. E_A is the mean activation energy of the impurities inside the crystal, while E_{GR} corresponds to the impurities on the surface of the detector.

The activation energies for the 2 and 6 mm detector are different. The crystals are probably not taken from the same ingot which may have resulted in a different crystal quality and/or compensation.

From the fact that the nine stable pixels show comparable results to the value obtained with all pixels together, I may conclude that the crystal is rather homogeneous.

The guard ring current depends mainly on the impurities on the surface of the semiconductor. The activation energy δE_{GR} of 0.47 ± 0.04 eV is therefore related to the surface mean activation energy. The activation of these impurities requires less energy and justifies again the use of a guard-ring surrounding the pixels.

Activation energy maps (like the one in Fig. 4.19) serve as a representation of the impurities inside a crystal and can be used to study the uniformity of our Cd(Zn)Te semiconductor detectors.

Beside that, the linear relation between ln(I) and 1/T serves as an additional tool to predict leakage currents at other temperatures. Also, the value of the activation energy may serve as an identification of the different prototypes.

4.5.5 Pixel energy resolution prediction

With the help of Fig. 4.8, leakage current maps can be used to predict the spectroscopic performances of the crystals. If I take the mean pixel leakage current of 12.0(±0.4) pA obtained with the 2 mm thick CdZnTe detector of Fig. 4.17 (at 0°C , 450 V bias), I can expect an electronic noise between 50 and 70 e^- . With a pair creation energy of 5 eV/pair for CdZnTe, the energy resolution due to electronics only is:

$$\begin{aligned} \mathrm{FWHM}_{elec} &= 2.35 \times 5 \times 50 = 0.59 \text{ keV at } 50 \text{ e}^- \\ &= 2.35 \times 5 \times 70 = 0.82 \text{ keV at } 70 \text{ e}^- \end{aligned} \tag{4.20}$$

In case of a photon energy of 59.54 keV and a Fano factor of 0.14, the energy resolution due to statistics is:

$$\mathrm{FWHM}_{stat} = 2.35 \times \sqrt{0.14 \times 59.54 \times 10^3/5} \times 5 = 0.48 \text{ keV} \tag{4.21}$$

Combining both contributions, the total predicted resolution FWHM_{tot} is found between ~0.8 and 1.0 keV. In the next section I will show that this is a reasonable prediction, but probably with an underestimation of the input capacitance (as used for single pixel CdTe detectors). The latter is because the CdZnTe pixelated crystals are mounted onto a substrate with rather poor dielectric properties. Also, the number and length of connections between pixels and the ASIC input creates extra parasitic capacitance which is not accounted for.

The new pixelated CdTe detectors are mounted on RO4003 material which has excellent dielectric properties, favoring low noise. In the next section I will show that the above prediction is more in line with the measured spectroscopic performances.

4.6 Spectroscopic measurements

The X-ray camera for Simbol–X will take images and spectra of astrophysical sources in the energy range of 0.5–80 keV. A good energy resolution of ∼120 eV (FWHM) at 6 keV and ∼1.3 keV (FWHM) at 68 keV is demanded. For the Cd(Zn)Te detector, especially the last condition is important, since low energy lines, up to 20 keV, are mainly resolved by the silicon active pixel sensors.

From the noise and leakage current measurements presented in the previous chapter, it has become clear that the prototype detectors have a leakage current sufficiently small to reach, or at least closely approach, the above requirements. In this section I show if spectroscopic measurements confirm this.

4.6.1 Single pixel CdTe detectors

In Sect. 4.3.2 I described the ENC measurements that were performed on the IDeF-X V1.0 ASIC. In configuration c) a single pixel CdTe Schottky detector of $4.1 \times 4.1 \times 0.5$ mm^3 was directly connected to the input #8 of the ASIC.

Besides measuring the ENC, I also performed spectroscopic measurements using the same set-up. The detector has an indium planar electrode and a platinum pixel and guard ring. In order to operate the diode in reverse mode, a positive bias voltage must be applied at the indium contact. In that case, holes drift to the pixel side while electrons move to the planar electrode. The voltage is set to 330 V, at a temperature of ∼22^{o}C . The detector is irradiated from the pixel side with an ^{241}Am source. Since most of the interactions take place in the first layer, the induced signals mainly come from the quick electrons. They traverse the entire detector within ∼10 ns, while holes need ∼100 ns. Therefore, if no polarisation is present, charge loss is negligible and ballistic deficit minimised. This leads to an excellent energy resolution of ∼1.0 keV FWHM at 59.54 keV and 735 eV FWHM at 13.9 keV, as shows the spectrum in Fig. 4.21.

Progress The last five years, our group booked major progress in the improvement of the spectroscopic performances of CdTe detectors. This is illustrated in Fig. 4.22, which shows the evolution of the spectroscopic quality of an ^{241}Am spectrum the last couple of years. The first spectrum is taken in 2001, with the ISGRI camera of INTEGRAL, and shows an energy resolution of 5.6 keV (FWHM) at 59.54 keV. The second is taken last year, in 2005, with a prototype detector of ECLAIRs (see Schanne et al. (2004)). It concerns a CdTe Schottky detector of $4 \times 4 \times 1$ mm^3, biased at 600 V, 24^{o}C , connected to IDeF-X V1.0. An energy resolution of 1.8 keV (FWHM) at 59.54 keV is obtained. The third spectrum is taken recently (2006) using a CdTe Schottky detector of $2 \times 2 \times 0.5$ mm^3, biased at 350 V, 24^{o}C . The resolution at 59.54 keV is 1.1 keV (FWHM) for the complete peak, and 0.9 keV if only the right side is fitted. For low energies, 0.73 keV at 13.9 keV is measured.

Note the large asymmetry of the high energy peak in the ISGRI spectrum, which is due to hole loss.

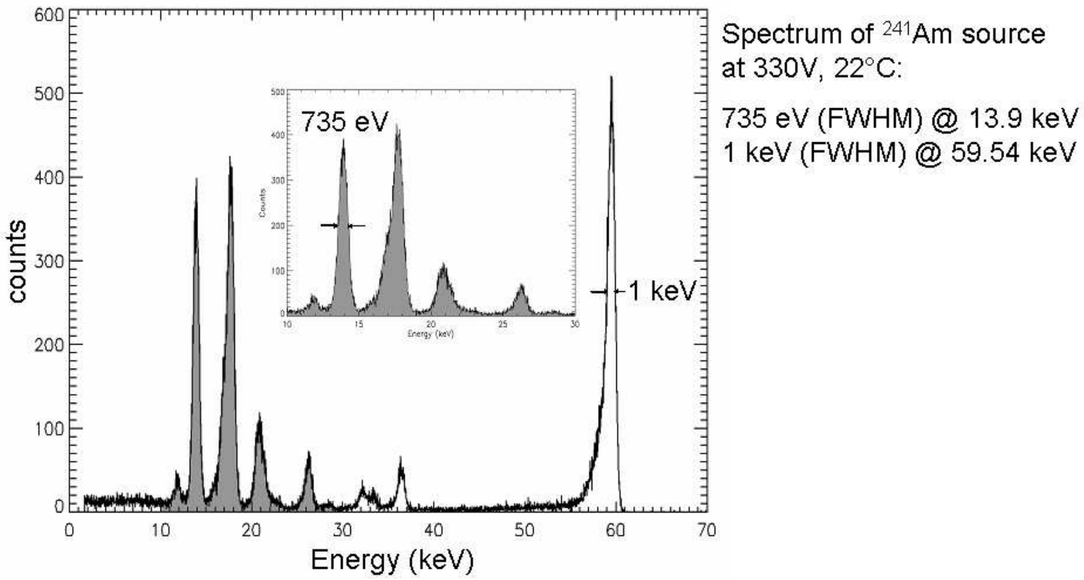

Figure 4.21: ^{241}Am spectrum obtained with a CdTe detector connected to the IDeF-X V1.0 ASIC. The peaking time is 6 μs and the detector leakage current ~15 pA.

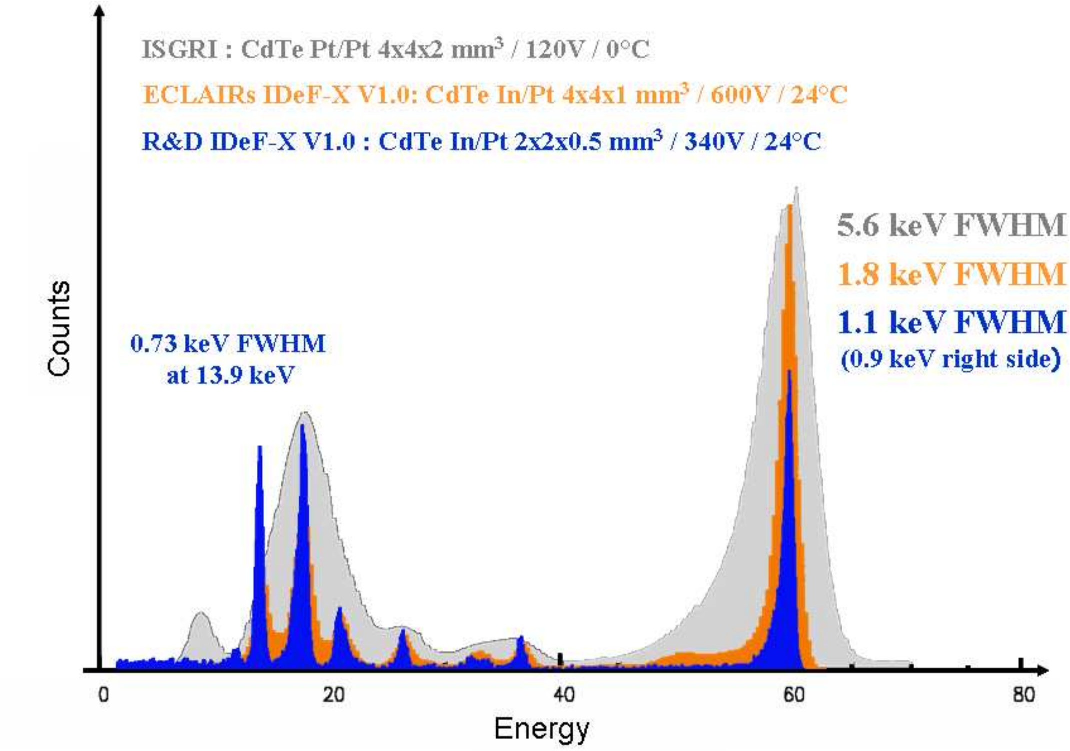

Figure 4.22: Evolution of the spectroscopic performances, from the ISGRI camera of INTEGRAL (2001) up to the R&D of IDeF-X in 2005 and 2006.

CdTe proves to be a worthy competitor of germanium at these energies. This is illustrated in Fig. 4.23, showing in the upper plot, the energy spectrum obtained with a CdTe Schottky detector and below a spectrum from a Ge detector. An energy resolution of 1.06 keV at 59.54 keV and 750 eV at 13.9 keV is obtained with CdTe and 1.14 keV and 1.1 keV, respectively, for germanium. The tail on the left side of the 59.54 keV peak in the CdTe spectrum is due to polarisation.
The values are taken from a Gaussian fit on the right side of the high energy peak. In this case, the polarisation effect is not considered in the spectral response evolution. I would like to emphasise the difference in operating conditions: 360 V at 22^{o}C for CdTe and 5000 V at 77 K for Ge.
The above results proof the excellent performances of CdTe Schottky crystals in combination with the IDeF-X electronics. The required energy resolution for Simbol–X is easily fulfilled (for this specific detector).

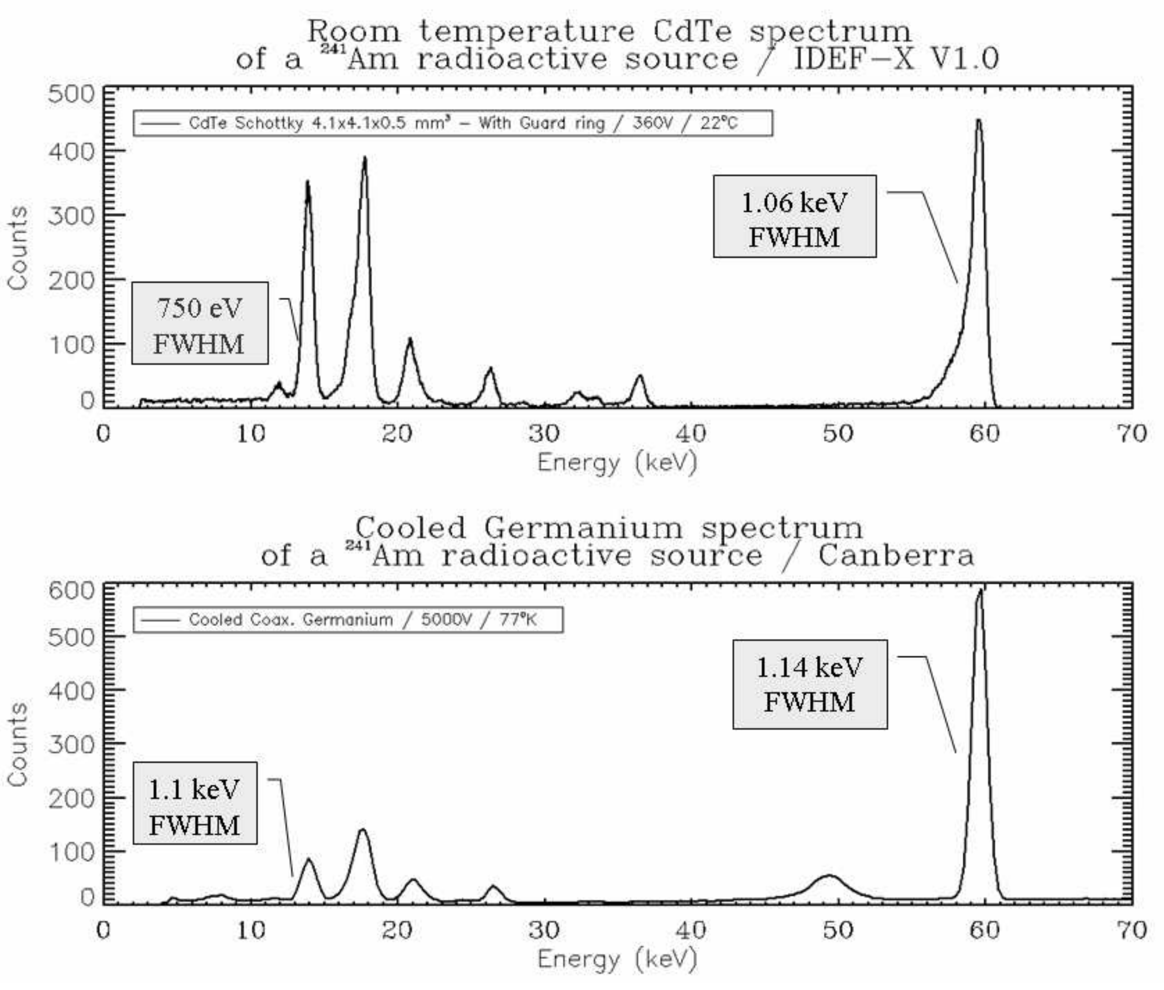

Figure 4.23: Comparison between the spectra of a single pixel CdTe Schottky and a standard Ge detector. CdTe operates at 360 V and 22^{o}C while Ge requires a temperature of 77 K and 5000 V bias voltage.

Comparison between measurement and prediction With the results of the leakage current measurements presented in the previous chapter, and charge carrier creation statistics, I can compare the predicted values with the spectroscopic measurements.

The leakage current in the CdTe detector was measured to be ∼15 pA at 330 V, and its capacitance ∼0.7 pF. The corresponding electronic noise is then ∼66 e^- ENC or $2.35 \times 4.42 \times 66 = 685$ eV (FWHM_{elec}). The statistical fluctuation of the number of e^- /h^+ pairs created by photons of 59.54 keV in combination with a Fano factor of 0.2, gives a FWHM_{stat} of $2.35 \times \sqrt{0.2 \times 59.54 \times 4.42 \times 10^3/4.42} = 539$ eV. Combining both contributions leads to the following predicted energy resolution at 59.54 keV:

$$\begin{aligned} \text{FWHM}_{tot}(\text{eV}) &= \sqrt{\text{FWHM}^2_{elec} + \text{FWHM}^2_{stat}} \\ &= \sqrt{685^2 + 539^2} = 872 \text{ eV} \end{aligned} \tag{4.22}$$

Which agrees with the right side fit resolution in Fig. 4.22. The calculation does not take into account the polarisation effect, neither does the fit.

At lower energies, e.g. 13.9 keV, the polarisation effect is negligible because interactions take place near the non-blocking (Pt) contact, leading to an induced current mainly created by electrons. Charge loss by holes is then limited. At this energy, the predicted resolution is 733 eV, which nicely corresponds with the measured value of 735 eV.

After the promising results obtained with single pixel detectors, I now present the results obtained with 64 pixels Cd(Zn)Te detectors.

4.6.2 Multi-pixel CdTe and CdZnTe detectors

Setup A dedicated experimental setup, as shown in Fig. 4.24, is constructed to mount detectors of different thickness and type. Four fully functional IDeF-X V1.0 ASICs are properly installed and coupled to the 4×16 pixels of the crystal. The detectors are equipped with custom flex kapton, in order to avoid dielectric losses and cross-talk between pixels.

The electronics and detector are positioned on a copper plate which can be thermally controlled. The whole system is put in a large, grounded test-chamber which allows controlling humidity and serves as an electromagnetic shield. The ASIC's output signals are sent to multiple ADCs or multiplexers outside the chamber and read out by a standard multi-channel analyser for further analysis. Any humidity is evacuated by injecting nitrogen into the chamber. An ^{241}Am (or ^{57}Co) radioactive source is placed a few centimeter above the detector.

Fitting algorithm Spectra are taken at different bias voltages, temperatures and electronics peaking times. I use the energy resolution at the 59.54 keV peak as comparing parameter between the different measurements.

Since not all 64 spectra per detector show sufficient quality, I use a fitting algorithm which selects specific spectra to be included into the analysis. I detail the procedure, using the four spectra depicted in Fig. 4.25, obtained with a Pt//CdTe//Pt detector, 300 V bias,

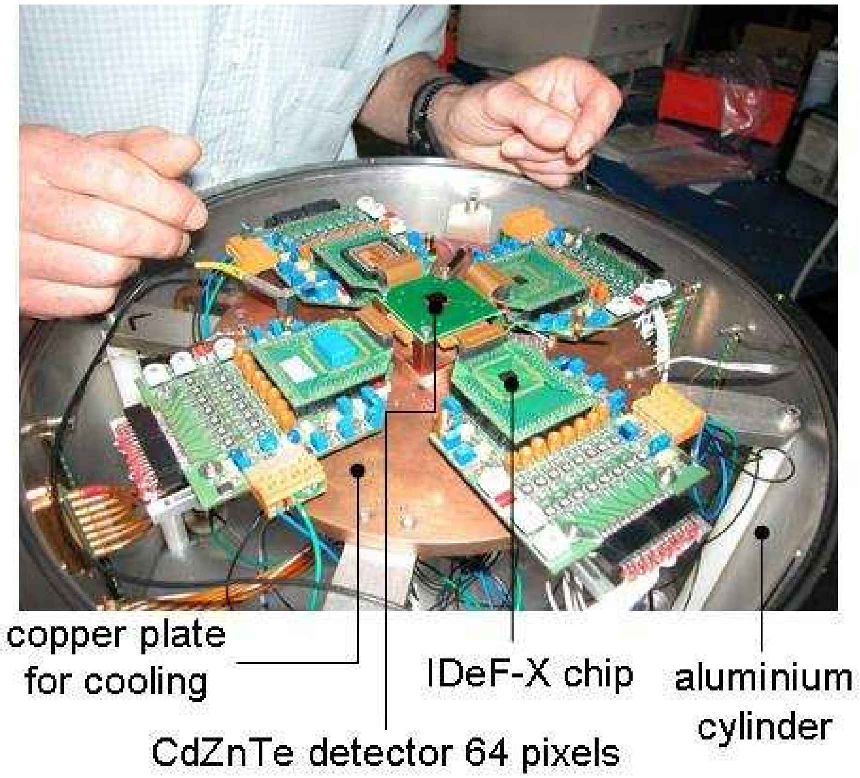

Figure 4.24: Measurement setup for the spectroscopic measurements on 64 pixels Cd(Zn)Te detectors. Four IDeF-X ASICs are connected to the 4 × 16 pixels. The whole system is placed in an Al cylinder.

-37^{o}C and 2.4 μs peaking time.

First, I search peaks in the spectrum (using the ROOT routine “TSpectrum”, with $\sigma = 6$). I demand that there should be at least two clear peaks, that, in principle, should correspond with the most prominent ^{241}Am lines: at 17.8 keV and 59.54 keV. Fig. 4.25 shows that three out of four depicted spectra fulfil this requirement. Pixel 3 does not, due to heavy noise and an affected gain.

Pixel 1 shows an extra peak around 50 keV, created by photons from the ^{241}Am source, that scatter back from the substrate (illustrated in Fig. 4.26). In order to be detected by the detector, their angle of reflection (θ) must be between 140^o and 180^o, corresponding to an energy of ∼50 keV. This value is obtained with the well-known relation for Compton scattering:

$$\lambda_f - \lambda_i = \frac{\hbar}{m_e c}(1 - cos(\theta)) \tag{4.23}$$

With λ_f the initial and λ_f the final photon wavelength, $\frac{\hbar}{m_e c} = 0.00243$ nm and θ the backscatter angle. Nearly all pixels at the border of the detector show this extra peak.

Although spectra like those of pixel 1 are correct, the extra peak may influence the energy resolution at 59.54 keV. I therefore exclude them from the analysis, by demanding that the 59.54 keV peak is isolated within a certain range. That is, it is not allowed to have a

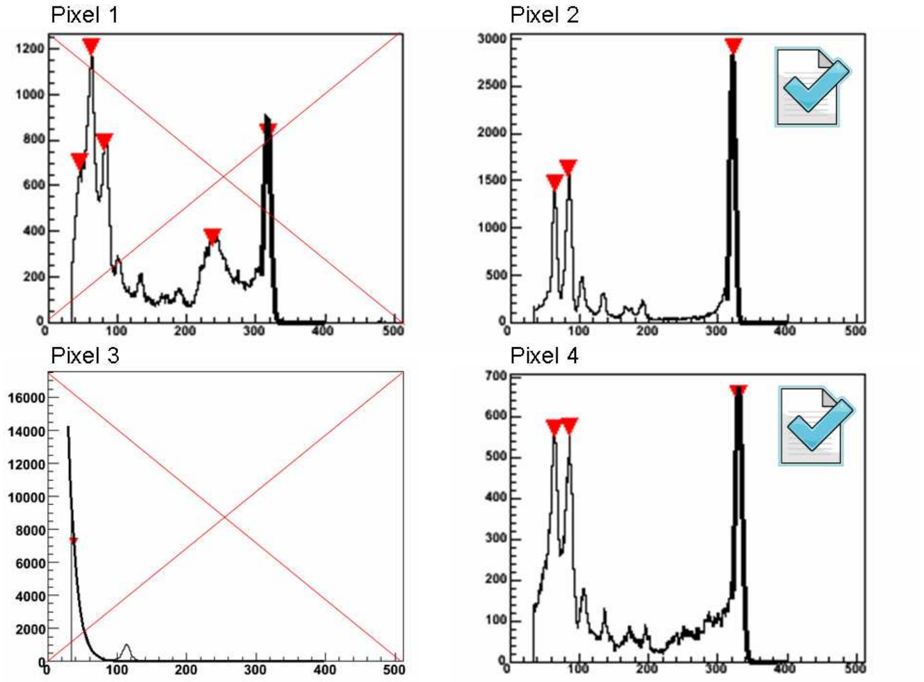

Figure 4.25: Pixel 1 shows an abnormal shape, due to a strong backscatter component of ^{241}Am , bouncing of the substrate. Pixel 2 and 4 are correct and are accepted for further evaluation. Pixel 3 is noisy and the gain is affected. It is not included in the analysis.

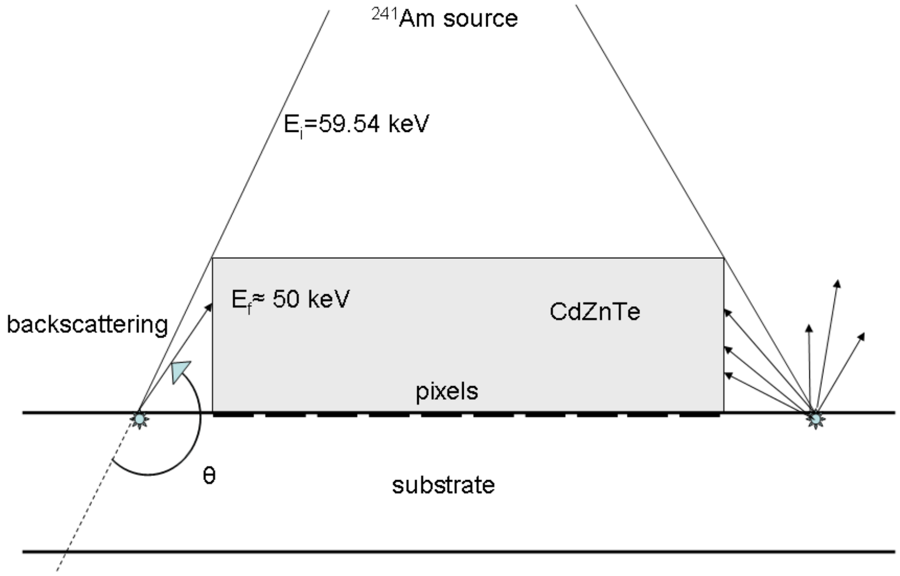

Figure 4.26: Photons from the ^{241}Am source bounce back from the substrate and enter detector. Therefore, the angle of reflection, θ, must be between 140^o and 180^o. The reflected photon will have an energy of ∼50 keV. Especially pixels at the border will be sensitive to these photons.

neigbour closer than 150 bins. Pixel 1 is then excluded.
The value of 150 is not fixed, but can be adapted if necessary (for example if a spectrum has a low gain).
Pixel 2 and 4 are both correct and will be included for further analysis, although the latter is probably subjected to some backscattering too.
I also demand that the number of peaks must be less than 8 (and bigger than one) and that the resolution (FWHM) at 59.54 keV is between 0.4 and 5 keV.
From the spectra that are still left, I take the mean resolution (FWHM) at 59.54 keV and the corresponding standard deviation (represented with error bars), which are plotted as a function of the different parameters.

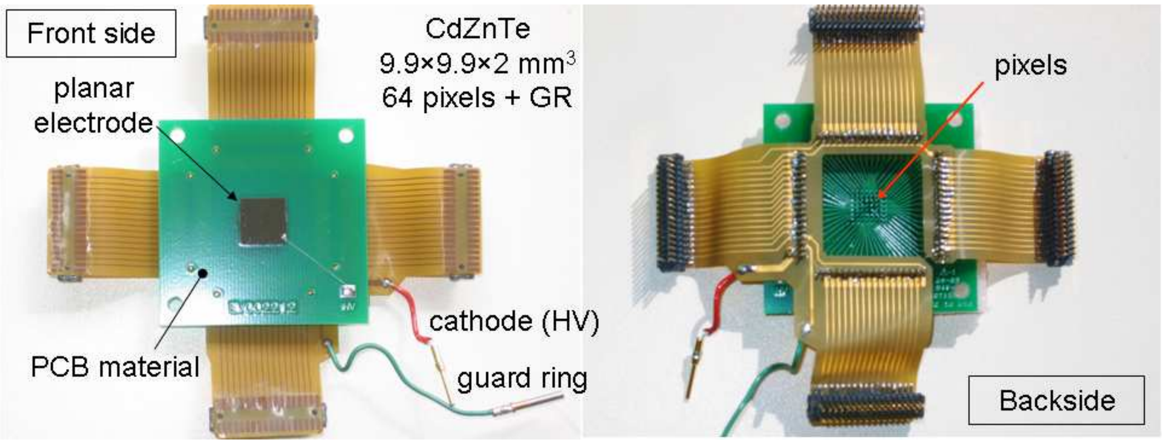

Figure 4.27: The CdZnTe detectors are mounted on standard FR4 PCB material. A special designed flex kapton connects the pixels with the four ASICs.

Pt//CdZnTe//Pt The following results have been obtained with a 64 pixels CdZnTe detector ($9.9 \times 9.9 \times 2$ mm^3), as shown in Fig. 4.27. The crystal is mounted on FR4 standard epoxy substrate. The special connector and flex kapton are connected to the four IDeF-X ASICs. The high voltage is applied at the Pt planar electrode. A separate wire is used to connect the GR.
Fig. 4.28 shows a collection of 16 spectra taken at -38°C , 9.6 μs peaking time and 600 V bias. All spectra fulfil the above fitting conditions, except one which is indicated with the red cross and which has only one distinguishable peak. The algorithm does not exclude pixels having a limited gain (indicated with the diamonds).
The low gain is most likely due to the electronics. If the current is too high, the ASIC cannot sufficiently amplify the signal (this is related to the offset setting of the input transistor).
This explication is valid for pixels that have a relatively high leakage current, but a low gain. It is also possible to have pixels that do not show any current during the leakage current measurements, but have a spectrum with a low gain. In this case, the reason is

most probably not the current but a bad pixel-substrate connection. A spectrum can still be present, thanks to a capacitive coupling between the substrate pad and pixel.

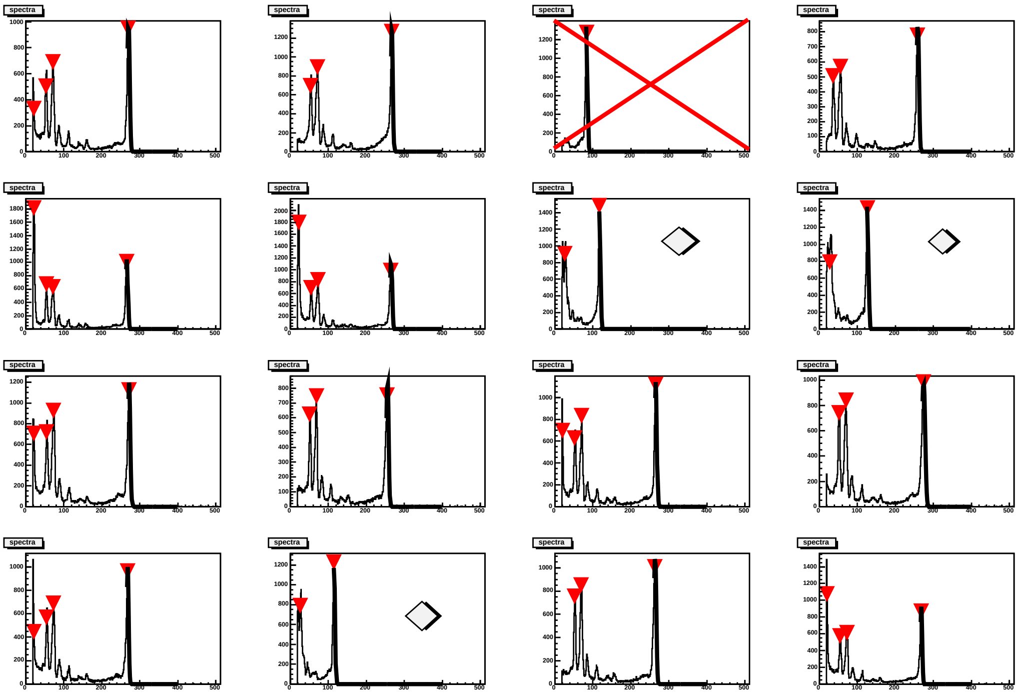

Figure 4.28: Sixteen spectra taken from one ASIC connected to a Pt//CdZnTe//Pt detector of $9.9 \times 9.9 \times 2$ mm^3, biased at 600 V, -38^{o}C and 9.6 μs peaking time. The spectra indicated with a diamond show a low gain but are included for further analysis. The red cross means that the spectrum is excluded.

In Fig. 4.29 I show the results of nearly three months of spectroscopic measurements. These were very time consuming for the following reasons: the switch to change the peaking time is mounted on the electronics board. At temperatures below 5^{o}C we cannot open the chamber without risk, because this would lead to condensation of water on the detector and electronics, resulting in short-circuits. We therefore were obliged to augment the temperature after every measurement series, to change the peaking time. As it took several hours to stabilise the temperature, especially below 0^{o}C , the whole process was very time consuming.

I use again the described algorithm. In addition, a low energy cut at channel 25 is applied, corresponding to ~5 keV (but depending on the gain), to avoid the large noise peak which is sometimes present if threshold of the ADC is chosen too low. The number of pixels that fulfil the ensemble of conditions set by the algorithm, depends on the operating conditions, but is roughly 60 out of 64 pixels.

The curves show that the best energy resolution is obtained at a 9.6 μs peaking time, -35^{o}C degrees and 600 V bias, namely ~1.4 keV at 59.54 keV. The high value of the peaking time means that the parallel noise contribution is very low, which indicates that the leakage current is small. Leakage current measurement on the same detector show

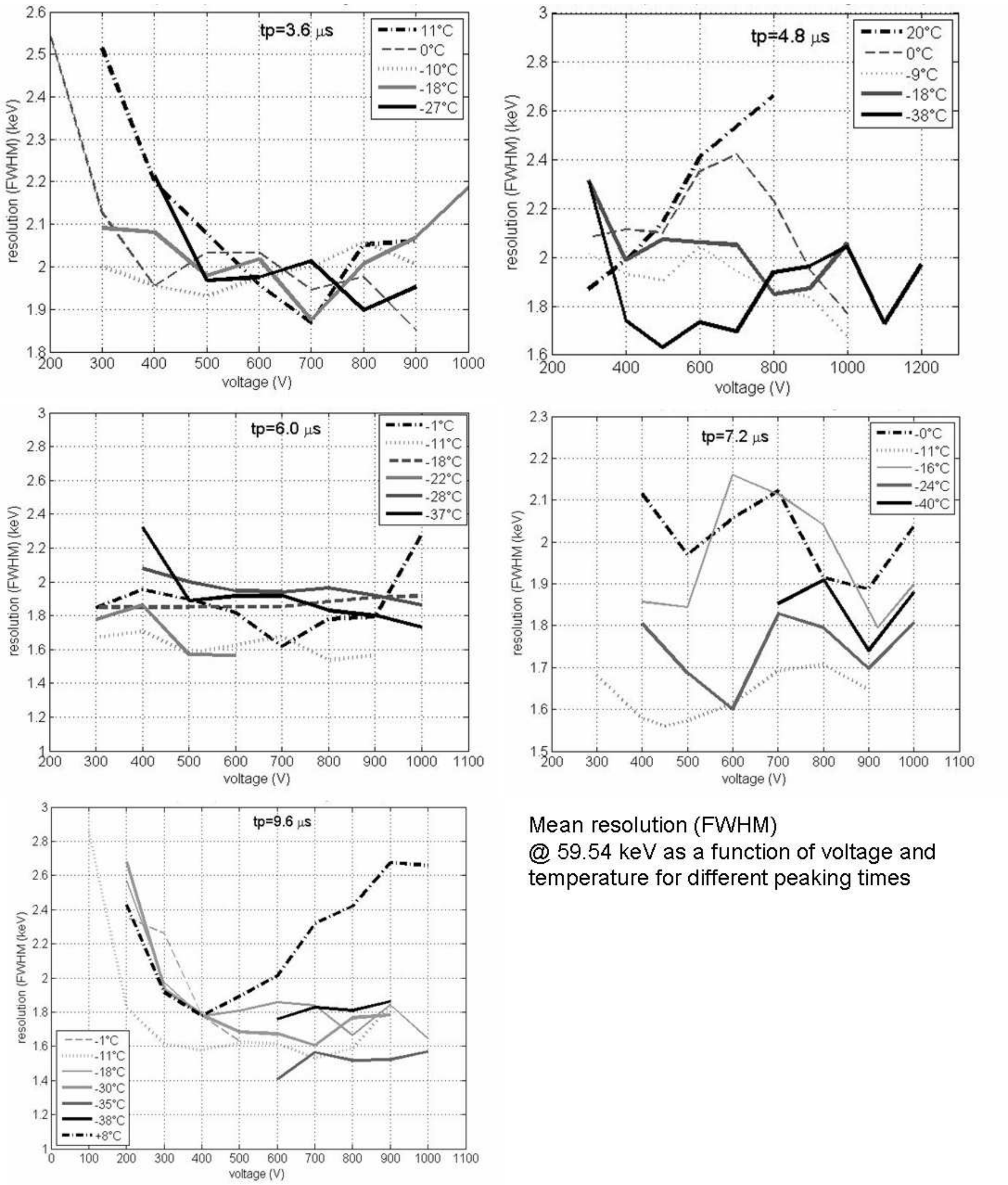

Mean resolution (FWHM)
@ 59.54 keV as a function of voltage and
temperature for different peaking times

Figure 4.29: Spectroscopic results of a 2 mm thick CdZnTe detector with platinum contacts at both sides.

indeed a very small current of a few pico-ampere per pixel. (Cf. Sect. 4.2, that parallel noise is proportional to the square root of the leakage current and peaking time, while the series noise increases if the peaking time become smaller, or as the temperature rises.)
The optimal bias voltage, for which the spectroscopic performance is the best, mainly depends on the temperature. High voltages mean a high leakage current, but quick charge carrier collection. For low temperatures the leakage current decreases and higher voltages can be applied. For a 9.6 μs peaking time, the optimal voltage is between 600-700 V, at temperatures below 0^oC .
For this prototype detector, a temperature of -35^oC would be the optimum to reach the best resolution (∼1.4 keV at 59.54 keV, 600 V).
The temperature choice for Simbol–X will be a consequence of the studies presented in this thesis. The present configuration of Simbol–X foresees an operating temperature of -40^oC for both the LED and HED. The value has been anticipated to guarantee homogeneous low currents in a large number of channels. If this is combined with a low detector capacitance, uniform performances are to be expected.

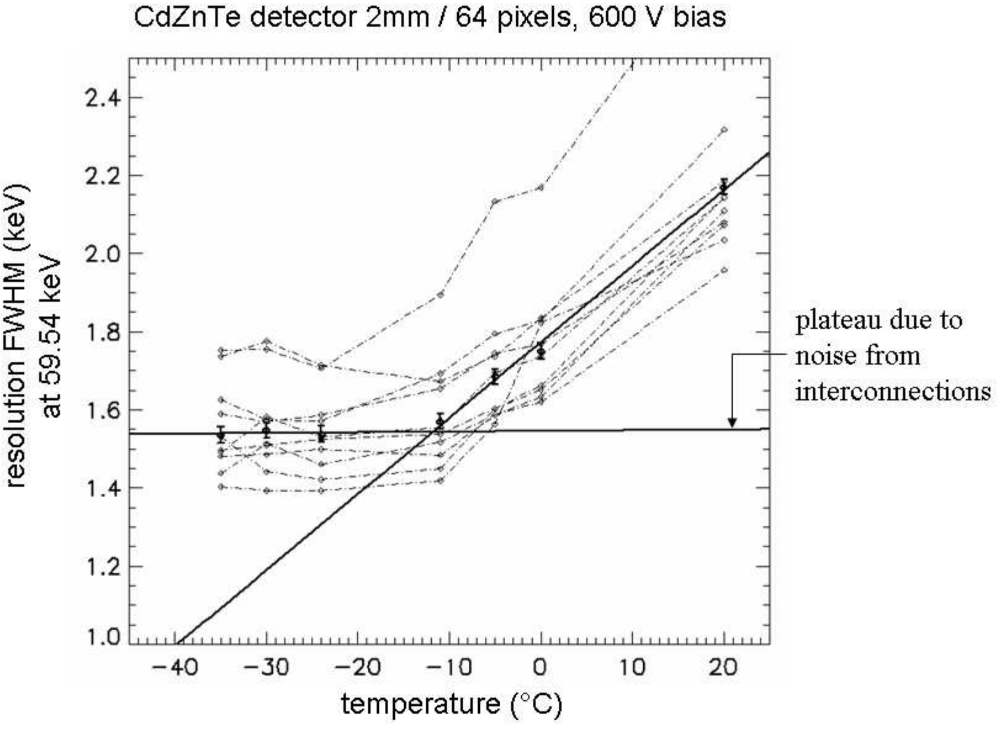

Figure 4.30: The resolution as a function of temperature for several pixels individually.

In Fig. 4.30 I show the resolution as a function of the temperature for several pixels individually, at a bias voltage of 600 V and 9.6 μs peaking time. The curves nicely descend until they reach a plateau below -10^oC . Better resolutions cannot be reached, which is due to the noise generated by the interconnections and the PCB material on which the crystals are mounted.

However, if we would continue the descending trend of the curves, and ignore the plateau, we should be able to arrive at an energy resolution of 1 keV (FWHM) at 59.54 keV, at a temperature of -40°C .

This initiated the search for an alternative substrate material, with superior dielectric properties, in order to limit the noise. This led again to the RO4003 material, used for the leakage current measurement circuits. The CdTe detectors in the following paragraphs are all equipped with this high quality PCB material in combination with the custom flex kapton.

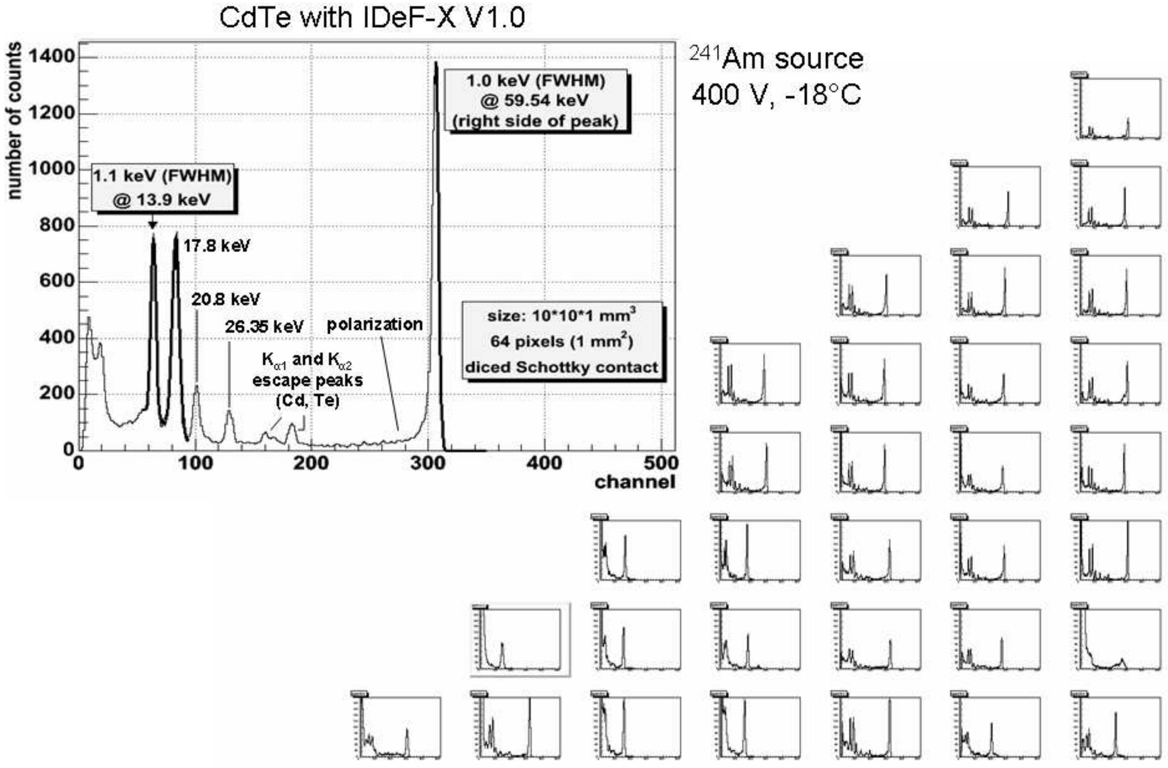

Figure 4.31: 32 spectra taken with two IDeF-X V1.0 ASICs connected to the diced In//CdTe//Pt detector. On the left, one of the spectra obtained. It has a 1 keV energy resolution at 59.54 keV and 1.1 keV at 13.9 keV.

In//CdTe//Pt: diced The following data are taken with CdTe detectors of $10\times10\times1$ mm^3, having 1 mm^2 diced indium pixels and a platinum planar electrode. The slits are 100 μm deep (and therefore partly penetrate the CdTe).

It is expected that the presence of Schottky contacts at the pixel side will lead to comparable results as obtained with single pixel CdTe Schottky detectors (low leakage current and thus better spectroscopic performance).

In Fig. 4.31 I show 32 spectra, taken with two ASICs connected to the detector, biased at -400 V (planar side), at -18°C . The best spectrum is picked out and shown on the left. An excellent energy resolution of 1 keV at 59.54 keV (fit on the right side) and 1.1

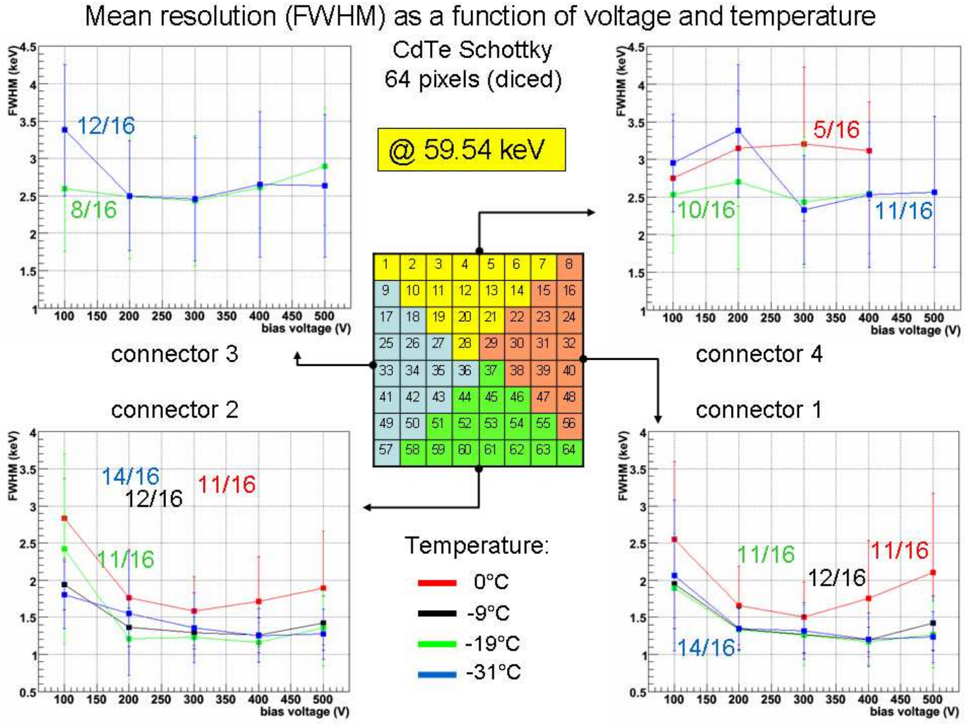

Figure 4.32: The spectroscopic performances of a CdTe detector of 10 × 10 × 1 mm^3, having 1 mm^2 diced indium pixels and a platinum planar electrode. Shown are the energy resolutions at different temperatures and voltages for each of the four ASICs separately. The peaking time is fixed at 9.6 μs.

keV at 13.9 keV is obtained. The escape peaks of Cd and Te are clearly visible. A small polarisation effect is visible at the left side of the 59.54 keV peak.

Every pixel shows a spectrum, although with different quality: some have a very low gain or a very broad high energy peak, while others show excellent spectra, with narrow peaks and low noise.

Fig. 4.32 depicts the mean energy resolution (FWHM) at 59.54 keV, as a function of voltage and temperature, at a peaking time of 9.6 μs, for the four IDeF-X ASICs separately. I use the same algorithm as before, to fit the peaks. The amount of pixels (out of 16) that pass the fitting conditions is shown in the same graph. From these pixels, I take the mean and standard deviation (represented by the error bars).

I directly observe a difference in comportment of the four ASICs. Connector 1 and 2 show very good results. The amount of accepted spectra ranges from 11 to 14 out of 16. Both ASICs have an optimal operating temperature between -9^{o}C and -31^{o}C , at a bias voltage of -400 V, to obtain the best resolution, namely $\sim 1.2 \pm 0.2$ keV. Several individual pixels are able to reach an energy resolution below 1 keV.

At 0^{o}C , the optimum voltage must be lowered to -300 V, due to a higher leakage current. The best resolution is then 1.5 ± 0.5 keV for connector 1 and 1.6 ± 0.5 keV for connector 2.

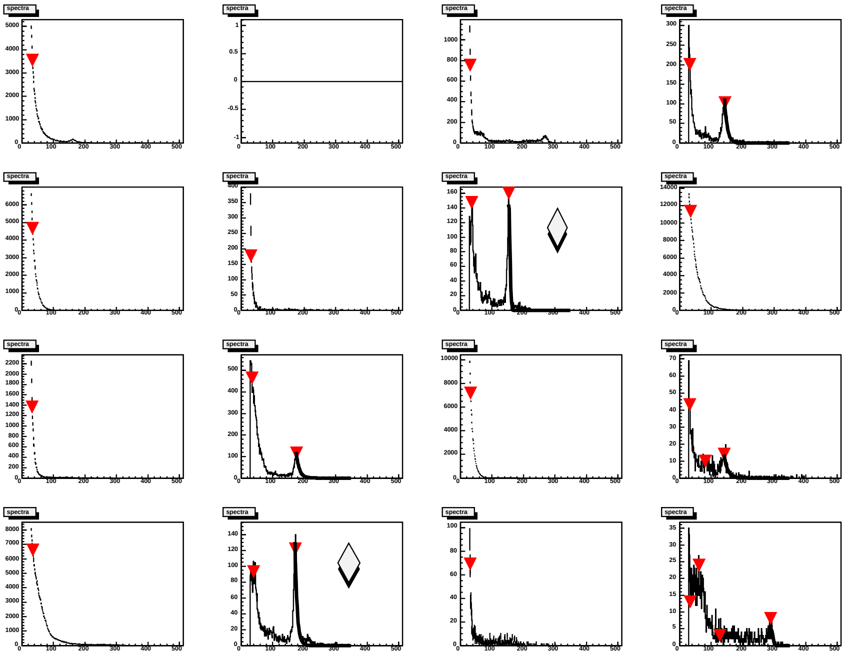

Figure 4.33: An example of sixteen spectra measured at connector 3. The detector is biased at -400 V, at a temperature of 0^{o}C . Only two spectra fulfil the conditions demanded by the fitting algorithm. These are marked by the diamond.

Connector 3 and 4 show many bad spectra, especially at higher temperatures, where the amount of good pixels drastically decreases. This is illustrated in Fig. 4.33, in which I show sixteen channels of connector 3, at 0^{o}C , -300 V. Only 2 spectra fulfil the conditions (marked with the diamond). At lower temperatures, the situation improves, and a resolution of 2.4 $\pm$ 0.9 keV, -300 V, at -31^{o}C , is obtained for connector 3, and 2.3 $\pm$ 0.7 keV for connector 4 (at the same temperature and bias voltage).

The explanation for the different results of the four ASICs is threefold: 1) the connections, wires and platform used to install the electronics, slightly differ from one ASIC to another, 2) the settings of the ASICs, and then especially the offset of the input transistor, are not the same. The relation of the transistor offset to the spectroscopic performance is still under investigation. 3) It is also possible that different parts of the crystal were already bad.

Unfortunately, the above crystal broke off from its substrate and I was obliged to take another In//CdTe//Te detector to continue the measurements.

In Fig. 4.34, I show the comparison between a leakage current map and 64 spectra taken with a second In//CdTe//Pt detector. In the upper part, the current map is depicted which is taken at a temperature of 20^{o}C , -400 V bias. The pixel current varies from less than 100 pA/pix (white), up to ~1 nA/pix (black). All pixels are connected.

Below is the spectrum map. A spectrum and leakage current measurement at the same position in the two figures can directly be compared.

The green square highlights a pixel which is located in a zone with low leakage currents

(<100 pA/pix). Its spectrum is excellent, showing a energy resolution of 1.3 keV at 59.54 keV. The pixels around it have comparable spectra and all correspond with a low current. The pixels that are marked with a red square do not show a spectrum at all. If we look at the leakage current at the same position, we see that these are relatively high (∼1 nA/pix). On the other hand, there are also pixels having a comparable current and show a proper spectrum. An example of such a pixel is indicated by the orange square. The opposite situation exists as well: a low current, but no spectrum. The reason for this behaviour is not completely understood. It is (again) probably due to a difference in (offset) settings of the read-out channels of the ASIC. A high current may result in a saturation of one channel, while others continue operating properly (although with a bad energy resolution). By comparing the DC output values of every ASIC channel with the leakage current and spectral resolution, we hope to get the explanation for this behaviour. Investigation is still in progress.

To create a more visible relation between current, energy resolution and gain, I show in Fig. 4.35 three different scatter plots. Plot A depicts the current against the resolution. Plot B shows the gain, represented by the channel number of the 59.54 keV peak, plotted against the current. The third plot, C, is a scatter plot of the resolution against the gain. In this case I fitted the total high energy peak, thus not the right side only.

The relation between current and resolution in plot A shows a concentration of points in the area defined by $0 < I_{pix} < 2 \cdot 10^{-10}$ A and $1 < R < 2$ keV (with R the resolution at 59.54 keV). However the spreading is rather large. Points located at zero resolution correspond with pixels that do not fulfil the fitting conditions.

In plot B, I do not see a relation between gain and current either. The expectation was to see a lower gain at higher currents.

Plot C shows a clear concentration around channel 300 and a resolution of 1.5 keV. If the gain gets smaller, the resolution gets worse. This is evident, because the resolution is calculated as the width of the peak, proportional to the channel of the peak mean. If the shape stays the same, the above ratio increases as the gain gets smaller.

I discuss these results in Sect. 4.7.

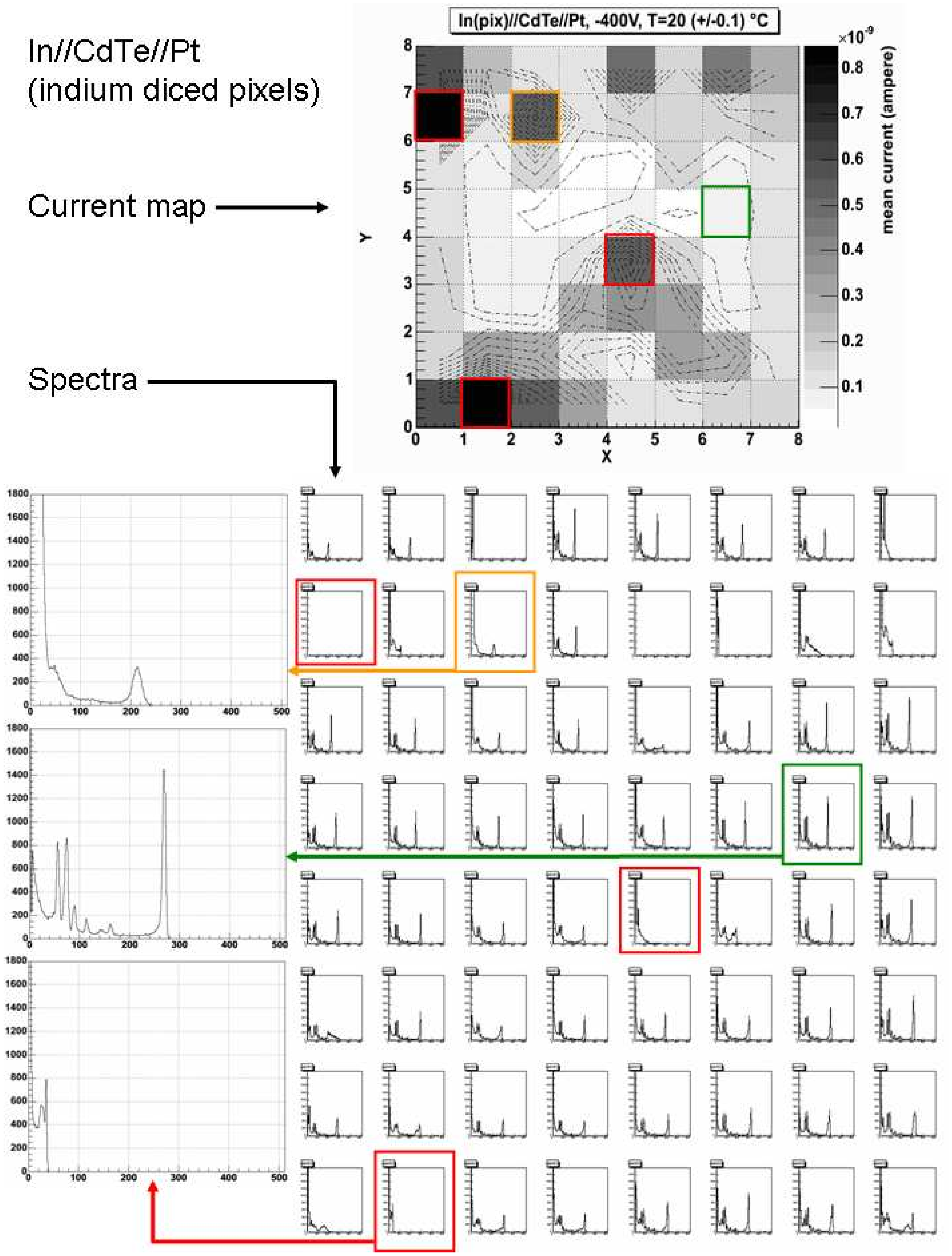

Figure 4.34: Correspondence between leakage current and spectra obtained with a In//CdTe//Pt detector ($10 \times 10 \times 1$ mm^3), biased at -400 V, at 20^{o}C . Highlighted pixels are special which are explained in the text.

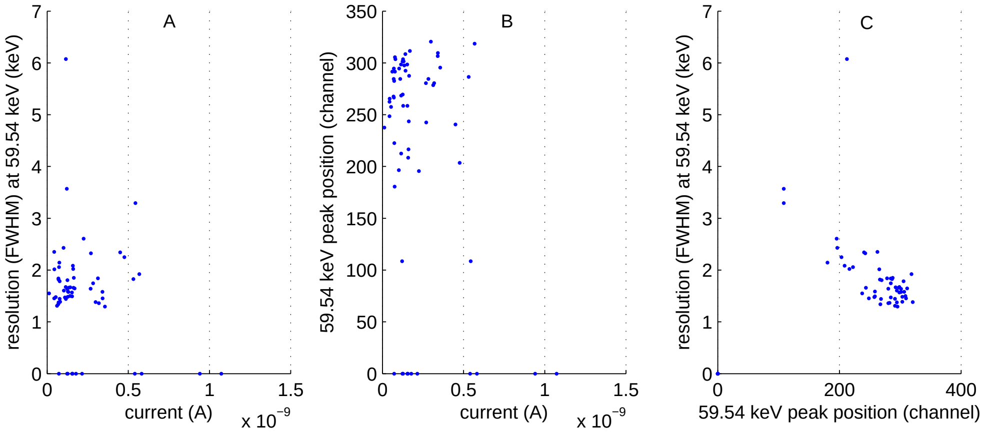

Figure 4.35:

Pt//CdTe//Pt The third type of detector that is tested, is a CdTe crystal with platinum pixels and planar electrode. CdTe has a smaller band-gap than CdZnTe and since there are no blocking contacts present, the applied bias voltage must be limited in order to reduce the leakage current.

Like the In//CdTe//Pt detector, these crystals are also mounted on RO4003 material in combination with the custom flex kapton.

Spectroscopic measurements are performed at -30 and -37^{o}C , at bias voltages ranging from -150 to -300 V applied at the planar electrode. The peaking time is set at 9.6 μs. Fig. 4.36 shows the mean resolution at 59.54 keV as a function of voltage for both temperatures. The same fitting algorithm is used again. The error bars represent the spread (or standard deviation) of the mean resolution. The amount of selected pixels (out of 64) is given by the numbers between parentheses.

The best resolution is obtained at -37^{o}C and a bias voltage of -200 V, namely 1.3 $\pm$ 0.1 keV (43/64 pixels included). The absence of a Schottky contact limits the applied voltage: higher bias voltages directly lead to an increase of the leakage current, resulting in more parallel noise and worse spectroscopic performance.

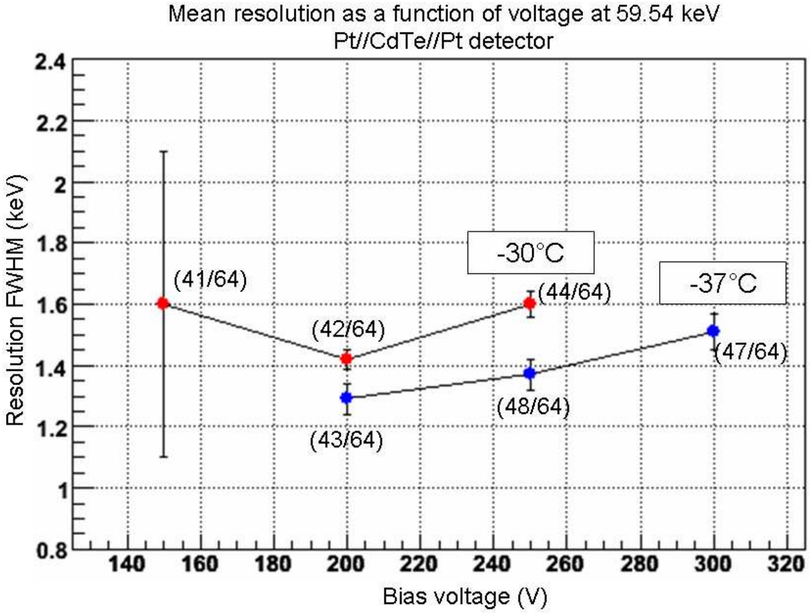

Figure 4.36: The spectroscopic performances of a CdTe detector with platinum electrodes.

4.7 Discussion

Noise Noise is an important factor in the performance of the mini X-ray camera. The noise characteristics of the IDeF-X ASIC have been studied and discussed. A very low intrinsic noise of 35 e^- is measured with the output channels in air. Connecting a single pixel CdTe Schottky detector (330 V, 22^{o}C) to one of the channels, increases the noise up to 66 e^- ENC, due to ~2.7 pF capacitance of detector and housing, and a leakage current of ~15 pA.

Leakage current The leakage current is a key parameter of the performance of the camera. Therefore, four custom made electronic circuits allow accurate measurements (in the order of tens of femto amperes) of the leakage current per pixel.

Current maps of several detectors, at different operating conditions, have been obtained. The leakage current is used to acquire activation energy maps of impurities inside the crystals. The circuits also serve as a tool to control the crystal-substrate contacts. I showed that bad contacts may lead to low gain and even no spectra at all.

Furthermore, I showed that it is possible to make energy resolution predictions. Especially for single pixel detectors and at low energies, this works very well. Predicted values are in good agreement with the measurement results.

Spectroscopy Different spectroscopic measurements on 64 pixels detectors have shown that CdTe equipped with indium pixels gives the best results, namely 1.2 ± 0.2 keV (FWHM) at 59.54 keV, $-31<T<-19^o$C, -400 V. CdZnTe (~1.4 keV, -35^{o}C , 600 V) and CdTe (1.3±0.1 keV, -37^{o}C , 200 V), which both have platinum pixels and planar electrodes, come close to this value. It is expected that the performance of CdZnTe detectors can easily be improved by replacing the FR4 standard epoxy substrate with high quality RO4003. Further studies must verify this expectation.

Correlation I have compared spectroscopic results with measured leakage currents. For single pixel detectors this works very fine, although the polarisation effect may result in inferior performances, which are not indicated by the leakage current.
For pixelated detectors, I compared the current map of an In//CdTe//Pt detector with its spectra mapping (see Fig. 4.34 and 4.35). It is not evident to see a clear correlation, although the majority of the pixels show no, or worse, performance at high currents.

Uniformity The above results lead to an important observation, namely the non-uniformity of the pixel performances. I see a large variation in the quality of spectra, concerning gain, resolution and noise. Several explanations have been given for this, e.g. different electronics settings, a difference in the setup (connections, wires), or bad pixel-substrate connections. It is very important for future prototypes to improve this condition.
The fact that I do not see a clear correlation between current and spectroscopy can probably also be explained by the non-uniformity of pixels. If all channels have equal operating conditions, better correlation should be observed.
Another reason for the non-uniformity is given by Luke, Amman and Lee (2004), who say that Te-inclusions in CdZnTe cause a difference in e^- /h^+ trapping.

Detector choice At this point it is not obvious to make a proper choice of the crystal type that should be used for the Simbol–X high energy detector. The spectroscopic requirements are easily met by the In//CdTe//Pt detectors, but can probably also be reached with CdZnTe, mounted on a different substrate. The decision does therefore not directly depend on the spectroscopic performances.
More important is the uniformity of the crystals. To my opinion and according tho the samples I tested, this mainly has a mechanical (contacts, substrate) or electronics origin. I do not think that the crystal type plays an important role.
To summarise:

- **CdZnTe**: Shows good spectroscopic performance but in our case not sufficient, yet. The HEFT experiment has proven that it is possible to reach energy resolutions below 1 keV at 59.54 keV in combination with extremely low-noise electronics. Disadvantage is that the production of CdZnTe is still a difficult and expensive process in which a perfect crystal homogeneity is hard to reach.

- **CdTe**: the material is known for its excellent crystal uniformity and is capable to fulfill the Simbol–X requirements. The material gives the possibility as well to use blocking contacts to reduce leakage currents. CdTe detectors cannot be chosen too

thick (∼1 mm max.). Thick crystals demand a higher bias voltage to keep the same charge collection time. For example, if the thickness is doubled, the applied voltage must be four times as high ($t_{coll} = \frac{L}{v} = \frac{L^2}{\mu V}$). As a consequence, the leakage current increases, leading to more noise and worse spectroscopic performance.
On the other hand, the CEA/Saclay has gained an important experience in the use of CdTe, by the construction of the ISGRI gamma-camera in the INTEGRAL satellite. This fact should not be underestimated.
Furthermore, our group stands in good contact with the CdTe producer ACRORAD in Japan, which is also exceptionally valuable.

Chapter 5

Detector modelling and simulation

In parallel to the electronics and detector characterisation, I developed a complete simulation chain, from photons interactions in the crystal, up to the read-out electronics output. It has become an indispensable tool in order to better understand detector behaviour and is used to predict and to optimize spectroscopic performances of existing and non-existing detector geometries. Furthermore, it provides us with important data concerning charge sharing effects between pixels and the multiplicity of interactions inside the Cd(Zn)Te material. The information is of major importance for detector design, fixing threshold levels, read-out algorithms and data-analysis.

The program is constructed in such a way that every element and every parameter can be controlled individually. Its segmented structure, which is schematically depicted in Fig.5.1, gives the possibility to replace individual blocks, without rewriting the entire code.

It starts with the simulation of photon interactions inside Cd(Zn)Te crystals using the

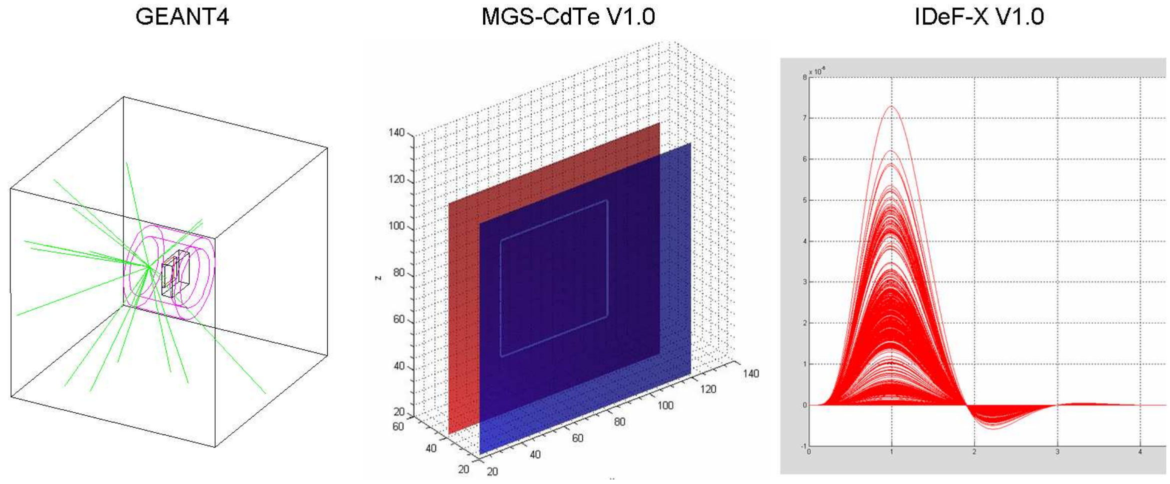

Figure 5.1: The simulation scheme. Left: photons are shot on a CdTe Schottky detector in its housing. Middle: the MGS–CdTe V1.0 model of the same detector. Right: the read-out electronics response.

GEANT4 toolkit (see next section). This Monte Carlo program models the different geometries of prototype detectors and calculates the energy and position of every interaction inside. This information is returned to serve as the input for the second element of the chain: MGS-CdTe V1.0 (see Sect. 5.2). This Matlab based program, which was initially developed at the IReS in Strasbourg (France), is used to model different detector geometries, and simulates the charge carrier creation and transport, charge loss and the induced signals on the pixels, per interaction.

The induced currents are then convolved with the numerical impulse response of the IDeF-X V1.0 ASIC, delivered by the Cadence program[1]. By adding the proper electronics noise, estimated or obtained from measurements, the resulting output signals can directly be compared with measurements on physical detectors.

While in the above chain, interactions are treated individually, GEANT4 is also used to study in a statistical way the size of the charge cloud after an interaction, as well as event multiplicity and the detector efficiency.

MGS–V1.0 is also used to study the influence of the detector geometry on the shape and amplitude of the induced signals. An important result was already given in Fig. 3.16, which showed the relation between the small-pixel-effect and the detector thickness and pixel size.

Preliminary results obtained with the simulation chain have been presented in Dirks et al. (2004).

In the now following section I explain in detail the functioning of GEANT4 and present the results obtained with it, as a stand-alone program.

5.1 GEANT4

5.1.1 General description

Particle interactions inside the Cd(Zn)Te crystals are simulated using the GEANT4 toolkit.[2] It provides a complete set of tools for all areas of detector simulation: geometry, tracking, detector response, run, event and track management, visualisation and user interface. GEANT4 exploits advanced software engineering techniques and object-oriented technology to achieve transparency of the physics implementation and hence provide the possibility of validating the physics results.

5.1.2 Low energy electro-magnetic processes

By including the Low Energy Electromagnetic Physics Package[3] (LEEPP), GEANT4 can handle diverse interactions of particles with matter over a wide energy range: from 250

---

[1] See http://www.cadence.com/

[2] See http://geant4.cern.ch/geant4

[3] See http://www.ge.infn.it/geant4/lowE/

eV up to several TeV.

The energy range of Simbol–X (0.5 to 80 keV) necessitates the use of low energy electromagnetic (EM) processes, that include the low energy photo-electric effect, low energy Compton scattering, Rayleigh scattering and low energy ionisation. Fluorescence of excited atoms is considered as well.

In GEANT4 the user has to decide which EM processes are called during the simulation, for every particle type. In my case, I define that an electron can invoke the following processes: multiple scattering, low energy ionisation and low energy Bremsstrahlung. A photon can call low energy Compton, low energy photo-electric and low energy Rayleigh processes.

Below 100 keV, the majority of the interactions in Cd(Zn)Te is due to the photo-electric effect, resulting in a photo-electron that loses its energy by ionisation. If the vacancy in the atomic shell is filled by another electron, from a higher shell, an X-ray is emitted, which may interact as well or escape the detector, leaving behind the characteristic escape lines in the spectrum.

The photo-electric and Compton effect are examples of discrete processes while ionisation and Brehmsstrahlung are continuous processes. In order to correctly simulate the latter, GEANT4 should calculate an infinite number of interactions, which is of course not possible. The trajectory is therefore divided into steps, which length depends on the chosen cut in range.

5.1.3 Cut in range

At the beginning of a simulation step in GEANT4, all invoked processes give their proposed step length depending on the cross section. The smallest of these steps is taken to be the physical-step-length of the particle. The cut in range is the threshold, below which no secondary particles will be generated. It is defined as a distance, but GEANT4 internally translates it to an energy level, which is specific for the chosen material. In other words, if a particle is left with a minimum amount of energy, it cannot create any secondary particles anymore. Therefore, a particle created in a discrete process, like the photo-electron after a photoelectric interaction, does not create any secondary particles if the step-size is large. Instead, it releases all of its energy in one last step. Only when the proposed step of one of the physical processes is small enough, second, third or higher order particles can be created, until the minimum energy is reached again.

For example, suppose that (low energy) ionisation is the only process invoked, proposing a very short step for the photo-electron to create secondary particles. If the user-defined step length (or cut in range) is larger than the proposed step, no secondaries will be created and the particle deposits all of its energy in a single point.

If the user-defined step length is smaller, the chance to create secondaries increases and the number of interactions per photon as well. Instead of one point, a series of interactions is generated –the charge cloud– which is more likely to represent what really happens in-

side the detector.
The advantage of a small step is, that the interaction position becomes more precise, though the precision of the deposed energy decreases. Knowledge of the size of the simulated charge cloud can therefore be obtained with small step sizes.
Unfortunately, due to the large amount of interactions, this can lead to very long calculation times. This does not directly concern GEANT4, but mainly MGS–CdTe V1.0. It has to calculate the induced signal for each interaction. Depending on the chosen time-step, this can take up to two minutes per interaction.
The question that arises, is how small the cut in range must be taken to accurately simulate the charge cloud, but to keep the calculation time reasonable.

5.1.4 Charge cloud

In 3.4.2 I explained that an initial point charge, generated in Cd(Zn)Te, could create a charge cloud due to diffusion. I calculated that its size can reach a maximum of $4.3 \cdot 10^{-2}$ mm. This is small compared to 1 mm^2 pixels, and does not have to be taken into account.
EM-processes as ionisation, Compton-, multiple scattering and Brehmsstrahlung make that the assumption of an initial point charge is not true. Interactions can take place at many different positions, sometimes more than a pixel size away from the point-of-first-interaction. This is mostly due to secondary photons emitted by the atom due to fluorescence, but Compton scattering is possible too, especially at higher energies (E_γ>250 keV, see Fig. 3.9). This is illustrated in Fig. 5.2.
A primary photon γ_1 enters the detector and undergoes a low energy (LE) photo-electric (PE) effect. A photo-electron is created which looses its energy close to the point-of-first-interaction. A fluorescence X-ray, γ_2, is emitted and creates a second photo-electron some distance away. This electron also looses its energy by ionisation. Another characteristic X-ray is emitted, which causes a third LE photo-electric interaction and corresponding photo-electron. The ensemble is considered as a charge cloud.
To define its size, I use the transversal distance from the point-of-first-interaction: $R = \sqrt{x^2 + z^2}$. Since the electric field inside the detector is nearly homogeneous, charge carriers will drift in a straight line to the pixels. In that case, only the size in the (x,y)-plane is important.
I distinguish between the actual distance, R_{abs}, and the weighted distance R_{weight}, defined as:

$$R_{weight} = R_{abs} \times E_i / E_{mean/int} \tag{5.1}$$

With E_i the energy (keV) of the ith interaction and $E_{mean/int}$ the mean energy per interaction, defined as $\frac{1}{N}\sum_{i=1}^{N} E_i$, with N the total number of interactions.
I introduce R_{weight} to express the importance of an interaction. Interactions that occur far away, will make the charge cloud appear larger. But if the energy deposition is small, its influence will be less significant.
The values for R_{abs} and R_{weight} are obtained by simulating photon interactions in a CdZnTe detector of $10 \times 10 \times 2$ mm^3. The crystal is bombarded with photons of 59.54

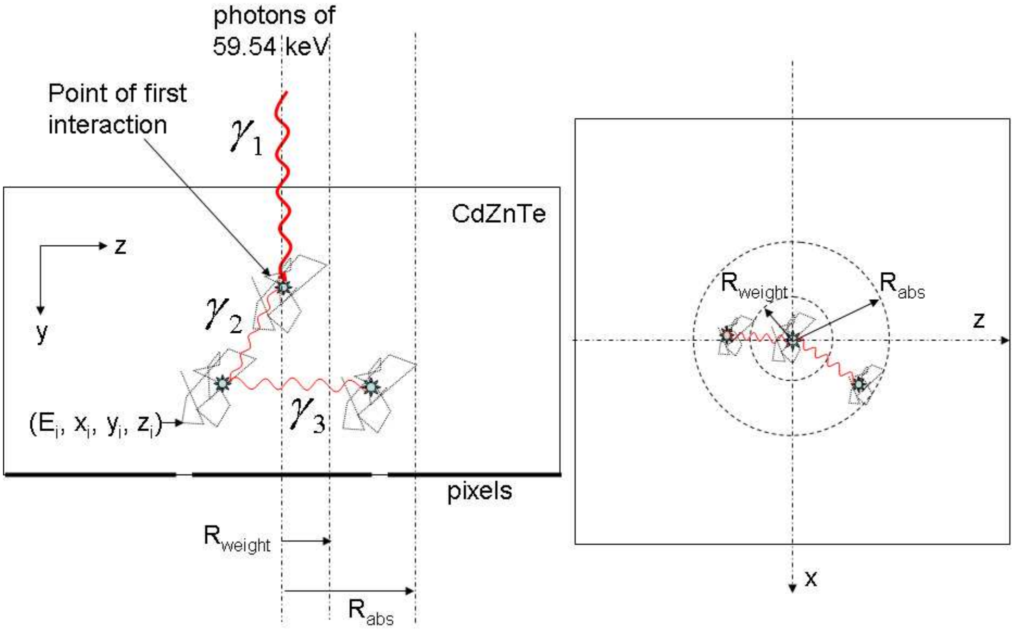

Figure 5.2: Example of the creation of a charge cloud: the primary photon γ_1 enters the detector and interacts by means of the low energy photo-electric effect. A photo-electron is created, which looses its energy by ionisation (creation of e$^-$ /h$^+$ -pairs), close to the point-of-first-interaction. A fluorescence X-ray, γ_2, is emitted and creates a second photo-electric interaction. The corresponding photo-electron looses its energy again by ionisation. Another photon is created, γ_3, which transfers its energy to a third photo-electron. R_{abs} is the transversal distance from the first interaction. R_{weigth} is the distance weighted with the energy deposited. For every interaction, i, GEANT4 returns the energy E_i and the position (x_i, y_i, z_i).

keV (moving in the y-direction). GEANT4 returns the energy and position for each interaction.

Fig. 5.3 shows four scatter plots of the energy per interaction against R_{abs}, obtained with 50000 photons. The cut in range is chosen to be 1 nm, 100 nm, 0.01 mm and 1 mm. For each cut an example is shown of how a single photon interaction would look like. For 1 nm many ionisation interactions take place, while for 1 mm only few occur. We see this also in the scatter-plots.

At a 1 nm step, the number of interactions is very high (~80 per photon). The invoked ionisation or scattering processes propose step lengths that are larger than the user defined step and are therefore allowed to be carried out. This results in numerous interactions, but with little energy deposition each.

If the user defined step is increased, ionisation becomes less probable, leading to a smaller number of interactions, but with more energy deposition per interaction. This can be seen in the plot of the 1 mm step: since the energy deposition is not spread out over multiple interactions, discrete processes become visible, e.g. the creation of a photo-electron having an energy equal to the photon energy minus the electron binding energy ($E_{e^-} = E_\gamma - E_b$),

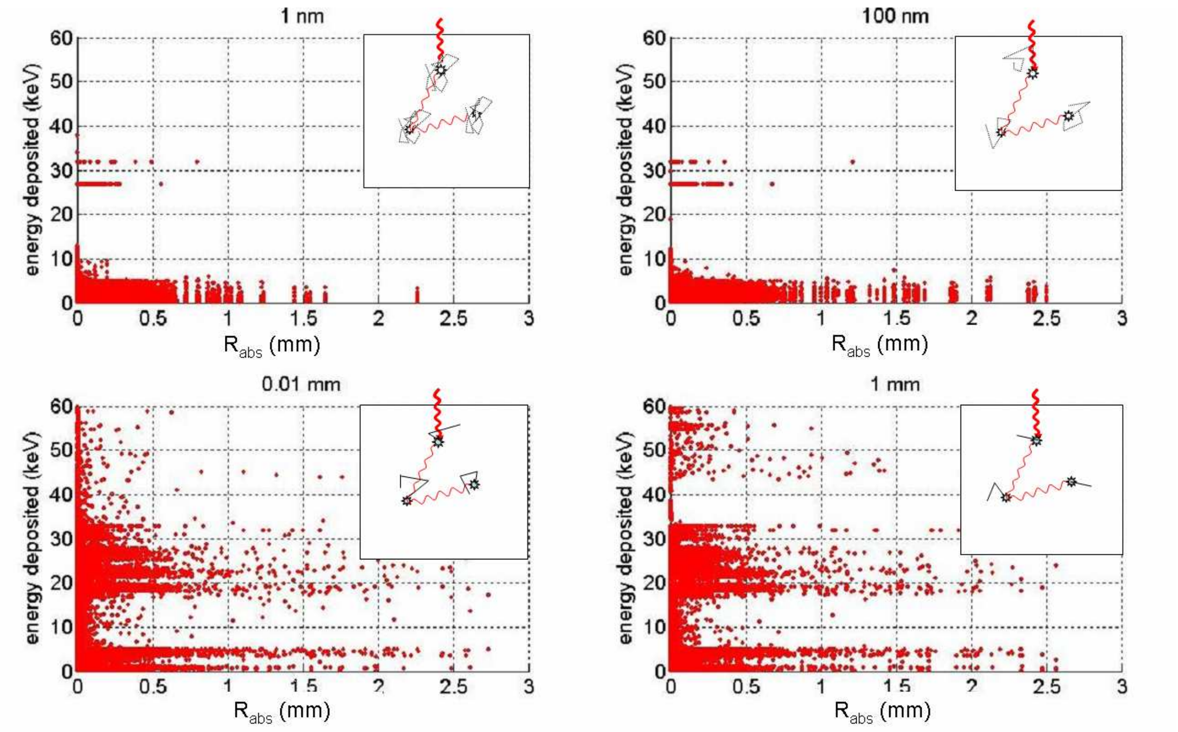

Figure 5.3: The energy deposition per interaction against R_{abs}, for a chosen cut in range of 1 nm, 100 nm, 0.01 mm and 1 mm. The small images show an approximation of how the situation would look like for a single photon.

depositing all of its energy in one point.

At 1 and 100 nm multiple interactions take place at nearly the same position. These correspond with tracks of ionising electrons.

Regarding the interaction position, we see that R_{abs} can reach values up to ~2.5 mm, much larger than the pixel size of 1 mm. In Fig. 5.6 I will show the number of interactions that take place in a specific range of R_{abs}, but before that I first need to find the optimum cut in range value.

Therefore I consider the mean and weighted mean interaction distance, $\overline{R}_{abs}$ and $\overline{R}_{weight}$, as a function of the chosen step. This is shown in Fig. 5.4. The red curves give the mean interaction distance, $\overline{R}_{abs}$, from the point-of-first interaction for a total of 20000 photons, as a function of the chosen cut-in-range. Two different energies are considered: 59.54 keV and 100 keV. The blue curves give the weighted mean interaction distance, $\overline{R}_{weight}$.

The error bars are obtained by performing ten times the same simulation per cut-in-range value and taking the standard deviation of the ten values of $\overline{R}_{abs}$ and $\overline{R}_{weight}$.

We see that the weighted mean at 59.54 keV, represented by the blue curve, keeps a constant value of ~32 μm . At 100 keV, the $\overline{R}_{weight}$ shows more fluctuations. Up to 1 μm, it keeps a rather constant value of 54 μm , then slightly increases and drops to 50 μm for the 0.1 and 1 mm step.

$\overline{R}_{abs}$ shows a different behaviour. It is constant up to 1 μm, for both energies and then

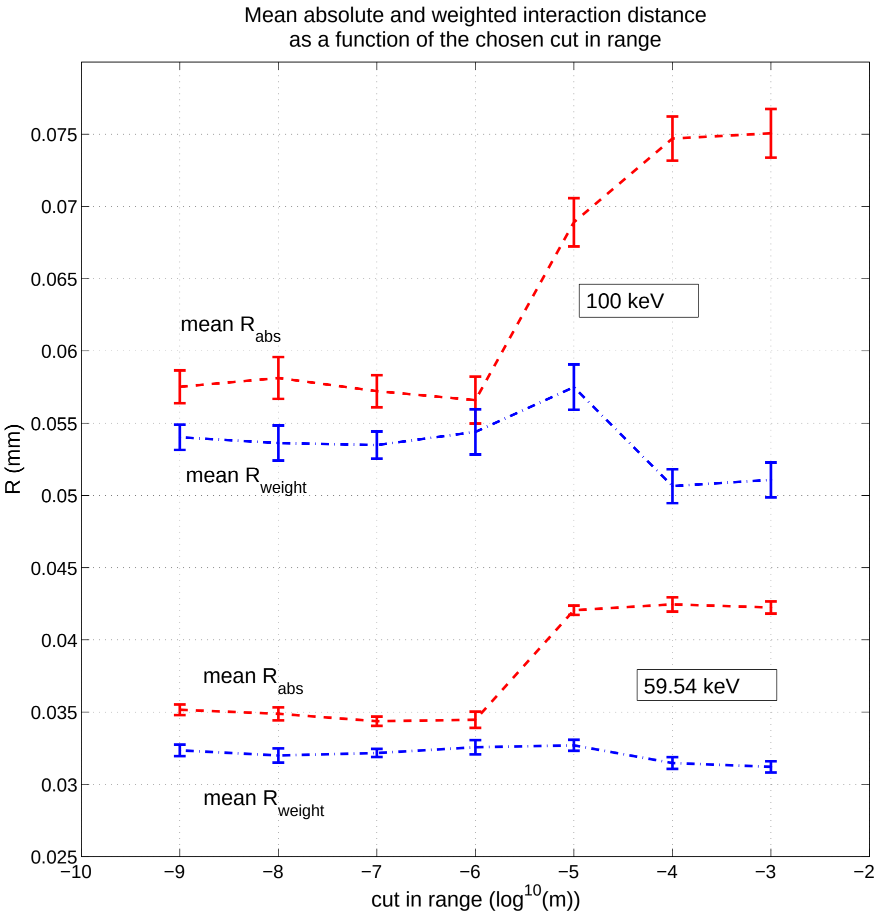

Figure 5.4: $\overline{R_{abs}}$ and $\overline{R_{weight}}$ as a function of the chosen cut in range for photons energies of 59.54 keV and 100 keV.

quickly rises. For 59.54 keV, $\overline{R_{abs}}$ is 35 μm below 1 μm and 42 μm for higher cuts-in-range. For 100 keV, $\overline{R_{abs}}$ is 57 μm below 1 μm and 75 μm for 0.1 and 1 mm.

The charge cloud is larger at 100 keV than at 59.54 keV. Evidently, because electrons have more energy to travel a larger distance. We also see that $\overline{R_{abs}}$ becomes larger at higher cuts. This means, that although less interactions take place, they interact further away from the point-of-first-interaction, creating a larger simulated charge cloud.

Compared to the pixel size of 1 mm^2, $\overline{R_{abs}}$ and $\overline{R_{weight}}$ are negligible, but if smaller pixels are used ($< 500^2$ μm^2), the size of the cloud becomes important.

Independent of the pixel size, is the importance of the charge cloud created by interactions near the border of a pixel, or in the volume between two neighbouring pixels. In both cases, the charge is distributed over more than one pixel, and the amount of charge sharing depends on the size of the cloud.

Our prototypes detectors have an inter-pixel spacing of 0.1 mm. A mean R_{weigth} of 32 μm at 59.54 keV is therefore not negligible anymore. In Fig. 5.6 I will show the actual

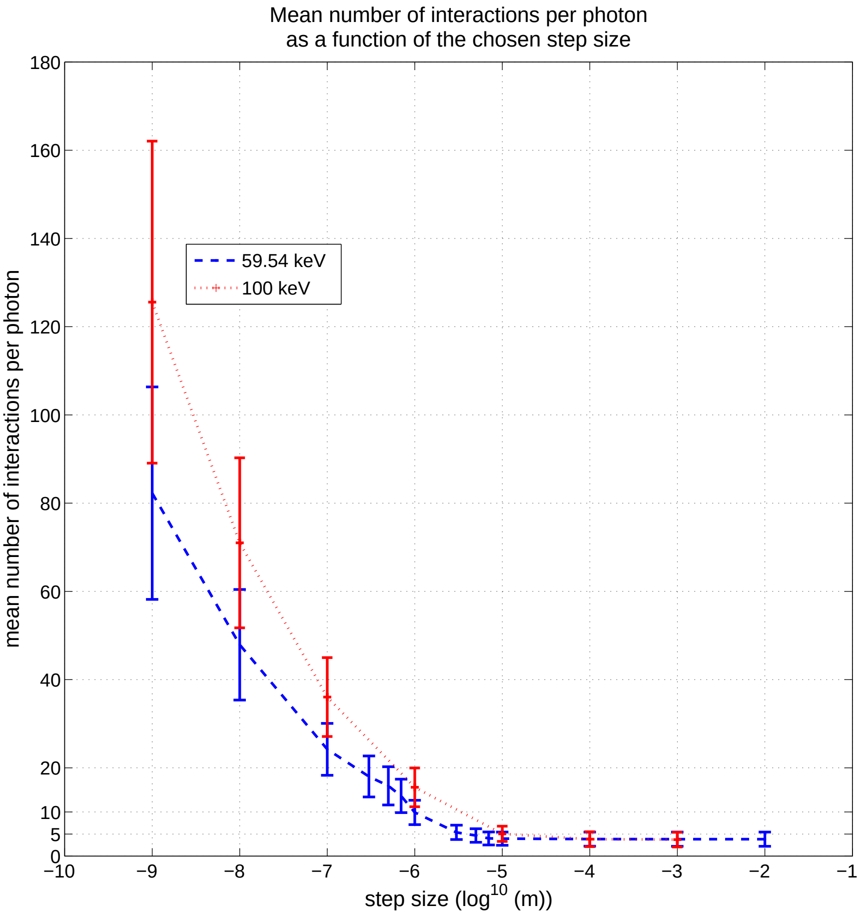

Figure 5.5: Mean number of simulated interaction per photon, as a function of the chosen cut in range. The red curve corresponds to photons of 100 keV and the blue to 59.54 keV.

number of interactions taking place within a certain distance.

In Fig. 5.5 I present the mean number of interactions per photon as a function of the chosen cut in range. The error bars give the standard deviation on the number. The red curve corresponds to photons of 100 keV and the blue to 59.54 keV.
As the cut-in-range gets smaller, up to ∼80 interactions per photon can occur for 59.54 keV photons and more than ∼125 at 100 keV. Above 100 μm, the number of interactions becomes constant. Then about four interactions per photon take place. This means that within 4 interactions all of the photon energy is deposited.
By combining the results of Fig. 5.4 and 5.5, I can now choose an optimum cut-in-range. Assuming that small values represent best reality, and keeping the number of interactions reasonable, a cut of 1 μm should be taken. But, since the size of the cloud is very small, for all choices of the cut, and the fact that I gain a factor of 2.5 in calculation time, I perform the final detector simulations (see Fig. 5.4) using a cut-in-range of 10 μm. I will

therefore slightly overestimate the size of the cloud. However, for future simulations I advise to take 1 μm as optimum cut-in-range.

I would like to make a final remark here. Hecht's hypothesis (see Sect. 3.5.2) that the induced charge must be considered as a point charge, is still valid. GEANT4 samples the charge cloud by a number of interactions which depends on the chosen cut-in-range, and then simulates each interaction as a point charge.

5.1.5 Charge sharing

In the above calculation, I considered the mean absolute and weighted size of the charge cloud. It led to a proper choice of the parameter which specifies the size of the simulated charge cloud by GEANT4.

In this section I show the actual percentages of interactions that take place within a certain distance from the point-of-first-interaction. I therefore take the optimum cut-in-range of 1 μm and simulate 50000 photons of 80 keV interacting in the same CdZnTe crystal as before.

The left side of Fig. 5.6 shows the histogram of the lateral distance from the point-of-first-interaction. If the photon interacts in the middle of a pixel of 1 mm^2, 98.04% of the interactions take place within 0.45 mm (half a pixel size), 1.63% interacts between 0.45 and 1 mm, and 0.33% deposits its energy at a distance further than 1 mm.

On the right I show the detector layout with circles corresponding to the above lateral distances. It shows the two extreme cases, namely photon interactions in the centre of a pixel and those in the middle of four pixels.

The fractions in those same regions, of the total energy deposited, are plotted in Fig. 5.7. It shows an identical plot like those of Fig. 5.3, but now for 80 keV photons and a cut-in-rang of 1 μm . The results are summarised below (Table 5.1):

	$0 \leq R \leq 0.45$ mm	$0.45 < R \leq 1$ mm	$R > 1$ mm
interactions	98.04%	1.63%	0.33%
energy deposited	98.33%	1.37%	0.30%

Table 5.1: The percentages give in a specific range of distance, the fraction of the total number of interactions and of the total energy deposited.

Regarding the right side of Fig. 5.6 again, I can conclude that in order to be sure to collect the signal of all interactions, a matrix of 3-by-3 pixels must be read-out, at minimum. The centre pixel will have the largest signal.

A matrix of 4-by-4 should be read-out if an interaction in the centre of four pixels takes place (in that case none of the four has the largest signal). The chance that this occurs is however extremely small.

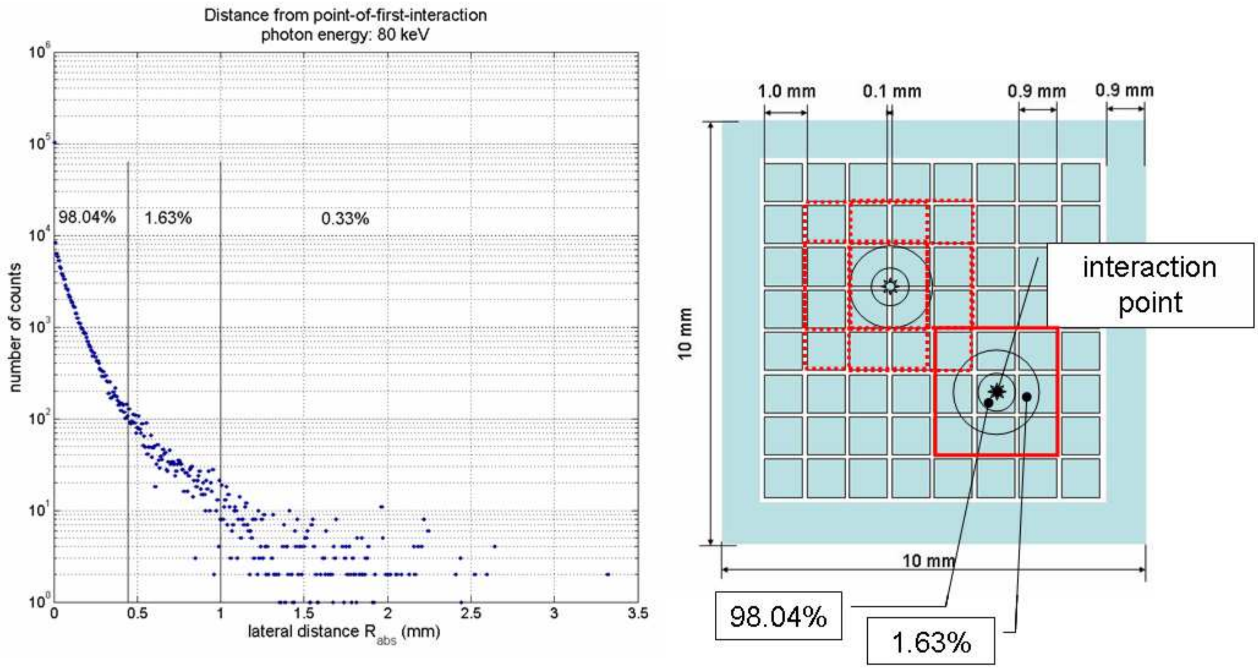

Figure 5.6: Left: histogram of the lateral interaction distance for 50000 photons of 80 keV, creating a total of 194442 interactions. Right: detector layout, showing two cases: photons hitting in the centre of a pixel and in the middle of four pixels.

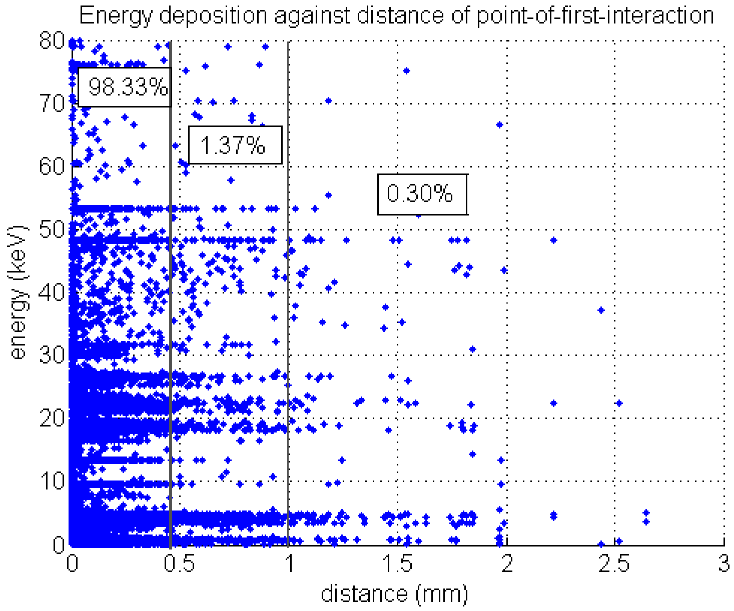

Figure 5.7: Scatterplot of the energy deposition against the R_{abs} for each interaction. The percentages give the fraction of the total energy deposited within a certain range of distance.

A dedicated experimental setup for the charge sharing measurement in real detectors is in an advanced stage. Preliminary measurements have revealed that the simulated percentages are coherent. This is shown in Fig. 5.8, which contains a scatterplot of the charge sharing events (at 59.54 keV) between two pixels which are next to each other. It concerns a CdTe detector with indium diced pixels of 1 mm^2. The detector is irradiated uniformly with an ^{241}Am source. The spectra next to it, are obtained with shared events only. The percentage of shared events is ~1.6%, which is coherent with the value of 1.37% I obtained with GEANT4 (in that case I included all energies). The measured value is therefore somewhat higher.

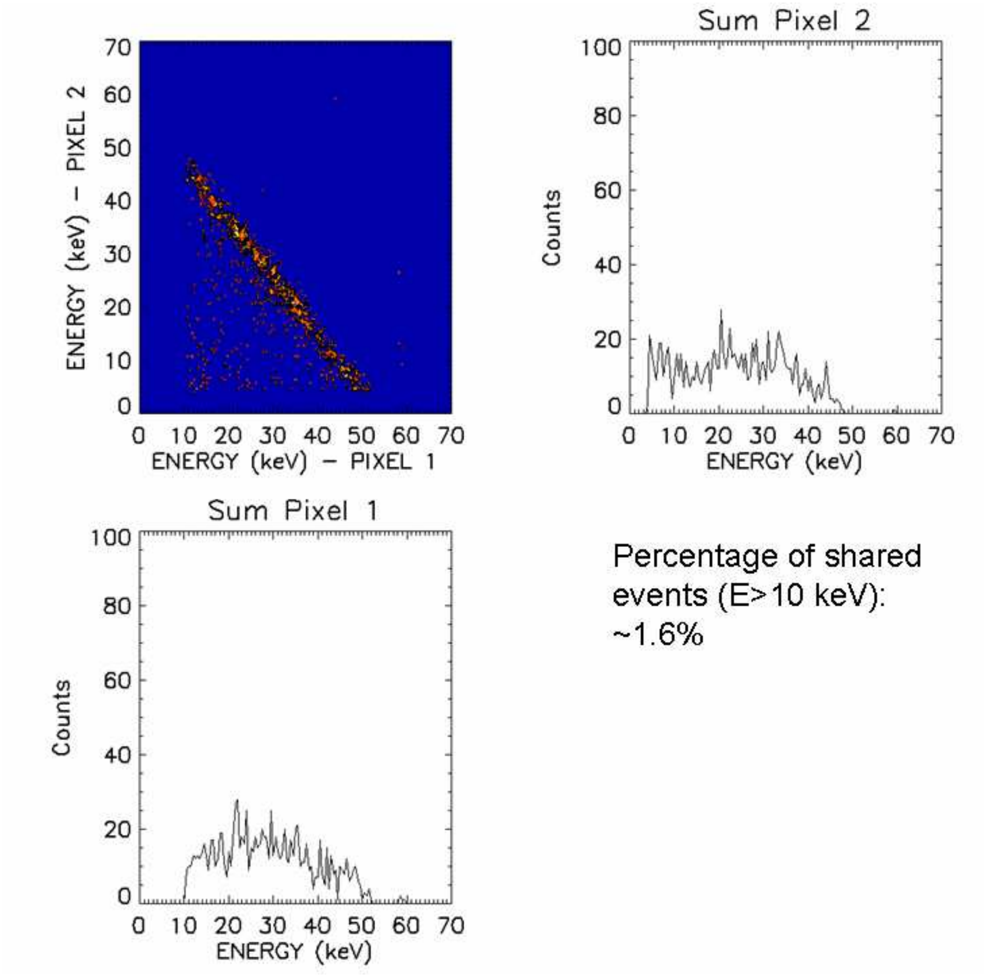

Figure 5.8: Charge sharing events in a CdTe detector with 1 mm^2 diced indium pixels. The detector is irradiated uniformly with an ^{241}Am source. The shared events correspond with the 59.54 keV energy peak. The spectra next to it are obtained with shared events having an energy higher than 10 keV.

5.1.6 Simulated detection efficiency

As a stand-alone program, GEANT4 is also used to simulate the detection efficiency of CdTe and CdZnTe. Therefore I model a crystal of $5 \times 5 \times 10$ cm^3. I take this large size to avoid that too many X-rays, created by fluorescence, escape the detector. A number of N=50000 photons is shot on the centre of the crystal. In the analysis the block is virtually divided into pieces. I will show two different ways to express the efficiency of the material:

Number of counts In this case, the number of photons that has an interaction (Compton scattering, photo-electric) is compared with the initial number that is shot on the material (N). Even if only a small amount of the photon energy is deposited, it is included in the efficiency.

Total absorbed energy (photo-peak efficiency) Here, only the photons which deposit all of their energy are included. This corresponds with photons in the photo-peak of a spectrum.

In the second case, at energies in the neighbourhood of the characteristic fluorescence lines, the efficiency will be lower. Some of the fluorescence X-rays will escape the detector and do not deposit all of their energy. This effect is not visible when the number-of-counts efficiency is used.

The results for CdTe and CdZnTe are shown in Fig. 5.9. The red curve in the count efficiency of CdTe is a measurement taken with a CdTe detector of $4 \times 4 \times 2$ mm^3. At energies below 100 keV the curves nicely overlap each other. At higher energies, there are only a few measurement data points available, which makes a comparison difficult to perform.

The simulation shows no significant difference between CdTe and CdZnTe. Operating up to energies of 80 keV, both detector types need to have a thickness of at least 2 mm in order to stop or count 95% of the photons.

Detection efficiency should not play a role in the final choice between both material types for the Simbol–X mission.

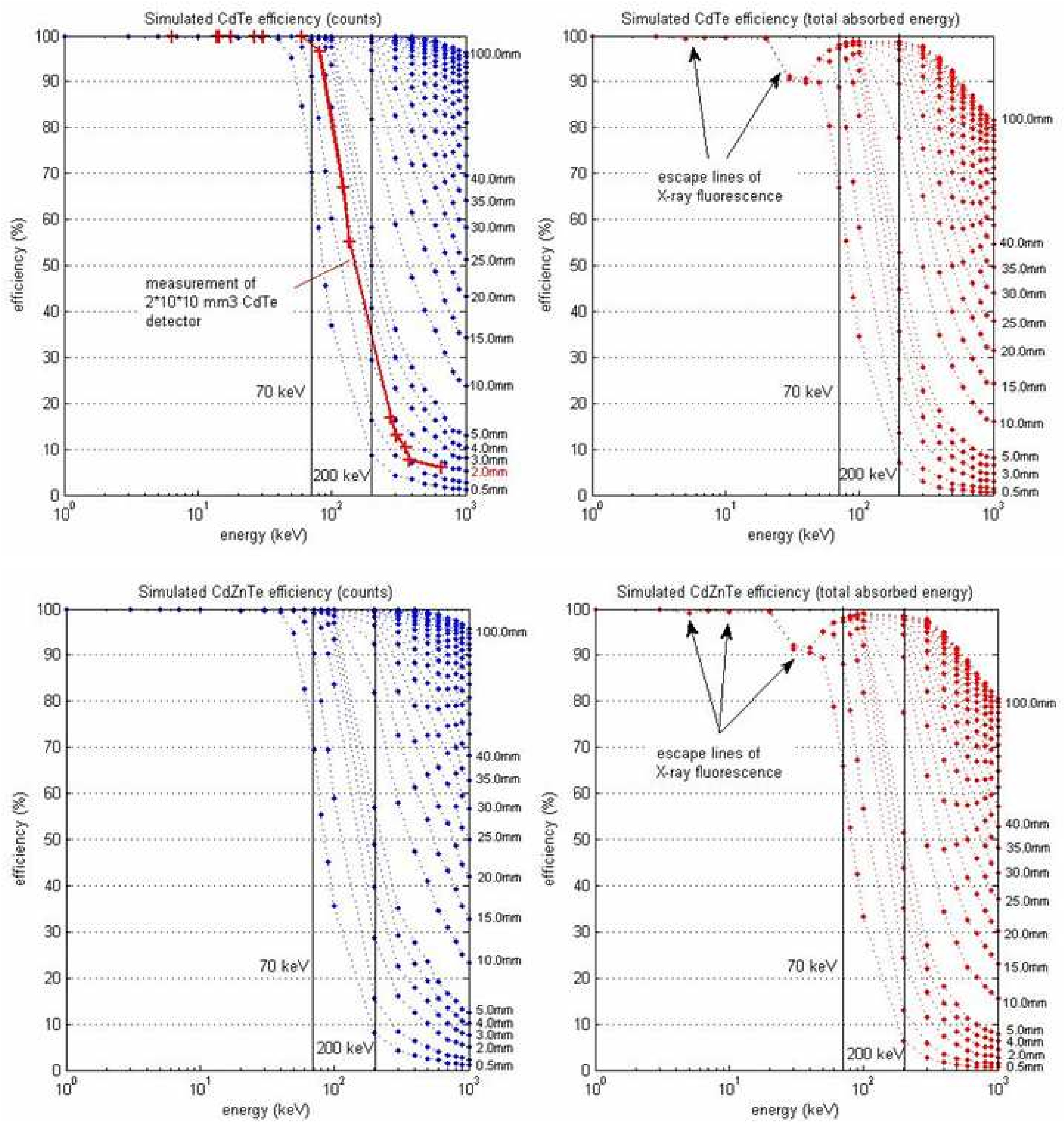

Figure 5.9: Above: CdTe detection efficiencies expressed in the number of counts and the total absorbed energy. The red curve is a measurement taken with a CdTe detector of $4 \times 4 \times 2$ mm^3. Below: the efficiencies for CdZnTe.

5.1.7 Modelling of single and 64 pixels Cd(Zn)Te detectors

The above results have exposed the power and capabilities of GEANT4 as an independent simulation tool. In this section I will explain the use of the program as a part of the complete detector simulation chain.

Using the building blocks of GEANT4, nearly all possible detector geometries can be created, from single detector blocks to the extremely complex structures (e.g. the ATLAS detector at CERN). For the simulation of Cd(Zn)Te detectors I limit the geometry to a single piece of Cd(Zn)Te crystal. For CdTe the housing must be modelled too, in order to include backscattered photons. For CdZnTe this is not necessary, because the surroundings are too far away from the crystal to influence the results.

Fig. 5.10 shows the GEANT4 model of a CdTe prototype detector in its housing. Its size is $4.1 \times 4.1 \times 0.5$ mm^3 and is covered with a 1000 Å thick platinum electrode at the cathode and an indium electrode at the anode. The real detector has a pixel and GR at the platinum side. In the GEANT4 model this can be considered as a single planar electrode. The space between pixel and GR does not influence the particle interactions.

Like the physical detector, the crystal is mounted onto a Al_2O_3-substrate and placed in an aluminium housing. A radioactive point source is placed 5 mm above the detector and irradiates the platinum side with user defined photon energies.

Geometries are also created for the 64 pixels Cd(Zn)Te detectors as I will show in Sect. 5.6. GEANT4 simulates the different interactions and returns the energy and position per interaction, labeled with the photon number. These data are sent to MGS-CdTe V1.0 for further treatment.

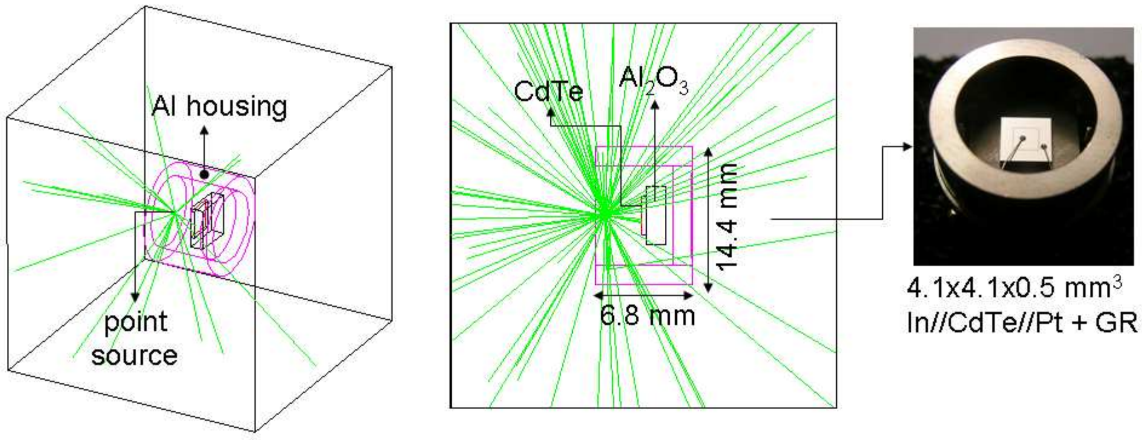

Figure 5.10: GEANT4 model of a prototype CdTe detector in its package. The platinum side is irradiated by a point source with user defined energy.

5.2 MGS-CdTe v1.0

The second element of the simulation chain is MGS-CdTe V1.0. MGS (Medina et al. 2004) stands for Multi Geometry Simulation and was initially developed at IReS, Strasbourg (France). Originally, this Matlab based program was used to characterise the performances of large segmented germanium detectors using numerical methods with no restriction to geometry.

Keeping only the core elements I completely adapted it for small, single or multi-pixel Cd(Zn)Te detectors. In order to make a distinction between the original and adapted program, I call my version MGS-CdTe V1.0.

The code is structured in a progressive way, starting from the definition of the crystal geometry up to the generation of induced pulse shapes at the contacts. I will briefly explain each element.

5.2.1 Geometry modelling

The program uses a rectangular grid to represent the space in which the different detector geometries are placed. The size of this 3D matrix is variable but limited by the active memory of the computer (in my case the maximum grid is $\sim 1.2 \times 10^9$ elements).

The simulated geometry must be sampled sufficiently. Therefore, the grid size (the matrix) must be chosen large enough. The distance between two grid points must represent a physical distance which is smaller than the smallest structures of the detector. Large detectors covered with small pixels are therefore difficult to simulate.

To be consistent with the input data from GEANT4, the Matlab geometry model must exactly match the one created in GEANT4. Fig. 5.11 shows a visualisation of the single pixel CdTe detector with exactly the same geometry as shown before in Fig. 5.10. The Al surroundings and substrate are not included, because they are relatively far away (∼1 cm) and will therefore not influence the electric field. If ground structures are used that are closer to the detector, one has to consider their simulation as well.

The size of the detector is again $4.1 \times 4.1 \times 0.5$ mm^3 with a single pixel of 2.0×2.0 mm^2 and a guard ring of 1 mm large. The grid pitch is 0.05 mm.

5.2.2 Alternative geometries

Beside the existing geometries, non-existing detectors with different sizes, pixel-size, guard ring configurations etc, can be modelled too. For example, Fig. 5.12 shows two geometries with different guard ring positions on a pixelated CdZnTe detector. The upper plot shows the normal configuration, that is, the guard ring surrounding the pixels at the anode side. The lower plot has a guard ring (0.4 mm large) on the side. Since the GR creates an insensitive zone I want to know how the detector behaviour is modified by a GR on the side (and filling up the space at the anode by pixels). This configuration diminishes the insensitive zone while the surface currents are still absorbed.

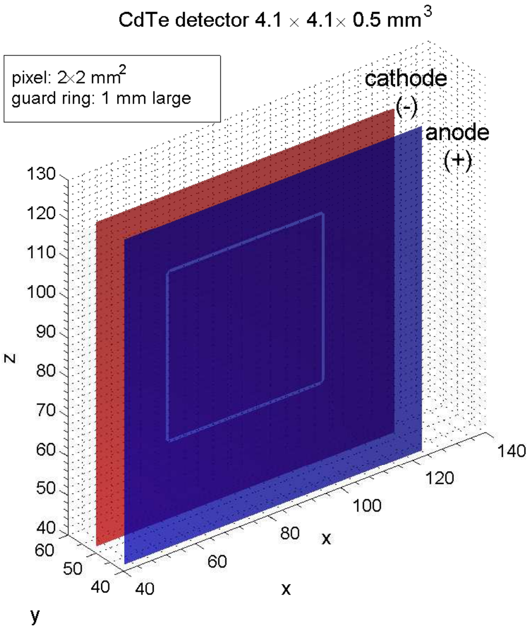

Figure 5.11: Matlab model of a CdTe detector, 4.1 × 4.1 × 0.5 mm^3, with a pixel-size of 2.0 × 2.0 mm^2 and a guard ring of 1 mm large.

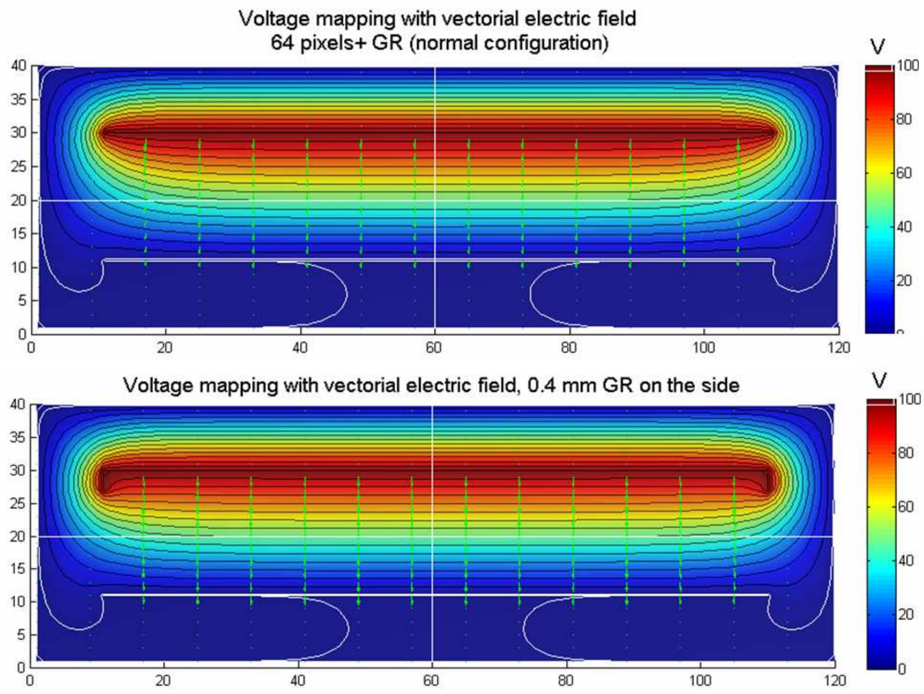

Figure 5.12: Matlab geometries with corresponding electric vector field for two different guard ring positions. Above: guard ring at the anode surface. Below: GR at the sides.

As the figure shows, the electric field (see next section) is slightly different in both situation. With the GR on the side, it is more homogenous in the rest of the detector. Charge carriers will therefore follow a straight line to the pixel. Carriers created near the border, which would normally not be detected, are now seen by the pixels that replaced the GR. Only a small amount will drift the GR on the side.
Unfortunately, due to limitations in the technology of photo-lithography and electrode deposition, it is not possible to create the above configuration.

5.2.3 Electrical properties

After having defined the geometry, the potential and electric field need to be calculated by solving Poisson's equation:

$$\bigtriangledown^2\Phi = -\frac{\rho(x)}{\epsilon_0\epsilon_r} \tag{5.2}$$

With Φ the potential field, ρ(x) the space charge as a function of the position x, and $\epsilon_0\epsilon_r$ the permittivity of free-space multiplied by the relative permittivity of material (see Table 3.1).
The above problem in 3D cannot be solved analytically, but requires a numerical method. Two important approaches exist: the finite element and the finite difference method.
The first divides the region of interest in subelements adapted to the boundaries[4] and covers it without overlap. In each of these elements an analytical approximation to the solution is made. This technique is especially useful for complex geometries since the number of subelements can be changed as a function of the complexity of the shape.
A commercially available program, Femlab, uses this technique. I tested it and concluded that it is very powerful but too expensive compared to its benefits. (Our geometries are too "simple" for the program.)
The second method is based on finite difference calculation. It uses a regular mesh superimposed on the region of interest. As all the prototype detectors have rectangular shapes, this method is very appropriate and can be directly used in Matlab without any additional program.
In the one-dimensional case the Laplace equation with fixed potentials $U(x_1) = u_1$ and $U(x_2) = u_2$ at the electrodes, is:

$$\bigtriangledown^2\Phi = 0,\ \Phi(0) = 0,\ \Phi(1) = 1 \tag{5.3}$$

Which gives $\Phi(x) = x$. To solve the numerical solution, the domain $x_1 < x < x_2$ is divided into N segments which form the grid. At i, Laplace's equation is approximated by:

$$[(\Phi_{i+1} - \Phi_i) - (\Phi_i - \Phi_{i-1})]/(1/N)^2 = 0 \tag{5.4}$$

---

[4] The problem has (rectangular) Dirichlet boundary conditions, namely the fixed voltages at the electrodes.

The finite difference method uses an iterative technique to find a series of approximate solutions that converge to the exact solution. Therefore the following basis is taken:

$$\Phi_i = \frac{\Phi_{i+1} + \Phi_{i-1}}{2} \tag{5.5}$$

Initially all points Φ_i are 0 except for the end points. Then, at every iteration the new value of Φ_i is calculated. The iteration continues until the maximum difference between the present and previous value of all Φ_i's is smaller than a user defined value. This "error" is an input parameter of MGS-CdTe V1.0.

To accelerate the above process, MGS uses variations of the above principle, called *overrelaxation* and *successive overrelaxation* (SOR). These techniques add an extra term to Eq. 5.5:

$$\Phi_i = w\frac{\Phi_{i+1} + \Phi_{i-1}}{2} + (1-w)\Phi_i \tag{5.6}$$

With w a non-zero constant. In this case, the rate of convergence and the accuracy of the iteration improve substantially. A description of the relaxation method for the one- and two-dimensional case can be found in Reitz, Milford, and Christy (1993).

For the different detector simulations I use either the relaxation or the quick SOR method (in 3D). The maximum error is set to 10^{-5}.

The result of the above iteration is a 3D matrix filled with the potential values at each grid point. Using interpolation, an estimation can be made of the voltage at inter-grid positions, which makes that the simulation is not completely fixed by the grid.

To obtain the corresponding electric field, I take the gradient of the above potential map: $\vec{E} = -\nabla\Phi$. Four matrices are returned, which give the E_x, E_y, E_z and $E = \sqrt{E_x^2 + E_y^2 + E_z^2}$ for each grid point. An example of the simulated voltage map and electric field was already shown in Fig. 5.12.

Now the electric field is known, Eq. 3.25, $\vec{v} = -\mu\vec{E}$, is used to calculate four matrices which give the instantaneous velocity for electrons and holes separately at each point. This allows me to calculate the trajectories of charge carriers inside the semiconductor.

Fig. 5.13 shows three geometries of a 4-pixels detector with varying inter-pixel space and size. These models are used to study the trajectory of the electron/holes with varying interspacing between pixels, which are shown on the right. The green arrows represent the electric field vectors.

Interactions take place in the centre of the detector, near the (negative) cathode. In this case, holes (black) are directly absorbed by the planar electrode while electrons (red) traverse the complete detector.

The increase of the interpixel spacing causes that the electric field is bent in such a way that the electrons are always collected by a pixel (except if the charge carrier is exact in the middle of course).

In order to guarantee a homogeneous electric field, leading to straight charge carrier trajectories to the pixels, the space between pixels must be chosen as small as possible. However, in practise, putting them too close may result in small leakage currents. This is due to a potential difference in the order of millivolts between pixels, caused by the electronics.

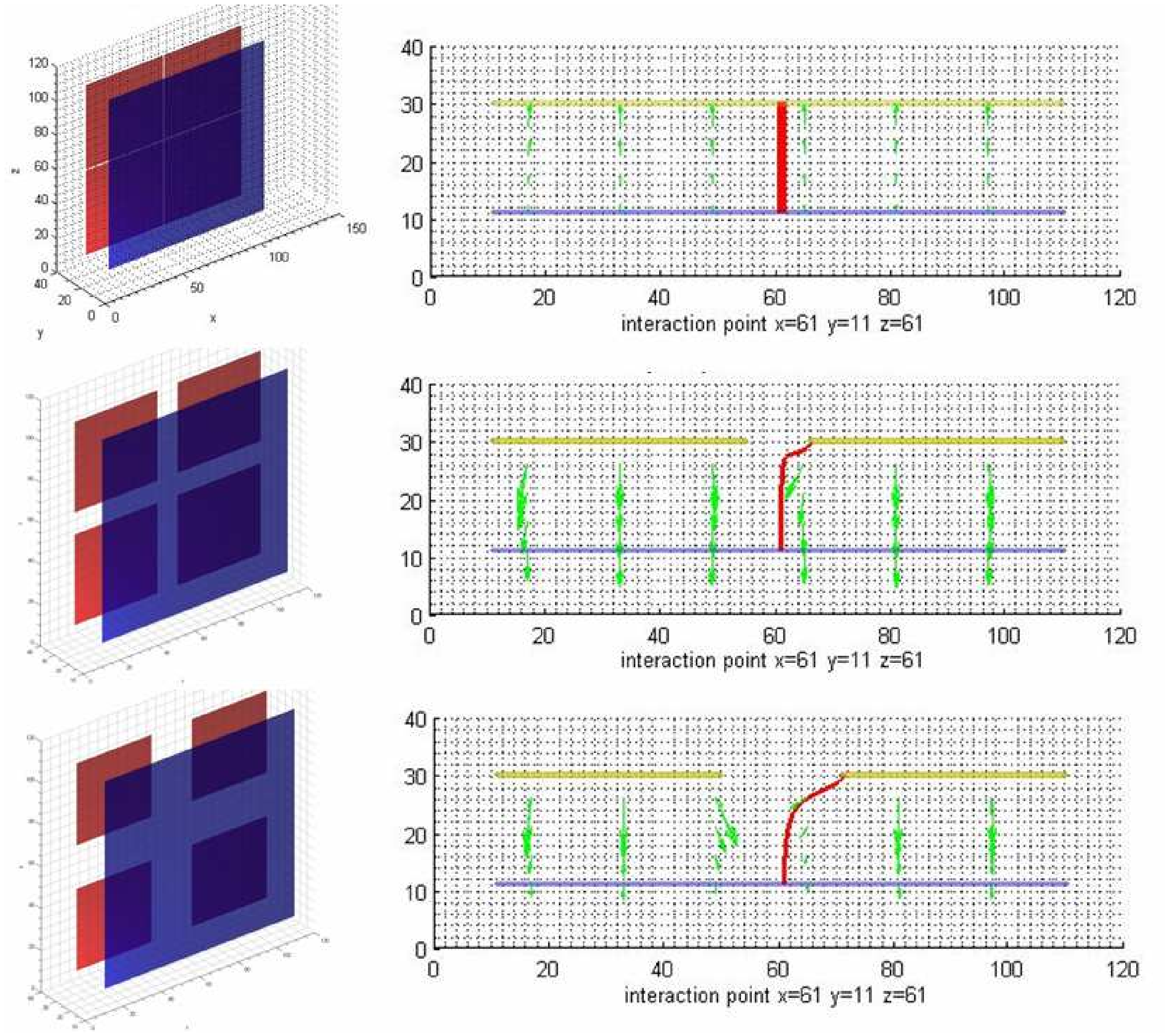

Figure 5.13: Three 4-pixels geometries having different interspacing and pixel size. Shown on the right are the corresponding electron/hole trajectories in case of an interaction near the cathode in the centre of the detector. The red curves correspond to electrons. Holes arrive directly at the electrode.

5.2.4 Weighting field

In order to simulate the induced current on a specific electrode due to the moving charge carriers, the corresponding weighting field has to be calculated. As explained in Sect. 3.5, this non-physical field can be obtained by connecting all electrodes to ground, except for the one concerned, which must be put at 1 V, and by removing all space charge. The resulting electric field, created by the electrode, is known as the weighting field, E_w. The corresponding potential is called the weighting potential, Φ_w.

Fig. 5.14 shows a visualisation of the simulated weighting field and weighting equipotential lines of the planar electrode, and, of an individual pixel of a 64 pixels Cd(Zn)Te detector ($9.9 \times 9.9 \times 2$ mm^3).

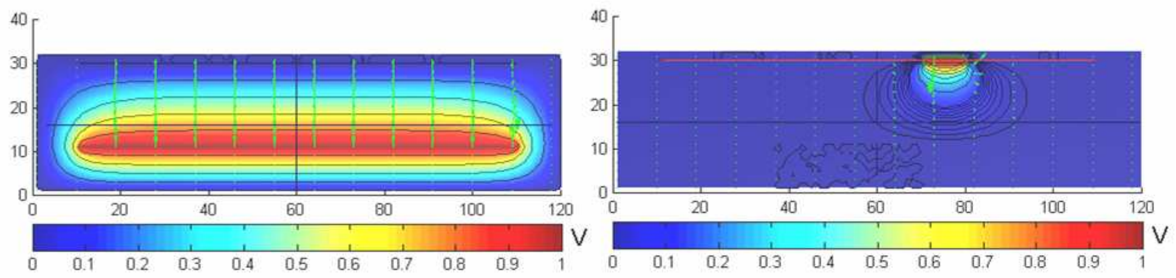

Figure 5.14: Weighting field of a planar electrode and a single pixel of a 64 pixels detector ($9.9 \times 9.9 \times 2$ mm^3). Note the special shape of the pixel weighting field, which causes the small-pixel-effect.

The shape of the field plays an important role in the detector functioning. In Sect. 3.5.4 I explained that small-pixels create a special weighting field. It is shaped in such a way that charge carriers induce most of their signal near the pixel. If electrons are collected at the pixel side, the hole contribution is then relatively small. Hole charge loss resulting in loss of signal, is therefore limited.

MGS-CdTe V1.0 is a perfect tool to make preliminary studies on the weighting field of (yet) non-existing geometries. The present prototype detectors, that are tested with the IDeF-X V1.0 ASIC, have all 64 pixels of 1 mm^2 pitch. Technologically it is rather difficult to make a proper rooting from these small pixels to the electronics input channels. In the case of 256 pixels of 500×500 μm^2 this is even a bigger challenge. In order to avoid the large step from 1 to 0.5 mm pixels, we want to use prototype crystals with just several small pixels in the middle, surrounded by a large guard ring. This allows a relatively easy connection to the chip, but with the desired pixel size.
MGS–CdTe V1.0 is used to test the functioning of these crystals in this specific configuration. We are especially interested to know if the shape of the pixel weighting field is changed by the large electrode surrounding them.
Fig. 5.15 shows, on the left, the detector configuration in 2-D. The model is 10 mm large and 1, 2, 3 and 4 mm thick (the spacing between two grid points is 0.05 mm). Five small pixels of 0.5 mm are positioned in the center surrounded by two large pixels (representing the GR). The weighting field of the centre pixel is shown at every thickness.
On the right, the same detector is shown but with a varying number of pixels. In the upper plot, the detector has only one small pixel, the middle plot shows four pixels and the one below has fifteen small pixels.
The shape of a single pixel weighting field is not altered by the presence of a larger guard ring nor by a varying number of pixels next to it.
The influence of the detector thickness on the weighting field has already been explained in Sect. 3.5.4 with the help of Fig. 3.16. I show the same figure here again (see Fig. 5.16). On the left, the weighting potential (V$_{weight}$) is depicted, created by the centre pixel, as a function of the normalised position (x/Z) inside the detector (below the pixel), for four

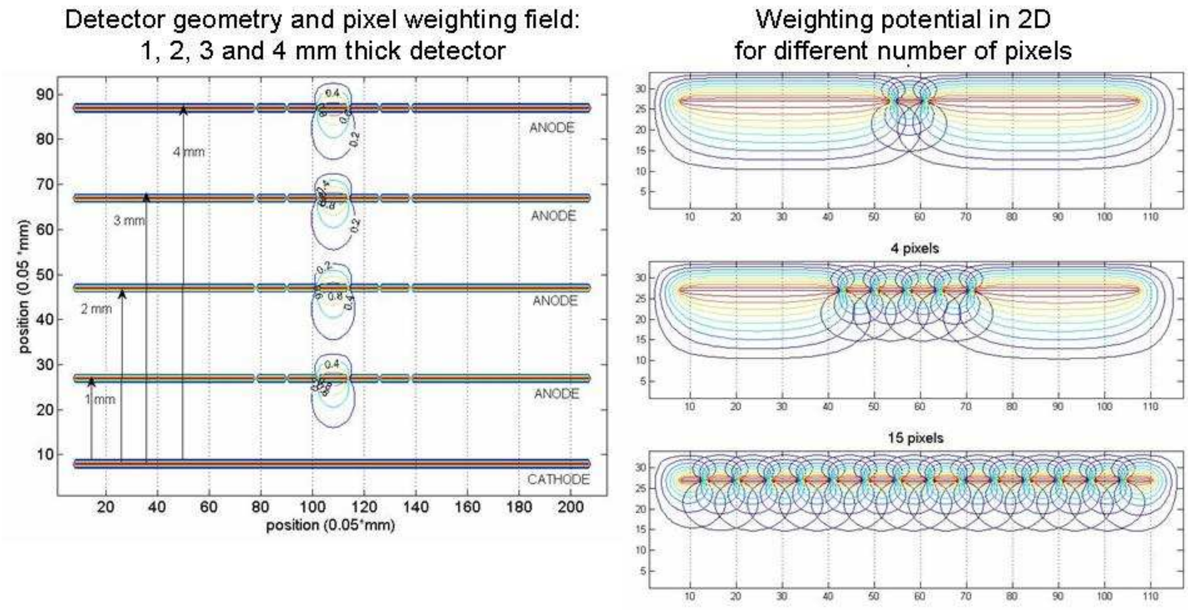

Figure 5.15: Left: pixel weighting field for different detector thickness. Right: weighting fields in case of a varying number of pixels.

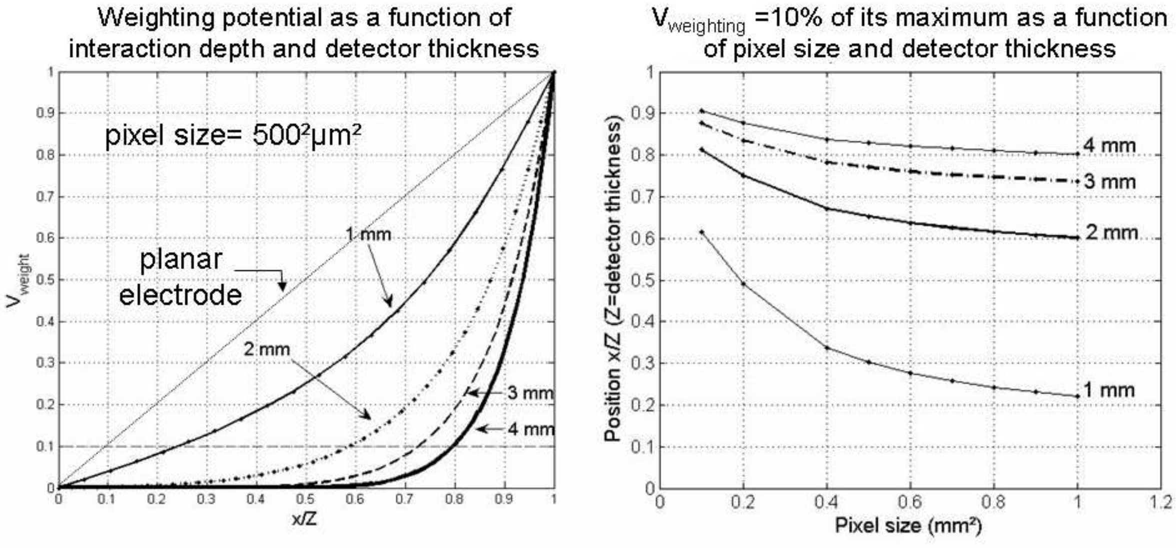

Figure 5.16: Left: weighting potential as a function of position (x/Z) and detector thickness. Right: position of V$_{weight}$=0.1 V as a function of pixel size and detector thickness.

different detector thicknesses. The planar electrode is located at x/Z=0 and the pixels at x/Z=1. The pixel size is fixed at 0.5 mm. The straight line corresponds with a planar electrode (no small-pixel-effect).

The figure clearly shows that the small-pixel-effect gets stronger, as the pixel-size in relation to the detector thickness becomes smaller. Thick detectors with small pixels are

therefore especially suited to exploit the effect. But, as I explained in the discussion of the previous chapter, thick detectors demand a higher bias voltage to guarantee quick charge collection. This leads to a higher leakage current and thus more noise. A compromise between pixel size, detector thickness and bias voltage, must therefore be found.
The right side of the same figure shows the normalised position at which the weighting potential has reached 10% of its maximum value (0.1 V). It is plotted as a function of the pixel size and for different detector thicknesses. In a 2 mm detector with 1 mm^2 pixels, the charge carriers see V_{weight}=0.1 V at x/Z=0.6 while for a 1 mm thick detector the position will be x/Z=0.22. In the latter case, this means that even for interactions near the (planar) cathode, the unwanted hole contribution to the signal will remain significant.

Suppose now, that we want to know the signal on a pixel which is next to the pixel to which the charge carriers drift. This was already nicely illustrated in Fig. 3.17, in which I showed the trajectory of the charge carrier moving in the weighting field of the neighbour. Fig. 5.17 shows the weighting potential as seen by the charge carrier in the same situation (labeled “outside pixel region”). It first experiences an increase of the potential, up to a certain maximum and then decreases to zero as it touches the neighbouring pixel. In Sect. 5.6 I will show that an arrival at zero voltage is not always the case, due to charge loss.
The second curve, labeled “center of pixel”, depicts the potential as seen by a charge carrier drifting to the center of the pixel considered. It clearly experiences the small-pixel-effect: the potential quickly rises when approaching the pixel.

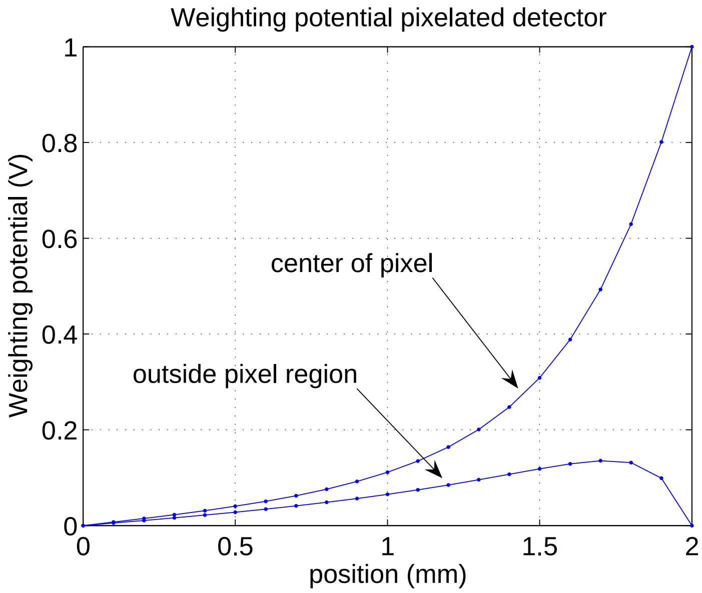

Figure 5.17: The weighting potential seen by a charge carrier moving in the field of the target pixel (labeled “centre of pixel”) and in the weighting field of a neighbouring pixel (labeled “outside pixel region”).

5.2.5 Induced signals

Now the velocity at every point of the electron and hole trajectory and the weighting fields are known, I can calculate the induced current and charge on the electrodes using Eq. 3.40 and 3.41.

Using the deposited energy of the interaction, delivered by GEANT4, I first calculate the number of e^- /h^+ -pairs created inside the crystal. The number is slightly varied in such a way, that if we would take the same energy deposition for many interactions, the number of e^- /h^+ -pairs would follow a normal distribution. In addition I add the Fano-factor. This leads to the following expression for the number of charge carriers, N:

$$N = \sqrt{F \times E_i/w} \times randn(1) + E_i/w \tag{5.7}$$

With N the number of e^- /h^+ pairs, F the Fano factor, E_i the interaction energy (eV) and w the pair creation energy (eV/pair). Randn(1) returns a pseudorandom, scalar value drawn from a normal distribution with mean 0 and standard deviation 1.

After that, the charge loss is included using Hecht's relation (Eq. 3.40 and 3.41). The vector containing the (same) number of pairs at each position, is multiplied by the following exponential function:

$$N_i = N \times e^{-t_i/\tau} \tag{5.8}$$

With N_i the number of pairs at time $i \times \Delta t$, t_i the time and τ the electron or hole life time.

The above vector, containing the corrected number of pairs at each position, is then multiplied by the scalar product of velocity and electric weighting field, and the unit charge. The result is a vector with the induced current at every position of the trajectory. Its integral is the total induced charge as function of time.

In Fig. 5.18 I show the total induced charge for different interaction positions, in the same detectors as I showed before (see Fig. 5.13). The distance between two grid points 0.1 mm. The detector measures 10.1-by-10.1 mm^2 and is 2 mm thick. It has four pixels with a varying size depending on the inter-pixel gap. In a) and b) the pixels are 5-by-5 mm^2 with a 0.1 mm gap, while in c) and d) the gap is 2.1 mm, and the pixels 4-by-4 mm^2.

In a) the interaction takes place above the corner of one of the pixels (1), near the planar electrode. The signal comes mainly from the electrons. We see that the charge induction starts slowly and increases when approaching the pixel. A signal is generated on neighbouring pixels as well, but becomes zero when the charge arrives at the pixel.

In b) the interaction takes place in the middle of the detector, above the centre of a pixel. The induced signal consists of two components: the first part is induced by electrons and holes, while the second part is due to holes only, which are much slower.

In c) the interaction takes place in the middle of the detector, near the planar electrode. Due to smaller pixels and a large gap, the small-pixel-effect is relatively strong.

The last plot, d), shows an interaction in the exact middle of the detector. The pixel to which the electrons drift, shows an initial quick signal (electrons+holes), followed by a slower component (holes only). It is interesting to note that neighbouring pixels can even

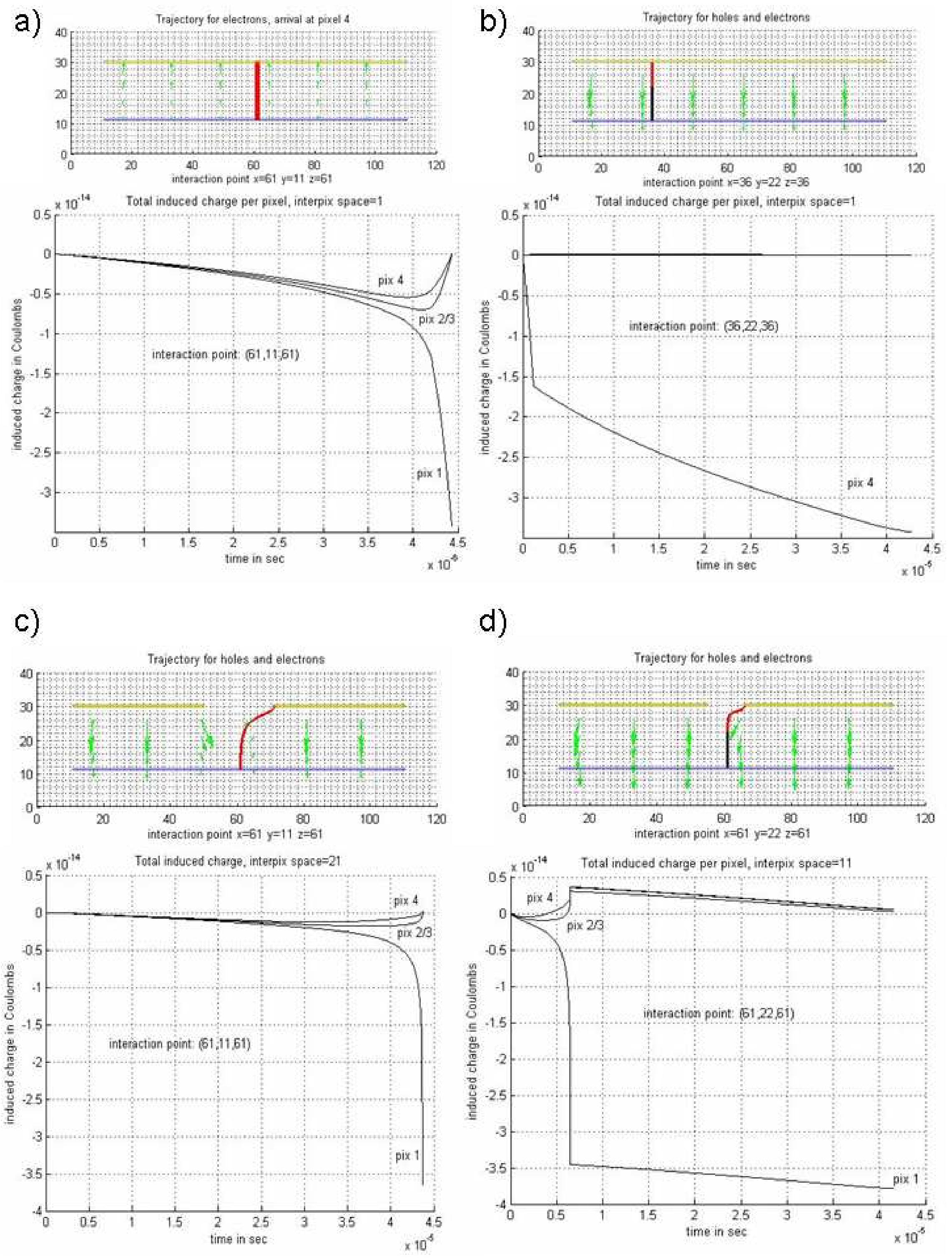

Figure 5.18: a) Trajectory and induced charge after an interaction near the planar electrode, above the corner of one pixel. Interpixel spacing is very small (0.1 mm) b) Interaction in the middle of the detector, above the centre of a pixel. c) Interaction near the planar electrode, in the middle of the detector. Interpixel spacing relatively large: 2.1 mm. d) Interaction exactly in the middle of the detector, again with a large gap of 2.1 mm and a pixel size of 4-by-4 mm^2.

have a bipolar induced charge signal, which implies that the induced current switches sign two times.

From these plots it has become clear that neighbouring pixels are also subjected to signal induction, even when there is no physical charge drifting towards them. I would like to emphasise that this is a different effect than that caused by the charge cloud, as explained in the previous section (Sect. 5.1.4). Instead of interactions taking place above the pixels and inducing a signal, it is the special shape of the weighting field that causes an electromagnetic signal induction on neighbouring pixels.
These currents are characterised by the fact that their integral, the induced charge, should be exactly be zero, if all carriers arrive at the electrode. This is only true if there is no charge loss present. Since real detector experience a certain amount of charge loss, mainly due to trapping of holes, the induced currents of electrons and holes do not cancel out each other anymore, and a non-zero induced charge can exist.
The value and shape of induced signals on neighbouring pixels, contains precious information of the interaction position, timing and the amount of charge loss.
An excellent article which discusses in detail the signal induction on pixels of semiconductor detectors, and which explains the effects I mentioned above, is written by Eskin, Barrett and Barber (1999).

5.3 Electronics modelling

The simulated induced currents serve as an input to the electronics model of the IDeF-X V1.0 ASIC. To simulate the electronics response I use the numerical impulse response of the ASIC which is obtained from the Cadence program.
Cadence is a well-established design and simulation program which consists of front-to-back tools and services for all aspects of semiconductor design.
Fig. 5.19 shows the impulse response of IDeF-X V1.0 at a peaking time of 9.6 μs. The amplitude is expressed in volts per femto-Coulomb (V/fC). The choice of this peaking time is based on measurements results. It showed in general the best spectroscopic performances.
The induced current, expressed as Coulombs per second for each time step, is convolved with the impulse response as follows:

$$V_{out}(t) = \int_{j-k}^{j=0} H(t-u) I_{ind}(u) du \tag{5.9}$$

With V_{out}(t) the output signal, H(t) the impulse response and I$_{ind}$(t) the induced current. V_{out}(t) is the amplitude as a function of time measured at the output of the ASIC, in case of *zero* electronics noise. By representing the maximum amplitude of each simulated pulse in a histogram, and after proper calibration, the energy spectrum is obtained which can be compared with measured spectra.

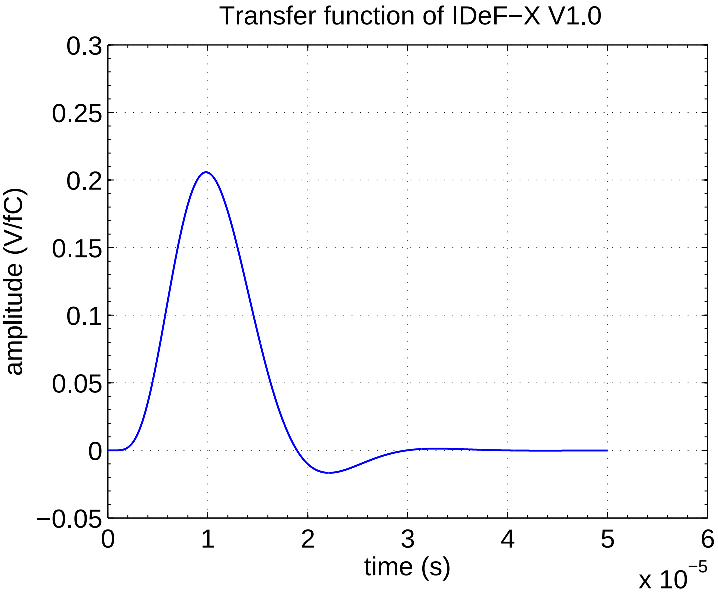

Figure 5.19: IDeF-X V1.0 numerical transfer function.

In order to simulate the electronics noise, the impulse response function should in principle be completed with a second transfer function simulating the exact noise contribution of each element in the ASIC. This noise model has recently been finished but could not be implemented yet. For the next version of MGS–CdTe, this should be included however.
In the present version, I use a simple but effective approximation of the noise. In Sect. 4.2 I showed that the standard variation of the maximum amplitude of a real detector can be expressed as a specific number of e$^-$ ENC. In the simulation I do the same.
First, I sum the induced currents from all interactions created by a single primary photon. This total current is then convolved with the impulse response, which returns the simulated output voltage. To vary the maximum amplitude of this signal, I first need the standard deviation as a function of ENC:

$$V_{std} = ENC \times 1.609 \cdot 10^{-9} \times V_{transfmax} \times 10^{-15} \tag{5.10}$$

With $V_{transfmax}$ the peak of the impulse response, which is equal to 0.2058 V/fC. This is implemented as follows:

$$V_{new} = V_{max} + \mathrm{randn}(1) * V_{std} \tag{5.11}$$

With randn(1) a random number generator that draws from a normal distribution with mean zero and standard deviation one. By multiplying it with V_{std} and adding V_{max}, the correct varying maximum amplitude V_{new} is obtained.

5.4 Modelling and simulation of a single pixel CdTe Schottky detector

In this section I show the results of the detector response simulation of a single pixel CdTe Schottky detector. Its geometry was already shown in Fig. 5.10 (GEANT4) and 5.11 (Matlab).

5.4.1 Parameter settings

The optimal cut in range in GEANT4 has been calculated before and is 10 μm . The spacing between two grid points corresponds to 0.05 mm and the time step is taken 0.1 ns. In order to operate the diode in reverse mode, a bias voltage of +350 V is applied at the indium planar electrode. In this way the holes, and not the electrons, are collected at the pixel. The small-pixel-effect is negligible because the detector is only 0.5 mm thick and has a large pixel of 1 mm^2.

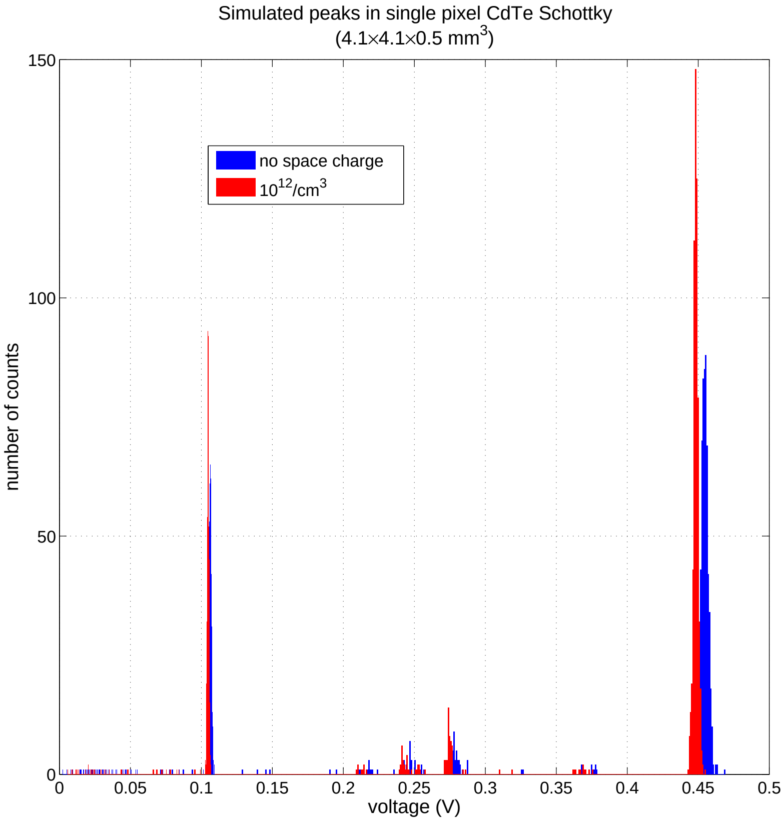

Figure 5.20: Simulated 13.9 keV and 59.54 keV energy peaks with a single pixel CdTe Schottky detector, in the case of 0 (blue) and $10^{12}/\text{cm}^3$ (red) impurities inside the crystal. Only a small difference in gain and spectral resolution is observed (0.71 keV (FWHM) instead of 0.74 keV (FWHM) at 59.54 keV). No electronics noise is added.

Photons, having energies equal to those of the ^{241}Am spectrum, are shot on the detector from the pixel side. The spectrum comprises the following main energies: 59.54 (35.9%), 26.35 (2.4%), 20.8 (4.7%), 17.8 (18%), 13.9 (12.5%) and 11.9 (0.8%) keV.

I do not consider impurities present in the crystal. A simulation of the 13.9 and 59.54 keV peak only, with an impurity concentration of 0 and $10^{12}/\text{cm}^3$, shows no significant difference (see Fig. 5.20). The inclusion of impurities only leads to a small loss of gain at higher energies due to a modified electric field, and a slightly better energy resolution at 59.54 keV (0.71 keV instead of 0.74 keV (FWHM)).

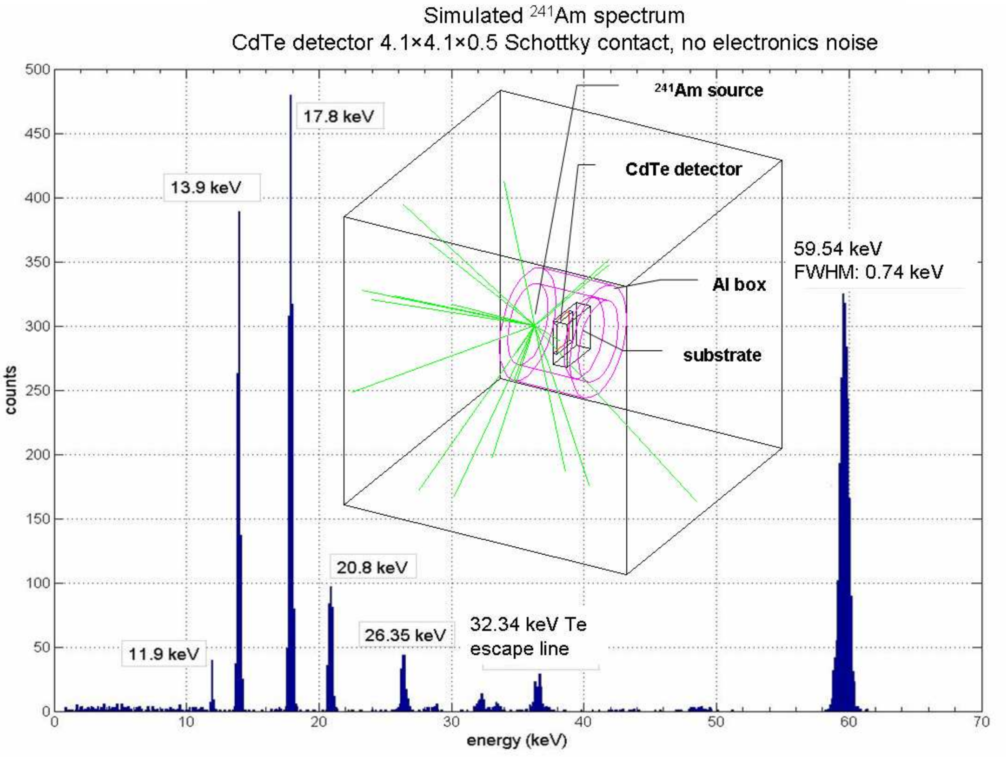

Figure 5.21: Simulated ^{241}Am spectrum of a single pixel CdTe detector in its housing. The program uses a spacing between two grid points corresponding to 0.05 mm and a time step of 0.1 ns. A bias voltage of 350 V is applied.

5.4.2 Simulated ^{241}Am spectrum

Fig. 5.21 shows the simulated spectrum using the above operating conditions. It clearly shows the different energy lines, including the escape lines of Cd and Te.

The limited energy resolution is due to a variation of the number of electrons/holes pairs created inside the detector, and a position dependent signal induction, due to charge loss. At this moment no electronics noise is included yet. An excellent energy resolution of 0.74 keV (FWHM) at 59.54 keV and 0.24 keV at 13.9 keV is obtained. Unfortunately, the values are not representative for the real detector performances since they do not include the electronics noise yet. They represent the intrinsic resolution limits of the detector. In other words, this simulation predicts that the diode should be able to reach the above energy resolution, if no read-out electronics are connected to it.

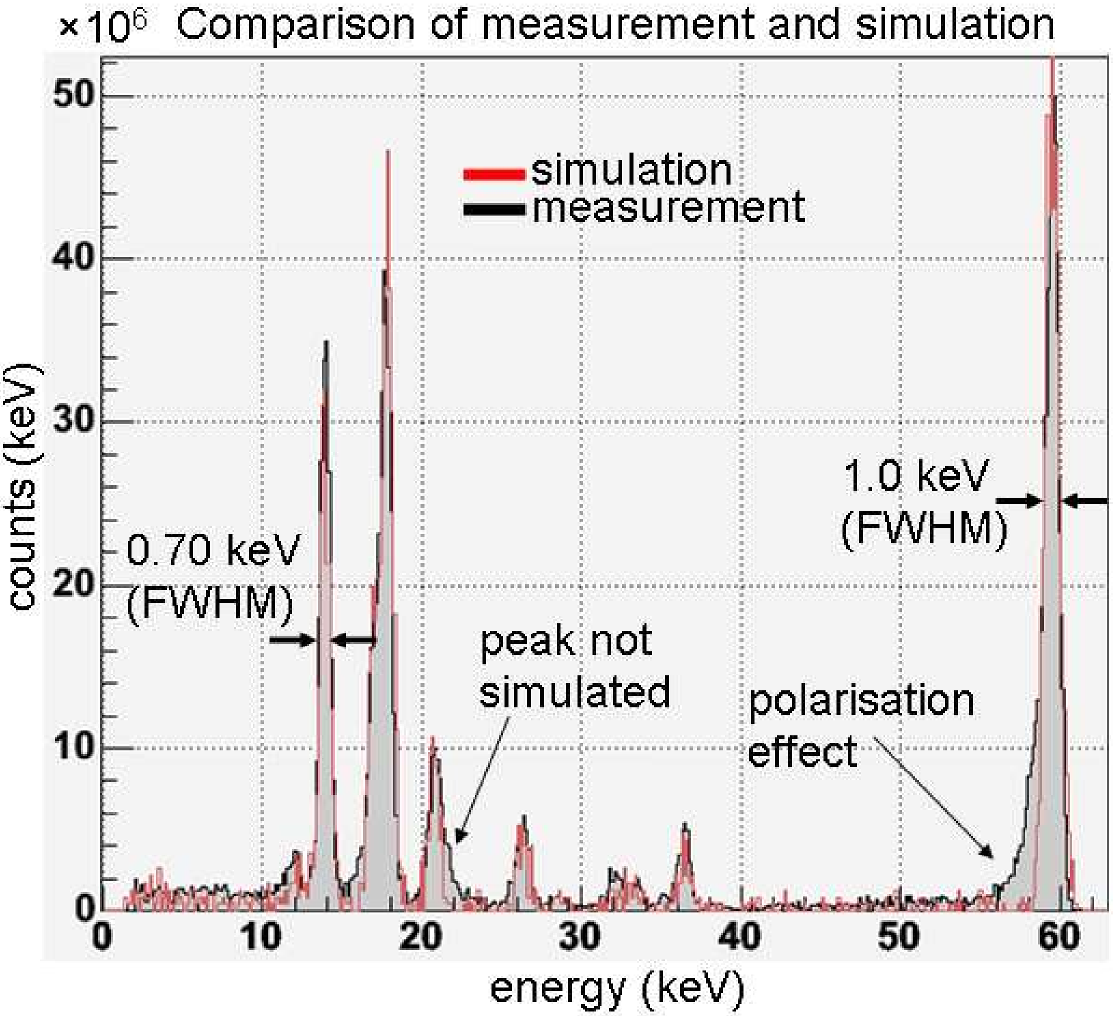

Figure 5.22: Comparison of the simulated (red) and measured (black) ^{241}Am spectrum obtained with a $4.1 \times 4.1 \times 0.5$ mm^3 CdTe detector, with Schottky contact. The bias voltage is 350 V and the temperature 22^{o}C . The signal is taken from the pixel.

5.4.3 Comparison

Representative noise values are obtained by using the results of the leakage current measurements on the real detector. A current of ∼15 pA was measured, corresponding to 66 e$^-$ ENC electronic noise (including the noise from capacitance of detector and setup). Using the method from the previous section (see Eq. 5.10 and 5.11), I implement this specific noise in the simulation code.

I now have the (nearly) complete energy spectrum of ^{241}Am (with some peaks missing, that are not simulated), which is, after proper calibration, compared with a real measurement, obtained with exactly the same operating conditions. This important result is shown in Fig. 5.22.

The agreement between simulation (in red) and measurement (in black) is excellent. The simulated peaks nicely overlap their counterparts in the real spectrum. Both show an energy resolution of ∼1.0 keV (FWHM) at 59.54 keV and 0.70 keV at 13.9 keV. The time-dependent polarisation effect in the real detector, which is revealed by the tail at the left of the 59.54 keV peak, is not simulated. In Sect. 5.5 I present a method to implement this.

Evidently, this good agreement, in shape and peak proportions, is very important, because it verifies the correctness of the complete simulation chain. It says that simulated signals can be sufficiently trusted to explain and predict detector behaviour.

5.4.4 Predictions

An example of its predictive capacities is depicted in Fig. 5.23, in which I present the simulated energy resolution as a function of electronics noise for different energy peaks. These results are obtained by fitting the peaks in simulated spectra with gaussian functions and taking their FWHM ($= 2.35 \times \sigma$). The error bars correspond with the fit error. The fact that the curves are not smooth, is due to the random nature of the noise that is added.

The simulation predicts that, without any noise, the detector should in principle be able to have an energy resolution of 0.74 keV at 59.54 keV and 0.24 keV at 13.9 keV. However, since the read-out electronics has a intrinsic noise of 32 e^- ENC, the best resolution we could reach, is ∼0.8 keV at 59.54 keV.

With the single pixel CdTe Schottky detector, having 66 e^- ENC noise, a resolution of ∼1.0 keV at 59.54 keV is predicted. This exactly matches the measurement (see Sect. 4.6.1).

5.5 The simulation of polarisation

As explained in Sect. 3.6, CdTe detectors equipped with indium electrodes experience a polarisation effect. Since this effect is time-dependent, it is difficult to implement it into the simulation. The electric field must constantly be re-calculated which is a time-consuming process. For example, the calculation of the potential map of the above detector with a grid size of 0.05 mm takes about 10 minutes (with a 1.86 GHz processor). Also, the time to calculate the signal of a single interaction can rise up to almost two minutes, in case of a time step of 0.1 ns (and a mean calculation time of ∼60 sec.) In order to have a rather representative energy peak, several hundreds of photons, each having multiple interactions, must be simulated. A single peak simulation may therefore take easily hours of calculation, even without the modification of the potential map.

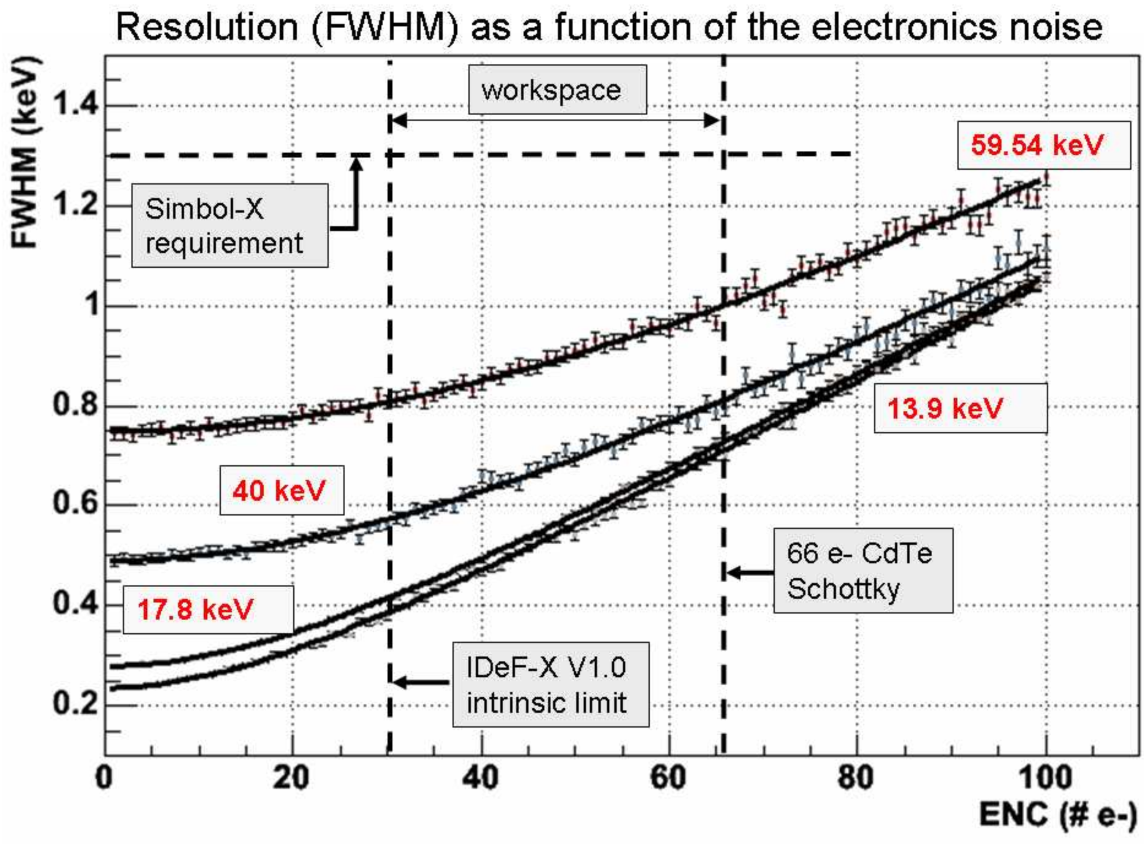

Figure 5.23: Energy resolution as a function of (electronics) noise (in ENC) at four different energies. This graph is obtained by fitting the simulated energy peaks with gaussian distributions and taking the FWHM. The error on the resolution consists of the fitted error plus the calibration error.

5.5.1 Variable hole lifetime

To avoid time-consuming calculations I propose an alternative method, based on the explanation of Bell on the polarisation effect (see Sect. 3.6). He said that, as time passes, different space charge regions appear inside the detector, resulting in a non-homogeneous electric field.

In the space charge region close to the positive indium electrode, the electric field will be stronger than in the rest of the detector. When holes and electrons move in the zone with the *weak* E-field, their velocity becomes smaller and they are easily exposed to charge trapping. Since electrons are ∼10 times faster than holes, this concerns the holes most, and I will therefore concentrate on them.

The above situation is comparable as if holes would have a shorter lifetime, implying quicker charge loss (see Eq. 3.39).

Another possibility to create a comparable situation, without touching the electric field, is a modification, and in this case, a lowering of the hole mobility. Then, the velocity of holes is decreased, meaning that they will spent more time inside the volume concerned, and

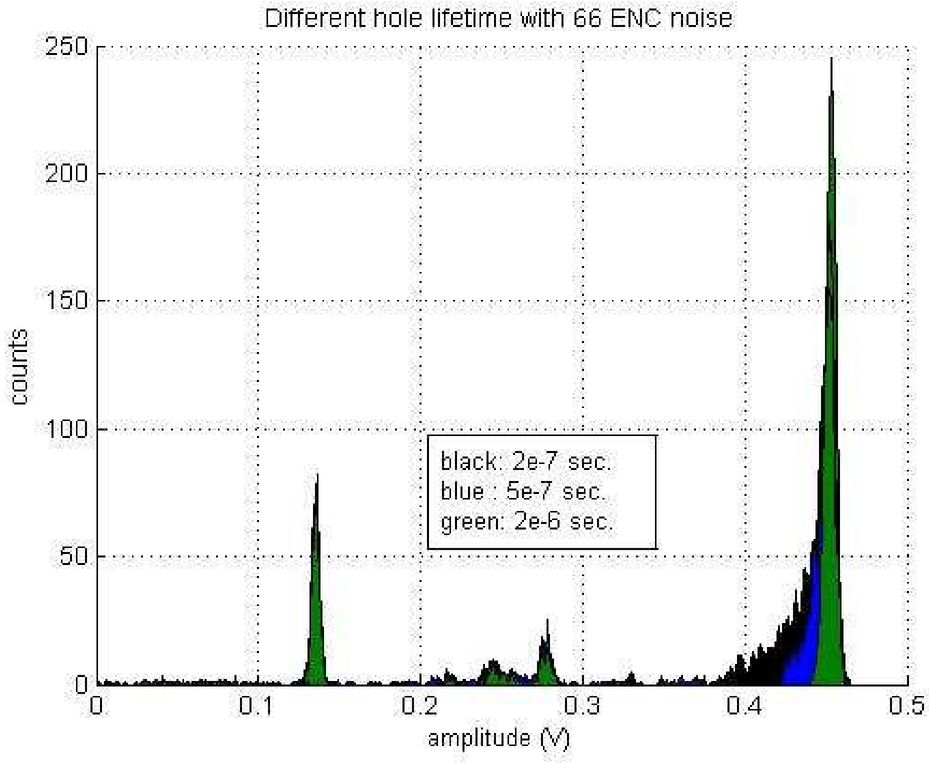

Figure 5.24: Simulated detector response at two different energies, 17.8 and 59.54 keV, for different hole lifetimes: τ_{hole}= 2e-7 s, 5e-7 s and 2e-6 s. For short lifetimes the charge loss increases as can be seen by the large tail. The effect is negligible for the 17.8 keV peak.

therefore experience more charge trapping. Another effect of a change in hole mobility, is that the amplitude of the induced signal is modified too, because of the lower charge carrier velocity.

I did not simulate the influence of hole mobility yet. Since this demands a modification deeper in the program (a recalculation of the velocity matrix) I chose to test a hole lifetime modification first.

I therefore use MGS–CdTe to simulate the 17.8 keV and 59.54 keV peak, at three different values for the hole lifetime: 2e-7, 5e-7 and 2e-6 s (and keeping the electron lifetime constant at 1.2e-6 s). The results are shown in Fig. 5.24.

We can clearly see the broadening of the high energy peak to lower values, with decreasing hole lifetime. The low energy peak on the other hand, is not influenced. This is in agreement with real measurements. Low energy photons interact near the negative electrode. Therefore only the fast electrons “see” the weak field region. Due to their limited charge loss, the polarisation effect is then limited.

The above method can therefore be considered as a simple and rather good approximation of the polarisation effect. Even better would be to slowly decrease the hole lifetime during the simulation. In that case, the time dependence can be approximated too.

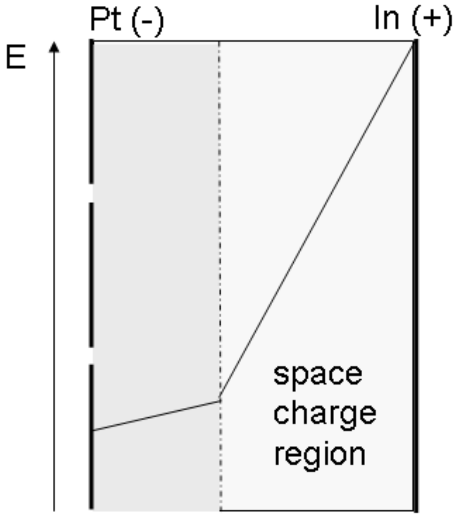

Figure 5.25: Artificially created electric field, used in the simulation. A strong field exists near the indium electrode due to the creation of a space charge. A weak component exists in the rest of the detector.

5.5.2 Variable electric field

A constant modification of the space charge and therefore the electric field, is a time-consuming process and therefore not an option in the final simulation program. But, to see the influence of the existence of two different space charge regions, I simulate one static case.

Therefore I create first an artificial electric field map, which is to my opinion representative for the real situation. I schematically depicted it in Fig. 5.25. It has a strong component near the positive electrode due to the heavy space charge region, and a weak component in the rest of the detector.

This map in 3 dimensions serves as input for the program and is used to calculate the velocity matrix (using the correct values for the electron and hole mobilities).

Its effect on the simulated energy spectrum is depicted in Fig. 5.26. Three histograms are shown, each corresponding with the 59.54 keV peak for three different situations: 1) brown: a hole lifetime of 2e-6 s and constant electric field (I do not use the modified field of Fig. 5.25) , 2) blue: a hole lifetime of 5e-7 s and constant electric field, and 3) green: a hole lifetime of 2e-6 s, in combination with the modified electric field.

The brown histogram shows nearly no tailing. The hole charge loss is negligible. If the hole lifetime is decreased, tailing occurs as shown by the blue histogram, due to increased hole loss. Both peaks have however the same gain. The green histogram shows a considerably lower gain in combination with heavy tailing.

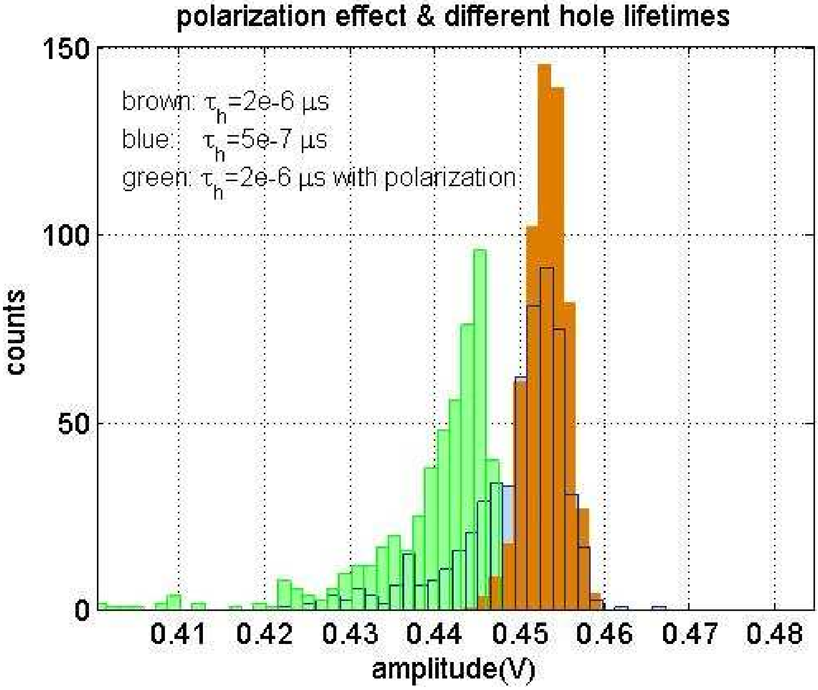

Figure 5.26: Simulated 59.54 keV peaks for three different cases: 1) brown: hole lifetime is 2e-6 s, 2) blue: hole lifetime is 5e-7 s, and 3) green: hole lifetime 2e-6 s and a modified electric field.

5.5.3 Conclusion

I have presented an alternative method to simulate the polarisation effect, namely the modification of the hole lifetime. It leads to a correct simulation of the tailing in the high energy peak due to an increase of charge loss, but does not simulate the shift to the left of the peak value. However, the method is easy to implement, has no influence on the calculation time, and, if varied in time, can model the time dependence of polarisation.
The best simulation of polarisation is of course a variable space charge region inside the crystal. This has been illustrated by one static case, in which I approximated the two space charge regions by a weak electric field near the negative electrode and a strong component near the positive electrode. This gives the correct tailing and a shift of the high energy peak.

5.6 Simulation of 64 pixels detectors

MGS–CdTe V1.0 has proven its power and capabilities with the excellent results obtained from the simulation of a single pixel CdTe Schottky detector. In this section, I present the results of simulations of 64 pixels Cd(Zn)Te detectors with ohmic contacts.

5.6.1 Geometry model

The GEANT4 model of this detector is very simple. It consists of a block of Cd(Zn)Te of $9.9 \times 9.9 \times 2$ mm^{3}covered with platinum electrodes of 1000 Å thick. As explained before, in the GEANT4 geometry it is not necessary to model the pixels.

The corresponding Matlab model is shown in Fig. 5.27. The spacing between grid points is 0.1 mm. Smaller values are not possible due to a limitation of the maximum matrix size Matlab can handle (because of limited memory of the PC). The numbers on the axes must be multiplied by 0.1 mm to obtain real values.

On the right, is the simulated potential map which is calculated using the successive over-relaxation (SOR) method. The maximum voltage difference between two iterations is set to 1e-5. The bias voltage is 500 V applied at the pixel side, and the planar electrode is at ground potential. In future simulations this should be inversed, that is, the pixels (and the borders of the grid) should be set at zero volt, and the planar electrode at -500 V. In that way, the model is completely compatible with the real configuration and border effects are included. (For programming reasons I had to switch the potential, but this has now been adapted. However, the presented results are all obtained with the pixels at 500 V).

Next, the corresponding electric field and velocity map are calculated. The electron and hole mobilities are taken from Table 3.1: $\mu_e = 1350$ and $\mu_h = 120$ cm^2/V.s. Since CdZnTe or CdTe with ohmic contacts will not, or only be slightly depleted (there always exists a small difference between the metal and semiconductor work-function), I do not consider space charge. In combination with an inter-pixel spacing of only 0.1 mm, this leads to a homogeneous electric field inside the crystal. If pixelated detectors with diced indium contacts are considered, space charge must however be taken into account.

After that, the weighting field, which is used to obtain the induced signal, of each electrode is calculated (see Fig. 5.14). The electron lifetime is τ_e=3e-6 s and τ_h=1e-6 s for the holes. A Fano factor of 0.14 is used for spectra response calculation.

5.6.2 Induced signals

To study the different induced signals, I first consider the case in which a single interaction deposits 1 keV above the centre of a pixel. I study the signals on the target pixel and its eight neighbours. The signal on the planar cathode is used as a comparison.

Fig. 5.28 shows the induced current on the nine pixels of a 3-by-3 matrix. The green curve corresponds to the hole, the red to the electron and the blue to the total induced current. Since the interaction is close to the cathode, the signal is mainly generated by electrons.

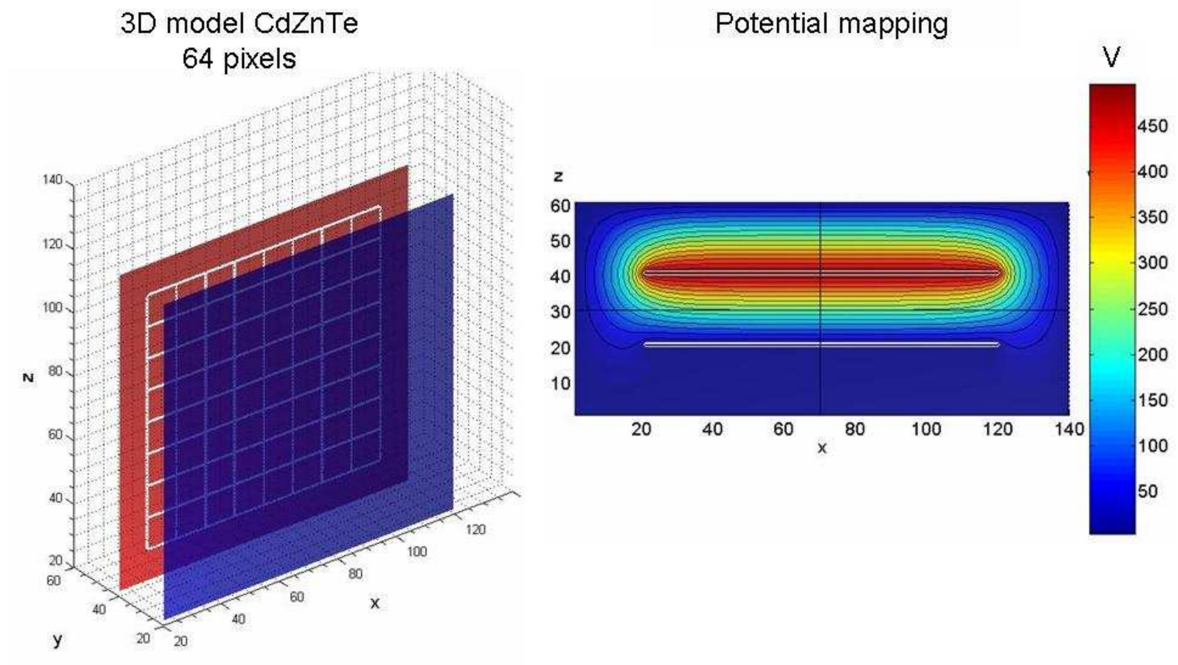

Figure 5.27: Left: 3D model of a CdZnTe detector of 9.9 × 9.9 × 2.0 mm^3 with 64 pixels of 0.9 mm^2 and a 0.9 mm guard ring. The distance between two grid points is equal to 0.1 mm. Right: the simulated potential map. The detector is biased at 500 V at the pixel side. The electric field in the bulk of the detector is nearly homogeneous.

Its duration is therefore very short, only ~6e-8 s.
The signal of the centre pixel clearly shows the small-pixel-effect. It starts nearly at zero and quickly rises when approaching the pixel. I have to remark here, that the shape of the last part of the signal is not completely correct. Since I use a limited time-step (1 ns in this case), MGS–CdTe cannot exactly simulate the end of the trajectory. This is a limitation of the program which I will discuss in detail in Sect. 5.7.
Regarding the Fig. 5.28 again, we see that neighbouring pixels show a signal as well. Due to the special shape of the pixel weighting field, the induced currents can be bipolar (as explained in Sect. 5.2.5). They first start positive and then switch sign to become negative. If no charge loss is present, their integrals should exactly be zero.

Fig. 5.29 depicts the induced currents in case of an interaction in the middle of four pixels (in the upper left corner). All four have exactly the same maximum amplitude ($\sim 2.7 \cdot 10^{-10}$ A), while the neighbouring pixels show again a bipolar signal.
Like in Fig. 5.18, we see that the shape and amplitude of the induced signals are position dependent. As explained before, it would be very useful to exactly know their shape and amplitude, since this contains precious information on the exact interaction position and timing, and, as I will show later on, the amount of charge loss.
Of course, the above signals first need to be convolved with the electronics response function. In Fig. 5.30 I show the simulated signals after convolution, of several individual

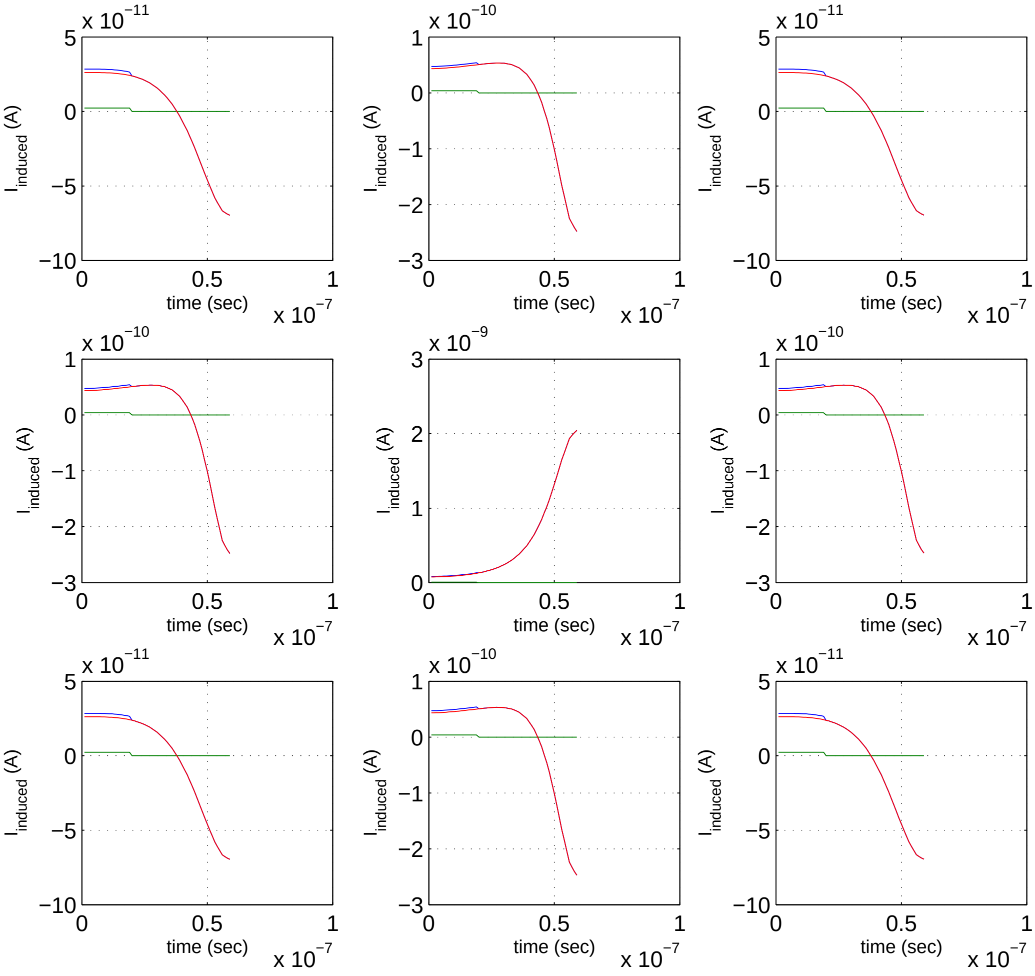

Figure 5.28: Induced currents on nine neighboring pixels after an energy deposit of 1 keV near the cathode right above the center pixel. Red is the electron signal, green the hole signal and blue the sum of both.

interactions created by a single photon hitting the middle of the centre pixel. The actual output of IDeF-X is the sum of the signals.

All curves show a certain amount of under- or overshoot. For the target pixel this is only due to the electronics filtering of the ASIC, but for the neighbours, this is also due to the presence of the bipolar current.

We directly observe that the signals on the neighbouring pixels are not negligible. Their (negative) amplitude can easily reach values equal to several percents of the main positive signal on the target pixel. Unfortunately, IDeF-X V1.0 is designed in such a way that it can only measure one signal polarity. This means that, since the main signal (on the target pixel) is positive, the only information we can obtain from the neighbours, comes from the positive blob. But as we can see in the same figure, its amplitude is very small

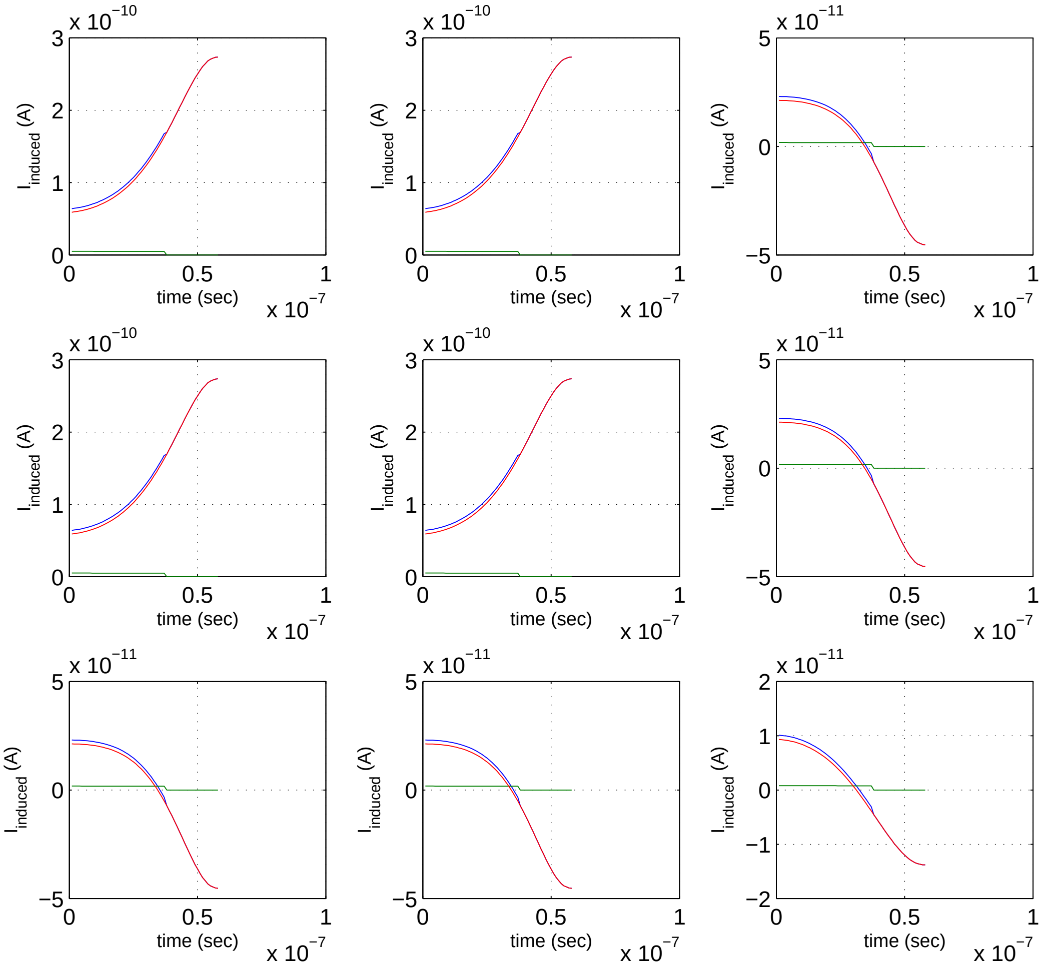

Figure 5.29: Induced currents on nine neighbouring pixels after an energy deposit of 1 keV near the cathode in the middle of four pixels. Red is the electron signal, green the hole signal and blue the sum of both.

and will be very difficult to detect.

Therefore, if we want to get your hands on the information hidden in the signals of neighbouring pixels, the design of future versions of IDeF-X must include the possibility to read bipolar signals and have a sufficiently low noise.

5.6.3 Signals with and without charge loss

As explained before, if there would be no charge trapping, pixels would always detect the full signal of the charge carriers created in a photon interaction. The signal would be independent of the interaction depth. And any point charge moving outside the pixel boundary will create zero net charge. On the other side, if charge loss is included, due to

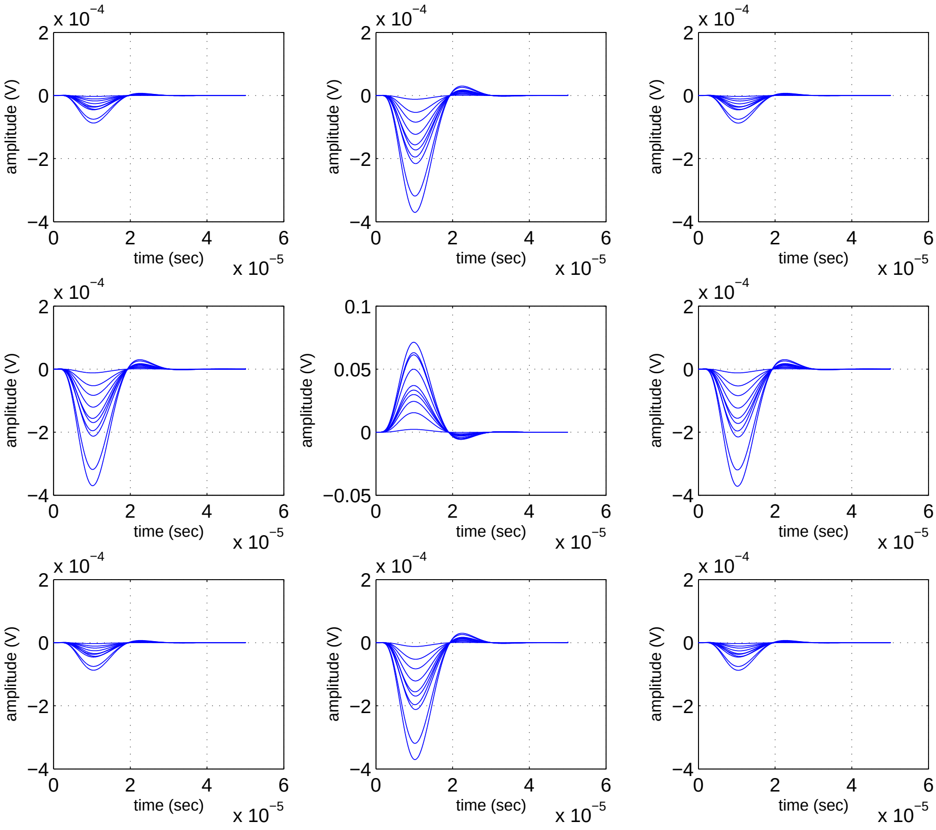

Figure 5.30: Complete detector response of nine neighboring pixels in case of several interactions above the center pixel. The induced currents are convoluted with the IDeF-X v1.0 transfer function.

charge trapping, negative charges can appear at neighbouring pixels as well.

To study both situations, I simulate interactions in the pixelated CdZnTe detector ($9.9 \times 9.9 \times 2$ mm^3) again (500 V bias). I consider three different interaction positions: in the centre of a pixel close to the planar electrode, in the middle of the detector and near the pixel side. Furthermore, I simulate the interactions with and without charge loss.

The results are depicted in Fig. 5.31 and show the induced current and charge on the centre pixel (red), the cathode (blue) and the total signal of all neighbours plus guard ring (black). The curves that include charge loss are dotted.

In the case of no charge loss, the total induced charge of the pixel and cathode must exactly be identical. The total induced charge on the neighbours and guard ring must therefore be zero.

If charge loss is included, a part of the charge is trapped inside the crystal and seen as a small negative charge on neighbouring pixels. The planar electrode does not experience this effect and behaves as if it were a planar detector

The upper plot shows the induced currents and charge, after an interaction near the pixel

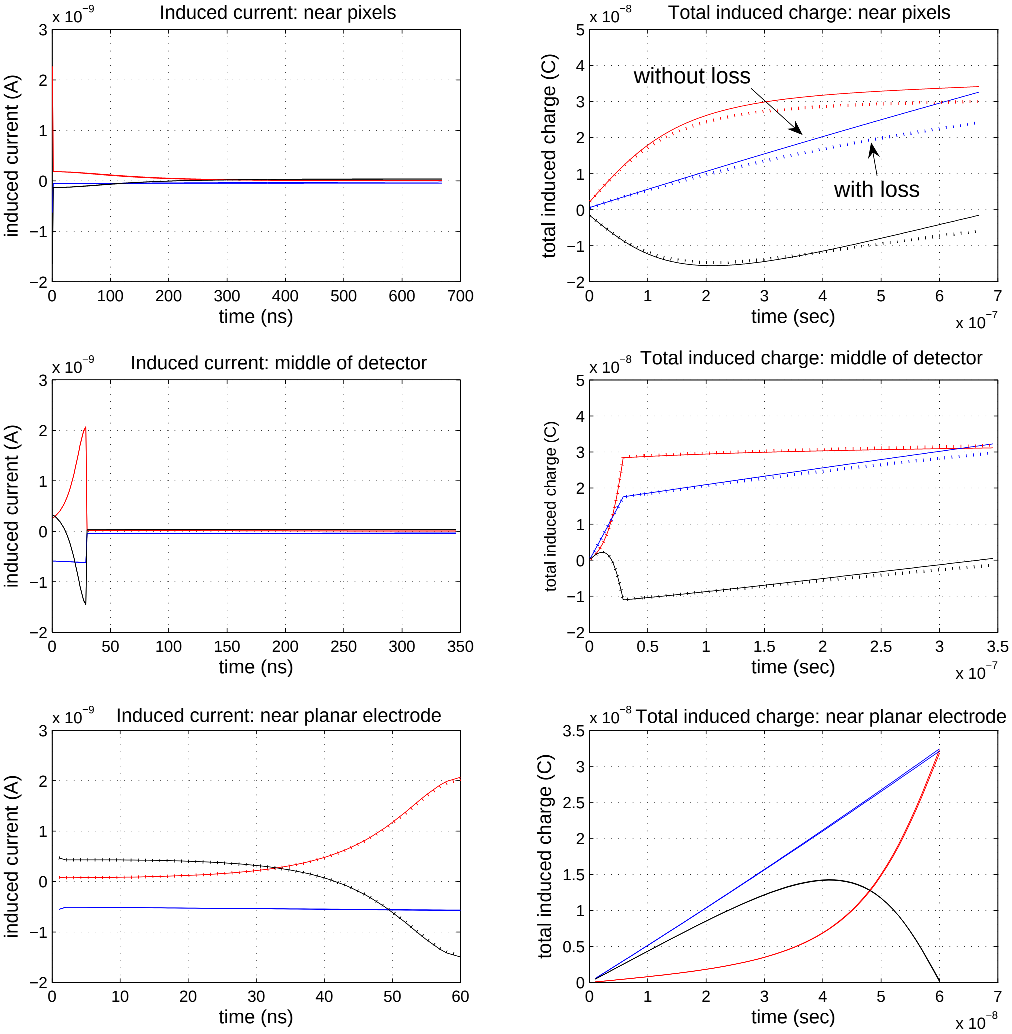

Figure 5.31: Simulated induced current and charge on the cathode (blue), pixel (red) and the total signal of neighbouring pixels plus guard ring (black), with (dotted) and without (solid) charge loss. a) Interaction near the pixel plane. b) Interaction in the middle. c) Interaction near the cathode or planar electrode.

side. The current mainly consists of a hole component (the electron induced current is slightly visible as a small peak at the start of the signal). Regarding the induced charge, we see that if no charge loss is included the cathode and pixel signal do not exactly cancel out each other. The difference is about 4.5% of the maximum pixel signal, equal to the total induced charge at neighbours and guard ring. This is not correct because theoretically these should have exactly zero induced charge.

If charge loss is included, both pixel and cathode signals get smaller but the pixel signal less than that of the cathode. Their difference is ∼19.6% of the induced charge on the pixel, and projected on the neighbours and guard ring. The two figures in the middle show the induced current and charge after an interaction in the centre of the detector. The signal has a clear electron component (the quickly rising part, as can be seen in the induced current signal), followed by a slow hole component. In case of no charge loss, the difference between cathode and pixel signal is very small, but still ~1.4% of the pixel signal. Again, this should be exactly zero. The difference in the case of charge loss, is ~4.4%.

In the two figures below, the signal is built up by electrons only. The difference in induced charge of the pixel and cathode is nearly zero, in case of no charge loss, but also if charge loss is included. Neighbouring pixels and the guard ring show no, or nearly no net induced charge.

I have not been able to completely identify why there is this limitation in the program that causes the non-zero charge induction on neighbouring pixels, if charge loss is not included. But I have seen that the situation improves (a value closer to zero) if a smaller time step is chosen. The fact that the error is larger for interactions near the pixel, presumes an involvement of the weighting field. Since this field is very inhomogeneous near the pixels, more sampling may be needed (obtained by a smaller time step, but also by a smaller grid pitch) to better simulate the signal induction in that region.

Therefore I also study the total induced charge as a function of the lateral position inside the detector. We have seen before that this also plays an important role in the total charge induction. This is illustrated in Fig. 5.32. It shows the total induced charge if we move the interaction position from the upper left corner in the centre pixel to the bottom right corner. The interaction takes place at three different depths: near the planar electrode (red), in the middle (blue) and near the pixels (black). Charge loss is not taken into account.

For an interaction near the planar electrode, the signal is independent of the position above the pixel. The charge on neighbouring electrodes is nearly zero.

If the interactions take place in the middle of the detector near the pixel plane, the induced charge is clearly influenced by the lateral position. Close to the edges and in the middle of the detector, the total charge becomes smaller while its neighbours pick up a small positive signal.

For the black curves, the situation is inversed. Moving towards the edges, leads to a relatively large increase of total induced charge while the neighbours pick up a negative signal. More information about this and related effects can be found in the paper written by Eskin, Barrett and Barber (1999).

In the following section I simulate the response of the detector after irradiation with 13.9 keV and 59.54 keV photons.

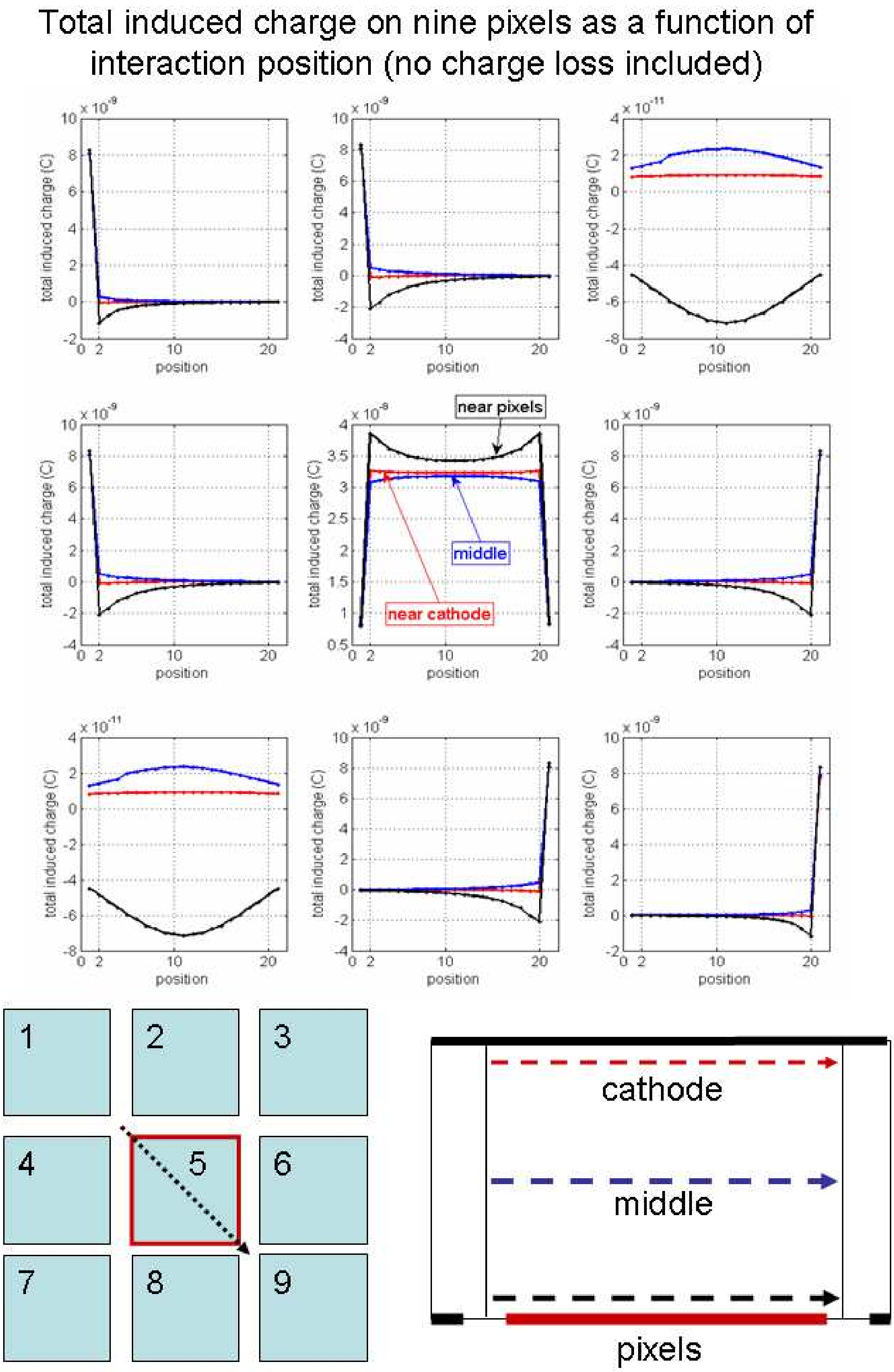

Figure 5.32: Total induced charge as a function of interaction depth and lateral position. The red curves correspond with interaction near the planar electrode, blue with interaction in the middle and black with interaction near the pixel plane. A clear dependence between the lateral position and the total induced charge exists for the blue and black curves.

5.6.4 Simulated spectrum

In GEANT4 a parallel, square photon beam is shot on a pixel of a 2 mm thick 64 pixels CdZnTe detector (see Fig. 5.33). It exactly covers the pixel surface of 0.45 × 0.45 mm^2 with uniformly distributed photons of 59.54 and 13.9 keV. By completely covering the pixel surface, I take into account every variation of the induced signal as a function of the interaction position within the pixel area.

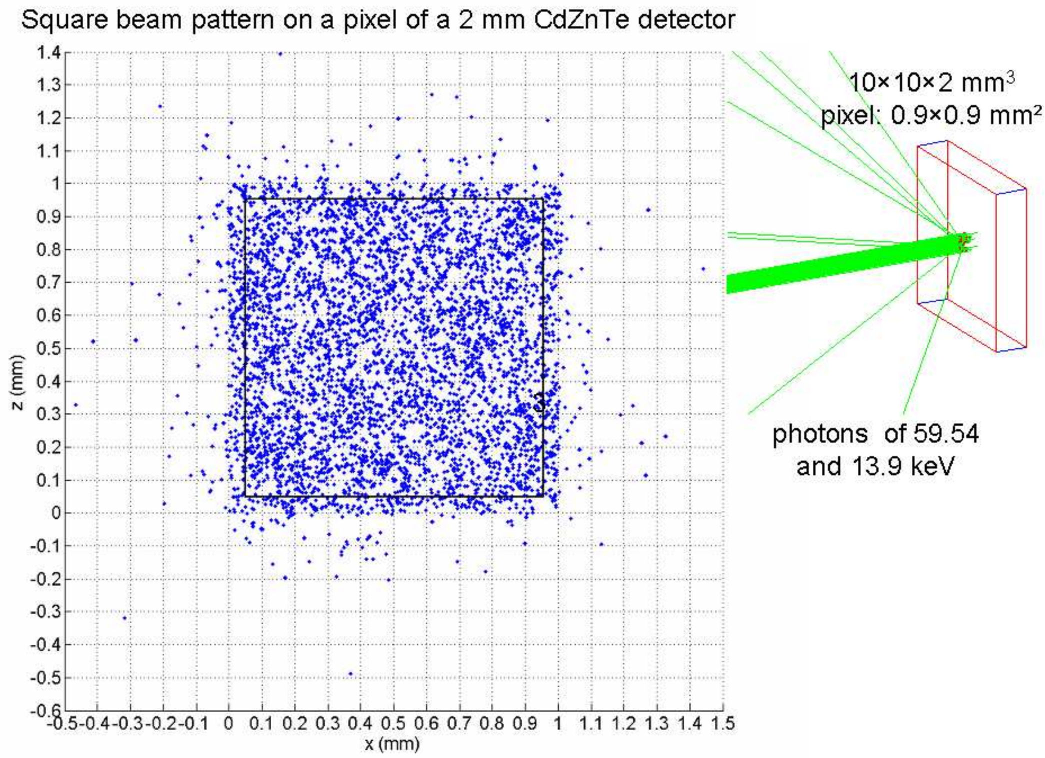

Figure 5.33: A parallel, square photon beam on a pixel of a 64 pixels CdZnTe detector. Every dot corresponds with a single interaction. The pixel surface of 0.45 × 0.45 mm^2 is uniformly radiated with photons of 59.54 and 13.9 keV. The pixel spectrum and charge sharing on neighboring pixels are studied.

With MGS-CdTe V1.0 the energy spectrum as measured by the centre pixel and its eight neighbours is simulated. The simulation is performed at a bias voltage of 500 V. The mean leakage current per pixel is obtained from the current map of Fig. 4.17 and is 12.0 ± 0.4 pA/pixel at -1.3^{o}C . Note that this measurement is taken at 450 V. I use interpolation to get a current of 13.4 ± 0.4 pA at 500 V, by assuming that no leakage current is present at zero bias.

The current in the cathode is equal to the sum of all pixel and guard ring currents: ∼3.1 nA (500 V, -1.3^{o}C).

To obtain the corresponding electronic noise of IDeF-X V1.0 at 13.4 pA and 3.1 nA, I use Fig. 4.8 again, which was discussed in Sect. 4.3.2. The ENC at 13.4 pA/pixel varies between 67 and 83 e$^-$ depending on the input capacitance. The capacitance of a single

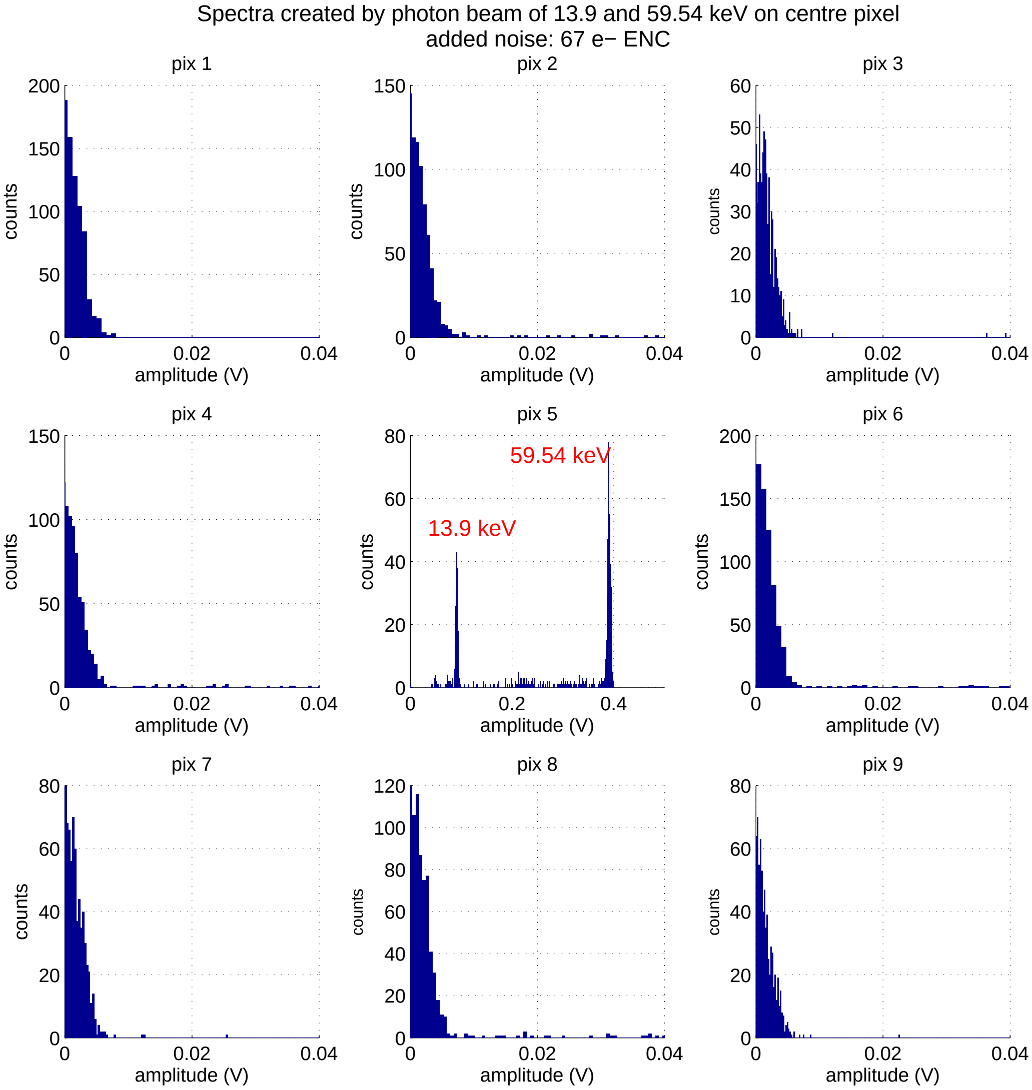

Figure 5.34: Simulated energy spectra created by the square beam with photon energies of 13.9 and 59.54 keV. Only the touched pixel plus its direct neighbours are studied. Clearly visible, is the charge sharing on neighbouring pixels.

pixel of a CdZnTe detector is ∼44 fF, and can therefore be neglected. The corresponding noise is then 67 e^- ENC. For 3.1 nA I take a 155 e^- ENC noise. Both values are added to the simulated output signals.

The spectra of the centre pixel and its eight neighbours are obtained by taking the (positive) maximum amplitude of the simulated output signals of the electronics, and representing them in a histogram. This is shown in Fig. 5.34, for the 59.54 and 13.9 peak. We clearly see that neighbouring pixels also pick up a part of the signal, either by a physical interaction taking place above its volume, or due to charge induction due to charge loss. The simulated pixel energy resolution is ∼0.90 keV (FWHM) at 13.9 keV and ∼1.06 keV

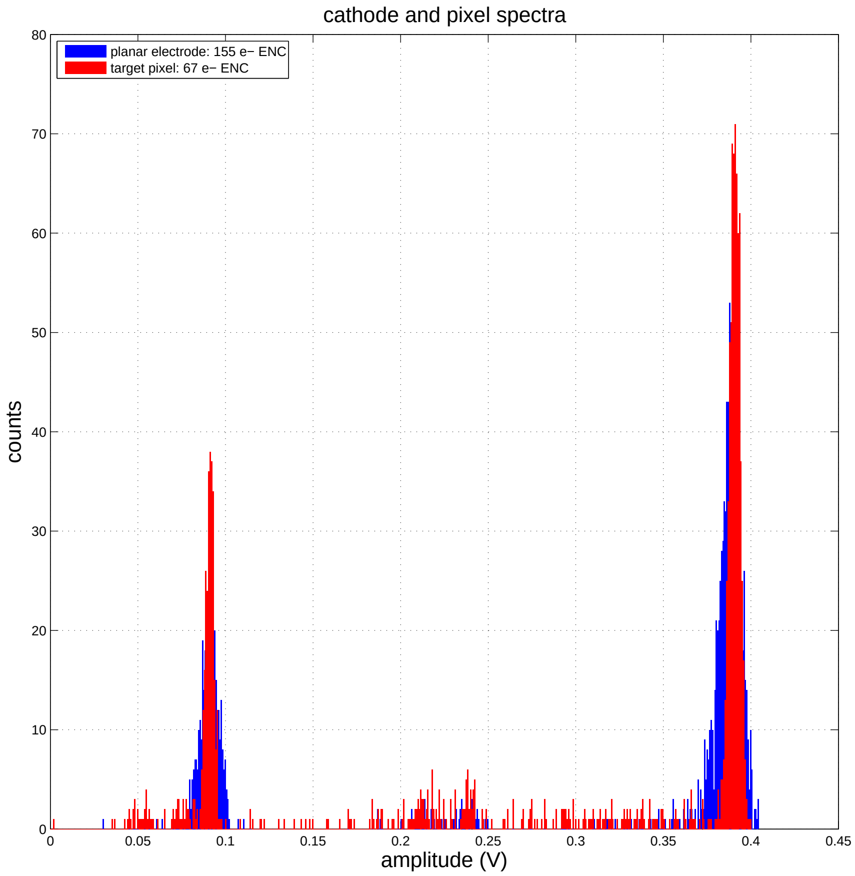

Figure 5.35: The energy response of the cathode compared with that of the centre pixel at 13.9 and 59.54 keV. The current in the cathode is the sum of pixel currents plus the guard ring. Therefore its corresponding noise is much higher than in the pixel. The result is a pixel energy resolution of ∼0.90 keV at 13.9 keV and ∼1.06 keV at 59.54 keV, and for the cathode ∼1.87 keV and 2.18 keV, respectively. The latter shows a tail to lower energies due to (hole) charge trapping which is not present in the pixel peak thanks to the small-pixel-effect.

at 59.54 keV. The measured mean resolution, at 500 V, -1.3^{o}C , 9.6 μs (see Fig. 4.29), was ∼1.6 keV at 59.54 keV.

In Fig. 5.35 I show the comparison between the response of the cathode and the centre pixel. Due to the larger current and exposure to (hole) charge loss (which is not the case for the pixel), the energy resolution of the cathode is ∼1.87 keV at 13.9 keV and 2.18 keV at 59.54 keV.

Like with the CdTe Schottky detector I also calculated the expected energy resolution of an individual pixel, as a function of the electronics noise. This is shown in Fig. 5.36. My model predict that in order to stay below the Simbol–X requirement of 1.3 keV (FWHM) at 59.54 keV, the maximum electronics noise in a single pixel may not exceed ∼95 e^-

ENC, corresponding with 300 pA/pix. The best resolution that can be obtained, is ~0.48 keV (FWHM) at 13.9 keV and 0.78 keV at 59.54 keV, at the IDeF-X ASIC intrinsic noise limit of 32 e^- .

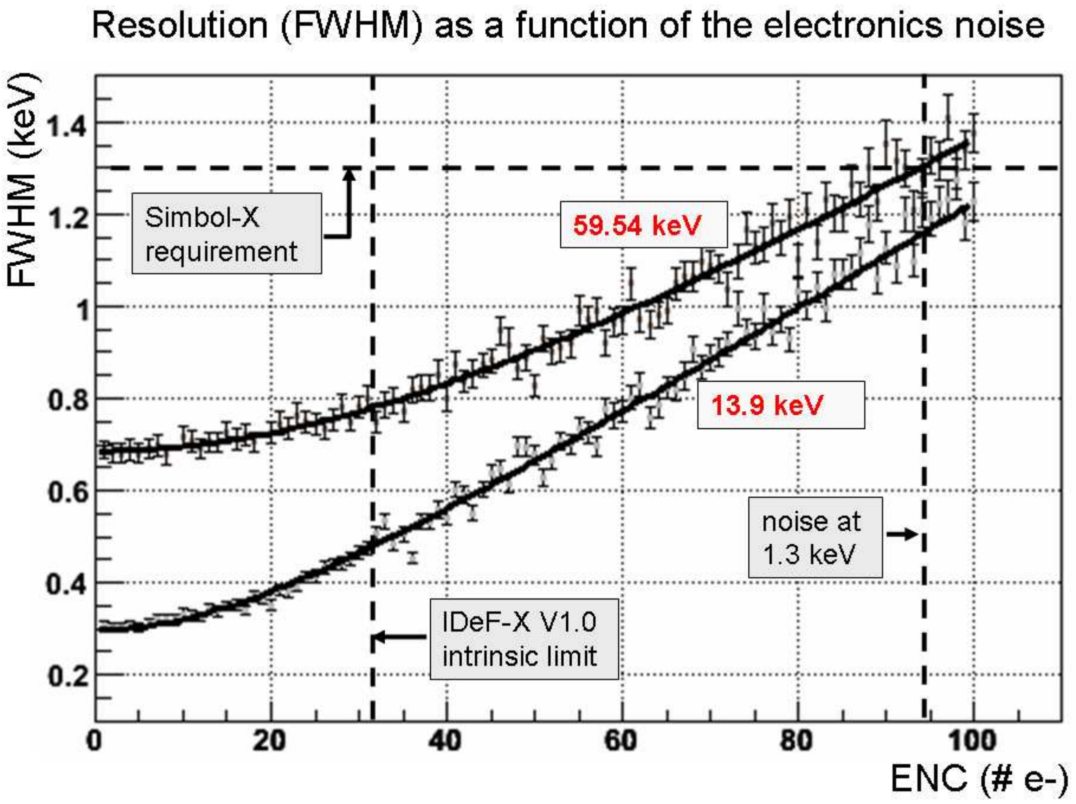

Figure 5.36: The simulated energy resolution (FWHM) at 13.9 and 59.54 keV as a function of the electronics noise, of an individual pixel of a CdZnTe detector, 9.9 × 9.9 × 2 mm^3, pixel size 0.9^2 mm^2, biased at 500 V.

5.7 Limitations

5.7.1 Sampling

I have shown that the program does not correctly simulated the predicted signals, if interactions take place close to the pixel plane. To my opinion, this is related to an insufficient sampling of the trajectory of the charge carriers in the inhomogeneous weighting field region, close to the pixels. As an argument I use the fact that decreasing the time step leads to improved results.

Related to this is the simulation of the end of the particle's trajectory. It is divided into discrete steps which size depends on the chosen step-in-time, $\triangle t$, multiplied by the velocity, v, at that point. In the optimal case ($\triangle t \rightarrow 0$) the trajectory should exactly end at the electrode (either the cathode or pixel). In the simulation I am limited to time steps of 1 and 0.1 ns otherwise the calculation time becomes too long. This means that the distance between electrode and the last possible step has a maximum of $\triangle t \cdot v$. The signal induced within this distance is not included in the total induced current. To my opinion this can partly explain the non-zero induced charge on neighbouring pixels.

A solution may be to calculate the exact distance to the electrode which misses and to interpolate the velocity and weighting field with a finer grid in this part of the trajectory. By adding the induced signal of this last part to the rest of the signal, may lead to a better results. Further investigation is necessary.

A better sampling can of course also be obtained by increasing the size of the matrix, which simulates the detector. I used a minimum distance between two grid points of 0.05 mm. This was possible for the single pixel CdTe Schottky detector, but not for the 64 pixels Cd(Zn)Te detectors. I had to use a 0.1 mm pitch, otherwise the matrix became too big. For 1 mm^2 pixels this is still reasonable (10 points per pixel), but for smaller pixel size this can become a very critical parameter.

A solution could be to make a zoom on the detector by simulating only a limited number of pixels. The problem with this method is, that one has to change the border conditions, otherwise a continues transition between the pixels in the zoom and the rest of the detector is not guaranteed. This would lead to border effects (e.g. non-homogeneous electric field) at positions which normally would not be exposed to that.

5.7.2 Calculation time

The simulation of interactions in GEANT4 is very fast and does not cause any problems. The bottleneck is MGS–CdTe. First of all, the calculation of the weighting fields of all electrodes of a 64 pixels detector, takes a lot of time (half a day). The study of different detector geometries is therefore a time consuming task. If one is only interested in a qualitative study of the detector response, a 2-D approach is more appropriate. For example, the results presented in Fig. 5.15 and 5.15, have been obtained in this way.

The calculation of the charge carrier trajectories is a long process as well. I think that this can be accelerated by a modification of the algorithm.

Chapter 6

Conclusions & Perspectives

The work presented in this thesis has been performed within the research and development of the high energy camera for the Simbol–X space mission. The aim is to construct an X-ray mini-camera that will operate in the energy range from 5 to 80 keV. An energy resolution of 1.3 keV (FWHM) at 68 keV is demanded, which is especially important for the detection of the ^{44}Ti lines. Small pixels of $\sim$500 × 500 mm^2 are necessary to cover the full point-spread function, which size depends on the chosen focal length and mirror quality.
To achieve this, custom made electronics, with extremely low noise, connected to high quality CdTe or CdZnTe crystals are necessary. Moreover, operation in space demands a design which is radiation hard and which has a low power consumption.

Therefore, I formulated the following objectives at the beginning of my thesis: first of all, to have a complete understanding of the functioning of the read-out electronics and the Cd(Zn)Te semiconductor detectors. Second, to perform a detailed characterisation (of noise and spectroscopic performances) of both. This includes the development of the necessary measurement tools. And third, the most challenging, to create a complete detector simulation program, from photon interaction, to the electronics read-out.

I have shown that we successfully designed and tested a fully functional read-out electronics: the IDeF-X V1.0 ASIC. The 16-channels chip is constructed using standard AMS technology and is designed to be DC coupled to low capacitance multi-pixel Cd(Zn)Te detectors.
Although radiation hardness and low power consumption are very important, the decision was made in this early stage of the research to give low noise performance the top priority. Nevertheless, the electronics shows already good radiation hardness to 1.17 and 1.33 MeV gamma-rays, at a 1 krad/h dose rate and up to 224 krad of accumulated dose. The absorbed dose for Simbol–X after three years in orbit, is expected to be $\sim$10 krad. No degradation is seen at that level.
The power consumption is $\sim$2.3 mW/channel, which is comparable with that of ISGRI, but will be optimised in the next prototypes. For Simbol–X the power consumption must

be limited to ∼1 mW per channel.

To test the noise characteristics of the ASIC, the Equivalent Noise Charge (ENC) as a function of the input capacitance and leakage current has been measured. The intrinsic noise is 32 e^- ENC per channel, and rises up to ∼66 e^- if connected to a single pixel CdTe Schottky detector ($4.1 \times 4.1 \times 0.5$ mm^3), which is biased at 330 V at 22^{o}C . The extra noise is created by a leakage current of ∼15 pA and by the ∼2.7 pF capacitance of detector and housing.
I showed that the noise is very sensitive to the input capacitance and leakage current. Since the capacitance of Cd(Zn)Te detectors is very small (<1 pF), the leakage current is the most important source of noise. It was therefore very important to know its value in the individual pixels of multi-pixel Cd(Zn)Te detectors, that are DC connected to the ASIC.
Therefore, I constructed a dedicated electronics circuit able to precisely measure (in the order of pA) the small leakage current per pixel. Current maps of different detectors have been presented. The mean current per pixel ranges from less than 100 fA at -12^{o}C , -250 V, up to 100 pA, 20^{o}C , -500 V, with standard deviations varying from less than 10 fA at the lowest temperatures and voltages, up to several pico-amperes for higher values.
Using the relation between current and temperature, the current maps have been translated to energy activation maps, which are a representation of the impurities inside the crystals. A 2 mm thick CdZnTe detector showed a mean activation energy of 0.65 ± 0.03 eV, and 0.76 ± 0.04 eV if the detector is 6 mm thick. These values are close to the intrinsic activation energy equal to half of the band-gap (∼0.78 eV).
An activation energy of 0.47 ± 0.04 eV was measured using the guard ring current. This relatively low value is due to the surface impurities which need less energy to be activated. The tool has become indispensable for characterising detectors at different operating conditions and is now used to control the interconnections between pixels and substrate as well.

Spectroscopic measurements have been made with the IDeF-X V1.0 ASIC connected to different types of detectors. A single pixel CdTe Schottky detector showed an excellent energy resolution of 1.0 keV (FWHM), at 59.54 keV. The best results for pixelated detectors were obtained with a CdTe detector having 64 diced indium pixels, which showed a mean resolution of 1.2 keV at 59.54 keV.
Although the Simbol–X requirement of 1.3 keV at 59.54 keV is easily achieved with these detectors (regarding their mean resolution), we see that there exists a large spread in performance between pixels. For the diced indium CdTe detector, several pixels showed an excellent resolution of less than 1 keV (FHWM) at 59.54 keV, while others only reached ∼4 keV (FWHM).
For Simbol–X, uniformity in the detector performance is extremely important. Improvement is therefore necessary. Ironically, it is not the detector current or its capacitance, neither the electronics, but the setup (substrate, connections, wires, etc.) that has be-

come the limiting factor in the mean performance and its spread. Especially the CdZnTe detectors mounted on standard epoxy material (FR4) were noisier and experienced more problems related to the pixel-substrate connection, than the CdTe detectors on high quality RO4003 substrate, taking advantage of the very low dielectric losses.
This is why the choice between CdTe or CdZnTe for Simbol–X cannot be made yet. Both materials have the potential, and CdTe already showed, to be able to fulfil the requirements for Simbol–X. All future crystal samples will therefore be mounted on RO4003, and equipped with the custom flex kapton, to allow proper comparison.
The above problems will probably not concern the final X-ray mini-camera for Simbol–X, since crystals and electronics will be directly connected to each other, with minimised intermediate connections (only 5 mm long instead of several centimeters).

In parallel to the above electronics and detector characterisation, I developed a complete simulation chain, from photon interactions in the crystal, charge carrier creation and transport, signal induction, up to the read-out electronics output, including the transfer function and noise calculation. The tool is mandatory to better understand the detector behaviour, but it is also used to predict and optimise the spectroscopic performances of existing and non-existing detector geometries.
It has been constructed in such a way that every element and every parameter can be controlled individually. Its segmented architecture gives the possibility to replace individual blocks. For example, the geometry file can easily be replaced by another one, or, if one wants to use other read-out electronics, the impulse response function just has to be changed, once it is calculated and tabulated.
To validate the program, simulated data has been compared with measurements on real detectors, and show excellent agreement.
The spectroscopic performances of single pixel CdTe Schottky and 64 pixels Cd(Zn)Te detectors, as a function of the electronics noise, are predicted and verified with actual measurements.
The program has been used to study signal induction in single and multi-pixels detectors. This gave important information on charge sharing and event multiplicity. I showed that it is absolutely necessary to read-out the triggered pixel and its eight neighbours, in order to measure the total (∼99.7%) induced signal.
Furthermore, the program confirmed the existence of bipolar signals on neighbouring pixels. Since the normal and weighting fields inside the real detector can be properly simulated, the shape and amplitude of these signals can be used to obtain more information about the interactions. This concerns an improved knowledge of the interaction position, timing and amount of charge loss. It is very important to study this in detail, because this may have important implications for the design of the next generation read-out electronics, as well as for the Simbol–X electronics architecture, data rate and performances.
First of all, the present version of IDeF-X can measure only one signal polarity. This means that only a part of the bipolar signal can be seen. Secondly, this last statement is only true if the low energy threshold of the electronics is sufficiently low, otherwise

nothing can be seen. In the laboratory, we achieved to obtain a low energy threshold of ∼1.5 keV (in practice this means ∼4 keV for the flight version, when all systems margins are taken into account). As illustrated in Fig. 5.30, the signals on neighbouring pixels are in general a factor of 1000 smaller (and with opposite sign) than the signals on the target pixel. A very low energy threshold is therefore mandatory, or one should consider the use of special filtering stages correlated in time.
A third consequence is that instead of using a pure analogue read-out, we may have to use digital electronic filtering. This means sampling the signal (instead of taking its maximum alone) and would therefore lead to a better knowledge of its shape. However, this has consequences again on the data collection and power consumption. My simulation tool, providing the signal shapes, will help to specify the design parameters for such filters.

For the next version of MGS-CdTe, it would be very interesting to implement measured current maps. In this way, the performance of every pixel can be simulated with its proper noise. Related to this, is the implementation of the complete detector and electronics noise model. Instead of adding the noise to the final simulated output signal, the noise simulation would be an integral part of the complete simulation chain.
Furthermore, in order to reduce the computing time, it would be a good idea to start a database with simulated detector characteristics (normal electric and weighting fields) of fixed detector geometries. During a simulation, the program can access the database to look for existing data and use it, without having to re-compute the same data again.
One should also study the possibility to integrate MGS–CdTe into the general simulation program of Simbol–X. It uses a complete geometrical model of Simbol–X, mainly to study particle background levels inside the different satellite components.

The fruit of the research described in this thesis will of course be the hybridisation of electronics and crystals in a compact X-ray mini-camera. A first prototype, named Caliste, which has been developed in cooperation with an industrial partner, will be delivered soon. It is an extremely compact ($10 \times 10 \times 20$ mm^3) and lightweight mini-camera. Eight modules, each having 2×4 of such cameras will eventually cover the focal plane of Simbol–X and help us to reveal the secrets of the hard X-ray Universe.

To summarise: in this study I have showed that I completely understand the detector and read-out electronics. I have shown that the strict and exigent requirements for Simbol-X are in reach, already with our prototype detectors and ASIC. My simulation program will be an indispensable tool for further development and study, and I can say, without doubt, that we will be able to successfully construct the high energy camera for Simbol–X. The goals have been reached.

References

Bélanger et al. (2004, February). Detection of Hard X-Ray Emission from the Galactic Nuclear Region with INTEGRAL. *apjl 601*, L163–L166.

Bell et al. (1974). Time-dependent polarization of cdte gamma-ray detectors. *NIM 117*, 267–271.

Chang and Sansen (1991). *Low-Noise Wide-Band Amplifiers in Biploar and CMOS Technologies*. Kluwer Academic Publishers. ISBN: 0-792-39096-2.

Churazov et al. (2006, August). INTEGRAL observations of the cosmic X-ray background in the 5-100 keV range via occultation by the Earth. *A&A*.

Dirks et al. (2006, November). Leakage current measurements on pixelated CdZnTe detectors. *Nuclear Instruments and Methods in Physics Research A 567*, 145–149.

Dirks et al. (2006, July). The focal plane of the Simbol-X space mission. In *Millimeter and Submillimeter Detectors and Instrumentation for Astronomy III. Edited by Zmuidzinas, Jonas; Holland, Wayne S.; Withington, Stafford; Duncan, William D.. Proceedings of the SPIE, Volume 6276, pp. 627617 (2006).*

Dirks et al. (2004, September). 3D modeling of Cd(Zn)Te detectors for the Simbol-X space mission. In A. D. Holland (Ed.), *Optical and Infrared Detectors for Astronomy. Edited by Garnett, James D.; Beletic, James W. Proceedings of the SPIE, Volume 5501, pp. 412-422 (2004).*, pp. 412–422.

Eskin, Barrett and Barber (1999, January). Signals induced in semiconductor gamma-ray imaging detectors. *Journal of Applied Physics 85*, 647–659.

Fano (1947, July). Ionization Yield of Radiations. II. The Fluctuations of the Number of Ions. *Physical Review 72*, 26–29.

Ferrando et al. (2004). SIMBOL-X, a new generation hard X-ray telescope. Volume 5168 of *Proc. SPIE*, pp. 65–76.

Ferrando et al. (2006). SIMBOL-X: mission overview. Volume 6266-17 of *Proc. SPIE.*

Fraboni (2005, December). Recovery of radiation damage in CdTe detectors. *IEEE Transactions on Nuclear Science 52*, 3085–3090.

Fraboni et al. (2006, August). Time and thermal recovery of irradiated CdZnTe detectors. *Semiconductor Science Technology 21*, 1034–1040.

Gehrels et al. (2004, August). The Swift Gamma-Ray Burst Mission. *ApJ 611*, 1005–1020.

Gevin et al. (2005). IDeF-X V1.0: Performances of a New CMOS Multi Channel Analogue Readout ASIC for Cd(Zn)Te Detectors. Volume 1 of *Nuclear Science Symposium Conference Record, 2005 IEEE*, pp. 433 – 437.

Giacconi and Gursky (1962). Evidence for X-rays from sources outside the Solar System. *Physical Review Letters 9-11*, 439–+.

Hasinger (2000). X-ray Surveys of the Obscured Universe. *LNP Vol. 548: ISO Survey of a Dusty Universe 548*, 423–+.

Jansen et al. (2001, January). XMM-Newton observatory. I. The spacecraft and operations. *A&A 365*, L1–L6.

Knoll (2000). *Radiation Detection and Measurement.* John Wiley & Sons. ISBN: 0-471-07338-5.

Lebrun (2005). The ISGRI CdTe gamma camera in-flight performance. *IEEE Transactions on Nuclear Science 52-6.*

Lebrun et al. (1996, October). ISGRI: a CdTe array imager for INTEGRAL. In B. D. Ramsey and T. A. Parnell (Eds.), *Proc. SPIE Vol. 2806, p. 258-268, Gamma-Ray and Cosmic-Ray Detectors, Techniques, and Missions, Brian D. Ramsey; Thomas A. Parnell; Eds.*, pp. 258–268.

Lebrun et al. (2004, March). Compact sources as the origin of the soft γ-ray emission of the Milky Way. *Nature 428*, 293–296.

Limousin (2001). *Mise en œuvre et étude des propriétés spectrales de la gamma-caméra ISGRI.* Ph. D. thesis, Université de Toulouse III.

Limousin et al. (2005). IDeF–X ASIC for Cd(Zn)Te spectro-imaging systems. *IEEE Transactions on Nuclear Science 52-5.*

Luke, Amman and Lee (2004). Factors Affecting Energy Resolution of Coplanar-Grid CdZnTe Detectors. *IEEE Transactions on Nuclear Science 51.*

Lutz (1999). *Semiconductor Radiation Detectors.* Springer. ISBN: 3-540-64859-3.

Manach (2005). *Etude, tests et mise au point d'un détecteur semi-conducteur pixélisé en mode comptage pour l'imagerie gamma dans les installations nucléaires.* Ph. D. thesis, Université de Caen/Basse-Normandie.

Medina et al. (2004). A simple method for the characterisation of HPGe detectors. Instrumentation and Measurement Technology Conference.

Pareschi et al. (2005, August). Development of grazing-incidence multilayer mirrors by direct Ni electroforming replication: a status report. In O. Citterio and S. L. O'Dell (Eds.), *Optics for EUV, X-Ray, and Gamma-Ray Astronomy II. Edited by Citterio, Oberto; O'Dell, Stephen L. Proceedings of the SPIE, Volume 5900, pp. 47-58 (2005).*, pp. 47–58.

Reitz, Milford and Christy (1993). *Foundations of electromagnetic theory.* Addison-Wesley Publishing Company, Inc. ISBN: 0-201-52624-7.

Renaud et al. (2006, August). The Signature of ^{44}Ti in Cassiopeia A Revealed by IBIS/ISGRI on INTEGRAL. *ApJ 647*, L41–L44.

Schanne et al. (2004). The space borne multi-wave-length gamma-ray burst detector ECLAIRs. Proc. IEEE NSS-MIC.

Schmitt et al. (1991, February). A soft X-ray image of the Moon. *Nature 349*, 583–587.

Strüder et al. (2006). Active X-ray pixel sensors with scalable pixel sizes from 1 μm^2 to 10^8 μm^2 in Heaven and on Earth. Volume 6276-48 of *Proc. SPIE.*

Tanaka et al. (2004, February). Recent achievements of the high resolution Schottky CdTe diode for γ-ray detectors. *New Astronomy Review 48*, 309–313.

Weisskopf et al. (2003, August). An Overview of the Performance of the Chandra X-ray Observatory. *Experimental Astronomy 16*, 1–68.

Winkler et al. (2003, November). The INTEGRAL mission. *A&A 411*, L1–L6.

Samenvatting

De internationale gemeenschap van astrofysici heeft dringend behoefte aan een nieuw instrument om meer inzicht te krijgen in the oorsprong van de kosmische Röntgen achtergrondstraling, the fysica van zwarte gaten en deeltjes acceleratie mechanismen, in het energie gebied van 0.5 tot 80 keV. Bestaande instrumenten, als Chandra en XMM-Newton, laten zeer goede resultaten zien tot ongeveer 10 keV, maar hebben onvoldoende gevoeligheid daarboven. Om dezelfde prestaties te behouden, of zelfs te overtreffen, tot aan energieën van ∼80 keV, moeten speciale spiegels worden toegepast, die de energetische straling kunnen reflecteren door gebruik te maken van een scherende invalshoek. Dit vereist een brandpuntsafstand van minstens 20 m. Satellieten van deze grootte kunnen niet door bestaande raketten worden gelanceerd. Daarom worden de spiegel en detector op twee aparte satellieten gemonteerd die in formatie vliegen. De Simbol–X ruimtemissie zal het eerste project van dit type zijn.

Een optimale gevoeligheid voor energieën tot aan 80 keV kan niet alleen worden bereikt met een grote brandpuntsafstand, maar vraagt ook een detector met een hoge ruimtelijke resolutie, waarbij de detectie efficiëntie gewaarborgd blijft. CEA/Saclay/DAPNIA ontwikkelt dit cruciale element voor de Simbol–X missie.

De spectro-imager bestaat uit verschillende modules, elk opgebouwd uit individuele Röntgen mini-camera's. Een camera is een hybridisatie van speciaal voor dit doeleinde ontwikkelde uitlees-elektronica gekoppeld aan een Cd(Zn)Te halfgeleider kristal. Het geheel moet in staat zijn om efficiënt fotonen te detecteren tot aan 80 keV, met een energie resolutie van ∼1.3 keV (FWHM) bij 68 keV. The kristallen moeten verder worden uitgerust met kleine pixels ($\sim 500 \times 500\ \mu\mathrm{m}^2$) om de 15 arcsec. ruimtelijke resolutie te bereiken. Optimale gevoeligheid en goede spectrale resolutie vereisen elektronica met een extreem lage interne ruis, in combinatie met halfgeleider kristallen van zeer goede kwaliteit.

De uitlees elektronica, IDeF-X, staande voor *Imaging Detector Front-end for X-rays*, wordt ook door de CEA/Saclay ontwikkeld. Een grondige kennis van zijn werking en een uitvoerige test campagne vormt een gedeelte van het gepresenteerde werk.

De spectroscopische prestaties van de detector unit zijn direct gerelateerd aan de hoeveelheid elektronische ruis. De ruis karakteristieken van de ASIC zijn daarom uitgebreid onderzocht als functie van de ingangscapaciteit en de ingangsstroom, twee belangrijke ruisbronnen. Gezien het feit dat de chip DC aan een Cd(Zn)Te kristal wordt gekoppeld, is het erg belangrijk te weten, wat de waarde van de lekstroom per pixel is die door de elektronica zal stromen.

Om deze extreem kleine stroompjes (in de orde van $\sim 10^{-12}$ A) in 64 Cd(Zn)Te detectoren precies te kunnen meten, heb ik speciale elektronische circuits ontwikkeld. De pixelstroompjes zijn gerepresenteerd in zogenoemde "stroommaps". Deze zijn verkregen met verschillende detectoren in diverse randcondities. De relatie tussen de stroom en de temperatuur geeft de mogelijkheid om activerings-energie van het kristal per pixel te verkrijgen, wat resulteert in activerings-energie mappen. Verder dienen de metingen aan de pixelstroom, om de mechanische eigenschappen van de connectie tussen pixel en substraat te onderzoeken.

De spectroscopische prestaties van verschillende 64 pixels CdTe en CdZnTe kristallen zijn verkregen door deze te koppelen aan vier volledig functionerende 16-channels IDeF-X V1.0 ASICs. De resultaten leveren de optimale randcondities (bias spanning, piektijd van elektronica, temperatuur) om de beste energie resolutie bij 60 keV te verkrijgen (energie piek van een ^{241}Am bron). Een CdTe detector (360 V bias, 22^{o}C) met slechts één pixel, laat een uitstekende energie resolutie van 1 keV (FWHM) zien. Dit resultaat is ook bereikt met verschillende individuele pixels van een 64 pixels CdTe detector (400 V bias, -18^{o}C) met gezaagde indium pixels.

Om de werking van de detector beter te kunnen begrijpen en om voorspellingen te kunnen doen van zijn prestaties, heb ik een compleet simulatie programma geschreven. Deze start met de simulatie van foton interacties in het kristal en vervolgt deze tot aan de output van de elektronica. Ik combineer daarvoor GEANT4 om individuele interacties in Cd(Zn)Te te simuleren en MGS–CdTe V1.0 om de productie van elektron-gaten paren, ladingsdrager transport, ladingsverlies en de inductie van signalen op de elektrodes te simuleren. Door de gesimuleerde geïnduceerde stroom te convolueren met de impulse response van de IDeF-X ASIC, wordt een complete detector response verkregen. Gesimuleerde energie spectra zijn vergeleken met metingen en vertonen uitstekende gelijkenis.

GEANT4 en MGS–CdTe worden ook gebruikt om individuele aspecten van de detector te bestuderen, waaronder de grootte van de ladingswolk na een interactie, de multipliciteit van interacties en de detectie efficiëntie.

Het simulatie-programma dient als een krachtig hulpmiddel voor het voorspellen van geïnduceerde signalen, het bepalen van de mate van interferentie tussen pixels en voor het definiëren van een pixel uitleesstrategie voor Simbol–X.